THE UNIVERSITY *of* EDINBURGH

Electrochemical Deposition of Small Molecules for Electronic Materials

Emily Marieke Allwright

Thesis submitted for the Degree of PhD

The University of Edinburgh

October 2014

Declaration

I hereby declare that this thesis was composed by myself and that the work described within is my own, except where clearly mentioned otherwise. It has not been submitted in whole or in part for any other degree, diploma or qualification.

Emily Marieke Allwright

October 2014

The most exciting phrase to hear in science, the one that heralds new discoveries, is not ‘Eureka!’ but ‘That’s funny...’

Isaac Asimov

Acknowledgments

First and foremost, I would like to thank Neil Robertson for his guidance and support throughout my Masters project and then during my PhD. Over the past years he has supported me as I developed my interest in research and materials science. His help during all of my research projects has been much appreciated and his advice was invaluable when my research stalled or went off course. Thanks also for the endless proof-reading that you have done over the years.

I am particularly grateful to the *Fonds National de la Recherche,* Luxembourg for their generous funding, enabling me to continue to develop my passion for materials chemistry.

Special thanks to Phillip Dale and Dominik, Jan, João, Helen, Rabie and Marc from the Laboratory for Photovoltaics of the University of Luxembourg for their help with the analysis of my films and for trying to teach a chemist to speak physics.

I would like to thank Prof. Kunio Awaga and Prof. Michio M. Matsushita for their time and hospitality when I visited Nagoya, Japan. I would also like to thank Hirofumi Yoshikawa, Shuku, Chihiro, Shimizu and Steffen from the Research Centre for Materials Sciences & Department of Chemistry, Nagoya University for their help in the lab.

My thanks also go to:

- The Inorganic Corridor for the general banter and chats in the corridor. Everyone knows about Matt's secret stashes, right?

- The members of the Robertson Group, past and present, for their help throughout my PhD. I would especially like to thank the solar girls: Tracy, for your supervision in my Masters year and for all your advice and organising through the years, Nina for helping me with my self-confidence and Martina for the tiramisu and help with the spelling. Also thanks to visiting PhD student Michał for being an excellent flatmate and gig partner. I would also like to thank Luca for all his help as a post-Doc - glad I could help you with the Pyridine - and Georg for our general agreement.

- Kayley, Sara and Karen for their gossip and encouragement during my various fitness activities and Pam for reminding me that there are no mistakes just improvised solos, as “Anyone who has never made a mistake has never tried anything new.” - Albert Einstein.

- Anne-Marie, Anoushé and Laura for making my trips home feel like I never left.

- Dave, David, Craig, Naomi, Will, Louise, Kathleen, Jai, James, Selina and Ellie for keeping me sane and well fed during the several group dinner parties as well as keeping me watered while we mapped the pubs of Edinburgh. I’m sure the great ship Monkwood has not sailed its last party yet. You guys rock.

- Julie and Colin for being my comrades throughout my PhD. We did it guys!

- And finally my family, especially my Mum and Dad, for their beer tokens and advice throughout the years, as well as taking time out of their busy retirements to read over several drafts I have sent them. Love you both.

Abstract

The method of the deposition of films of small molecules for use in electronic applications is just as important as the molecule design itself as the film's morphology and continuity influence the performance of the devices that they are incorporated in. The purpose of the work in this thesis was to develop a method of electrochemically depositing films of small molecules for potential use in electronic applications.

A method of electrochemically depositing films of chemically reduced low solubility dye molecules was successfully pioneered. The process was developed using N,N dibutyl-3,4,9,10-perylene-bis(dicarboxime), a simplified version of 3,4,9,10-perylene-tetracarboxylic bisbenzimidalzole. Both of these dyes have been used in electronic applications, but low solubility makes them difficult to deposit by traditional solution techniques. A series of films was electrochemically deposited onto FTO coated glass and field effect transistors using coulometry. These films were characterised by absorption spectroscopy, photoluminescence, scanning electron microscopy, X-ray diffraction and photo-electrochemistry.

The same deposition method was applied to copper phthalocyanine. These films were characterised by absorption spectroscopy, photoluminescence, scanning electron microscopy and X-ray diffraction. The developed method was used to deposit films of bilayers of dyes and to investigate the dye penetration during the deposition of copper phthalocyanine onto porous titanium dioxide.

Films of neutral copper and nickel dithiolenes were electrodeposited from air-stable TMA salts to investigate the absorbance of the near infrared species formed, as well as to investigate the conductivity of both complexes and the magnetoresponse of the neutral copper dithiolene which is air unstable when formed chemically.

Content

Abbreviations

ε	Molar absorption coefficient
λ	Wavelength
^{o}	Degree
^{o}C	Degree centigrade
Ag/AgCl electrode	Silver chloride electrode
DCM	Dichloromethane
DMSO	Dimethyl sulfoxide
DSSCs	Dye-Sensitised Solar Cells
BuPTCDI	N,N dibutyl-3,4,9,10-perylene-bis(dicarboxime)
CE	Counter electrode
Cu(Ti-C2)$_2$	Copper (2-(5-butylthiophene-2-yl)-1,2-dithiolene)$_2$
CuPc	Copper (II) Phthalocyanine
DSSCs	Dye-Sensitised Solar Cells
et al.	*et alli* (and others)
EtOH	Ethanol
eV	Electron volts
FET	Field Effect Transistor
FTO	Fluorine doped Tin Oxide Glass
HOMO	Highest Occupied Molecular Orbital
I	Current
IR	Infrared
I_{SD}	Current Source-Drain
K	Kelvin
LUMO	Lowest Unoccupied Molecular Orbital
MeCN	Acetonitrile
MeOH	Methanol
Ni(Ti-C2)$_2$	Nickel (2-(5-butylthiophene-2-yl)-1,2-dithiolene)$_2$

OFET	Organic Field Effect Transistor
OLED	Organic Light Emitting Diodes
OPVs	Organic Photovoltaics
PAH	Polyaromatic Hydrocarbons
PEDOT:PSS	Poly(3,4-ethylenedioxythiophene) Polystyrene sulfonate
PTCBI	3,4,9,10-perylene-tetracarboxylic bisbenzimidalzole
PTCDI	Perylene Tetracarboxylic Diimide
Q	Charge
Qcm^{-2}	Charge per cm^2
RE	Reference electrode
SEM	Scanning electron microscopy
$TBABF_4$	Tetrabutylammonium Tetrafluoroborate
$TBA[Ni(Ti\text{-}C2)_2]$	TBA nickel (2-(5-butylthiophene-2-yl)-1,2-dithiolene)$_2$
$TMA[Cu(Ti\text{-}C2)_2]$	TMA copper (2-(5-butylthiophene-2-yl)-1,2-dithiolene)$_2$
THF	Tetrahydrofuran
TiO_2	Titanium Dioxide
UV/Vis	Ultraviolet–visible
VD	Vapour Deposition
V	Potential
V_P	Pinch-off Potential
V_{SD}	Source-Drain Potential
V_{SG}	Source-Gate Potential
WE	Working electrode
XRD	X-ray diffraction
1D	One Dimensional
2D	Two Dimensional
3D	Three Dimensional

Structures

BuPTCDI

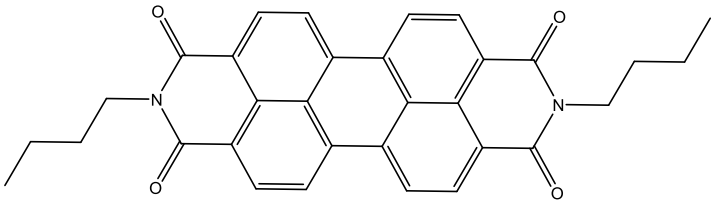

N,N dibutyl-3,4,9,10-perylene-bis(dicarboxime)

PTCBI

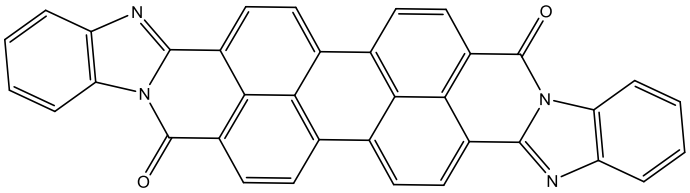

3,4,9,10-perylene-tetracarboxylic bisbenzimidalzole

CuPc

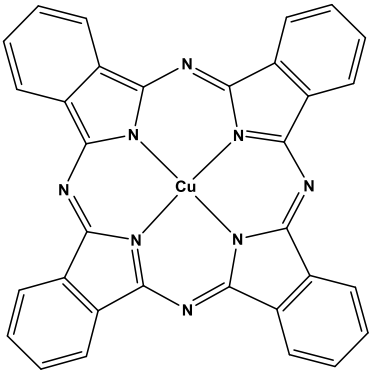

Copper Phthalocyanine

TBA[Ni(Ti-C2)$_2$]

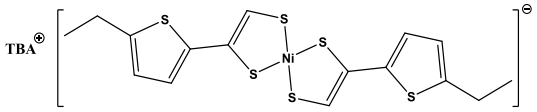

TBA nickel (2-(5-butylthiophene-2-yl)-1,2-dithiolene)$_2$

Ni(Ti-C2)$_2$

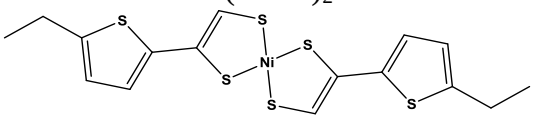

Nickel (2-(5-butylthiophene-2-yl)-1,2-dithiolene)$_2$

TMA[Cu(Ti-C2)$_2$]

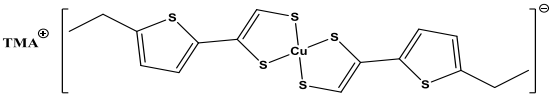

TMA copper (2-(5-butylthiophene-2-yl)-1,2-dithiolene)$_2$

Cu(Ti-C2)$_2$

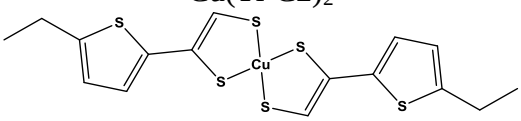

Copper (2-(5-butylthiophene-2-yl)-1,2-dithiolene)$_2$

1. Introduction

1.1. Organic Electronic Materials

At the beginning of the 20th century McCoy and Moore prepared an organic amalgam that had "Metallic Properties", opening the field of molecular electronic materials.[1] The electronic properties of organic thin films have been studied since the 1940s and they were incorporated into electronic devices and characterised in the 1970s.[2, 3]

The field of organic electronics requires the combined effort of specialists in several areas of expertise: synthetic chemistry, experimental physics, physical chemistry and theory.[4] This is because the charge-transport properties of molecules for organic electronic devices are not yet fully understood and the processes of charge transfer at all the boundaries in the devices play a key role.

1.1.1 Materials

Molecular electronic materials have to fulfil several requirements: they have to be redox stable, have a large degree of intermolecular interaction which allows the transfer of charge and have tuneable highest occupied molecular orbital (HOMO) levels and lowest unoccupied molecular orbital (LUMO) levels.

There are two main synthetic areas for molecular electronic materials: polymers and small molecules. Most small molecules are based on large carbon frameworks that result in a large delocalized π system. Currently most molecules being investigated in organic electronics can be classified as molecules made up of extended π-conjugated systems such as polyaromatic hydrocarbons (PAHs), porphyrins, phthalocyanines and perylene tetracarboxylic diimides (PTCDIs).[5] The other types of molecules are covalently bound π–n–π systems, where the π systems are part of a coordination complex such as metal dithiolenes.[6, 7] There are also other important classes of molecules such as tetrathiafulvalene and donor-acceptor molecules.

π-conjugated systems are molecules made up of fused benzene rings, which results in a large delocalized π system. Some simple PAHs are shown in Figure 1.1.

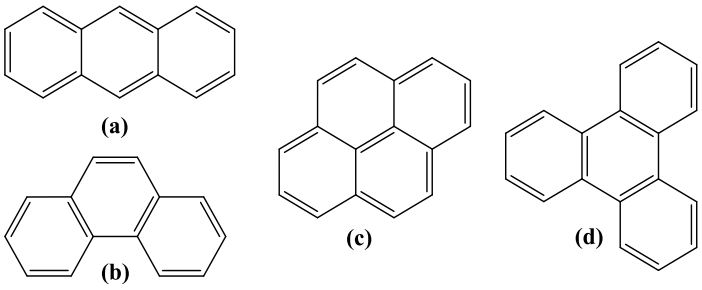

Figure 1.1: Simple PAHs: (a) anthracene, (b) phenanthrene (c) pyrene and (d) triphenylene

The small HOMO-LUMO gap of the large delocalised aromatic structures and the ability to stabilise redox processes by resonance make them one of the most studied families for organic electronics and extending the simple system to more complicated systems results in several subgroups of π-conjugated systems such as porphyrins, perylenes and PTCDIs as shown in Figure 1.2.[5]

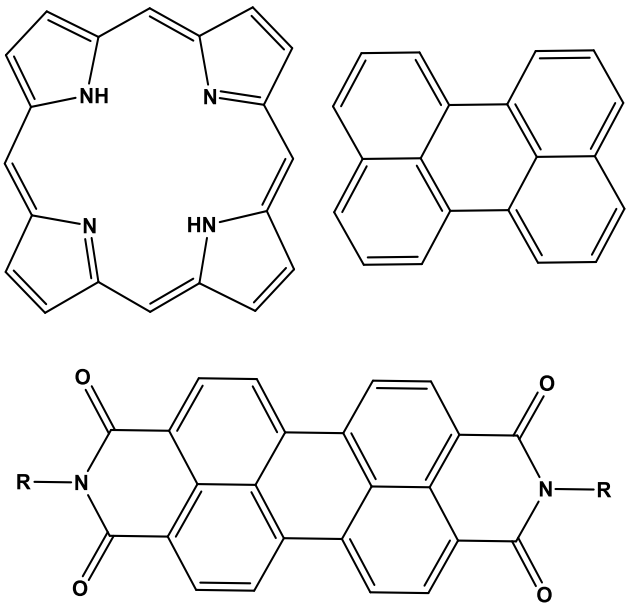

Figure 1.2: Porphyrin, perylene and PTCDI

Porphyrins, perylenes and PTCDIs have fused aromatic ring systems that allow them to create highly delocalised π systems. They are highly absorbent and can be tuned and functionalised to adjust different properties of the molecules, tailoring them to different requirements. Extending the fused aromatic system will change the HOMO and LUMO of the system resulting in a change in the electronic properties. Adding side groups and alkyl chains will change the packing in the solid form and the solubility.

Many fused aromatic systems were used in the initial investigation of electronic applications were designed as paints for outdoor use, e.g. automobile paints in the 1940s and 1950s, as their properties, such as insolubility, light and weather-fastness, thermal stability and chemical inertness, also make them suitable for organic electronics.[8] However, it was not until more recently that the first organic devices were developed: the first organic field effect transistor was reported in 1984 and the first organic bilayer device in 1986.[9, 10]

Metal dithiolenes are complexes that contain two non-innocent dithiolene ligands bound to a metal ion. The metal is bound to each dithiolene ligand via two sulfur sites, as shown in the generic complex in Figure 1.3.[5]

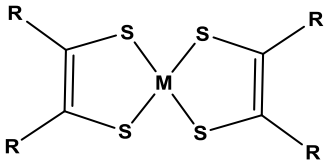

Figure 1.3: Metal dithiolene complex

With selected metal centres such as Ni, Pd or Pt, metal dithiolenes are redox stable, as shown in Figure 1.4. This has resulted in both the neutral and ionic forms of the molecules being investigated as crystalline materials at an academic level.

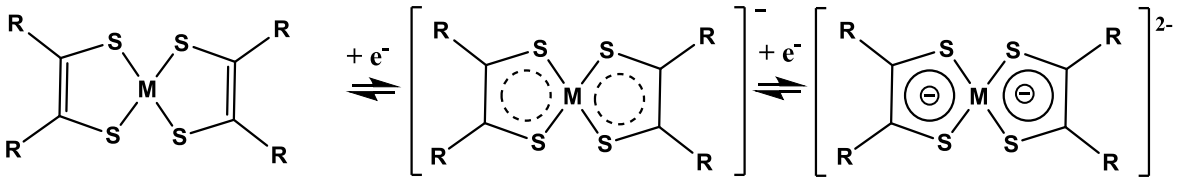

Figure 1.4: Stable redox states of metal dithiolene

The HOMO and LUMO of the molecules are mostly located on the donor ligands with the majority of the delocalised charge located on the sulfur molecules with the metal contributing slightly to the LUMO.[11]

The molecules are structurally flexible either by replacing the central metal and/or by functionalising the donor ligands. Most complexes studied for their use in molecular electronic materials have a planar arrangement. The planar structure means that they tend to form 1D columns unless the dithiolene ligand is tailored to disrupt the

stacking leading to 2D or 3D non-columnar arrangements.[11] Examples of metals contained in planar complexes include nickel, platinum, iron, cobalt and copper.[12]

1.1.2 Charge mobility

The conductivity of a molecular material, σ, can be determined by:

$$\sigma = n \times e \times \mu$$

Equation 1.1

where *e* is the electronic charge, *n* is charge carrier density and μ is the mobility of the charge carriers.[13] The mobility of the material depends on the charge transporting properties between molecules, its packing and its purity.

In organic materials the charge is transferred from site to site, with electrons being transported from HOMO to HOMO or holes being transported from LUMO to LUMO of the individual molecules and not via a delocalised conduction band responsible for the charge transport in metal and inorganic materials.[14] It has been suggested that transport occurs via polaron hopping.[15] A polaron is a localised lattice distortion produced by the electrostatic interaction of an electron or hole with neighbouring molecules.[16] If the interaction between the charge and the surrounding lattice is strong enough the charge may become trapped and only move via thermally induced hopping.[17] This means that the mobility of charges within organic materials increases with temperature contrary to inorganic materials.[16]

The packing of the molecules determines how well a charge can move through the solid and its direction. The degree of overlap in each dimension can result in different conductivities in different directions. Most planar molecules arrange in a "herringbone" arrangement as shown in Figure 1.5 (a).[18] If the material is packed in a face-to-edge, Figure 1.5 (a) (I), arrangement there is limited conductivity. This is due to the molecule interacting with only every second neighbouring molecule.[19] However, if the molecules are packed in a "herringbone" arrangement with face-to-face packing, charge transfer can occur between the stacked molecules. This is the case for most unsubstituted planar molecules used in molecular electronics such as pentacene, copper phthalocyanine and PTCDIs.[19-21] The packing of the

molecule can be changed by modifying the molecule with side groups that do not affect its HOMO and LUMO levels.[22] The side groups do not affect the delocalised π system, but sterically hinder the molecule, so it is unable to pack edge-to-surface and therefore stacks face-to-face.[23] If the side groups are small or in the same plane as the molecule the delocalised systems should stack, creating a one dimensional conduction channel, as shown in Figure 1.5 (b). The side groups have to be selected carefully so that they do not disrupt the stacking by introducing too much steric bulk.[24]

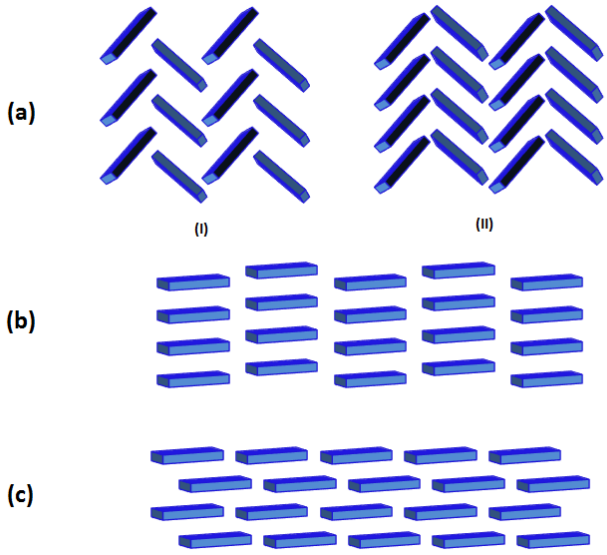

Figure 1.5: Possible stacking arrangement of planar molecules: (a) "herringbone" (I) face-to-edge arrangement and (II) face-to-face arrangement, (b) 1D columnar arrangement and (c) 2D "brick-wall" arrangement

If the side chains are designed correctly, they can cause the molecules to shift, causing the stacks to be disrupted.[25] This can result in a "brick-wall" configuration, as shown in Figure 1.5 (c), in which the molecules interact with two molecules above and below. This can form a 2-dimensional system as the charge can travel along the rows as well as up the stacks in a similar manner to graphene sheets. The design that results in the largest overlapping π system will give the best charge mobility.

The packing is not the only factor that will affect the mobility of the molecules. The presence of doping and faults will also increase or decrease the mobility by introducing or trapping charges.[26] When unintentional, the presence of extra

electrons or holes in the solid state can disrupt the flow of charges by filling vacancies or trapping electrons. This lowers the charge mobility of the solid and is why processing the molecules in a way which minimises faults and impurities is important. However, doping can also be used to enhance conductivity as it introduces extra charge carriers increasing the charge carrier density, n, in Equation 1.1. If a material is doped with extra electrons then it will become an n-type material with an excess of negative charges. A p-type material is the opposite with an excess of holes or positive charges.[27]

1.1.3 Devices

When incorporated into devices, the HOMO and LUMO energies of the molecules are just as important as the mobility as they determine the ease with which a charge can be injected into or from a material. Molecules with high energy HOMOs are good at donating electrons making them donor materials. Low energy LUMOs are good at accepting electrons making them acceptor materials.

1.1.3.1 Optical devices

Devices containing thin films of light absorbing and light emitting molecules are being investigated for several applications. Organic light emitting diodes, OLEDs, are being championed for use in the next generation of screen technology, promising thin, lightweight and bright screens, as well as flexible hand held devices such as mobile phones and e-paper technologies.[28] Due to being lightweight, flexible and low cost, excitonic solar cells that include organic photovoltaic (OPV) devices and dye-sensitised solar cells (DSSCs) could soon occupy niche markets as power sources for portable small devices.[29]

In the case of organic photovoltaics most devices contain a mixture of active materials between two electrodes, although devices with a single active material with two electrodes do exist. The advantage of a mixture is that each material can be tailored to fit one of the requirements for the device to function, rather than one material needing to fit all the requirements. The way materials are mixed can affect the efficiency of the device. They are deposited as heterojunctions which can take the form of bilayers or as mixed layers. In the case of bilayers it has been found that to maximise efficiency both layers should be around 100 nm thick and the junction

between the two materials should have the largest surface area possible.[30] The layers need to be thick enough to absorb enough light, but thin enough for the excitons, energetically bound hole and electron pairs, to reach the interface. Excitons can only migrate about 10 nm before decaying back to the ground state, meaning that devices with large interfaces perform better.[30] Three designs of bilayers are shown in Figure 1.6.

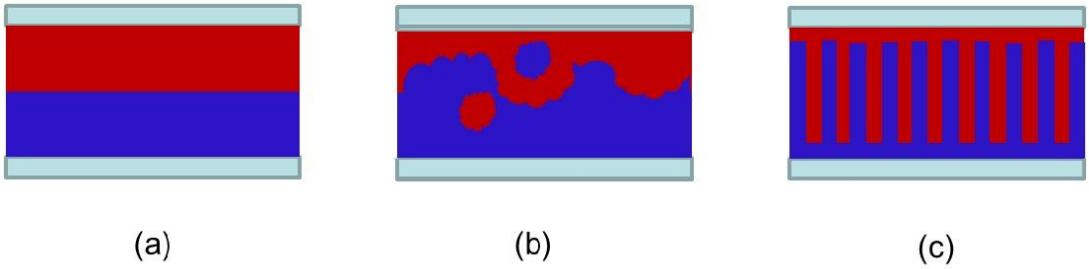

Figure 1.6: Schematic of (a) simple bilayer, (b) diffused bilayer and (c) structured bilayer

Schematic (a) shows just a simple bilayer: two films deposited on top of each other. This design is not ideal as there is only a minimum surface area between the two layers. The second schematic (b) is a diffused bilayer, where the layers are deposited unevenly or treated post deposition to make them diffuse into each other, increasing the surface area between the two. This method can result in clusters of material isolated from an electrode and in some cases it can lead to short circuiting when one of the layers is touching both electrodes. The third schematic (c) is the ideal structure of a bilayer device as the layers remain very thin, yet there is a large surface area between the two.

A scheme of the method of photocurrent generation is shown in Figure 1.7.

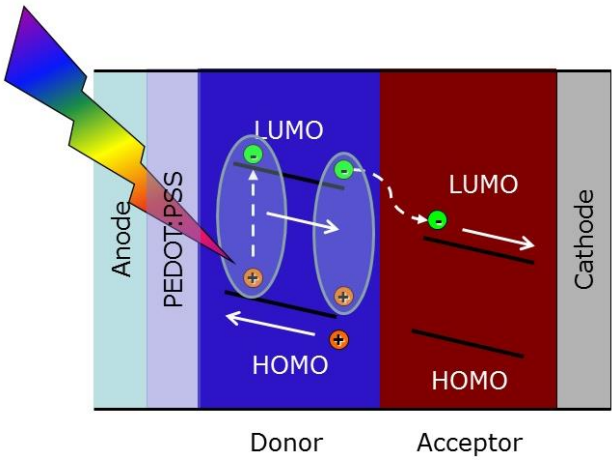

Figure 1.7: Schematic diagram of the photocurrent generation mechanism

The cell works through the formation of an exciton by the absorption of a photon. Excitons are "quanta of electronic excitation energy travelling in a periodic structure".[31] In other words, an electron is excited into the excited state by light, but not excited enough to be completely ionised. The excited electron and the hole left in the ground state are bound together via electrostatic interactions.[31] The hole and excited electron pair will migrate together until they either recombine or are separated by an interface of materials with different energy levels. The hole then migrates through the donor layer towards the anode and the electron migrates towards the cathode. In most cases the anode is a transparent electrode and the cathode is a metal with a work function tailored to facilitate electron transfer.[32]

Heterojunction solar cells usually contain two active materials and, depending on the set-up, at least one of them will be photoactive. Both are chosen to facilitate the transport of their respective charges towards the electrodes. The active materials can be organic small molecules or polymers.[10, 33-36]

Currently the solar cell market is dominated by inorganic technology with silicon leading at 93% of the sales and other inorganic materials making up the rest.[37] Molecular electronic solar cell efficiencies are now matching some of the inorganic commercial solar cells. Heterojunction devices have been reported at 11.1% efficient; DSSCs based on TiO_2 nanoparticles currently have a highest efficiency of

14.1%.[38, 39] Perovskite based solar cells developed in recent years have a highest reported efficiency of 17.9%.[39, 40]

1.1.3.2 Organic Field Effect Transistors

Similar to optical devices, organic electronics are being investigated to replace inorganic electronic components used in circuits. The simplest way to test the charge mobility of a material is to incorporate it in a field effect transistor (FET). FETs use an electrical field produced by one electrode to control the current flow between two others. There are three components to a basic design of an FET. These consist of a semiconductor layer in contact with two electrodes, a source and a drain. These are separated from a third electrode, a gate, by a thin insulating layer. There are four arrangements of electrodes possible depending on whether the gate and the source-drain electrodes are deposited on top of the semiconductor layer (top) or the semiconductor layer is deposited on top of the electrode (bottom). These arrangements are Top-gate & Top-contact, Bottom-gate & Top-contact, Top-gate & Bottom-contact and Bottom-gate & Bottom-contact. Bottom-gate & Bottom-contact FETs, as shown in Figure 1.8, are more commonly used in the initial testing of materials as they are pre-fabricated and a layer of semiconductor material just needs to be deposited on top.

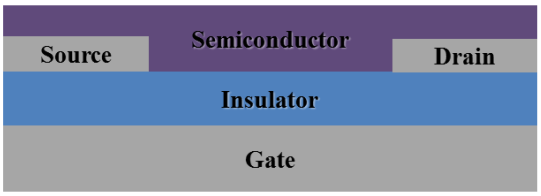

Figure 1.8: Schematic of a Bottom-gate & Bottom-contact Field Effect Transistor

The width and length of the material is taken into account when assessing the performance of the device. Therefore the electrodes are normally interdigitated with a set electrode and channel width, as shown in Figure 1.9.

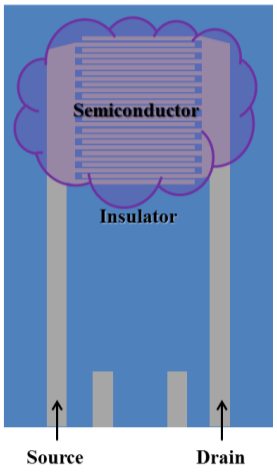

Figure 1.9: Schematic of a Field Effect Transistor chip with interdigitated electrodes with a bottom gate

The current between the source and the drain, (I_{SD}), is measured in response to the applied potential between the source and the drain (V_{SD}) and the potential between the source and the gate (V_{SG}). The mobility of the material is extrapolated from source-drain I-V characteristics at several gate potentials. A schematic of the typical current response to varying source-drain (V_{SD}) potentials at a fixed gate potential (V_{SG}) is shown in Figure 1.10.

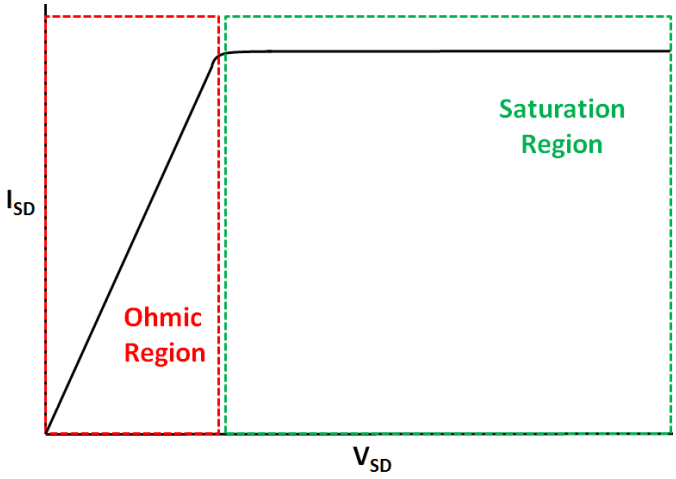

Figure 1.10: Schematic of the current response against increasing source-drain potential of a typical thin film FET

The current of a typical thin film FET has two regions: the Ohmic region where the current increases linearly with the increase in potential and the Saturation region where the current is constant. When a potential is initially applied between the source

and drain, current flows due to a potential gradient. If no gate potential is applied, then the current depends on the resistance of the materials. As the V_{SD} is increased the flow of electrons increases to maintain the resistance. When a potential is applied to the gate it causes the charge carriers in the semiconductor material to rearrange due to the applied electronic field. This causes a build-up of holes or electrons depending on the V_{SG}. At a certain potential the potential gradient of the V_{SD} and the build-up of the charge carriers due to the V_{SG} cause an area saturated with charge carriers and the current flow is controlled by this saturated area. This potential is known as the pinch-off potential (V_P). When the $V_{SD}<V_P$ the current still depends on the resistance of the material, which results in the linear increase in current that is classified as the Ohmic region. When the $V_{SD}>V_p$ then the current is dependent on the area saturated with charge carriers and remains constant which is known as the Saturation region.

Similar to organic photovoltaic devices, organic FETs are finding uses in niche applications such as use in OLED display devices.[41]

1.2 Deposition

1.2.1 Surface deposition

The formation of films occurs when molecules are transferred from one phase to another. The actual packing of the molecules in a film depends on the deposition method as much as the preferred packing of the molecules. If the deposition method is not optimised the films can be disjointed resulting in little interaction between neighbouring molecules or many disjointed small crystallites. If the method is optimised the formed films are coherent, forming continuous films with a large area of interacting neighbouring molecules or crystallites. There are two main ways that molecules can form a coherent film on a surface: either layer growth or nucleation, as shown in Figure 1.11.[42]

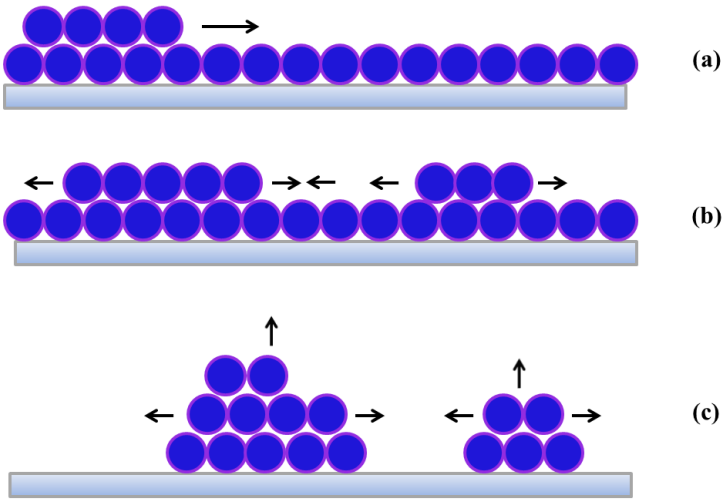

Figure 1.11: Coherent film deposition: (a), (b) layer growth and (c) nucleation

In layer growth a crystal enlarges by the spreading of layers or terraces as shown in Figure 1.11 (a) and (b). The shape of the layer depends on the π system of the molecule as well as the energy it contains when it deposits. This occurs when the interaction between the substrate and the film molecules is stronger than the molecule-molecule interaction.[26] Therefore it is more energetically favourable for a molecule to deposit on the substrate than on the already deposited molecules.

Nucleation is when a crystallite forms on the surface of the substrate and then grows in all directions. The crystallites grow until they coalesce, covering the entire substrate.[26] Growth then continues as a network of linked crystallites until they form into a continuous film.[42] Nucleation takes place when the interaction between neighbouring molecules is stronger than that between the substrate and the molecules.[26]

Although the way in which the films initially form is important, other processes can occur that affect the deposited film. As mentioned earlier the interaction between the molecules can result in a preferred orientation and features in the depositing film. Molecules or groups of molecules can migrate to grain boundaries where there is less surface tension. At high temperatures and pressures a phase transition can occur resulting in a rearrangement of all the molecules on the substrate.

Currently there are two main categories of methods of fabricating organic thin films: solution processing and vapour processing.

1.2.2 Solution Processing

Solution processing has been used for centuries and incorporates simple applications such as painting, drop coating and dip coating, small scale depositions such as spin coating and screen printing as well as industrial scale processing such as roll-to-roll, inkjet printing and spray coating.

The general process involves dissolving the solid material into a solvent and then spreading the resulting solution out. As the solvent evaporates the dissolved material remains as a film. Although the principles of the technique are quite simple, several factors have to be taken into account as they all affect the produced films: the stability and solubility of the material, the rate at which the solvent evaporates and how the material precipitates from the solution. Most techniques are designed to control these factors because solvent evaporation, occurring at an uneven rate, will result in the film not being uniform.[43] The volatility of the solvent is important because it controls the formation of menisci and the boundaries between the solid and the liquid phase.[44] This occurs due to the strong interaction of the solvent molecules with each other compared to the interaction between the solvent and the solid material molecules. This creates a transition region, as shown in Figure 1.12.

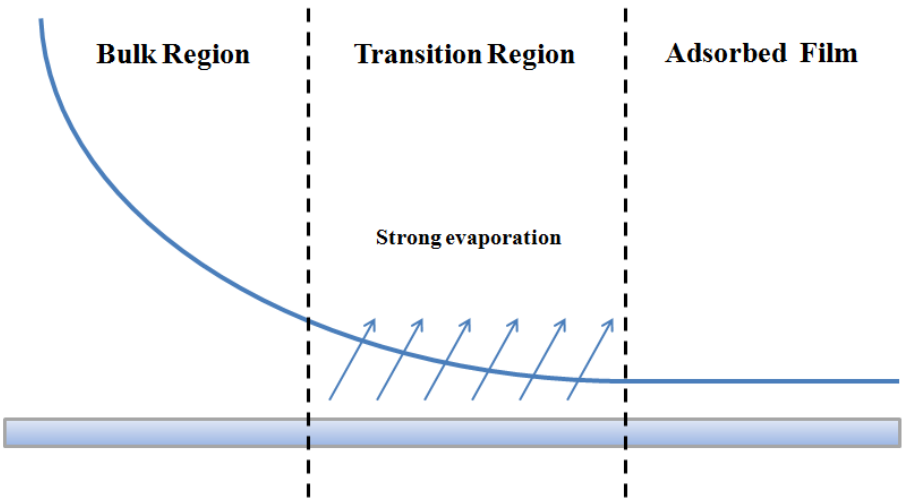

Figure 1.12: Regions for an evaporating meniscus

The bulk region, where the curvature of the interface is nearly constant, is the region where there is little interaction between the solution molecules and the substrate. The transition region is where surface tension between the solution and the substrate begins to become significant. This causes a curvature of the solution interface and evaporation occurs rapidly in this phase. The gradient and rapid evaporation cause solution from the bulk region to flow into the transition region. The adsorbed film region is where a thin film of solution is adsorbed onto the substrate. Due to the strong solution-substrate interaction a large amount of energy is required to vaporise the remaining solvent molecules and therefore little evaporation occurs.[44]

The molecule-substrate and molecule-molecule interaction also play a role in the deposition as mentioned earlier. If the evaporation of the solvent occurs in an uncontrolled manner it can lead to uneven bulk deposition. If the rate of molecules interacting with the substrate is slower than the rate of evaporation, then the concentration of molecules in the solution will increase. After a certain amount of the solvent has evaporated the solution will become saturated and bulk deposition occurs in the transition phase, resulting in a ring of rapidly deposited molecules.

1.2.2.1 Rapid Evaporation Techniques

The simplest form of film deposition involves applying the molecule to a substrate dissolved in a solvent and letting the solvent evaporate resulting in a film. The lack of control of this technique can result in inhomogeneous films so repeatability can be a problem.[43] Aside from drop casting, the most common rapid evaporation process used in small scale deposition in research is spin coating. The technique uses a combination of solution concentration and viscosity, a controlled flow of inert gas as well as centrifugal and viscous forces to ensure that the films deposited are reproducible.[45]

The process involves securing the substrate onto a spinning disk and applying the material dissolved in a highly volatile but viscous solution onto the substrate. The substrate is then spun under a flow of inert gas to obtain a film, as shown in Figure 1.13.

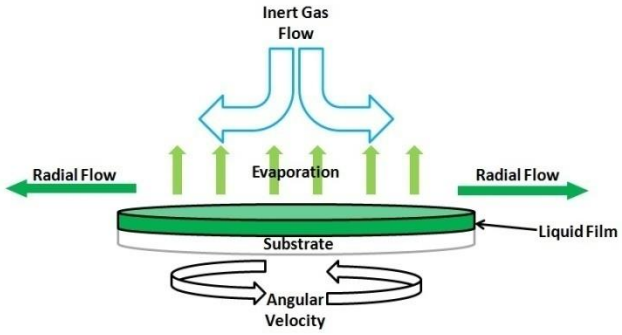

Figure 1.13: Schematic of a spin coating set-up

The process happens in two stages: initially the solution is applied to a substrate while it is static or spinning slowly. The solution is spread evenly by spinning the substrate slowly. The spin velocity of the substrate is then increased as the combination of the adhesive force of the solution to the substrate and the centrifugal force acting on the solution results in a strong sheering force. This causes radial flow of the solution meaning that most of the solution that is not strongly bound is ejected from the substrate. The remaining solvent then evaporates quickly due to the flow of inert gas.[46]

Since the concentration, spinning rates and airflow are controlled, the process results in highly controllable and repeatable films.

1.2.2.2 Slow Evaporation Techniques

Processes that involve the evaporation of a solution at a slower rate than the formation of molecule-substrate bonds are known as slow evaporation techniques. Printing, which is a commonly used technique both at a laboratory scale and at an industrial scale, is an example of this. Some techniques involve using a mask or screen while others use a nozzle to apply the solution in the desired pattern. One of the most common techniques is screen printing which is used to obtain large areas of inexpensive deposited films.[47]

A more recently developed technique is ink jet printing, which uses small nozzles to deposit a solution onto a substrate. A nozzle is used to create droplets which are electrostatically charged and accelerated towards the substrate using an electric field.[43] The technique requires the material to be dissolved in a highly viscous

solvent with low volatility as opposed to spin coating which uses a high volatility solvent.[43]

1.2.3 Vapour Processing

As the name indicates vapour deposition (VD) involves vaporising the material and then condensing it onto the desired substrate. The material is vaporised, which, depending on the latent heat of vaporisation, can be done thermally, by applying a vacuum or by a combination of both. A typical set-up is shown in Figure 1.14.

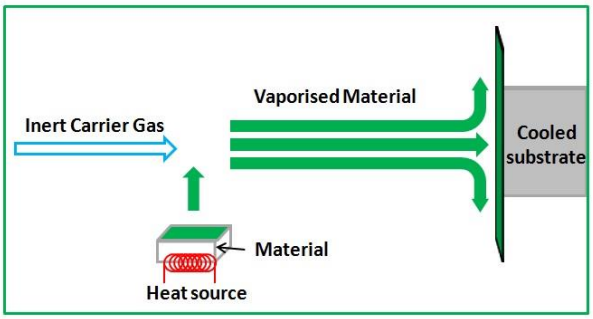

Figure 1.14: Typical set-up for vacuum thermal deposition

The material is vaporised by one of a number of techniques and then the vapour is transported via an inert carrier gas. The vapour then condenses on any cooler surface it comes into contact with, including the substrate.

If the material has a high latent heat of vaporisation, a vacuum with a pressure in the range of 10^{-6} to 10^{-8} Torr will normally be applied.[48] This results in a lower temperature being needed, as shown by the Clausius-Clapeyron relationship, Equation 1.2.

$$lnP = -\frac{\Delta H_{vap}}{R}\left(\frac{1}{T}\right)$$

Equation 1.2

where ΔH_{vap} is the latent heat of vaporisation, P is the pressure, T is the temperature and R is the ideal gas constant.

Vapour-based techniques are used for the small scale deposition of highly organised pure films.

1.3 Electrochemical deposition

Electrodeposition was developed during the Victorian era as a method of depositing a layer onto an electrode by the action of electricity. The earliest electrodeposition device appeared in the 1820s and is credited to M. Hohlfeld who ran a current through a wire in a smoke-filled bottle and noted that "with the passing of the first sparks the smoke vanished, the water from the smoke appearing on the bottom of the bottle".[49]

Electrodeposition is now a major cornerstone of industrial processes encompassing a range of techniques that use current and electric fields to deposit layers such as electrophoretic coating, electrostatic coating and electroplating.[50-53] Electroplating, more commonly known as electrochemical deposition, is the deposition of a layer by oxidation or reduction of charged molecules in an electrolyte solution onto a conducting surface by the application of a potential.[52]

1.3.1 Inorganic films

In 1836, copper was first electrodeposited using a Daniel cell and a technical report was published by De la Rue in the same year.[54, 55] Around the same time the technique was developed for other metals such as nickel and gold. Since then the technique has been tailored and developed for several industrial applications, such as zinc coating, copper deposition on chips, and it is used to purify several metals. The process involves the reduction of the metal cations in an electrolyte solution to the insoluble neutral metal on the cathode.

In the past four decades it has been used in the fabrication of inorganic electronic components such as thin film semiconductors.[56] Although semiconducting silicon and germanium have been deposited since the Victorian era, currently most electronic components are fabricated using vapour techniques which require high temperatures and a high vacuum due to the purity of the metal required.[57] The interest in electrochemical deposition as a preparation method for materials is based on the fact that it is an already established technique for producing large area films at low cost and temperature compared to vapour processing and solution processing, where the films normally require high-energy post-processes such as high

temperature annealing or firing.[58, 59] It is already used in the fabrication of some micrometre thick film devices, the best example being thin film solar cells made from electrodeposited cadmium, telluride and sulfur.[60]

1.3.2 Organic films

Using electrochemistry in the preparation of organic films is not a new concept. Film deposition by electropolymerisation has been used in the preparation of thin films since the 1980s.[61, 62] Thiophene is a well-known example of a monomer that can be electropolymerized into a conducting chain, as shown in Figure 1.15.

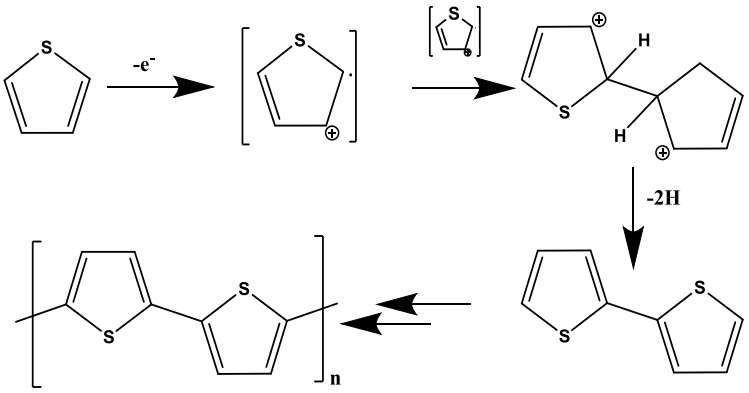

Figure 1.15: Electropolymerisation of thiophene to polythiophene

It was used in the first reported solid-state FET using an organic macromolecule.[63] More recently it has also been used in the fabrication of solar cells.[64] More complex molecules, such as modified cobalt porphyrins, have been made into chains via electropolymerization.[65]

For the last 30 years electrodeposition has also been used in electrocrystallisation to produce thin films and crystals of any conducting molecule, as under the right conditions the molecules will precipitate out of the solution onto the electrode, forming a crystal or a film.[66, 67] Electrodeposition of dithiolene salts has been used to form crystals for the last 20 years. Although the majority of the work has resulted in crystals some films have been produced, but these are ordered stacks of the dithiolene salt rather than the neutral dithiolene molecule.[68-70]

Electrochemical deposition has several advantages for the fabrication of films compared to other deposition techniques.

Compared to solution evaporation techniques:

- It allows the ordered deposition of redox-active materials that cannot be processed by other solution techniques due to poor solubility.[71]
- A homogeneous film can be obtained from a solution process method as it does not depend on the rate of evaporation of the solution, thus avoiding bulk precipitation or unwanted crystallisation.[72]

Compared to vapour deposition techniques, electrochemical deposition has the following advantages:

- It is much less energy-intensive as the set-up does not require a vacuum and is normally done at low temperatures. Even if the films require annealing, the energy required is a fraction of that required for vapour deposition.
- Equipment cost is also a consideration. At the laboratory scale a metallorganic chemical vapour system has an cost of about £1 million with a limited number of materials that can be used, whereas a computerised potentiostat costs about £5000.[60]
- The surface areas of the devices can also be scalable. Surface areas of vapour deposition chambers are usually limited, whereas the size of an electrochemical cell can be increased with less difficulty meaning a larger surface area electrode can be deposited on.
- When co-depositing two materials the properties of the materials can be controlled by the potential applied. Changing the potential can affect the amount of each material deposited.[73] Varying the potential during deposition can also result in different layers being deposited from the same solution.[74]

Until work within the Edinburgh group began, electrochemical deposition had not been investigated as a method for the deposition of a film of organic small molecules for use in molecular electronic devices. The only example in the literature of electrochemical deposition of a small organic molecule was in 2000 by Zaban *et al*. The technique was used to fabricate a DSSC using electrochemical deposition of a PTCDI.[75, 76] Zaban used electrodeposition of the anion molecule as a method of coating the high surface area of a TiO_2 electrode with a thin layer of dye. The process

is based on the fact that the anions of PTCDIs are more soluble than the neutral compounds.[77, 78] A layer of the PTCDI was compressed onto an FTO electrode and then electrochemically reduced using cyclic voltammetry. The resulting anion was electrodeposited onto a target electrode with the TiO_2 semiconductor. A schematic of the apparatus is shown below in Figure 1.16.

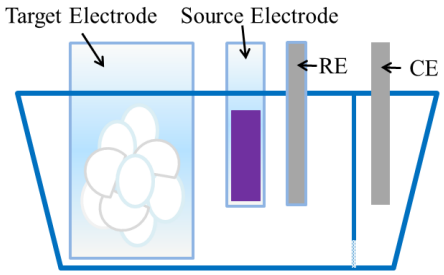

Figure 1.16: Simplified apparatus of the Zaban experiment

Although the process was successful, there were some limitations to the apparatus. The film characteristics were very dependent on three parameters: the distance between the source and target electrodes, the overpotential and the electrolyte concentration.[76] Since both the reduction and oxidation of the PTCDI were achieved electrochemically, the rate of deposition was dependent on the rate of reduction, the diffusion of the anion and the rate of oxidation.

Electrochemical deposition was also investigated within the Edinburgh group by Dalgleish *et al*. who compared the properties of films fabricated by solvent processing and electrochemical deposition. The study focused on a nickel dithiolene complex, $Ni(b\text{-}3ted)_2$, of which the neutral and anionic form could be synthesised. During the investigation of the electrochemical properties of the salt the deposition of a neutral film on the working electrode surface was observed.[79] This was investigated further by depositing films of the neutral complex by electrochemical deposition and solution evaporation methods and comparing the properties of the two.[80] The study found that the film deposited by electrochemical deposition contained large crystallite features, several microns in length as shown in

Figure 1.17 (right), compared to the smaller crystallites surrounded by clusters in the drop coated film as shown in Figure 1.17 (left).

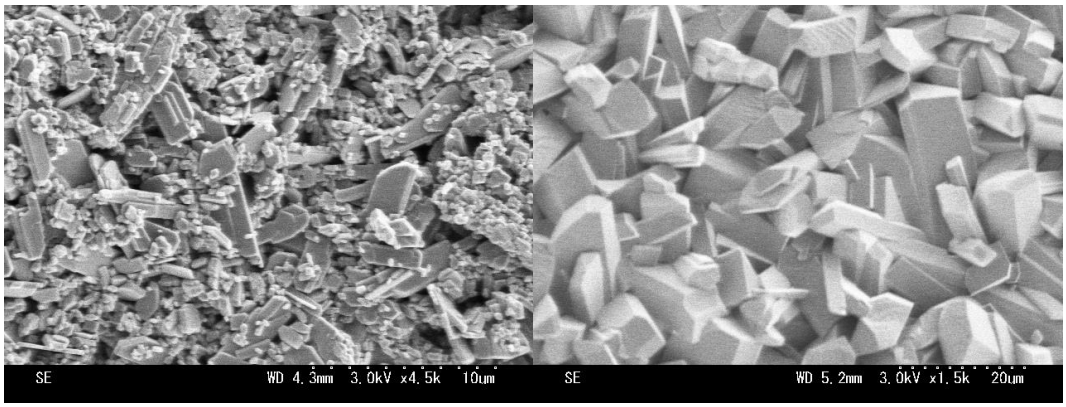

Figure 1.17: Drop coated film (left) and electrodeposited film (right) of Ni(b-3ted)$_2$

Further studies of the use of electrodeposition of dithiolene complexes were used to produce a film of a neutral copper bis-dithiolene complex.[81] This is unusual as neutral copper bis-dithiolenes are unstable in solution and will decompose if formed.[82] Thus the deposition of a film offered a chance to study the electronic absorption of the neutral complex. In both studies the molecules investigated had the unusual advantage that both the neutral and anionic states of molecules could be isolated and both were stable in air.

1.4 Research proposal

This thesis outlines the development and application of the electrochemical deposition of small molecules for use in organic electronics. The molecules investigated were chemically reduced and then electrochemically oxidised to produce films. Several small molecules were investigated in order to develop a protocol that could be used to electrochemically deposit any electroactive molecule for use in organic electronics.

Several small molecules with varying solubilities, such as N,N dibutyl-3,4,9,10-perylene-bis(dicarboxime), 3,4,9,10-perylene-tetracarboxylic bisbenzimidalzole and copper (II) phthalocyanine were studied. All three are normally vapour-processed or require the addition of solubilising groups to solvent process them. The conditions needed to produce repeatable thin films were established and the properties of the electrochemically deposited films such as the electronic absorption, emission, surface morphology and packing were investigated. The developed deposition technique was then applied to fabricate FETs and bilayers which were used to test the properties of the films.

The developed technique was also used to produce neutral metal dithiolenes films from the anion form. Again, the conditions needed to produce repeatable thin films were established and the properties of the electrochemically deposited films such as the electronic absorption, emission, surface morphology, packing, charge mobility and magnetic susceptibility were investigated.

2. Experimental techniques

2.1 Electrochemistry

Electrochemistry is the most common technique used for studying the redox properties of molecules. It is used to investigate the effects of oxidation, the loss of an electron, and reduction, the gain of an electron on molecules.

For oxidation or reduction to occur the electroactive species has to be transported towards the surface of the electrode. The steps involved in the reduction of species R are shown below:

- Mass transport $R_{(bulk)} \rightarrow R_{(electrode\ surface)}$
- Electron transfer $R_{(electrode\ surface)} + ne^- \rightarrow P_{(electrode\ surface)}$
- Mass transport $P_{(electrode\ surface)} \rightarrow P_{(bulk)}$

The overall rate of the reaction is controlled by the slowest step. The availability of electrons for the electron transfer is controlled by the electrode potential. A small change in potential can result in the amount of electrons available changing by orders of magnitude. Therefore the experimental parameters are usually set up in such a way that there is an abundance of electrons available so that electron transfer occurs rapidly making mass transport the slowest step. There are several types of transport processes that are considered as mass transport when combined. They are convection, migration and diffusion.

Transport due to convection can be divided into two categories: natural and forced. Natural convection arises from thermal and/or density differences within the solvent. These can both arise due to the electron transfer process. Thermal differences may be the result of exo- or endo-thermicity of the electron transfer. The electron transfer will also result in a change in density as there is more product near the electrode surface. Natural convection typically becomes significant in experiments that last more than a few seconds on large surface electrodes (mm or larger). Forced convection is when movement in the solution is due to external forces such as

stirring or gas bubbling and are normally introduced to swamp any movement due to natural convection as they are controllable and therefore reproducible.

Migration is caused by the electric field at the electrode/solvent interface caused by the application of a potential which attracts the ions causing them to move towards the opposite charge.

Diffusion arises from the uneven concentration distribution caused by the reactants undergoing electron transfer. With a planar electrode diffusion is characterised by Fick's Laws in a one dimensional form.

Fick's first law states that the flux, J, and the movement of any electroactive species, r, towards the surface of the electrode is given by:

$$J = -D_r \frac{dc_r}{dx}$$

Equation 2.1

where c_r is the concentration of species r close to the electrode surface, x is the distance from the electrode and D_r is the diffusion coefficient. D_r typically has a value in the order of 10^{-5} cm^2 s^{-1}.

Fick's second law accounts for the change in concentration of the electroactive species with time due to diffusion. This accounts for the flow of the species into and out of a defined area a distance x from the electrode surface and is given by the formula:

$$\frac{\partial [r]_0}{\partial t} = -D_r \frac{\partial^2 [r]_0}{\partial x^2}$$

Equation 2.2

where $[r]_o$ is the concentration of species present at the electrode surface, t is time and x is the distance from the electrode surface.

This can be integrated under the assumption of very fast electron transfer to give the Cottrell equation:

$$I_d = FnA[r^b]\sqrt{\left(\frac{D_r}{\pi t}\right)}$$

Equation 2.3

where I_d is the diffusion limited current for the reduction of r, r^b is the concentration of r in the bulk, F is the Faraday constant, n is the number of electrons in the electron transfer reaction and A is the electrode area. A plot of the I_d against the square route of time, $t^{½}$, will yield a straight line if the current is diffusion limited with a gradient of $nD_i^{½}$.[83]

To negate the effects of migration, electrochemical experiments are normally performed in an electrolyte solution. This consists of a high purity solvent with an electrolyte, a salt that ionises when dissolved. These ions are present for several reasons. The first is to increase the conductivity of the solvent, mitigating the solvent resistance between the working electrode and the counter electrode. The second reason is to make sure the electroactive species is not affected by migration. Since the ions of the electrolyte are present in a much higher concentration than the electroactive species, they will transport the majority of the charge through the solution. When a current is applied between the two electrodes it causes the cations to move towards cathode and the anions to move towards the anode. This movement of the ions is what causes the flow of current in the bulk of the solution. The third reason is that the charges attracted towards the electrodes will result in a reorganisation of the ions present in the electrolyte solution resulting in what is called a double layer, as shown in Figure 2.1.

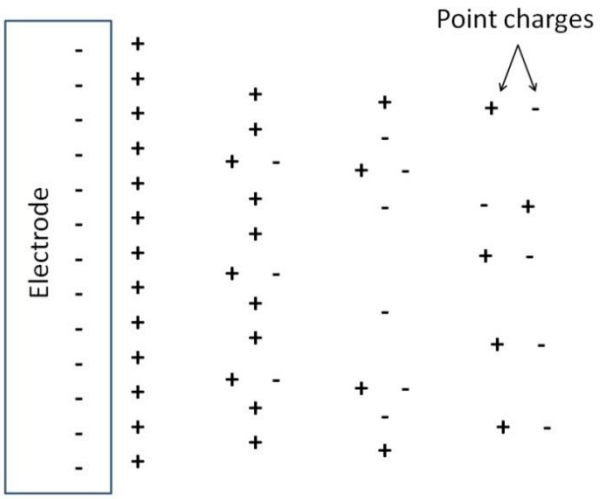

Figure 2.1: Schematic of the diffuse double layer

In Figure 2.1 the electrode has a negatively charged surface; the cations from the electrolyte solution have formed a positive covering layer as they are attracted to the large negative charge whereas the negative anions have been repelled. This rearrangement is called the diffuse double layer. This results in a potential difference between the electrode surface ($ø_m$) and the potential of the electrolyte solvent ($ø_s$), as shown in Figure 2.2.

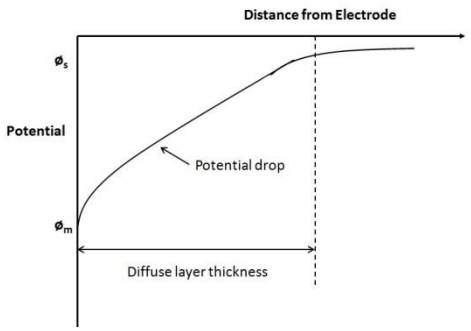

Figure 2.2: Potential drop in the double layer

The electrolyte helps to minimise the diffuse layer thickness, thus suppressing the double layer effect on mass transport.[84]

2.1.1 Experimental electrochemical set-up

An example of the standard three electrode system is shown in Figure 2.3. It contains 3 components: a working electrode, a reference electrode and a counter electrode.

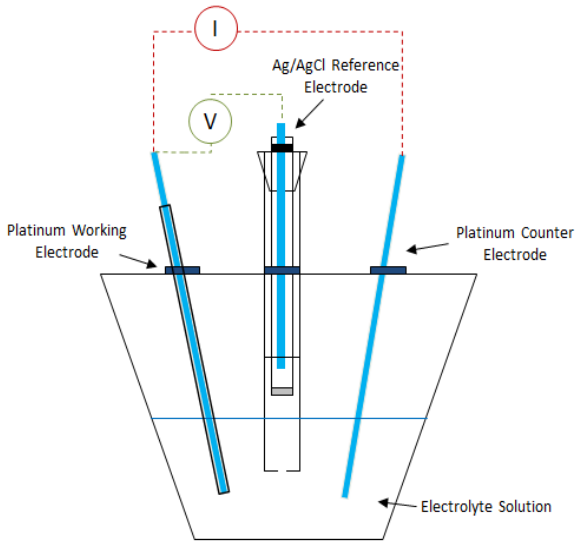

Figure 2.3: Standard three-electrode apparatus used for cyclic voltammetry and other electrochemical techniques

The apparatus is sealed and a nitrogen bubbler is used to remove any trace amount of O_2 present in the electrolyte as it is redox active. A background scan is performed to ensure that no redox species is present. The electroactive species being investigated is then dissolved in the electrolyte solution.

This set-up is used to ensure that only the potentials and current due to the species are being measured as the system is designed to mitigate any processes due to the solvent or electrodes. Measurements take place at the working electrode, a small area of inert surface. The most common materials used are glassy carbon™, gold and platinum. The surface must be inert to ensure the electrode does not react to form new redox species that could interfere with the reaction taking place. A potential is applied to the working electrode with respect to the reference electrode. The reference electrode has a very stable well-defined potential and therefore the overall voltage can be calculated using Equation 2.4.

$$V = E_{We} - E_{re} = \Delta E$$

Equation 2.4

The current is applied between the working electrode and the counter electrode, which is a large surface area electrode made of an inert material. This is done to avoid perturbing the voltage at the reference electrode which can arise from a large current.[85]

2.1.2 Cyclic voltammetry

The most common technique for determining the potentials and reversibility of the reduction and oxidation processes of the molecules is cyclic voltammetry. The technique uses a linear sweep experiment and works by measuring the current response to a potential that is cycled from an initial potential to a maximum potential then back to the initial potential, as shown in Figure 2.4.

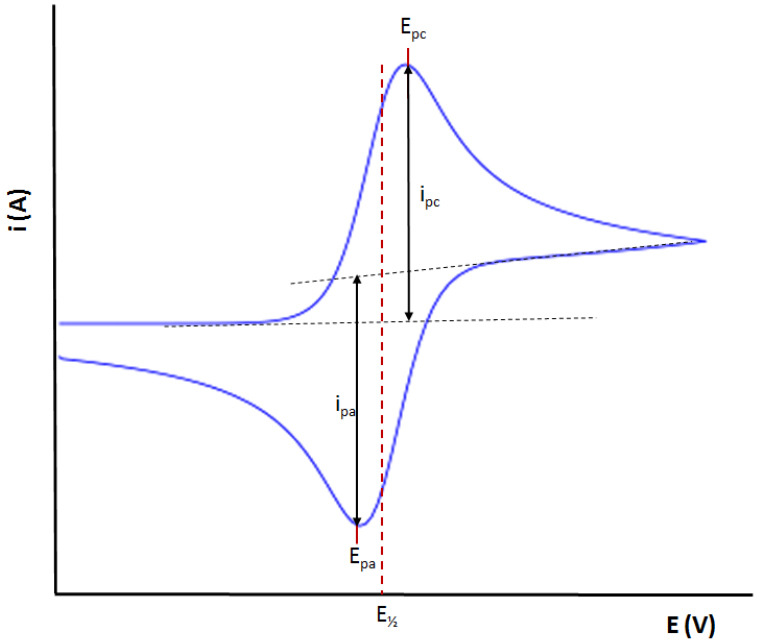

Figure 2.4: Typical voltammogram for a one-electron redox process

The shape of the voltammogram can be explained by what is happening in the immediate area around the working electrode. Initially the current measured is very small due to the charging of the double layer, as the potential is insufficient to induce oxidation. When an oxidation potential is reached the current increases exponentially. This will continue until all the species present at the electrode have been oxidised. A maximum is reached when the rate of oxidation is equal to the diffusion of the species in solution. The current then decreases as mass transport is

limited. Once the maximum voltage has been reached a reverse scan is performed. During the initial stages of the reverse scan the compound is still being oxidised until the potential to re-reduce the compound is reached. Once the reduction potential has been reached the current will decrease exponentially, doing the opposite of what it did during oxidation. Similar to oxidation a maximum is reached when the rate of reduction is equal to the diffusion of the molecule in solution. The current then increases until all the oxidised species formed have been reduced, the scan is finished or reaches another reactive species.

The current is monitored at several scan rates to ensure that the process is electrochemically and chemically reversible. For a process to be deemed electrochemically reversible the rate of electron transfer has to be faster than that of mass transport. This can be checked using a few criteria:

- The position of the current maxima, E_{pa} and $E_{pc,}$ should be approximately (59/n) mv apart due to Equation 2.5, where n is the number of electrons transferred.

$$E_{pc} - E_{pa} = 2.303\frac{RT}{nF}$$

Equation 2.5

- The values of the i_{pa} and i_{pc} have to be the same.
- The positions of the E_{pa} and the E_{pc} should not change with the scan rate.
- A plot of the current maxima against the square root of the scan rate should result in a straight line.

If the E_{pa} and E_{pc} change with the scan rate it means that the kinetics of the electron transport are slower than the experiment scan and the process is electrochemically irreversible. The process is deemed chemically irreversible if there is no return wave indicating that the product formed has reacted to form a new compound which cannot be returned to the original reactant during the reverse scan.

2.1.3 Chronocoulometry

Chronocoulometry, a potential-step technique, is an electrochemical quantitative method where the potential of the working electrode is changed from E_1 to E_2 instantaneously and the charge-time response monitored. Since the charge is equal to:

$$Q = \int I\, dt$$

Equation 2.6

The charge-time response depends on the current of the reaction, which in turn is dependent on whether the rate determining step of the reaction is that of the mass transport or the electron transfer. If the reaction is controlled by mass transport, then the current is dependent on the diffusion of the species in solution and it will decrease exponentially with time, as shown in Figure 2.5 (a). If the reaction is controlled by the electron transfer, the current will be constant as the concentration of the species at the surface will not change significantly. Therefore the current will be a straight line, as shown in Figure 2.5 (c). If the process is mixed controlled, the rate of diffusion and electron transfer are comparable and the current decreases over time but less steeply, as shown in Figure 2.5 (b).

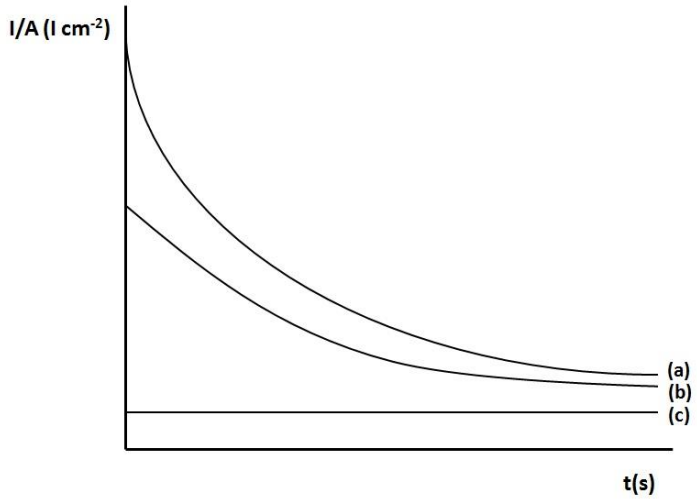

Figure 2.5: Currents for (a) Mass transport controlled reaction, (b) mixed reaction and (c) kinetic controlled reaction

Since the total charge passed depends on the current, the charge passed due to diffusion can be determined using Equation 2.3:

$$Q_d = \int FnA[r^b]\sqrt{\left(\frac{D_r}{\pi t}\right)}\,dt$$

Equation 2.7

$$\therefore Q_d = 2FnA[r^b]\sqrt{\left(\frac{D_r t}{\pi}\right)}$$

Equation 2.8

A typical plot of charge per cm^2 against time for a diffusion controlled process is shown in Figure 2.6.

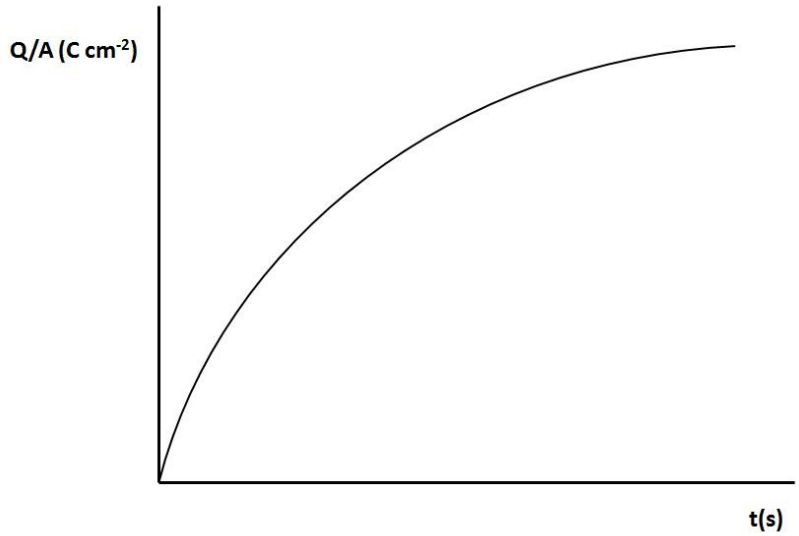

Figure 2.6: A typical charge per cm^2 against time curve for the reduction of a species under mass transport control

If the reaction is diffusion limited, a plot of charge passed against $t^{½}$ should in theory give a straight line through the origin as the rate of oxidation will depend on the transport of species towards the electrode surface. However, in practice this is not always the case as the intercept is affected by charge from other sources, as shown in Figure 2.7.

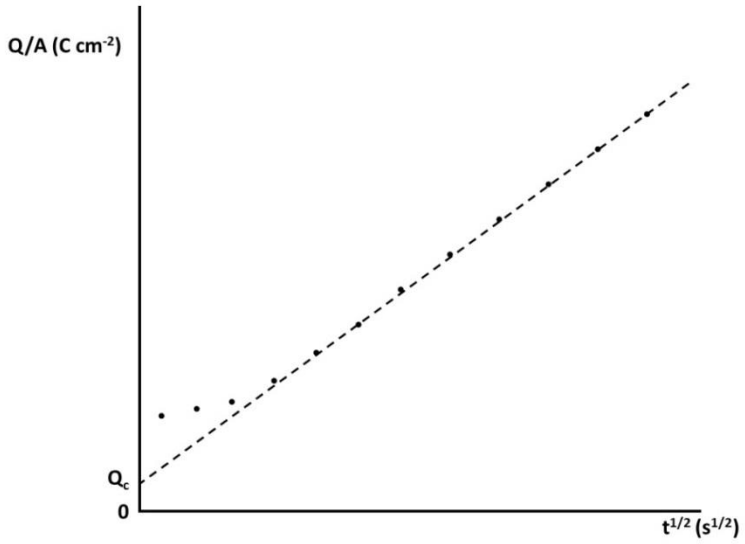

Figure 2.7: A typical plot of charge over area against time[½]

The slope of the line is proportional to the concentration of the reactant, $[r^b]$, and the intercept is due to charging of the double layer, Q_c. The increase in charge is proportional to the square root of the time because the reactant is transported to the surface of the electrode by diffusion, as shown by Equation 2.3.

The location of the intercept is also affected by adsorption if, during the initial potential, E_1, before the step change, some of the reactant has been adsorbed onto the surface of the electrode. When the potential is changed to E_2, the adsorbed reactant will be reduced instantly because it is already at the electrode surface. This will cause an initial burst of charge as it is not controlled by diffusion, but after this initial burst the total charge is no longer affected. Therefore the total charge is equal to:

$$Q = \int FnA[r^b]\sqrt{\left(\frac{D_r}{\pi t}\right)}dt + \int r_c dt + \int r_{ads} dt$$

Equation 2.9

$$\therefore Q = 2FnA[r^b]\sqrt{\left(\frac{D_r t}{\pi}\right)} + Q_c + Q_{ads}$$

Equation 2.10

where Q_c is the contribution of the double layer and Q_{ads} is the contribution from any adsorbed species. Therefore the intercept of the plot of Q against $t^{½}$ is $Q_{DL} + Q_{ads}$. The values of Q_{DL} and Q_{ads} can be determined by performing the same experiment in the presence and absence of species r.

The above conditions have assumed that all processes in the reaction are diffusion controlled. However if during the initial stages part of the reaction is influenced by kinetic control or mixed control, both kinetic and diffusion, then the plot will be slightly different. In case of electrodeposition, the adsorption of the species onto the substrate will result in a change in the kinetics of the system. This is because the electron transfer will have to occur over a larger distance due to adsorption of the film onto the electrode surface. In this case the plot of charge against $t^{½}$ results in a straight line which intercepts the x-axis, resulting in a negative intercepts the y-axis and is defined by:

$$Q = \frac{4nF\vec{k}}{\pi}[r^b]\left(t_L^{½}t^{½} - t_L\right)$$

Equation 2.11

where $t_L^{½}$ is the intercept on the x-axis and $\vec{k}$ is the rate constant for the cathodic process. In this case, the plot of charge against $t^{½}$, the straight line will intercept the y-axis at a negative value, resulting in an intercept of the x-axis. The value of $\vec{k}$ can be calculated from the slope and value t_L.

The value of D_r can still be calculated from the gradient using Equation 2.8, so the area where the graph is linear is diffusion controlled and the none-linear areas are a mixture of kinetic and diffusion controlled processes.

Electrochemical studies were recorded using the General Purpose Electrochemical System (GPES) software using an Autolab system containing a PGSTAT 30. The cyclic voltammetry set-up is as follows: The working electrode was a Pt disk electrode, the counter electrode was a large surface Pt electrode and the reference electrode was an Ag/AgCl reference electrode**.** The chronocoulometry was used to monitor the deposition of a film onto a conducting working electron from an

unstirred anionic electrolyte solution, using a modified 3 electrode set-up. To account for experimental variations, all scans were calibrated to $E_{½}$ = 0.624 V for ferrocene (Fc^{+}/Fc^{0}) unless stated otherwise.

2.1.4 Photo-electrochemistry

The effect of light on the redox properties of an electroactive material is studied using photo-electrochemistry. It compares the electronic properties of the compound when it is in the dark and when it is being irradiated with photons. This can be done by exposing the material immobilised as a thin film, set up as a working electrode in an electrochemical set-up, to a pulsating light source, as shown in Figure 2.8.

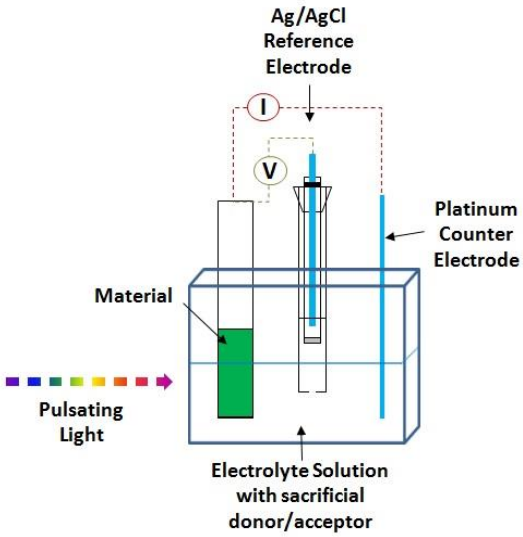

Figure 2.8: Photo-electrochemistry apparatus

The working electrode is surrounded by an electrolyte solution containing a sacrificial donor/acceptor that removes or donates electrons to the material, but is not recharged or discharged once it has reacted.

The current response is measured and the current obtained in the dark, the dark current, and the current when the sample is illuminated, light current, are compared. If the material is sensitive to light, then the current will be different. Figure 2.9 shows an anodic photoresponse where the light causes an increase in current at a fixed voltage.

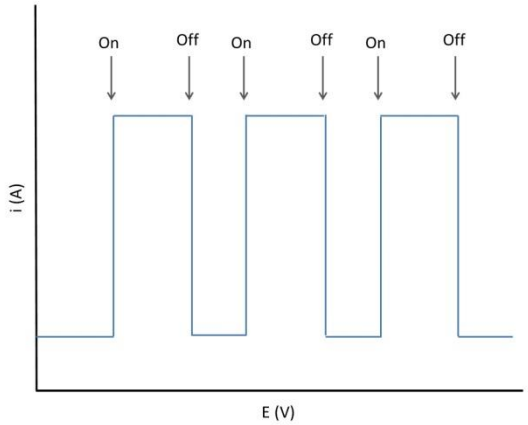

Figure 2.9: A schematic of current-potential characteristics of a material under chopped light

The photoresponse of the material depends on the potential applied to the system. Photosensitization occurs within a potential window and stops when the species is oxidised or reduced. When the applied potential results in injection from the conduction band of the material to the working electrode, the photocurrent is anodic, (a), and when the potential results in injection from the working electrode to the valence band of the material, the resulting photocurrent is cathodic, (b), as shown in Figure 2.10.

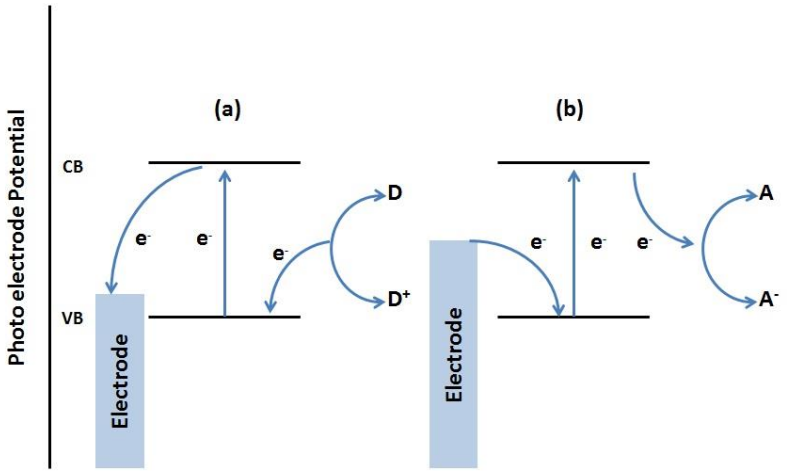

Figure 2.10: Process involved in (a) the anodic photocurrent and (b) the cathodic photocurrent

In both cases the excitation of the material makes the flow of current easier. In the case of the anodic current, the transfer is from the excited state, so the electron is at a higher energy level than the ground state. Therefore the applied voltage does not

need to be as low. In the case of the cathodic current, the excitation of the material leaves a gap in the HOMO of the molecule. Therefore the applied potential has to be just above the level of the HOMO rather than above the LUMO.

Photocurrents were recorded using a classical three-electrode set-up with a platinum wire counter electrode and a Ag/AgCl reference electrode with a 0.1M electrolyte aqueous solution with 0.1M of hydroquinone, a sacrificial electron donor. Chopped light from a 1000 W lamp was used as a light source. Electrochemical studies were recorded using the General Purpose Electrochemical System (GPES) software using an Autolab system containing a PGSTAT 30.

2.2 Electronic absorption Spectroscopy

Electronic absorption spectroscopy is used to study the photophysical properties of molecules or materials. It is used to investigate absorption of light by a material causing excitation between orbitals such as π-π transitions, metal to ligand charge transfer (MLCT), ligand to metal charge transfer (LMCT) and d-d bands.

The technique works by comparing the intensity of light in (I_0) against intensity of the light after it has passed through the sample (I), as shown in Figure 2.11.

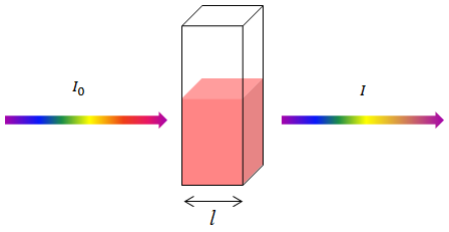

Figure 2.11: Schematic of the apparatus of an absorption spectroscopy experiment

The light is monochromated so that only one wavelength is passed through the sample at a given point. If the energy of the light is equal to the difference between the ground state and the excited state of the complex, it may be absorbed, exciting the molecule from the ground electronic state to an excited state if the transition complies with the selection rules.

The ratio of transmitted intensity, I, to the initial intensity, I_0, at a given frequency is called transmittance, T, at that frequency, as shown in Equation 2.12.

$$T = \frac{I}{I_0}$$

Equation 2.12

It was also discovered empirically that the transmitted intensity is linked to the length of the sample, l, the concentration, c, and the molar absorption coefficient, ε, as shown in Equation 2.13. This is known as the Beer-Lambert law:

$$I = I_0 10^{-\varepsilon c l}$$

Equation 2.13

The molar absorption coefficient depends on the frequency of the light and is greatest when the absorption is most intense. To simplify Equation 2.13, absorbance, A, was introduced:

$$A = -log_{10}\frac{I_0}{I}$$

Equation 2.14

which means that Beer-Lambert Law,

Equation 2.13 simplifies to:

$$A = \varepsilon c l$$

Equation 2.15

To verify that complexes follow the Beer-Lambert law, a plot is made of the absorbance at a specific wavelength, normally at $\lambda_{max,}$ against several concentrations. The results should give a straight line, where the gradient is equal to εl. An example Beer-Lambert plot is shown in Figure 2.12.

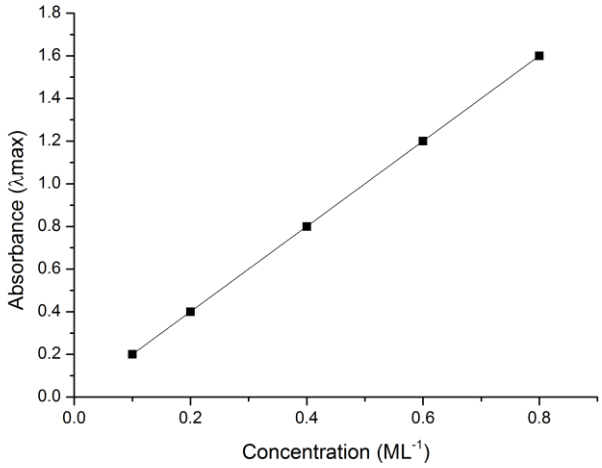

Figure 2.12: Example of a Beer-Lambert plot

If a straight line is not obtained it could be for several reasons. The first is aggregation. This usually happens at higher concentrations, meaning that the plot is initially a straight line but will tail off at higher concentrations. The second reason is that the molecule is only partially soluble in the solution.

Theoretically the transitions have to follow these main selection rules:

1) The spin selection rule,
   This rule states that the spin state of an electron cannot change during excitation. So an electron in a singlet state (S=0) can theoretically not undergo a transition to a triplet state (S=1). A transition when $\Delta S=0$ is called a spin-allowed transition, although in practice spin-orbit coupling can increase the intensity of a spin forbidden transition, which is normally very weak.
2) The Laporte selection rule:
   In a centrosymmetric molecule or ion the only allowed transitions are those that result in a change in parity. This means that transitions with the same inversion symmetry (g↔g and u↔u) are forbidden, but transitions between different inversion symmetries (g↔u and u↔g) are allowed.
3) $\Delta l=\pm 1$:
   In transition there is no change in parity if the quantum number, l, does not change. Therefore s-s, p-p, d-d and f-f transitions are forbidden, whereas s-p,

p-d and d-f result in a change in parity and are therefore allowed giving the selection rule.[86]

Different types of transitions result in different characteristics. The magnitude of the molar absorption coefficient of the transition can be used to help identify the type of transition occurring. Charge transfer between the ligand orbitals and the metal orbitals, metal to ligand charge transfers (MLCT) and ligand to metal charge transfers (LMCT) have molar absorption coefficients with very high intensities. They are also likely show solvatochromism, the variation of the transition frequency with solvent polarity.

UV/Vis spectra were recorded using a JASCO V-670 series spectrophotometer and the data collected using Spectra Manager™ II software.

2.3 Photoluminescence

Photoluminescence is used to study the re-emitted radiation of a compound after it has been excited by the absorption of radiation. It can be observed by exciting the sample by a fixed frequency of light and then monitoring the emitted radiation or by monitoring a fixed frequency and then scanning the excitation range. Luminescence can be conveniently grouped into two types. The first is when the emitted radiation from the excited state is the same multiplicity as the ground state. This is called florescence. Since the transition is spin-allowed, the process is very fast and typically occurs in nanoseconds. The second type of luminescence is via an excited state that does not have the same multiplicity as the ground state and is called phosphorescence. This spin-forbidden process is often slow. For phosphorescence to occur, intersystem crossing has to take place, which is a transition between the states with different multiplicities, typically a non-radiative transition between the singlet excited state and the triplet state. A schematic of the processes that take place for both types of luminescence is shown in Figure 2.13.

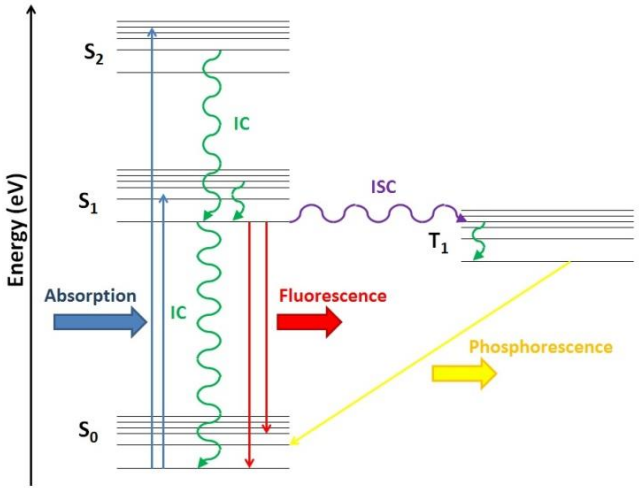

Figure 2.13: Energy level diagram of the processes of fluorescence and phosphorescence (IC, Internal conversion and ISC, Intersystem crossing)

2.3.1 Radiative and non-radiative decay

Not all of the energy absorbed is re-emitted as radiative decay. Some of the energy is lost in internal conversions, which means that some of the energy is lost as the excited electron decays down to the lowest possible excited state before it fluorescence back to the ground state via a radiative decay. This is why the emitted light normally spans a lower frequency (higher wavelength) range than the absorbed light. There are also other non-radiative processes that quench luminescence, such as when the molecule loses its energy to another molecule in the surrounding system. This could be the solvent or another impurity. For example oxygen molecules quench triplet states, since they exist in the triplet state. To avoid this, the solvent is purged with nitrogen to remove any oxygen and the sample is analysed at low temperature to minimise the effect of solvent collisions.

The frozen solution emission spectrum was recorded at 77 K using a Fluoromax2 fluorometer controlled by ISA main Software.

The photoluminescence measurements of the films were performed in a home-built confocal set-up for spatially resolved PL scans. The excitation source was a fibre coupled Ar^+ laser with a wavelength of 514.5 nm and the resulting excitation was detected with a 1024-element Si detector array.

2.4 Scanning Electron Microscopy

Scanning electron microscopy (SEM) is an imaging technique which uses similar principles to traditional optical microscopy, but instead of using visible light, SEM uses a beam of electrons focused by using a magnetic field. A simplified set-up is shown in Figure 2.14:

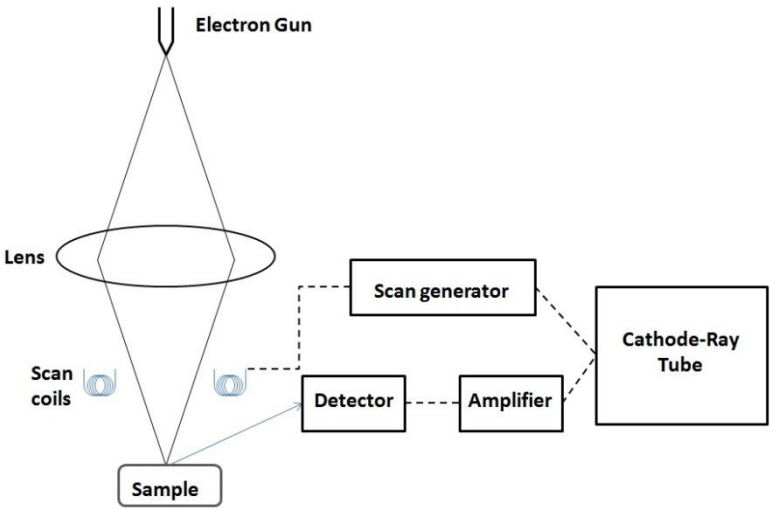

Figure 2.14: The components of a scanning electron microscope

The technique works by accelerating a beam of electrons through a voltage difference of several keV. The beam is then concentrated through a series of condenser lenses reducing it to only a few nm in diameter. It is directed by sets of scanning coils that deflect the beam in an x and y direction over the sample. An image is obtained by raster scanning over a rectangular area of the sample surface.

Images are produced by detecting electrons scattered by the sample surface. The two main types are backscattered electrons (BSE), where the beam electrons are scattered by the surface, and secondary electrons (SE), where the surface molecules emit secondary electrons from their inner shells. The latter is more commonly used. Secondary electrons have very little energy so to detect them they are attracted to and accelerated towards the detector by electric fields. These are designed so as not to affect the main beam or backscattered electrons. Once they have been accelerated enough they cause a scintillator to emit light, which produces a 2D image of the electron intensities that can be saved as an image.[87]

The image quality is controlled by several factors:[88]

- Accelerating voltage- the energy of the initial beam of electrons determines how much energy the electrons hitting the surface will have: the lower the voltage, the less energy they have. Using the right keV will ensure that the sample surface does not become charged and that the number of electrons hitting the surface will be roughly equal to the number of secondary electrons emitted.
- Spot size- the smaller the diameter of the electron beam the better the potential instrument resolution. However, a smaller beam means a smaller number of electrons reaching the surface. Therefore fewer secondary electrons will be emitted making the image noisy.
- Aperture- the angular aperture and the working distance affect the depth of field, meaning the distance between the highest feature in focus and the lowest feature in focus. Increasing the working distance, the distance from beam source to surface, will result in an increase in depth of field and increasing the aperture will result in a decrease in depth of field.
- Focus-as with all lenses the beam of electrons has to be aligned so that the focal point is on the surface of the sample.
- Magnification- unlike optical microscopy, magnification is not the result of a stronger lens but of performing raster scanning over a smaller area.

SEM images were obtained using Philips XL30CP with PGT Spirit X-ray analysis and HKL Channel 5 Electron Backscatter Diffraction (EBSD) systems. The specification of the instrument is a tungsten filament source electron gun and the resolution of the microscope is 3.5 nm at 30 kV using the secondary electron (SE) detector.

2.5 Powder X-ray diffraction

X-ray diffraction takes advantage of the fact that X-rays are scattered in all directions by the atomic electrons. If the atoms scattering the X-rays are separated by a distance comparable to the wavelength of the X-ray, then interference can occur. For an ordered array of scattering centres this can give rise to interference maxima and minima. In a crystalline solid which has a regular distribution of atoms, these can be seen as several repeating planes as shown in Figure 2.15.

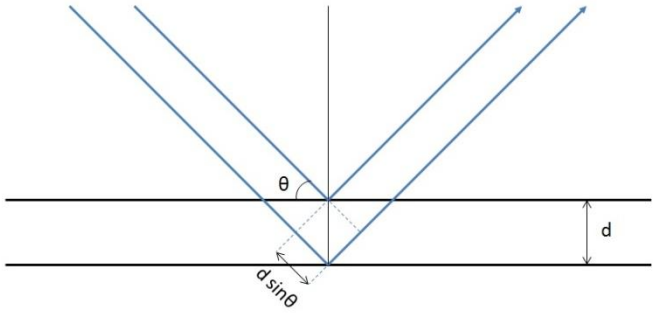

Figure 2.15: Derivation of Braggs Law between two diffracting planes

The scattering of the X-rays by the two parallel planes will produce an in phase or constructive interface diffracted X-ray beam if the additional distance travelled by the photons scattered from the lower plane is an integral number of wavelengths. This will depend on the interplaner distance, d, and will also be related to the angle of the incidence of the X-ray beam, θ. An integral wavelength difference d and θ are related by Equation 2.16, known as Bragg's equation.

$$2d\ sin\,\theta = n\lambda$$

Equation 2.16

where n is the integer and λ is the X-ray wavelength. In order for an X-ray beam diffracting off a particular lattice to be detected, the X-ray source, crystal and detector must be in the correct position.

In powder X-ray diffraction (XRD) the sample contains a polycrystalline material, and an enormous number of randomly oriented crystallites, typically 0.1 to 1 μm in length.[85] An X-ray beam striking this sample will diffract in all possible directions governed by Bragg's equation. Each crystallite will diffract in a different direction

due to its particular orientation. This will result in each lattice spacing giving rise to a cone shape. In order to measure these cones the detector moves along the circumference of a circle around the sample, as shown in Figure 2.16.

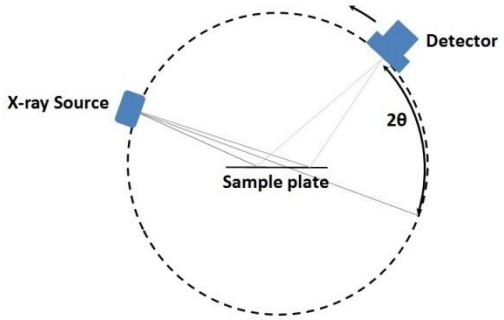

Figure 2.16: Schematic of a typical powder diffractometer

This cuts through the diffraction cones at various diffraction maxima meaning that the X-ray intensity can be plotted as a function of the detection angle 2θ.

X-ray diffraction of the film was performed on a Bruker Discover D8 with a Cu $K_{\alpha½}$ source and a scintillation detector.

3. Deposition of Perylene

3.1 Introduction

3.1.1 Single molecule properties

3,4,9,10-Perylenetetracarboxylic Diimides (PTCDIs) and other perylene based compounds have been extensively studied because of their optical and structural properties. Originally developed for use as fabric dyes about a century ago, they have since been modified and used in several applications. Due to their durability and weatherproof properties they are still used in an important class of high-performance pigments, used mainly for engineering resins and the colouration of automobile paints and synthetic fibres.[89]

The properties of perylene can be tuned by modifying the twelve points on the external carbons of the core, as shown in Figure 3.1.

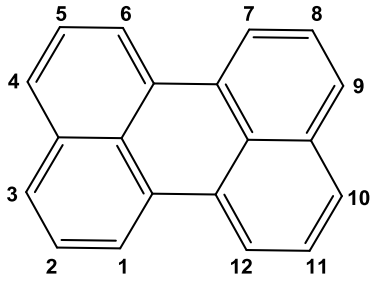

Figure 3.1: Structure of Perylene

Perylene can be modified in the peri-positions (labelled 3, 4, 9 and 10), the bay positions (labelled 1, 6, 7 and 12) and the ortho-positions (labelled 2, 5, 8 and 11). Most of the initial work on the synthesis of perylene analogues concentrated on 3,4,9,10-Perylenetetracarboxylic Diimides (PTCDIs). The structure of a typical PTCDI is shown in Figure 3.2.

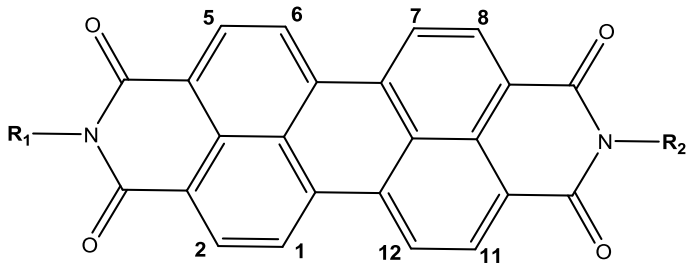

Figure 3.2: Structure of the PTCDI core molecules

PTCDIs can be modified in several ways: the two chains attached to the imide groups, R_1 and R_2, can be modified by substituting different groups, most commonly alkyl chains. The perylene core can also be modified at the bay positions (labelled 1, 6, 7 and 12) and the ortho-positions (labelled 2, 5, 8 and 11).[90] Modifying the bay or ortho positions will affect the optical and electronic properties in addition to affecting the solubility and packing of the molecules. Modifying the delocalised π system, where the HOMO and LUMO of the molecule are located as shown in Figure 3.3, by extending it with additional aromatic rings, allows the orbital energy levels and energy gap to be tuned.[91]

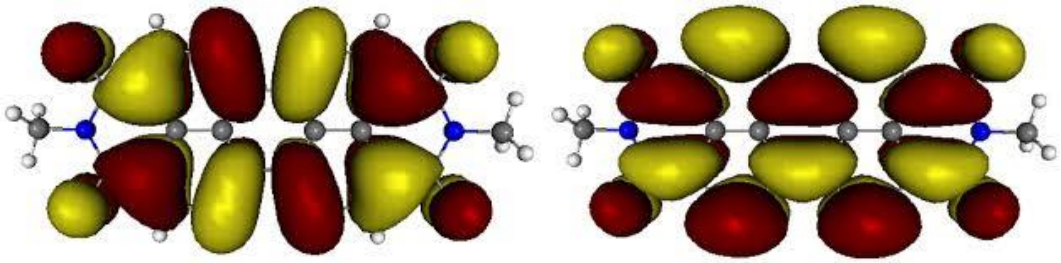

Figure 3.3: LUMO (left) and HOMO (right) of Me-PTCDI [92]

Modifying the imide groups, sometimes called the head and the tail, will affect the solubility and packing of the molecules, whilst having little effect on the optical and electronic properties of the complex. The absorbance of these perylene complexes will have three signature peaks in the range of 440 nm to 600 nm.[93] The redox properties of the PTCDI molecules are also controlled by the delocalised π system. Each pair of carbonyl groups at either end of the molecule can accept one electron each, as shown in the scheme in Figure 3.4.[94]

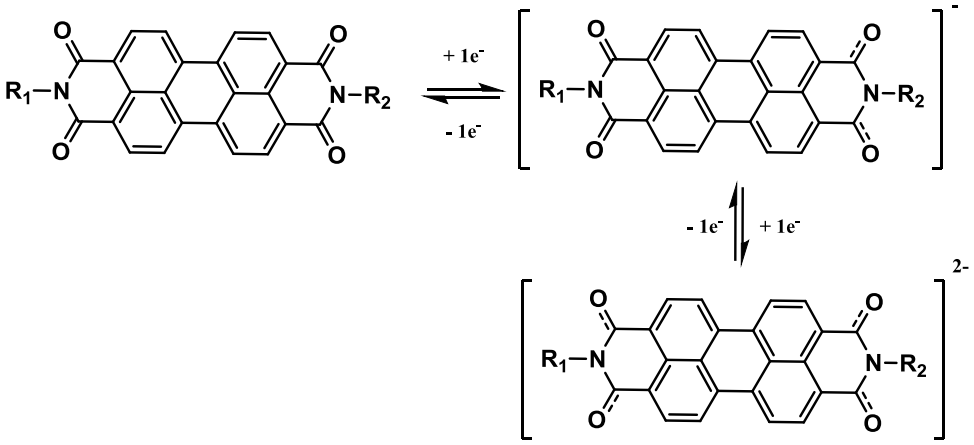

Figure 3.4: Anion radical, dianion formation for perylene diimides.

Because of the large π system located in the core of the molecule it is not very soluble. To make them suitable for solvent processing methods, PTCDIs require solubilising groups to be included such as alkyl chains at the imide positions.

3.1.2 Solid form

When packed in the solid form the π systems in the PTCDI molecules tend to π-π stack, as shown in Figure 3.5.

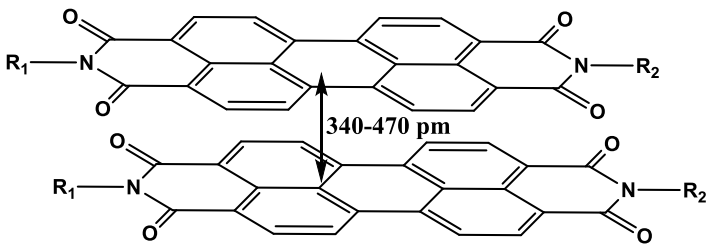

Figure 3.5: π–π-stacking of PTCDI molecules

The packing of the molecules in the solid depends largely on the steric bulk of the imide groups, R_1 and R_2. If the side group contains groups specifically designed to prevent π-π stacking then the solid form will contain randomly oriented molecules with no π-π interaction.[24] If the chain does not prevent stacking then, when single crystals of the molecule are grown or when the molecule self-assembles into a solid, the structure is normally a long needle shape due to a long chain of π stacked molecules with a stacking distance of between 3.4 Å and 4.7 Å depending on the imide groups.[8, 95] This occurs in both solution processed and vapour processed growths.[24] The imide groups can still affect the π-π distance by causing the stacked

cores to be displaced, i.e. not stack directly on top of each other. Some examples of displacement due to different imide groups in perylene dyes are shown in Figure 3.6.

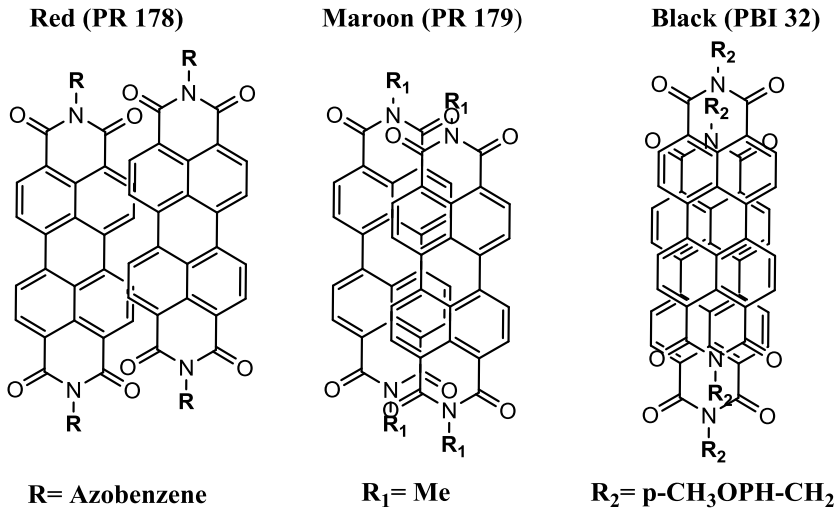

Figure 3.6: Transverse and longitudinal displacement of the stacked π systems in crystals of perylene based dyes: red (PR 178), maroon (PR 179) and black (PBI 32)

The different types of stacking result in the PTCDIs being crystallochromic.[96] The colour of the solid depends on the extent of the π-π overlap of the molecules when they are stacked. A study of the effect that transverse displacement of the molecules has on the colour was done by Klebe *et al*.[25] Molecules with a larger transverse displacement have the largest offset of π-π interaction. Therefore there is less interaction between the stacked delocalised π systems. This means that the molecule exhibits a similar electronic absorption to when it is in solution and therefore the solid appears red. An example of this is PR 178 from Figure 3.6 which is a brilliant shade of red. When there is a small transversal shift, there is an increase in π-π interaction, which results in a red-shift of the electronic absorption as there is a larger π delocalisation. This results in the solid appearing maroon in colour and an example of this is PR 179 from Figure 3.6. When there is no transversal displacement the delocalised π systems are directly on top of each other which results in a very strong interaction between the neighbouring π systems. This causes the solids to appear black due to the strongest electronic interaction possible between neighbouring molecules. An example of this is PBI 32 from Figure 3.6.

Another consequence of the large delocalised π system is charge transportation. The stable redox processes of the PTCDI molecules and the good π-π overlap between the stacked molecules mean that charges can be transported along the stack, as shown in Figure 3.7.

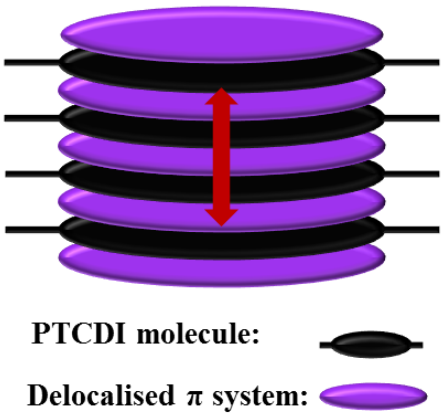

Figure 3.7: π-π stacking of several PTCDI molecules

Since the molecules tend to only stack on top of a single molecule, this results in transport along the stack perpendicular to the PTCDI molecule. Similar to the colour of the solid state, the displacement of the molecules when they stack can also change the electron transporting properties of the solid. When there is a large displacement between the molecules, the smaller π-π overlap will result in lower charge mobility. A study by Lehmann and Zahn found that the chain attached to the imide group could affect the charge mobility of the molecules by up to 4 orders of magnitude.[97] PTCDI molecules with imide groups which caused a large transversal displacement, such as dimethoxyethyl-PTCDI or Diphenyl-PTCDI, had low charge mobilities of $4x10^{-6}$ $cm^2 V^{-1} s^{-1}$ when incorporated into FETs, whereas molecules that cause smaller transversal displacement, such as diheptyl-PTCDI, has a higher charge mobility of $5x10^{-2}$ $cm^2 V^{-1} s^{-1}$. Charge mobilities as high as 0.6 $cm^2 V^{-1} s^{-1}$ have been measured for dipentyl-PTCDI FETs.

3.2 N,N dibutyl-3,4,9,10-perylene-bis(dicarboxime)

The initial investigation of electrodeposition was performed using N,N dibutyl-3,4,9,10-pereylene-bis(dicarboxime) (BuPTCDI), which has a short butyl chain substituted at the head and tail position, as shown in Figure 3.8.

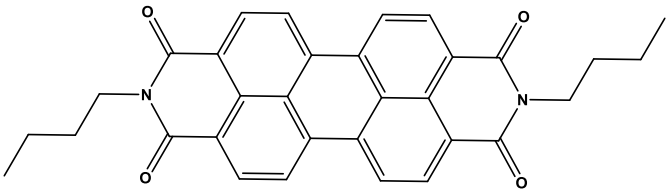

Figure 3.8: N,N dibutyl-3,4,9,10-perylene-bis(dicarboxime) BuPTCDI

BuPTCDI, a simple PTCDI structure, was chosen for initial investigation because it is a more soluble perylene and the chains were kept short in order to minimise any effect on the π-π stacking of the PTCDI core.[24]

3.2.1 Molecular properties

The BuPTCDI sample was synthesised according to the method described in section 3.5.

3.2.1.1 Absorption Spectroscopy

The absorbance of several concentrations of BuPTCDI in THF was measured by UV/Vis spectroscopy at 298 K and is shown in Figure 3.9.

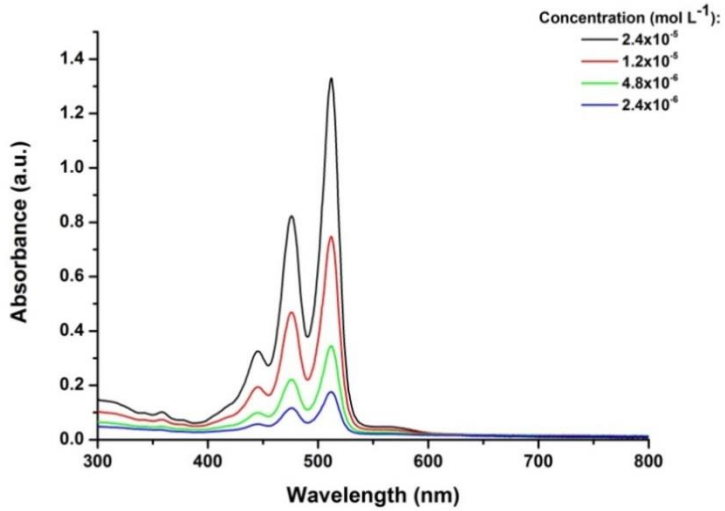

Figure 3.9: UV/Vis spectra of several concentrations of BuPTCDI in THF

PTCDI cores have a typical three-peak signature between 400 nm and 550 nm with high molar absorption coefficients which are unaffected by any imide substituted side chains.[93] For BuPTCDI dissolved in THF in Figure 3.9, the three peaks at 512 nm, 475 nm and 445 nm correspond to the first three vibrational peaks of the S_0 to S_1 transition. The three peaks have separations of 1520 cm^{-1} and 1420 cm^{-1} respectively, which correspond to the carbon-carbon stretching vibrations in an aromatic ring.[98] This agrees with the data obtained by Zhang *et al*. when investigating BuPTCDI.[99]

The molar extinction coefficients were calculated (Table 3.1) from the Beer-Lambert plot of the maxima against concentration shown in Figure 3.10.

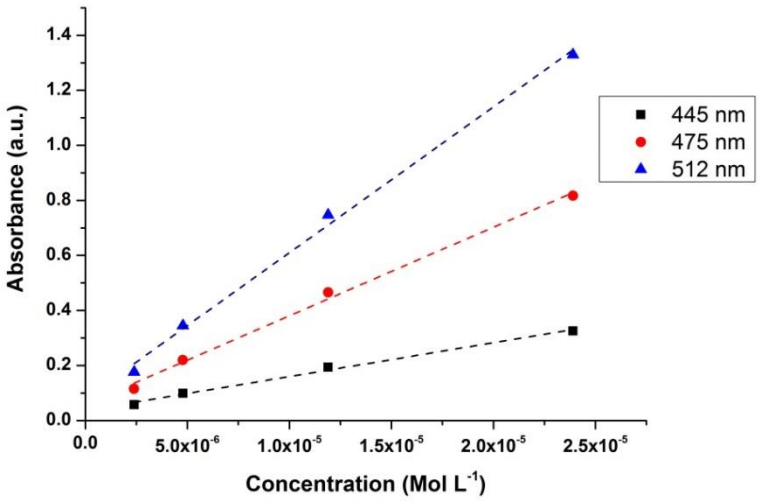

Figure 3.10: Absorbance against concentration for the BuPTCDI maxima

Table 3.1: Molar extinction coefficients of N,N dibutyl-3,4,9,10-pereylene-bis(dicarboxime)

λ_{max} (nm)	$\tilde{\nu}$ (cm^{-1})	ε (M^{-1} cm^{-1})
445	22500	12300
475	21000	32200
512	19500	53000

3.2.1.2 Emission Spectroscopy

Emission spectroscopy on BuPTCDI in THF at a concentration of 1.2×10^{-6} mol dm^{-3} was performed by exciting at the maximum observed during absorption spectroscopy in section 3.2.1.1. The normalised spectra for the emission and the excitation are shown in Figure 3.11. Measurements were also performed at 77 K to minimise any effects of the solvent, as shown in Figure 3.12.

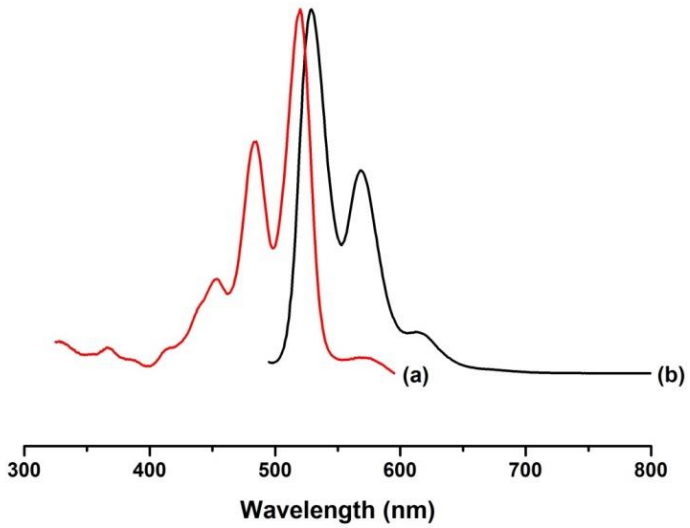

Figure 3.11: Normalised (a) excitation (emission at 615 nm) and (b) emission (with excitation at 475 nm) spectra of BuPTCDI at 298 K in THF

BuPTCDI in THF at 298 K shows $S_1 \rightarrow S_0$ fluorescence with emission maxima at 528 nm and 568 nm. The excitation maxima are at 520 nm, 485 nm and 454 nm. The proximity of the two peaks and the near mirror symmetry of the absorption and emission spectra suggest that there is little distortion in the configuration of the molecule when it is excited from the ground state to the excited state. This is consistent with the extensive delocalisation of the frontier orbitals over the whole molecule.[100]

The normalised spectrum of BuPTCDI in THF at 77 K is shown in Figure 3.12.

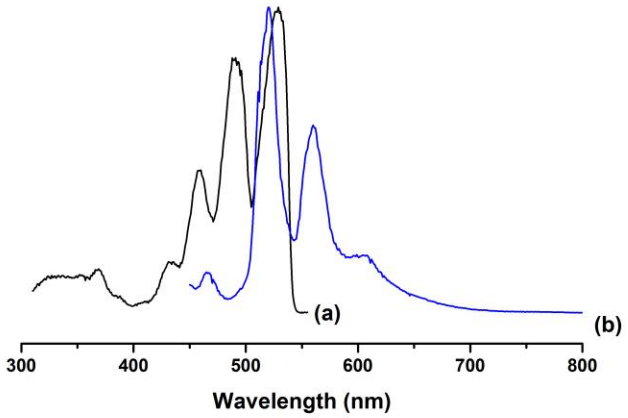

Figure 3.12: Normalised (a) excitation (emission at 575 nm) and (b) emission (with excitation at 445 nm) spectra of BuPTCDI at 77 K in THF

BuPTCDI at 77 K shows similar $S_1 \rightarrow S_0$ fluorescence with emission maxima 519 nm, 560 nm, and now the higher wavelength of 606 nm. The peaks in the excitation spectra are also clearer with maxima at 528 nm, 489 nm and 458 nm. A peak maximum at 432 nm that was negligible in the spectrum at 298 K is now clearly visible. The proximity of the two maxima suggests that there is no change in the geometry of the excited perylene compared to the geometry of the ground state. This is due to the rigidity of the perylene core that is flat and not sterically strained and in most solvents perylene is found to be highly fluorescent.[100] This implies that the small Stokes shift in the system at 298 K is due to solvent rearrangement.

Both spectra agree with the other emission spectroscopy data obtained for similar PTCDI molecules. The emission and excitation spectra normally have near mirror symmetry with a negligible Stokes shift, which is mostly due to solvent rearrangement.[101]

3.2.1.3 Electrochemistry

The electrochemical properties of BuPTCDI were measured using cyclic voltammetry. One reversible process was found at $E_{½}$ = -0.38 V and a pseudo reversible process was found at $E_{½}$ = -0.69 V against Ag/AgCl corrected with ferrocene and these are shown in Figure 3.13.

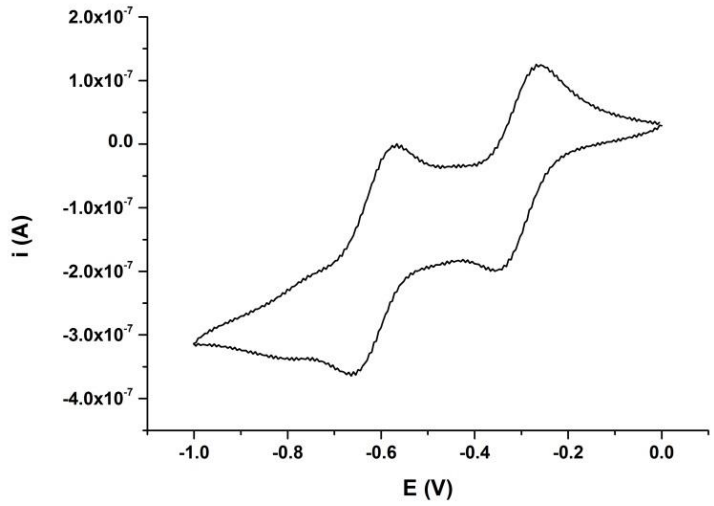

Figure 3.13: Cyclic voltammogram of BuPTCDI between -1.0 V and 0 V in 0.1M $TBABF_4$ in THF

To ensure that both processes were chemically and electrochemically reversible, scans at several scan rates were carried out for each process. The first series of scans were performed at several scan rates between -0.5 V and 0 V corresponding to the first process (Figure 3.14) and the second series between -1.0 V to -0.5 V for the second process (Figure 3.15).

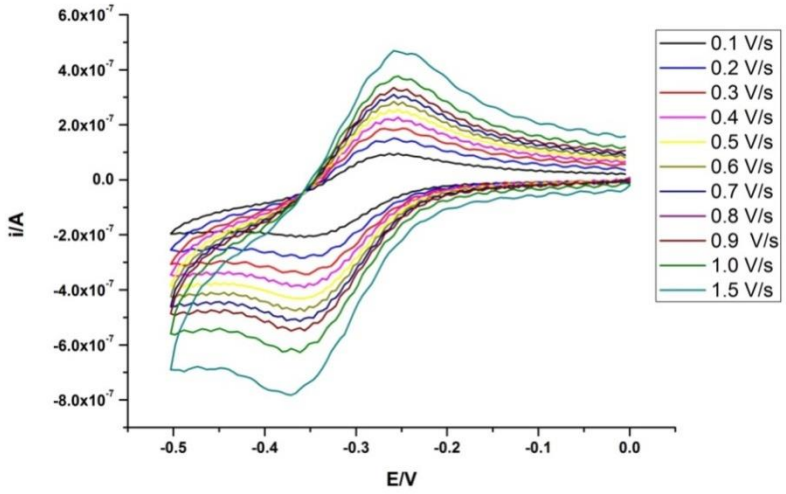

Figure 3.14: Cyclic voltammogram of BuPTCDI between -0.5 V and 0 V in 0.1M $TBABF_4$ in THF

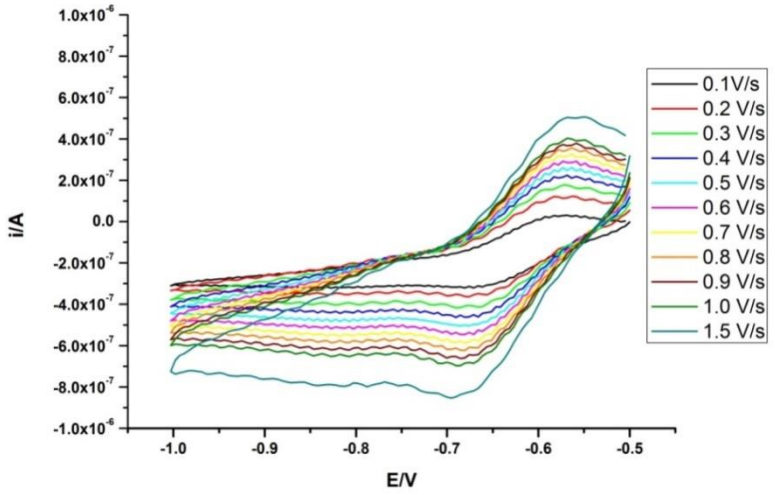

Figure 3.15: Cyclic voltammogram of BuPTCDI between -1.0 V and -0.5 V in 0.1M $TBABF_4$ in THF

The data were processed according to the rules mentioned in section 2.2.

Plots of current maxima against the square root of the scan rate are shown in Figure 3.16 and Figure 3.17.

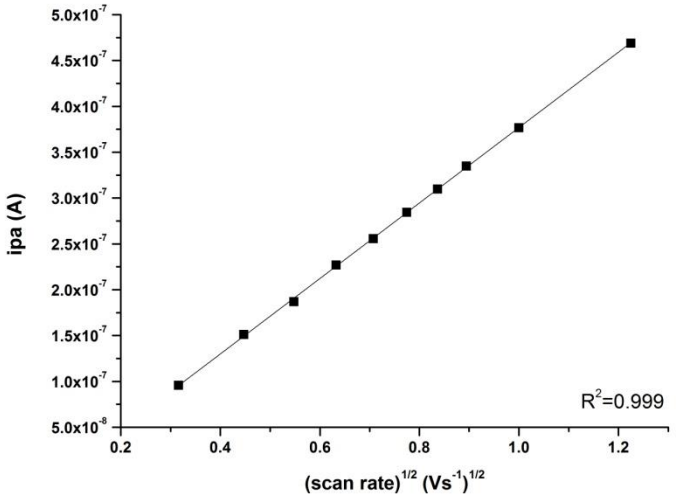

Figure 3.16: Current maxima against the square root of the scan rate for cyclic voltammogram of BuPTCDI between -0.5 V and 0 V in 0.1M $TBABF_4$ in THF

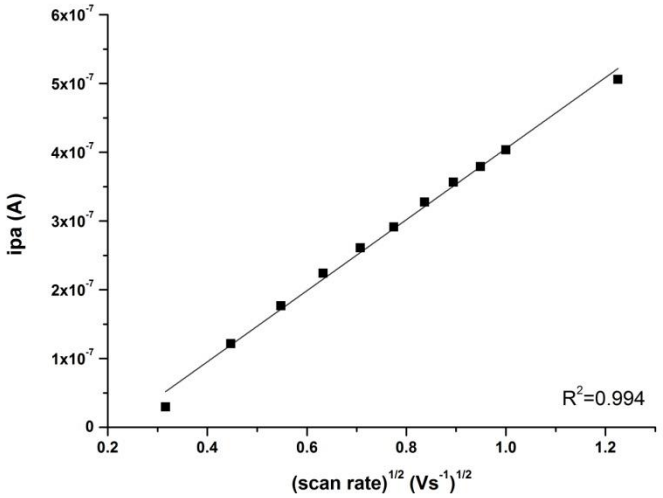

Figure 3.17: Current maxima against the square root of the scan rate for cyclic voltammogram of BuPTCDI between -1.0 V and -0.5 V in 0.1M $TBABF_4$ in THF

From the positions of the E_{pa} and E_{pc} and the straight line from Figure 3.16 it can be deduced that the redox process that occurs between 0 V and -0.5 V with $E_{½}$=-0.36 V is reversible. The reversibility of the first process is important as the molecule has to be stable for electrochemical deposition.

Even though the plot in Figure 3.17 shows an approximately straight line, the positions of the E_{pa} and E_{pc} are not constant suggesting that the kinetics of the

electron transport are slower than the experiment scan, which means that it is only pseudo reversible.

The proximity of the two processes suggests that the processes are independent and that the charge of the second reduction is largely unaffected by the first charge on the other side of the molecule. That is why the potential of the second process is not that much more negative. The presence of two processes agrees with the electrochemical data obtained for other perylene diimides.[94]

3.2.2 Films

3.2.2.1 Deposition

BuPTCDI was successfully electrochemically deposited from the anionic form, as shown in Figure 3.18.

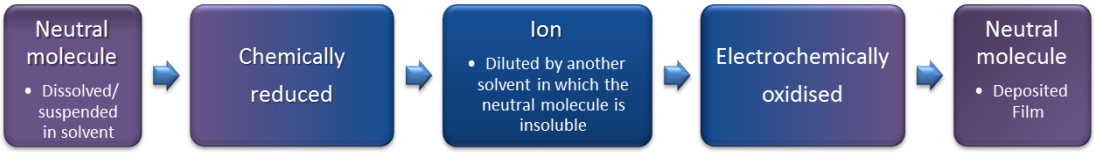

Figure 3.18: Flow diagram of the deposition process

The anion was prepared by exposing the neutral form suspended in THF to an excess of sodium in the form of a sodium mirror for between 3 and 12 hours approximately. The anionic form of BuPTCDI in THF was then filtered and diluted with MeCN electrolyte solution, in which the neutral form is not soluble, at a ratio of 1:10.

Depositions were performed using a three-electrode set-up. The substrate on which the molecule was being deposited was used as a working electrode. A platinum electrode was used as a reference electrode and another as the counter electrode. The counter electrode was in a separate cell connected to the rest of the experiment by a glass frit. This was done so that any electrochemical processes occurring at this electrode would be isolated and not have any effect on the deposition process taking place. A schematic of this apparatus is shown in Figure 3.19.

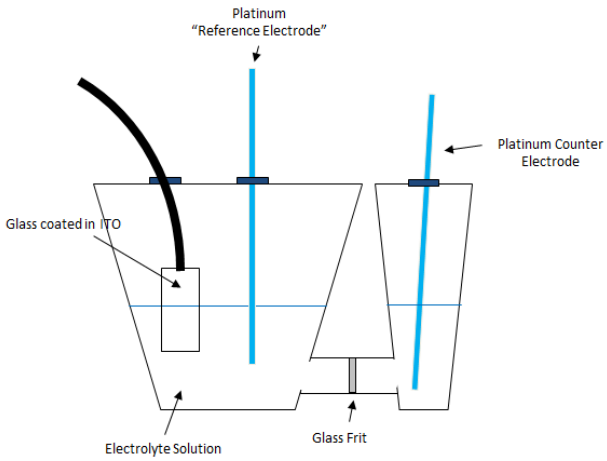

Figure 3.19: Modified three-electrode electrochemical apparatus for deposition with counter electrode isolated

To calibrate the system, ferrocene was used as the experiment used a platinum pseudo-reference electrode and not a standard Ag/AgCl reference electrode. The zero point was determined by running a cyclic voltammetry of ferrocene.

Since an overpotential was required for electrodeposition of BuPTCDI, several potentials were investigated to find the lowest potential required to deposit a film. This was done by changing the potential when all the other deposition conditions were kept the same until the lowest voltage capable of deposition was found. At a concentration of approximately $5x10^{-4}$ mol dm^{-3} a minimum voltage of 0.84 V was required. The lowest voltage that resulted in deposition was used as this would minimise film charging. A typical deposition charge per cm^2 of a film deposited at 0.84 V is shown in Figure 3.20.

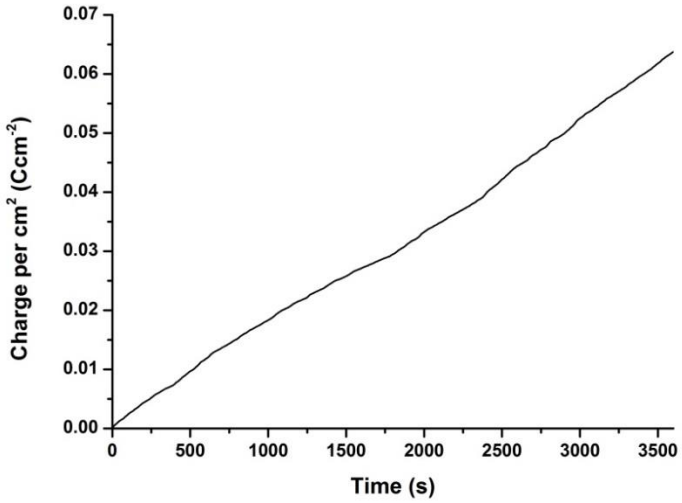

Figure 3.20: Total charge per cm^2 passed during a 60 minutes deposition while holding the potential at 0.84 V

The deposition is a straight line which suggests that the rate of deposition is kinetically controlled or mixed controlled, a combination of kinetic and diffusion control. The fact that it does not level off implies that the film is conductive since it continues to grow at a steady rate on top of already deposited molecules.

In the solid form the sample is a brick red colour, as shown in the film below in Figure 3.21.

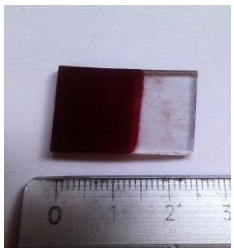

Figure 3.21: Picture of a BuPTCDI film deposited at 0.84 V for 30 minutes

To obtain more details about the stages of a typical deposition, a plot of charge per cm^2 against the square root of time, $t^{½}$, of a typical deposition is shown below in Figure 3.22.

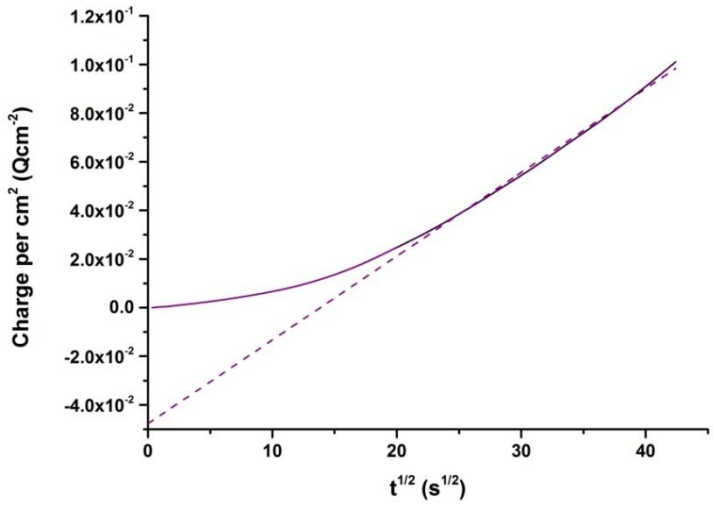

Figure 3.22: Total charge per cm^2 against $t^{½}$ for a 60 minutes deposition while holding the potential at 0.84 V with $[BuPTCDI]^-$

The plot of charge per cm^2 against $t^{½}$ can indicate much about the type of deposition. If a linear fit can be applied to part of the plot, then the rate of that part of the deposition is diffusion controlled based on:

$$Q = 2FnA[r^b]\sqrt{\left(\frac{D_r t}{\pi}\right)} + Q_c + Q_{abs}$$

Equation 2.10

If the plot is not straight then the rate of the deposition is influenced by kinetic factors, either completely or partially, where the rate of deposition is mixed controlled by both kinetic and diffusion factors.

Which axis the straight line intercepts upon extrapolation will also give information; if the line intercepts the y-axis in the positive region, then the reaction is completely diffusion controlled. If it intercepts the negative y-axis after having crossed the x-axis first, then the deposition rate has been mixed controlled at some point.

The latter part of the plot of charge per cm^2 against $t^{½}$ gave a straight line and a negative intercept. This confirms that the deposition has two stages: the initial stage where the deposition rate is mixed controlled and a second stage where the rate of deposition is diffusion controlled as the straight line intercepts the y-axis in the negative region. The current during the first few seconds of the absorption is influenced by several factors such as the initial reorganisation of the solvent due to form the double layer and the deposition of the $[BuPTCDI]^-$ molecules at the substrate surface. The kinetics of the system will then change due to the absorption of the film onto the surface of the electrode as this will affect the conditions of the electron transfer process. Until the kinetics of the electron transfer becomes constant the rate of deposition will be mixed controlled.

The two stages of deposition identified in the plot of Q cm^{-2} against $t^{½}$ are also present in the plot of the current measured during the deposition, which is shown in Figure 3.23.

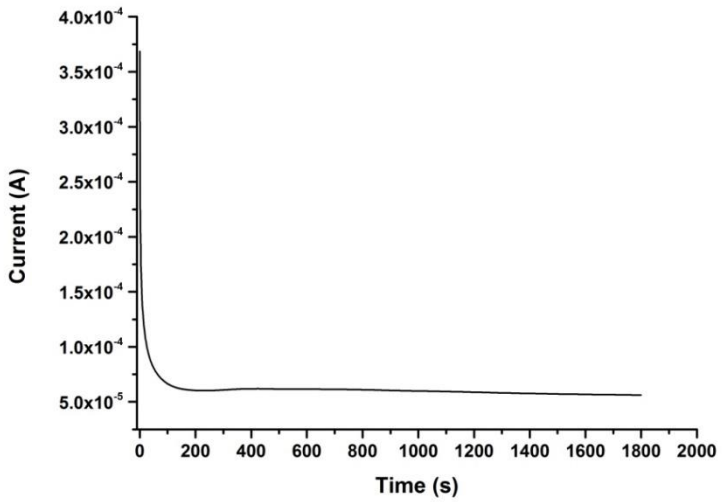

Figure 3.23: Current against time for 30 minutes deposition $[BuPTCDI]^-$ while holding the potential at 0.84 V

The current measured when the potential is initially applied is very high and drops rapidly for the first ~100 seconds. This is due to the reorganisation of the solvent to form the double layer and the deposition of the $[BuPTCDI]^-$ molecules already at the substrate surface. The current then decreases, as rate of electron transfer decreases due to the formation of the film on the substrate and the depletion of $[BuPTCDI]^-$ molecules around the electrode surface. Once the rate of electron transfer has stabilised the current will become linear as all molecules that come into contact with the substrate are brought there by diffusion.

The first five seconds of the deposition shows several stages as shown in Figure 3.24.

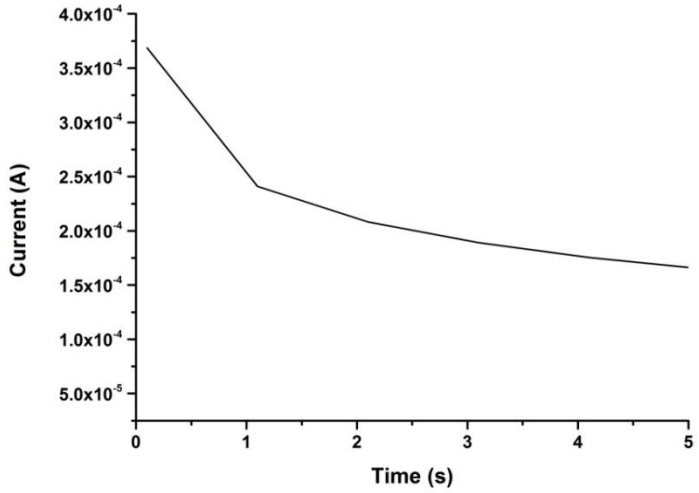

Figure 3.24: Zoom first five seconds of the current against time for 30 minutes deposition $[BuPTCDI]^-$ while holding the potential at 0.84 V

Initially there is a large drop in current due to the formation of the double layer and the absorption of any$[BuPTCDI]^-$ already present at the substrate surface**.** Then the absorption rate will then change due to the change in kinetics of the surface of the substrate. An expansion of the current after the initial decrease is shown in Figure 3.25.

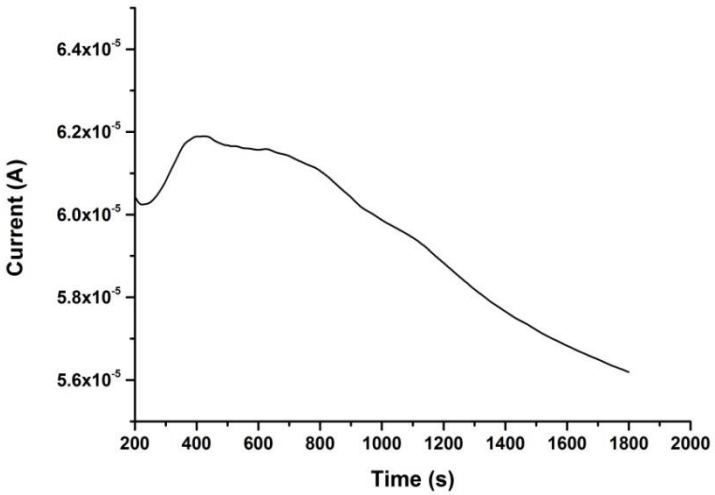

Figure 3.25: Current per cm^2 against time in more detail for the deposition of 30 minutes while holding the potential at 0.84 V.

After the initial drop in current at the start, as seen in Figure 3.23, the current increases before decreasing steadily. This indicates that the process is diffusion controlled as the current will fall at a rate of $t^{½}$ as predicted by:

$$I_d = FnA[r^b]\sqrt{\left(\frac{D_r}{\pi t}\right)}$$

Equation 2.3

If the deposition was kinetically controlled, the current would be constant as the concentration at the surface of the substrate would not change significantly. If the electron transfer of the electrodeposition was the rate determining factor of the process, then there would be little change in the concentration of anions at the substrate surface, < 5 %, meaning that diffusion would not play a significant role and Equation 2.3 would give a value that was independent of time.[84]

The current increase is not expected, but since it occurs after the large drop in current due to the slowing of electron transfer because of changes in the initial formation of the film, it is possible that it is the stage where the film has completely covered the substrate. Since the deposition of anions onto already deposited molecules will be more energetically favourable than nucleation onto the substrate, this could explain the increase in current of the deposition.

The concentration of $[BuPTCDI]^-$ was investigated to determine how the concentration affected the deposition rate. Depositions at several different concentrations were performed to determine which one gave the highest charge per cm^2. Different concentrations of $[BuPTCDI]^-$ were deposited at 0.84 V for 60 minutes, the data for which are displayed in Table 3.2:

Table 3.2: Concentration of $[BuPTCDI]^-$ with the deposition charge and the charge per cm^2 of a 60 minutes deposition.

Concentration (Moles dm^{-3})	Charge (C)	Charge per cm^2 (Ccm^{-2})
$5.82x10^{-4}$	0.01633	0.01060
$8.36x10^{-4}$	0.01845	0.02196
$8.22x10^{-4}$	0.02299	0.01533
$9.80x10^{-4}$	0.02348	0.01525
$9.95x10^{-4}$	0.02628	0.02346
$1.38x10^{-3}$	0.04437	0.02689
$1.61x10^{-3}$	0.09900	0.05893
$1.78x10^{-3}$	0.07120	0.11867
$2.01x10^{-3}$	0.10956	0.08695
$2.46x10^{-3}$	0.09574	0.07978
$3.00x10^{-3}$	0.09563	0.06375

A plot of charge per cm^2 against concentrations is shown in Figure 3.26.

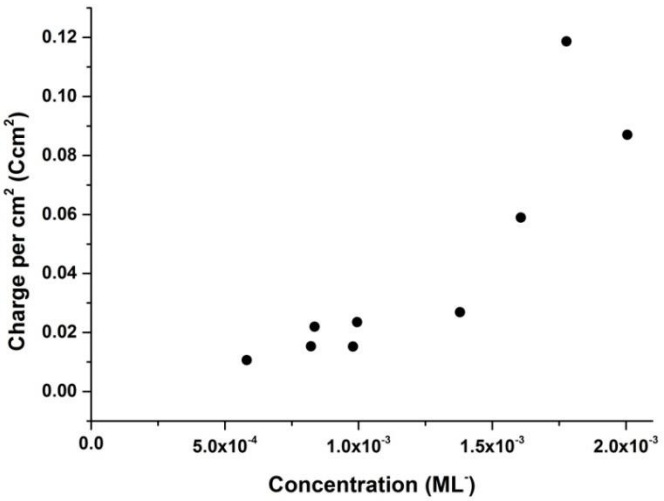

Figure 3.26: Plot of charge per cm^2 versus concentration for the 60 minutes depositions of BuPTCDI

From the plot it is possible to see that as the concentration increases, the amount of charge passed per cm^2 increases. This is because there is more $[BuPTCDI]^-$ available to reduce, resulting in more charge being passed.

At concentrations lower than $5.8x10^{-4}$ mol dm^{-3}, no films were deposited which means that this is the minimum concentration required for deposition at a potential of 0.84 V against ferrocene.

At concentrations higher than $2.0x10^{-3}$ mol dm^{-3} the charge per cm^2 started to decrease. If the highest charge per cm^2 possible during this time at this potential had been reached, then it would be expected that all depositions at higher concentrations would have the same the charge per cm^2. The decrease in charge per cm^2 suggests that something else is occurring in the deposition solution and a dark red coloured powder was found at the bottom of the electrochemical apparatus after deposition. Since an excess of sodium was used and the solution was filtered prior to dilution, it is doubtful that any unreacted BuPTCDI was already present. Therefore the powder must have formed after the dilution of the anionic solution in the MeCN electrolyte solution. This suggests that aggregation of the BuPTCDI molecules into stacks could have occurred, since molecules with single chain imide groups have been shown to π-π stack into one-dimensional nanostructures at high concentration.[24, 98] The stacked structures would not be soluble in the solution, so would precipitate out lowering the overall concentration of $[BuPTCDI]^-$ resulting in a drop of the total charge passed per cm^2.

3.2.2.2 Absorption Spectroscopy

3.2.2.2.1 Electronic Absorption of BuPTCDI films

UV/Vis spectroscopy measurements were performed on several of the films to assess the absorption of the electrodeposited films and compare them to the molecule in solution. The absorption of a typical BuPTCDI film is shown in Figure 3.27.

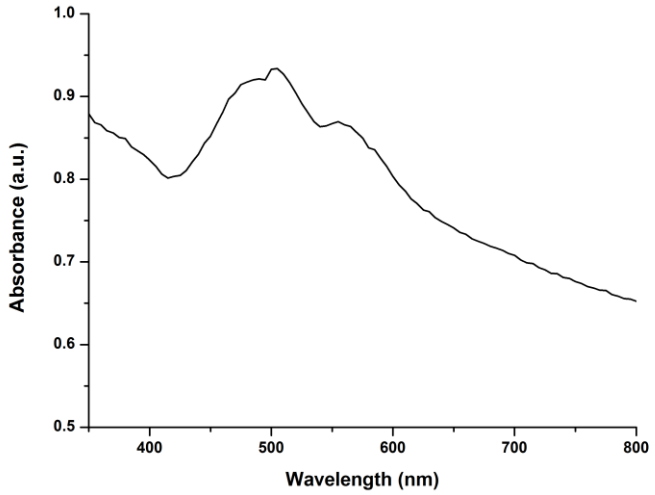

Figure 3.27: Absorption of the thin film deposited at 0.84 V for 30 minutes resulting in a charge per cm^2 of $5.28x10^{-2}$ Ccm^{-2}

The film shows a similar absorption to the compound in solution, but there are some changes to the intensities observed and some of the peaks have red-shifted. A comparison of the UV/Vis absorption of BuPTCDI as a thin film and dissolved in different solvents is shown in Figure 3.28.

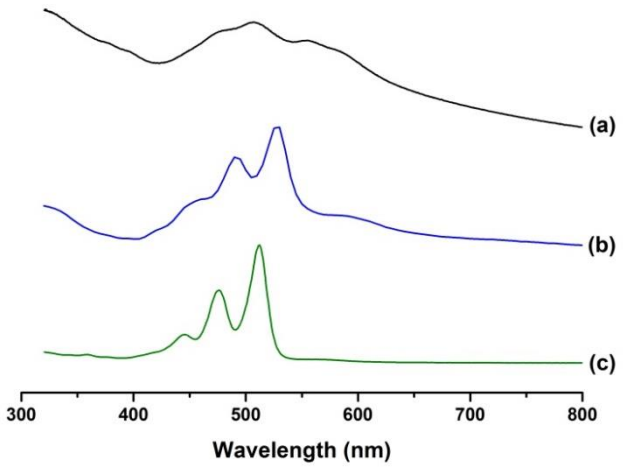

Figure 3.28: Absorbance of BuPTCDI (a) deposited on FTO, (b) dissolved in DMSO and (c) dissolved in THF. Spectra are offset for clarity.

The three perylene peaks observed in section 3.2.1.1 are clearly visible in the spectrum of the solution in THF (c), but become less visible in the similar spectrum in DMSO (b), and are not distinguishable in the thin film (a). The development of a shoulder at a longer wavelength than the maximum observed at around 570 nm in the spectra in DMSO and the film spectra is indicative of stacked π-π systems. This shoulder is just visible in the THF spectrum, more visible in the DMSO spectrum and is a dominant feature in the thin film spectrum. This is probably due to aggregation of the π systems in the central core of the perylene complex. As the concentration of BuPTCDI in solution increases, there is a higher probability of the π-systems stacking. In the solid film there is a network of π-stacked systems which makes the molecules suitable as an organic conductive material and therefore absorption due to this network is expected. The absorbance of the films is linked to their thicknesses; it increases until the films are too thick and light can no longer travel through the sample.

The electronic absorbances of several films with a different total charge per cm^2 are shown in Figure 3.29.

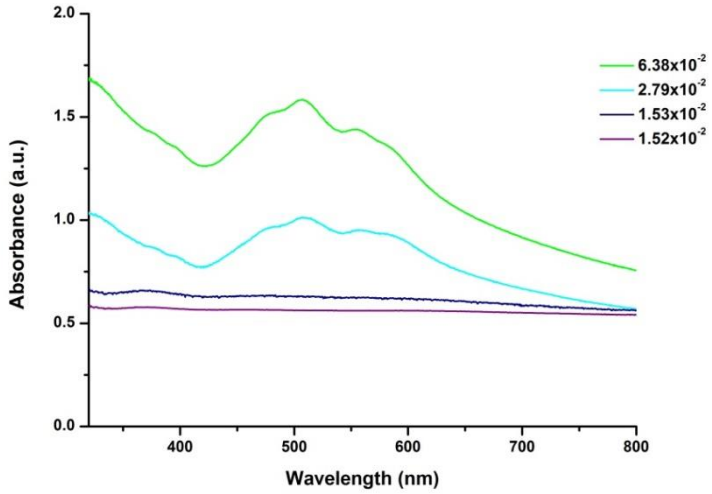

Figure 3.29: Absorbances of several films with different charges per cm^2

The larger the charge per cm^2 passed, the more the films absorb. The value for the maxima of the films is the same as they are made of the same compound. The width of the peaks also stays very constant, indicating that the difference in packing of the films is not too significant.

However, not all films showed the same clear spectra as in Figure 3.29; several of the spectra of films with similar thickness were completely dominated by light scattering due to differences in the films' packing and densities. The films are also not uniform, meaning that the electronic absorption will give similar, but not identical spectra depending on which region of the film the measurement is performed.

The difference in morphology of the films makes the absorbance unsuitable for determining the thickness of film as the amount absorbed can be heavily influenced by the scattering.

3.2.2.2.2 Comparison of electronic absorptions of electrodeposited BuPTCDI to the original BuPTCDI complex

To ensure that it was BuPTCDI that had been electrodeposited, films were dissolved from the FTO using DCM and compared to a sample of BuPTCDI dissolved in DCM, as shown in Figure 3.30.

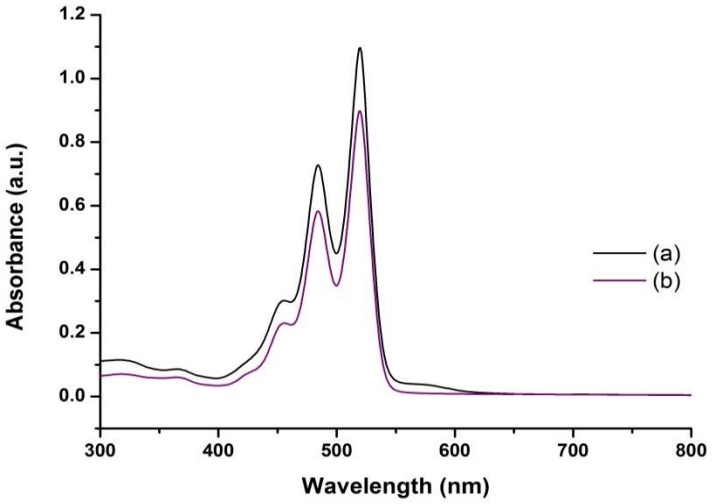

Figure 3.30: UV/Vis spectra of (a) BuPTCDI dissolved in DCM and (b) recovered electrodeposited BuPTCDI film in DCM

The spectrum of the dissolved electrodeposited BuPTCDI is identical to the spectrum of the BuPTCDI sample, confirming that the deposited film was BuPTCDI and that the molecule does not decompose during the electrodeposition process.

3.2.2.3 Emission Spectroscopy

Photoluminescence spectroscopy was performed on the films using an argon-ion laser. The measured response is shown in Figure 3.31.

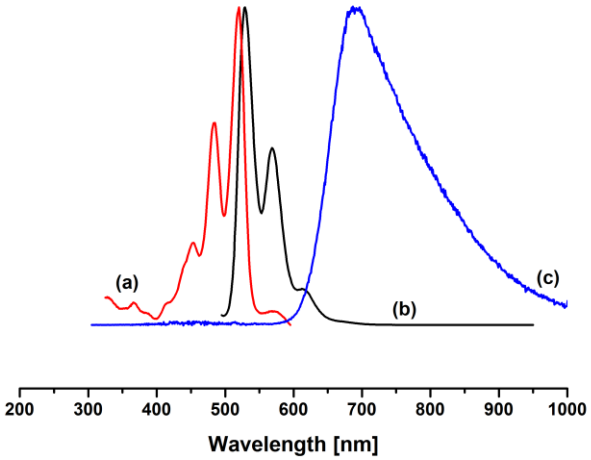

Figure 3.31: Normalised excitation (monitored at 614 nm) (a) and emission (excited at 475 nm) (b) spectra of BuPTCDI in THF and emission of a BuPTCDI film (excited at 514 nm) (c).

The photoluminescent response of the film is very different to the response of the powdered molecule in solution. The spectrum of the film (c) in Figure 3.31 is a broad featureless band with a maximum of approximately 679 nm. The red shift of the absorption between the spectrum in solution (b) and the spectrum of the film (c) is attributed to the interaction of the layers of molecules in the film. Rather than the excitation of the electron being confined to the delocalised π system of one molecule, it is in a delocalised π system of several molecules and therefore has a different band gap. This is most likely due to the excimers in the perylene film and is typical for thin solid films.[102, 103, 104]

3.2.2.4 Raman Spectroscopy

Raman spectroscopy was performed on a BuPTCDI film. The results are shown in Figure 3.32.

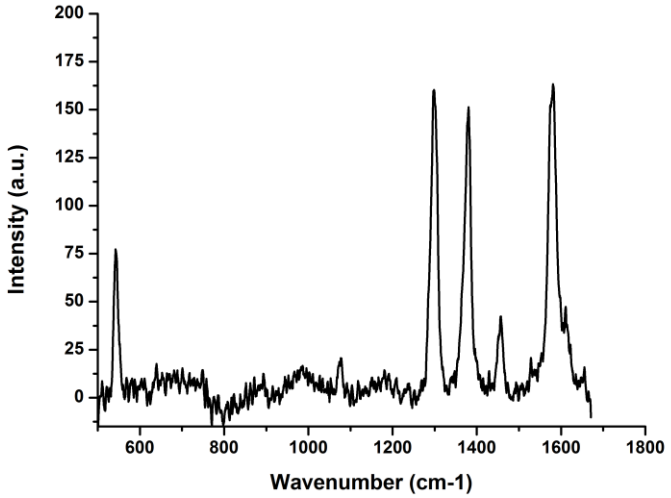

Figure 3.32: Raman scattering spectrum of the BuPTCDI film.

The spectrum of BuPTCDI was compared to the spectra of perylene-diimide thin films deposited by thermal evaporation techniques studied by Rodríguez-Llorente and was used to identify the assignment of the peaks present in Figure 3.32 present in Table 3.3.[105]

Table 3.3: Observed Raman wavenumbers (w) of a thin film of BuPTCDI

Peaks (cm^{-1})	Assignments
542	Perylene deformation
1076	C-H bend
1298	C-H bend + ring stretch
1381	Perylene ring stretch
1458	Perylene ring stretch
1581	C=C stretch

The overlap of the peaks confirms that the BuPTCDI and the other PTCDI films have similar properties, confirming that the central perylene core has not been altered by the electrodeposition technique.

3.2.2.5 Scanning Electron Microscopy

The morphology of several films deposited under different conditions was studied using SEM imaging. The technique allowed for images of the film surface to be recorded with high resolution and magnification.

A scan of the film deposited at a potential of 0.84 V for 30 minutes is shown in Figure 3.33 and in Figure 3.34.

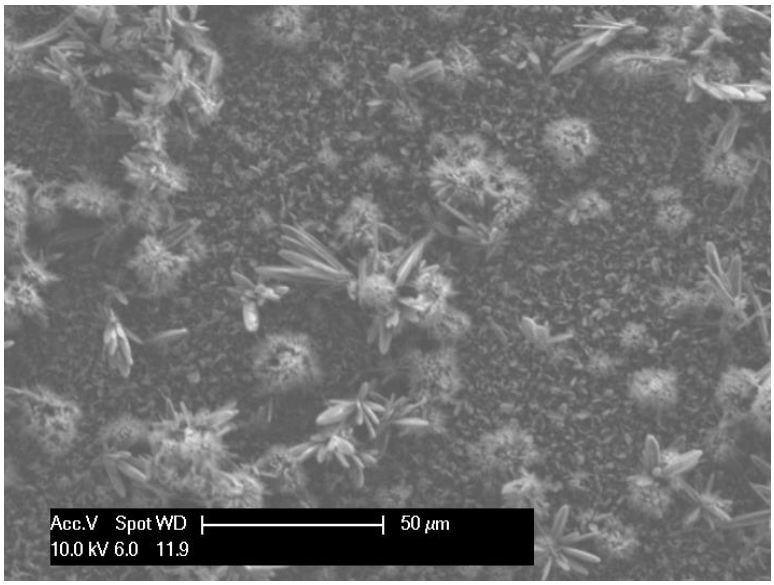

Figure 3.33: SEM image of a film deposited at 0.84 V for 30 minutes resulting in a charge per cm^2 of $1.19x10^{-1}$ Ccm^{-2}

From Figure 3.33 it is possible to see that the morphology of the film is not homogeneous as there are several raised clusters of BuPTCDI. Higher magnifications of the raised structures are shown in Figure 3.34.

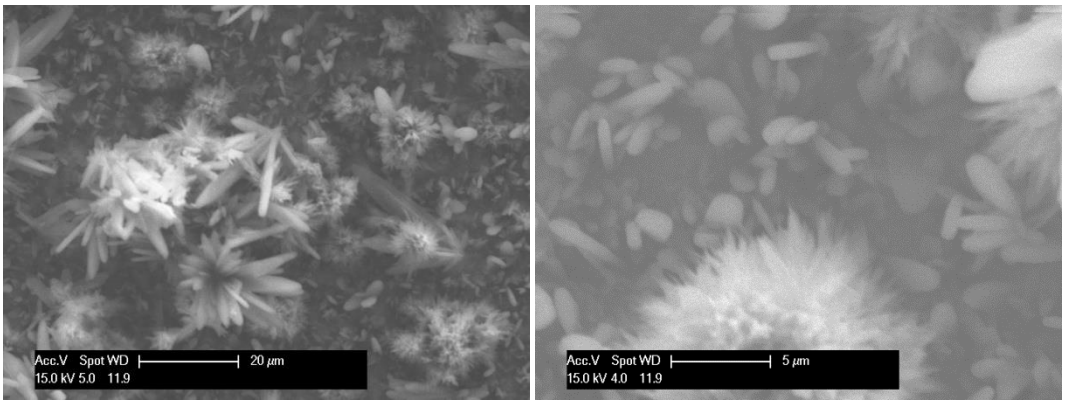

Figure 3.34: SEM images of a film deposited at 0.84 V for 30 minutes resulting in a charge per cm^2 of $1.19x10^{-1}$ Ccm^{-2}

Further magnification reveals that the films are composed of several clusters of densely packed long crystallite structures surrounded by smaller ones. The shape of the long crystallite structures agrees with the typical structure of self-assembled single alkyl chained PTCDI.[24, 106] The electrodeposited films are very different from films deposited by thermal evaporation which deposit in terrace formations. Despite the different formations, the molecules seem to be oriented with the core deposited parallel to the substrate in both cases. [107]

One reason why not all the seed crystals develop into long crystalline structures could be that perhaps not all the cores are parallel to the substrate. The delocalised π system is the part of the molecule that is electronically conductive and charge can only be carried perpendicular to this system. If the initial deposition is not parallel to the substrate it will insulate the area it covers. However, if it is parallel to the substrate, it can conduct the charge through it and will continue to develop during the deposition process. Another possibility is that some of the BuPTCDI molecules are deposited at an angle to the substrate, like the herringbone structure similar to the single crystal, resulting in the molecule being weakly connected. Molecules in this situation would still conduct, but may not be as conductive as molecules parallel to the surface, resulting in a slower growth.

A film deposited under the same conditions but using a solvent with a lower concentration is shown in Figure 3.35.

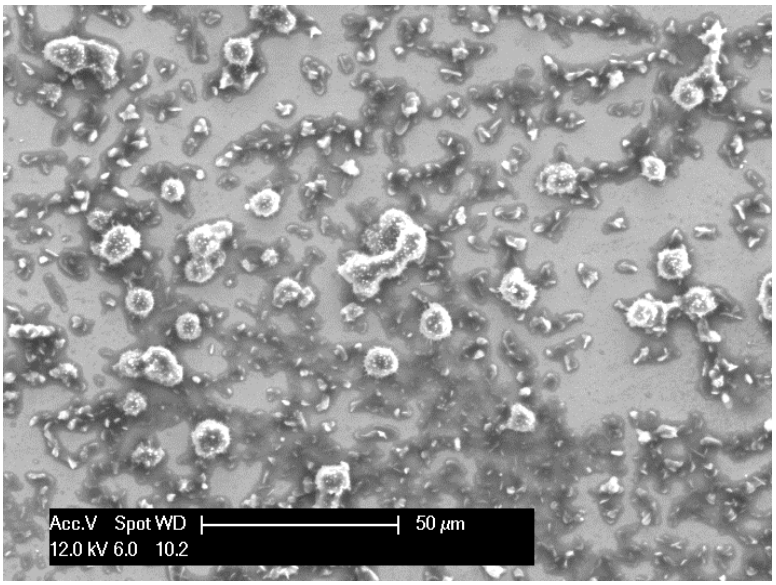

Figure 3.35: SEM image of a film deposited at 0.84 V for 60 minutes resulting in a charge per cm^2 of 1.53x10^{-2} Ccm^{-2}

The crystallites in Figure 3.35 suggest that the films form from the deposition of seed points which then grow to cover the surface of the FTO. The image shows several clusters as well as smaller depositions. This suggests that the films are made up of two parts: a lower layer made up of seed crystals that have deposited onto the FTO, followed by a second layer made up of the long thin crystallite structures observed in Figure 3.34.[108]

3.2.2.5.1 Thickness calculations

Using Equation 3.1 it is possible to estimate the thickness of a film based on the single crystal density and the charge per cm^2 passed, making the assumption that the packing will be the same.

$$Ox + ne^{-} \rightleftharpoons Red$$

Equation 3.1

Based on Faraday's constant and the charge passed it is possible to calculate the number of electrons passed.

$$Q = n(e) * F$$

Equation 3.2

where Q is the Charge (C), n(e) is the number of moles of Electrons and F is the Faraday Constant

$$\therefore n(e) = \frac{Q}{F}$$

Equation 3.3

Using the density and the volume of the film it is possible to work out the thickness.

$$\rho = \frac{m}{V}$$

Equation 3.4

where ρ is the density, m is the mass and V is the volume

Since:

$$V = hA^2$$

Equation 3.5

where A^2 is the area of the deposited film and h is the thickness. Therefore

$$\rho = \frac{m}{hA^2}$$

Equation 3.6

$$\therefore h = \frac{m}{\rho A^2}$$

Equation 3.7

Since

$$m = Mmm$$

Equation 3.8

where M is the number of moles and mm is the molar mass. Therefore:

$$h = \frac{Mmm}{\rho A^2}$$

Equation 3.9

$$\therefore M = \frac{h\rho A^2}{mm}$$

Equation 3.10

Assuming that n is 1 for Nerst equation (Equation 3.1), every electron supplied will reduce a molecule, then:

$$n(e) = M$$

Equation 3.11

$$\therefore \frac{Q}{F} = \frac{h\rho A^2}{mm}$$

Equation 3.12

$$\therefore \frac{Q}{A^2} = \frac{h\rho F}{mm}$$

Equation 3.13

$$\therefore h = \frac{mm}{\rho F}\frac{Q}{A^2}$$

Equation 3.14

The density of BuPTCDI is ρ=1.42 gcm^{-3} and the molecular mass is mm=502 gmol^{-1}. Using Equation 3.14 the thickness of the BuPTCDI films was estimated to be:

$$Thickness(\mu m) = 36.6 * \mathrm{C}cm^{-2}$$

Equation 3.15

where Ccm^{-2} is the charge passed per cm^2.

However, if n is 2 for Nerst equation (Equation 3.1), every two electrons supplied will reduce a molecule, then:

$$\therefore n(e) = \frac{Q}{2F}$$

Equation 3.16

Resulting in a thickness formula of :

$$h = \frac{mm}{2\rho F}\frac{Q}{A^2}$$

Equation 3.17

Using Equation 3.17 and the same values of density and molecular mass as Equation 3.15, the thickness of the BuPTCDI film was estimated to be:

$$Thickness(\mu m) = 18.3 * \ Ccm^{-2}$$

Equation 3.18

Therefore, if the electrodeposited films have a similar packing density to the crystal structure, a film with a charge per cm^2 of 0.1 Ccm^{-2} would have a thickness of between 1.8 and 3.6 µm.

To obtain the thickness of the electrodeposited films, the substrates were snapped in half and the films' cross sections were examined by SEM imaging. Example images of different thicknesses are show in Figure 3.36 and Figure 3.37.

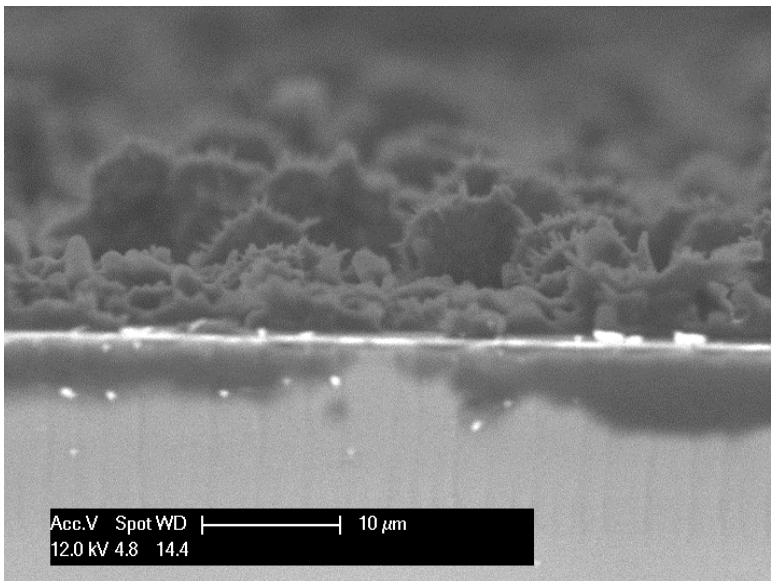

Figure 3.36: Cross section of a film with a Q=1.52x10^{-2} Ccm^{-2}

The film in Figure 3.36 is in the initial stages of deposition with several small clusters having formed on the FTO surface. The larger clusters from which the long crystallites seem to have formed are covered in small needle-shaped crystallites. These are probably the start of the larger needles observed in Figure 3.33.

After the initial seeding phase, deposition occurs onto already deposited BuPTCDI rather than onto the FTO surface, which results in further growth of the seeds. This probably happens because it is energetically more favourable for [BuPTCDI]$^{-}$ to deposit onto BuPTCDI.

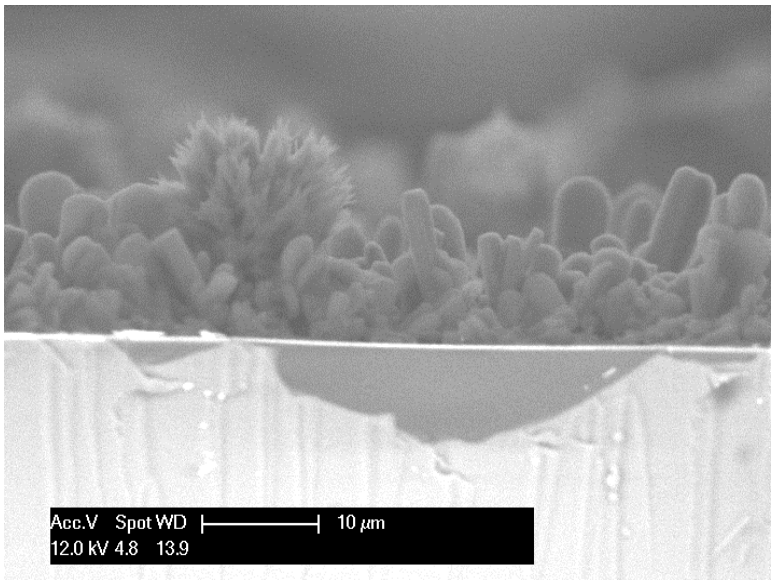

Figure 3.37: Cross section of a film with a Q=7.98x10^{-2} Ccm^{-2}

From the film present in Figure 3.37 it is possible to see two types of growth that have occurred. The majority of growth is in the form of long needle-like stacks, a couple of µm thick, growing almost perpendicular to the FTO surface. A cluster of very thin long needles a couple of µm thick and only a couple of nm wide are also present.

Since the film is a collection of several crystallite features of different heights and orientations, a range of the thicknesses can be given. The height of the smallest and largest crystallites were estimated and using them an average thickness of the film was calculated. Examples of the heights can be found in Table 3.4.

Table 3.4: BuPTCDI thickness calculations

Charge per cm^2 (Ccm^{-2})	Minimum height (µm)	Maximum height (µm)	Average Thickness (µm)	Range (µm)
1.06x10^{-2}	1.01	3.8	2.4	1.4
1.53x10^{-2}	3.37	9.3	6.3	3.0
1.88x10^{-2}	1.66	7.6	4.6	3.0
2.69x10^{-2}	1.73	9.12	5.4	3.7
2.79x10^{-2}	1.24	10.9	6.1	4.8
5.89x10^{-2}	5.85	15	10.4	4.6
7.98x10^{-2}	5.71	19	12.4	6.7

A plot of average thickness, with minimum and maximum film thickness shown as vertical bars against charge per cm^2 passed is show in Figure 3.38.

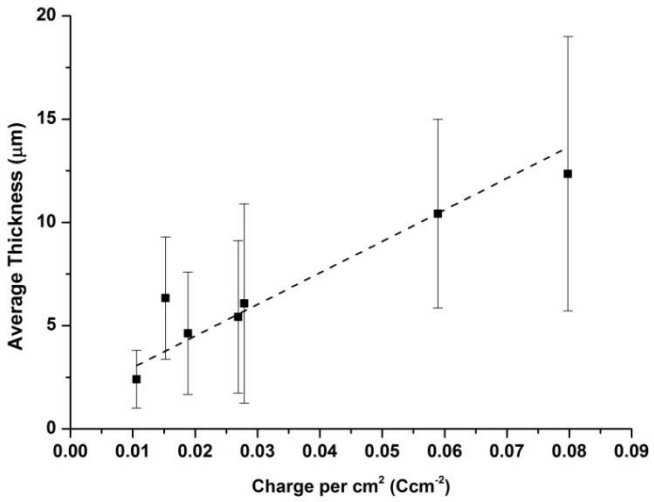

Figure 3.38: Average thickness against charge per cm^2

Figure 3.38 shows that there is a linear relation between the charge per cm^2 passed and the resulting average thickness.

From the gradient of the line plotted in Figure 3.38 it is possible to work out the following:

$$Thickness(\mu m) = 152.8 \pm 29.0 * \mathrm{C}cm^{-2}$$

Equation 3.19

The difference between the two thicknesses in Equation 3.15 and Equation 3.19 can be explained by the crystal packing of the films. The coverage of the FTO is not a uniform thin film but a cluster of several crystallites. These crystallites grow perpendicular to the FTO substrate resulting in several tall structures rather than a continuous homogeneous film. The deposition also seems to be efficient with the majority of the charge going towards the oxidised molecules adding crystallite growth, rather than charging the film.

3.2.2.6 X-ray diffraction

3.2.2.6.1 Assessment of XRD of electrodeposited BuPTCDI film

The X-ray diffraction pattern of an electrodeposited BuPTCDI film on FTO was recorded and is shown in Figure 3.39. The peaks present were compared to the simulated powder patterns of the two known single-crystal polymorphs obtained by Gräser[21] and Mizuguchi[109] respectively as shown in Figure 3.40, as well as the XRD patterns of other PTCDI films deposited by other techniques found in literature.

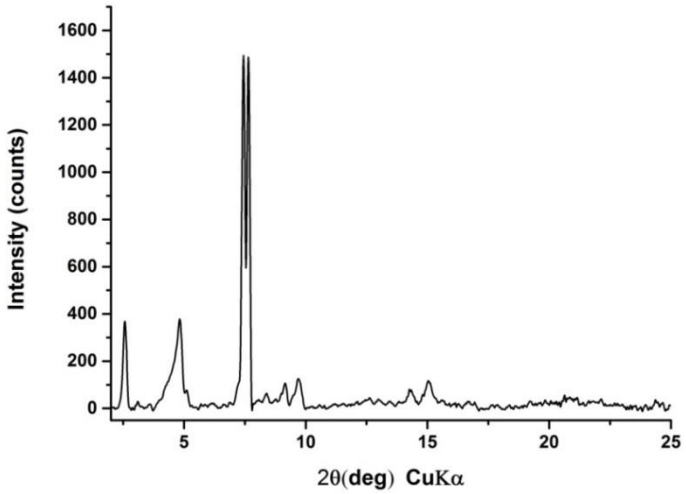

Figure 3.39:XRD pattern of electrodeposited BuPTCDI film deposited at 0.84 V for 60 minutes on FTO resulting in a total charge of 3.20×10^{-2} Ccm^{-2}

The XRD pattern of the film contains two intense peaks which dwarf several broader peaks. The dominance of the two peaks with d-spacings of 11.8 Å and 11.5 Å may suggest some preferred orientation for one of the phases. Using Bragg's Law the d-spacings corresponding to the peaks were calculated and are shown in Table 3.5.

Table 3.5: Calculations of d-spacings of the BuPTCDI film

BuPTCDI Film 2θ values	BuPTCDI Film d values (Å)
2.56	34.48
4.80	18.39
7.43	11.89
7.61	11.61
9.14	9.67
9.70	9.11
14.31	6.18
15.05	5.88

The average size of the crystallites, τ, can be estimated using the Scherrer equation:

$$\tau = \frac{K\lambda}{\beta \cos\theta}$$

Equation 3.20

where K is the shape factor, normally K=0.9, λ is the X-ray wavelength, β is the line width at half maximum intensity and θ is the Bragg angle.[110]

Table 3.6: Estimate of average crystal sizes of BuPTCDI

BuPTCDI Film 2θ values	β (º)	τ(Å)
2.56	0.18	448.9
4.80	0.37	214.9
7.43	0.15	523.7
7.61	0.15	523.8
9.14	0.28	284.6
9.70	0.30	265.7
14.31	0.35	228.8
15.05	0.39	205.5

The average size of the crystallites suggests that there are two sizes ranges, larger crystallites which are between 45 nm to 53 nm and smaller crystallites which are between 20 nm to 28 nm. This agrees with the cross-section SEM image in Figure 3.37 where there is a combination of needle-like crystallites and smaller clusters of material.

The location of the peaks in the electrodeposited film pattern shows that the packing of the molecules in the film is different to both known polymorphs, as shown in Figure 3.40.

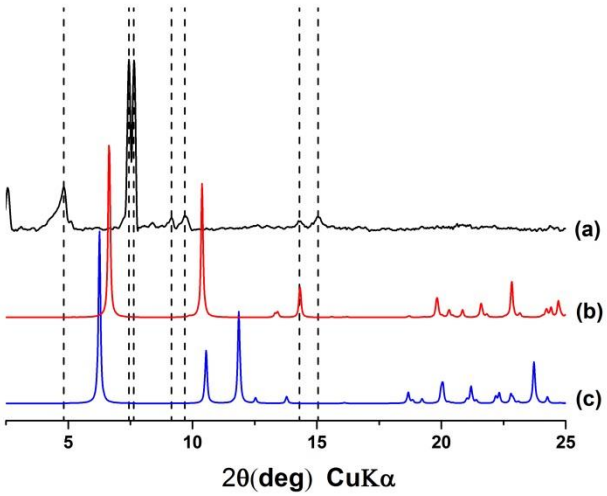

Figure 3.40: Different XRD patterns of BuPTCDI: Electrodeposited film (a) and the calculated patterns from the single crystal data from Mizuguchi (b) and Gräser (c).

It also does not match with films prepared by vapour deposition of similar PTCDIs with longer alkyl chains found in literature.[107, 111] This implies that the film crystallites are not a known structure of BuPTCDI. In both known crystal packings of BuPTCDI the perylene forms a herringbone-type packing with the smallest dimension for both structures being the π-π stacking of the cores with the addition of the butyl chains which do not extend along the molecular axis but are standing on the molecular plane.[95] The rest of the packing dimensions are influenced by the BuPTCDI molecule dimensions which are shown in Figure 3.41.

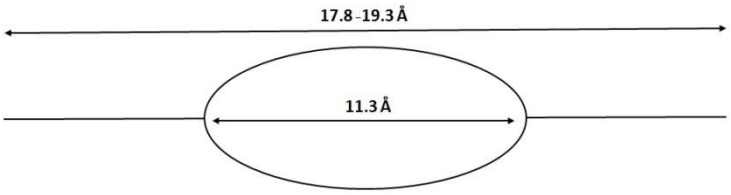

Figure 3.41: Schematic representation of the dimensions of a BuPTCDI molecule

The dimensions of cells for both known crystal structures are listed in Table 3.7. The shortest dimensions of both crystals are attributed to the π-π stacking distance of two BuPTCDI molecules.

Table 3.7: Cell dimensions of the two known crystal structures of BuPTCDI (Å)

	Gräser[21] (Å)	Mizuguchi[109] (Å)
a	4.73	18.41
b	28.23	4.63
c	9.40	27.61

In the packing reported by Gräser, the asymmetric unit of two molecules, the molecules are arranged in a zigzag fashion along the b-axis, as shown in the b c plane in Figure 3.42.

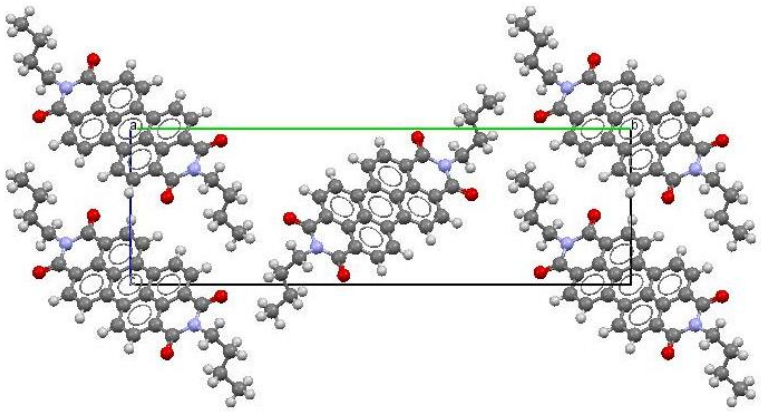

Figure 3.42: The b c plane (normal to the a axis) of the Gräser packing

The molecules are arranged in a herringbone stack fashion, as shown in Figure 3.43.

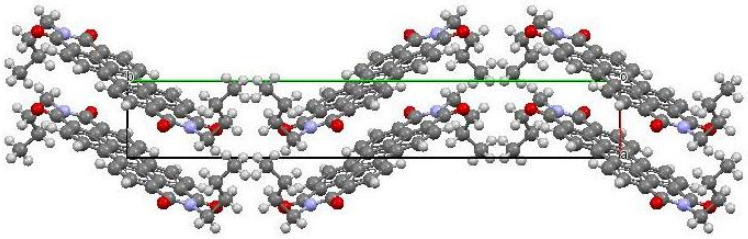

Figure 3.43: The a b plane (normal to the c axis) of the Gräser packing

All the molecules are π-stacked with a second BuPTCDI molecule, resulting in the smallest dimension of the unit cell being the distance of a π-π stack with the addition of the butyl chain, as shown in Figure 3.44.

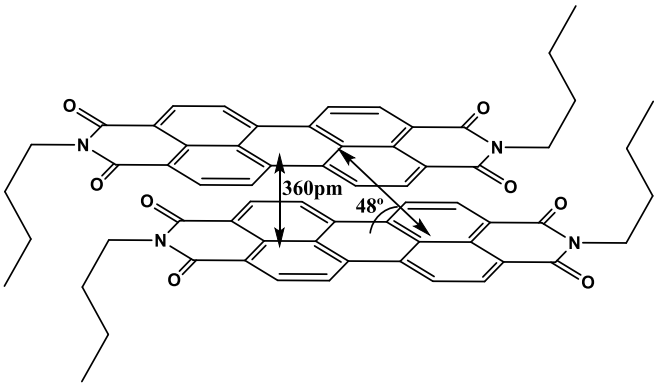

Figure 3.44: Molecular stack of two BuPTCDI molecules

The packing reported by Mizuguchi has an asymmetric unit of four molecules. These contain two types of BuPTCDI molecules with slightly different geometries of the butyl chain. Both molecules are on different centro-symmetric sites and alternate along the a and c axes, as shown in Figure 3.45.

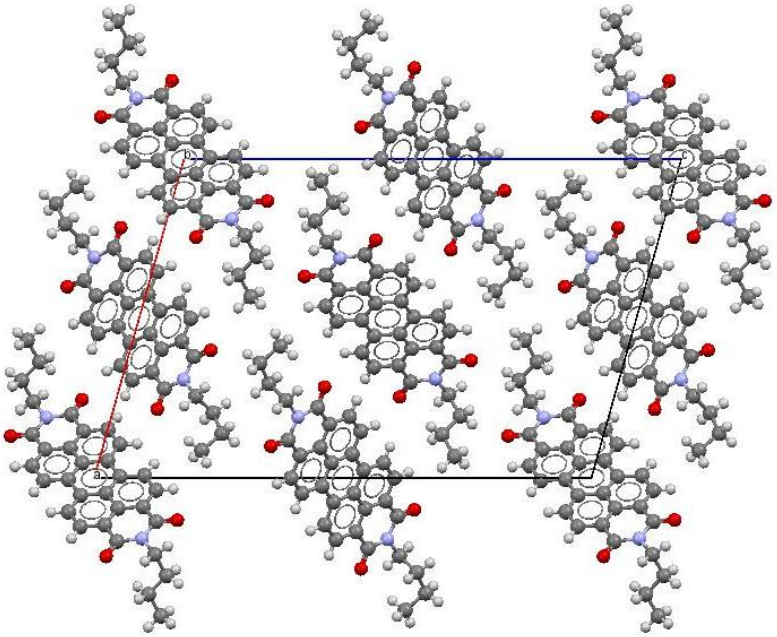

Figure 3.45: The a c plane (normal to the b axis) of the Mizuguchi packing

Similar to the Gräser packing the BuPTCDI molecules are arranged in a zigzag fashion but due to the different centro-symmetric molecules this occurs along the a c diagonal direction, as shown in Figure 3.46.

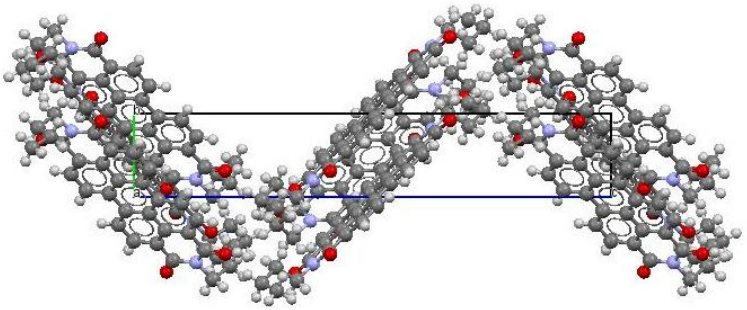

Figure 3.46: The b c plane (normal to the a axis) of the Mizuguchi packing

For the electrodeposited film, the largest d-spacings, 34.2 Å and 18.2 Å, are probably cell lengths, broadly comparable with literature structures (Table 3.7), although the longest axis is somewhat longer, perhaps suggesting a smaller tilt angle of the BuPTCDI stacks compared with the herringbone-type packing seen by Gräser and Mizuguchi. The published structures both show the third cell axis, corresponding to

the π-π stacking distance of the stacked cores, to be about 4.6 Å. The electrodeposited film data do not enable observation of a corresponding Bragg peak that would be expected at a high angle.

The electrodeposited film was also compared to the XRD pattern of a powder sample of BuPTCDI, as shown in Figure 3.47.

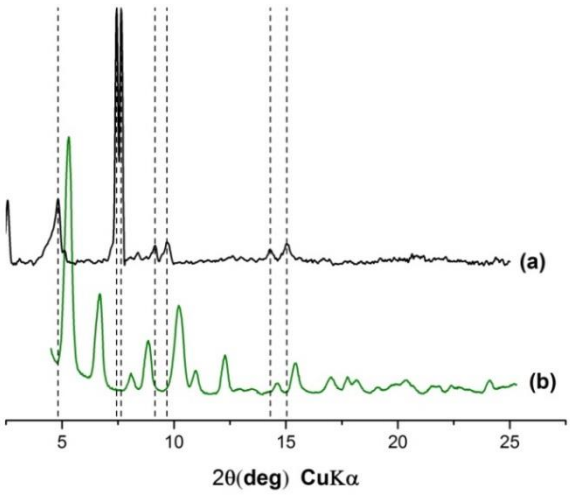

Figure 3.47: Different XRD patterns of BuPTCDI: Electrodeposited BuPTCDI film (a) and a powder sample of BUPTCDI (b).

Although some of the peaks appear to be in similar positions in the XRD patterns of the film and the powder, there is no actual overlap. This suggests that the molecules in the films are packed and oriented differently compared to the molecules in the powder.

So, although the XRD pattern of the electrodeposited film is similar to the XRD pattern of both the crystals and the powder, there is no overlap, implying that the crystal packing of the electrodeposited film is similar, but not identical. This suggests that the molecules in the electrodeposited film are packed in a new way.

3.2.2.7 Photo-electrochemistry

The photo-electrochemical properties of several films were investigated. Once the response of the untreated films was measured the films were treated with naphthol, a polymer that was electropolymerized to insulate any exposed FTO substrate that could affect the response measured. The investigation was performed in the presence of hydroquinone, a sacrificial reducing agent. The voltages are quoted against Ag/AgCl as the ferrocene standard was insoluble in the 0.1M KCL water based electrolyte used.

The response of the film to two different light sources was investigated first. The film was held at a fixed potential, in this case 0.1 V, and the film's current response was measured when exposed to chopped light from an LED lamp and a 1000 W halogen lamp, as shown in Figure 3.48.

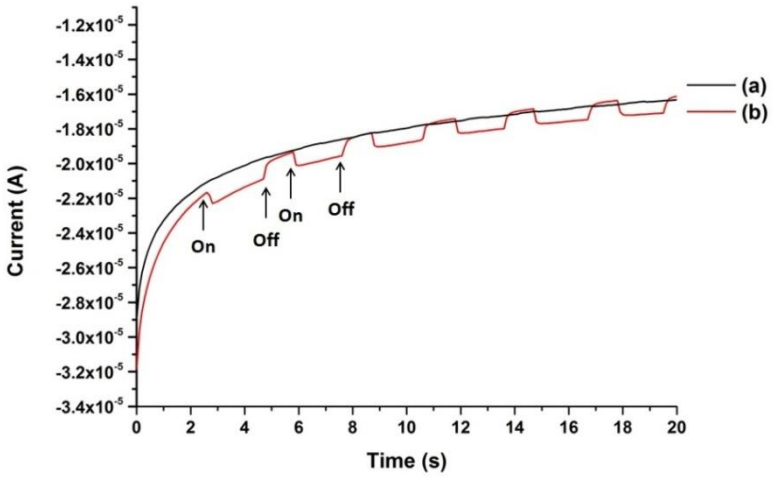

Figure 3.48: Current against time response of a film to a chopped (a) LED and (b) halogen lamp at a voltage of 0.1 V

During exposure to chopped LED light, the current measured showed no discernible difference when the film was exposed to light to when it was in the dark, meaning that the power from the LED is not strong enough to affect the current. The current measured when the film was exposed to the chopped light of a 1000 W halogen lamp shows a clear difference between the film when it is exposed to the light and when it

is in the dark. The current increases by -6.6x10^{-7} A when exposed to the light. When the light source is removed the film takes 0.4 seconds to return to the dark current.

Since the SEM images revealed that the films were made up of several crystallites, it is highly possible that the film has pores that allow the electrolyte to reach the FTO surface. Once a photo-electrochemical response had been established, the film was treated with naphthol to ensure that there was no direct interaction between the electrochemical solution and the FTO surface. After the charge required to cover a third of the area of the film was calculated, Q=0.35 mC, the naphthol was deposited on the surface of the film. The photo-electrochemical responses are shown as cyclic voltammograms in Figure 3.49.

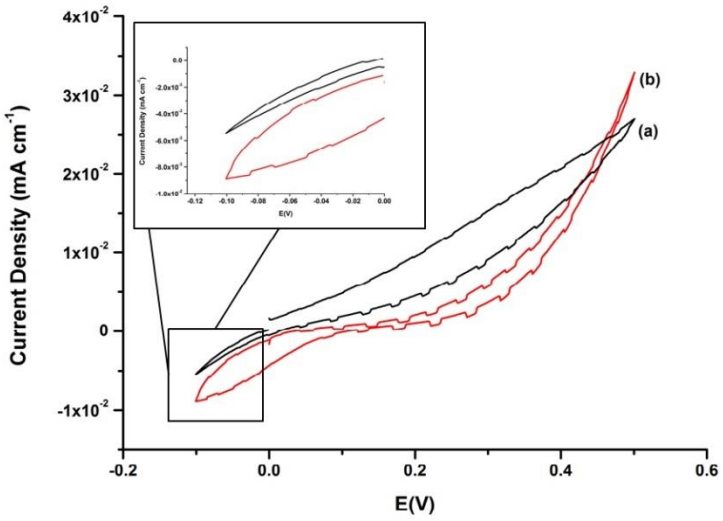

Figure 3.49: Cyclic voltammogram of current against applied voltage for (a) untreated film and (b) naphthol treated film when exposed to chopped light

The film shows an anodic photocurrent and a very weak cathodic photocurrents, depending on the applied bias. The measured current of the untreated film increases almost linearly against the applied voltage with a small photo-electrical response. This confirms that the film is porous as the system is short-circuiting, suggesting that the FTO is interacting with the electrolyte. After the treatment with the naphthol the current does not increase until it reaches about 0.2 V after which it increases very rapidly. A plot of current against time of a film exposed to chopped light while being held at a voltage of 0.1 V is shown in Figure 3.50.

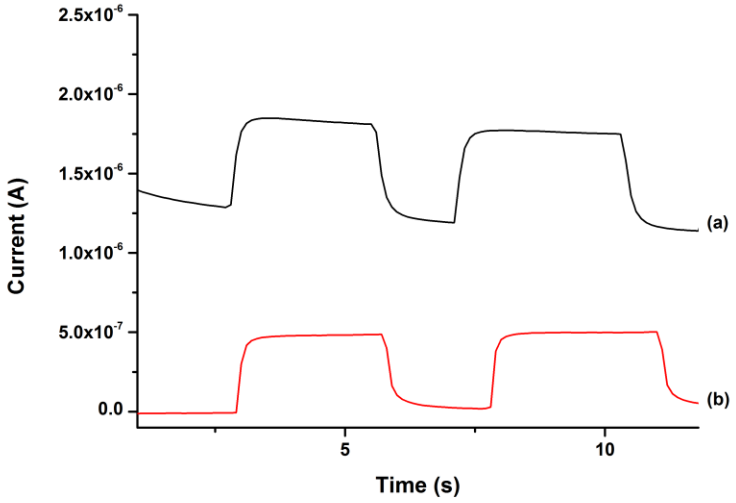

Figure 3.50: Current against time response of (a) untreated film and (b) naphthol treated film to a chopped halogen lamp at a voltage at 0.1 V

At a voltage of 0.1 V the untreated film has a higher dark current and a similar photoresponse. This agrees with the current measured during the cyclic voltammogram in Figure 3.49. The dark current in the untreated film is higher due to short-circuiting as the porous film allows for interaction between the FTO surface and the electrolyte solution. This suggests that in the cyclic voltammogram the photoresponse is the same for both films, but it is masked by the increasing current due to short-circuiting.

The film was treated several times with naphthol to ensure that it was not still porous. As mentioned, the first treatment was made with a charge of Q=0.35 mC, the second with a charge of Q=0.525 mC, the third with a charge of Q=0.875 mC, followed by the fourth with charges of Q=1.575 mC and fifth with charges of Q=2.275 mC. The current of the film exposed to chopped light at a voltage of 0.2 V is shown in Figure 3.51.

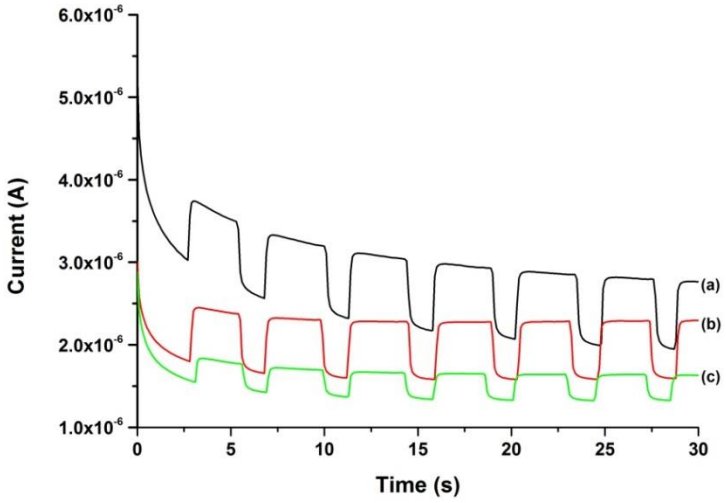

Figure 3.51: Current against time response of a film after (a) 1st, (b) 2nd and (c) 3rd naphthol treatment exposed to a chopped halogen light at a voltage of 0.2 V

After each treatment both the dark current and the photoresponse decrease. However, after the third treatment the photoresponse is almost halved while the dark current decrease is very small in comparison.

However, at a voltage higher than 0.25 V the response is the opposite, with the dark current and photoresponse increasing after the naphthol treatments as can be seen from the response of the treated film at 0.35 V shown in Figure 3.52.

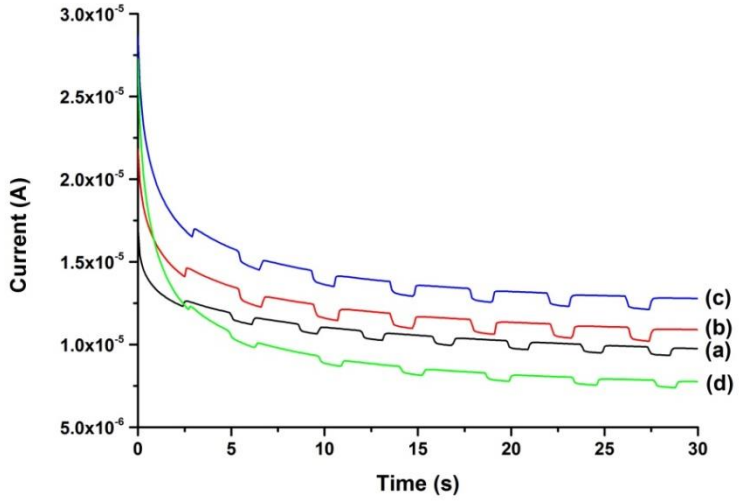

Figure 3.52: Current against time response of a film (a) untreated, after (b) 1st, (c) 2nd and (d) 3rd naphthol treatment, to a chopped light from a halogen lamp at a voltage of 0.35 V

The currents measured for the untreated and treated film are already an order of magnitude larger than the current measured at 0.1 V and 0.2 V. However, after the first naphthol treatment both the dark current and the photoresponse increase. The current of the untreated film increases by $4.00x10^{-7}$ A when the film is exposed to the light. After the first treatment it increases to $6.52x10^{-7}$ A. The dark current also increases from $9.34x10^{-6}$ A in the untreated film to $1.02x10^{-5}$ A in the first treated film and increases again after the second treatment to $1.21x10^{-5}$ A. This is due to the pores being filled which prevents the system from short-circuiting. However, after the second treatment, the photoresponse decreases slightly to $6.01x10^{-7}$ A. This could be due to the naphthol filling not only the pores but also covering some of the BuPTCDI film. This is confirmed by the fact that after the third naphthol treatment both the dark current and the photoresponse have decreased to $7.63x10^{-6}$ A and $2.95x10^{-7}$ A, which is even less than was measured for the untreated film. Consequently, after the third treatment the decrease in both types of current is due to a layer of naphthol covering the film rather than just filling the pores.

The results are consistent with what has been observed about the morphology of the electrodeposited films as their porous nature would affect the photoresponse as seen with the effects of the naphthol treatments. The response of the BuPTCDI shows it to be an anodic photoresistor which is consistent with other PTCDIs such as perylene-3,4,9,10-tetracarboxylic diimide.[112]

3.2.2.8 Field Effect Transistors (FETs)

The charge mobility of electrodeposited BuPTCDI was investigated by electrodepositing it onto interdigitated electrodes to fabricate field effect transistors (FETs). The resulting FET's I-V characteristics were measured while applying several gate potentials.

3.2.2.8.1 Deposition

Films of BuPTCDI were deposited onto 8 µm x 8 µm interdigitated electrodes by using the same electrodeposition method for BuPTCDI as developed in section 3.2.2.1. A plot of time against the charge per cm^2 passed during the fabrication of an FET is shown in Figure 3.53. The interdigated electrodes were held at a potential of 0.84 V for 60 minutes, resulting in a charge per cm^2 of 2.15 Ccm^{-2}.

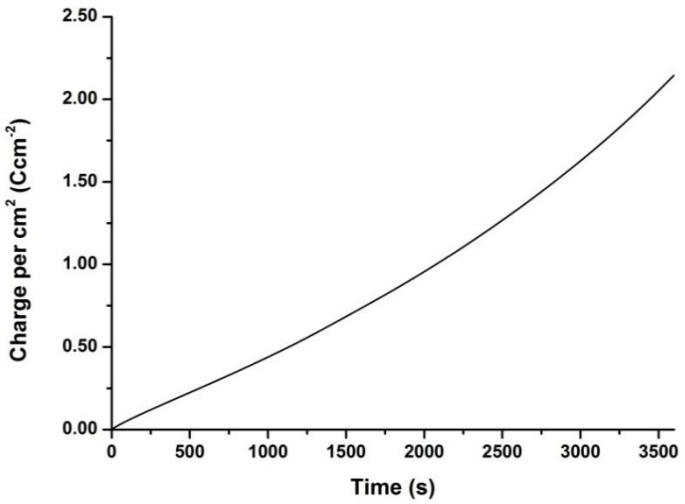

Figure 3.53: Deposition of BuPTCDI held at 0.84 V for 60 minutes on 8 µm x 8 µm interdigitated electrodes

The created FET was then rinsed with ethanol and held at a lower potential for 60 minutes in a 0.1M TBABF4 MeCN solution to ensure that the film had not become charged during the deposition process. A plot of time against charge per cm^2 for the discharging of the film deposited in Figure 3.53 is shown in Figure 3.54.

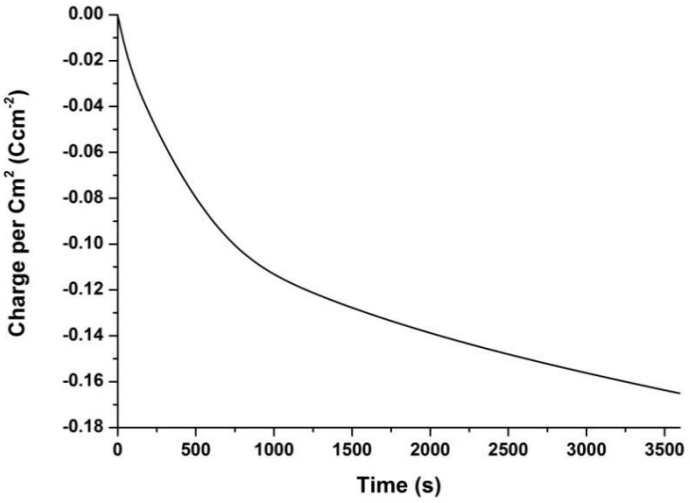

Figure 3.54: Interdigitated electrodes with BuPTCDI held at 0.34 V for 60 minutes

The negative value of the charge per cm^2 implies that the film was charged and that this process is discharging it. This is important as extra charges could affect the charge mobility measurements. From the charge per cm^2 passed during the deposition and the amount of charge per cm^2 during the discharging, it seems that approximately 7.5 % of the charge per cm^2 passed during the deposition has been stored in the film and did not contribute to film growth.

3.2.2.8.2 Charge mobility

Charge mobility measurements were performed on a discharged film of BuPTCDI on 8 μm x 8 μm interdigitated electrodes. The I-V characteristics of the film at positive gate potentials are shown in Figure 3.55.

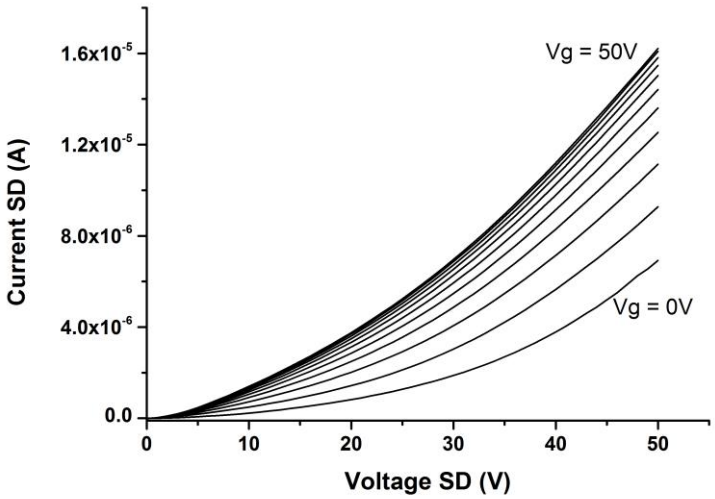

Figure 3.55: Drain current I_d against positive source-drain potential V_{SD} curves at various positive source-gate potentials for BuPTCDI field effect transistors.

The current flowing between the source and the drain increases with applied potential. It also increases with increasing positive gate potential. When no gate potential is applied the current increases in an exponential-like manner and does not reach saturation in the source-drain potential range applied. When a gate potential is applied there is an increase in the current measured, which is not linear with respect to the linear increase in gate potential. A plot of the current against the applied gate potential obtained at V_{SD} = 50 V is shown in Figure 3.56.

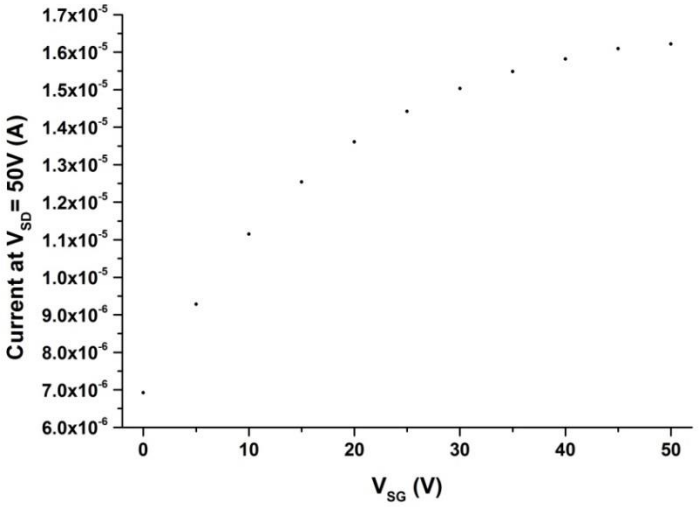

Figure 3.56: Current against applied positive gate potentials obtained at V_{SD} = 50 V

The increase in current appears to grow in a logarithmical-like fashion, increasing rapidly at first, but then slowing down and levelling off as higher potentials are applied. This suggests that the current reaches a maximum and increasing the gate potential will have little further effect.

The I-V characteristics of the film at negative gate potentials were also measured and are shown in Figure 3.57.

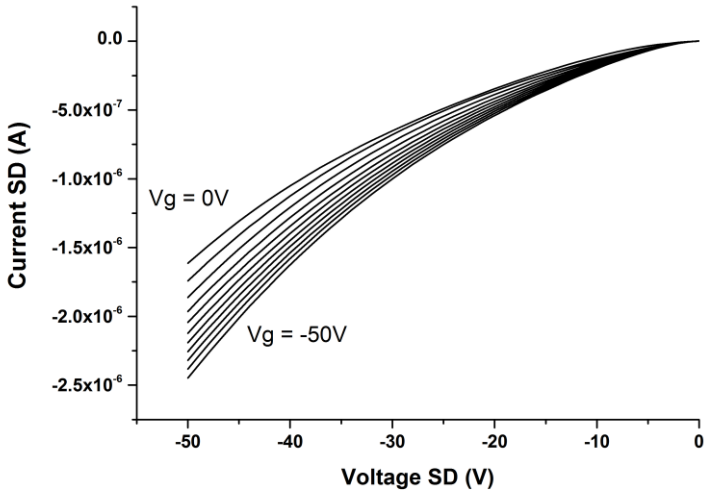

Figure 3.57: Drain current I_d against negative source-drain potential V_d curves at various negative source-gate potentials for BuPTCDI field effect transistor.

Similar to the positive potentials the negative current flow increases with the higher negative potentials between the source and drain. The current increases in an exponential-like way when no gate potential is applied and does not reach the saturation region. When a gate potential is applied there is an increase in the source-drain current. A plot of the current against the applied gate potential obtained at V_{SD} = -50 V is shown Figure 3.58.

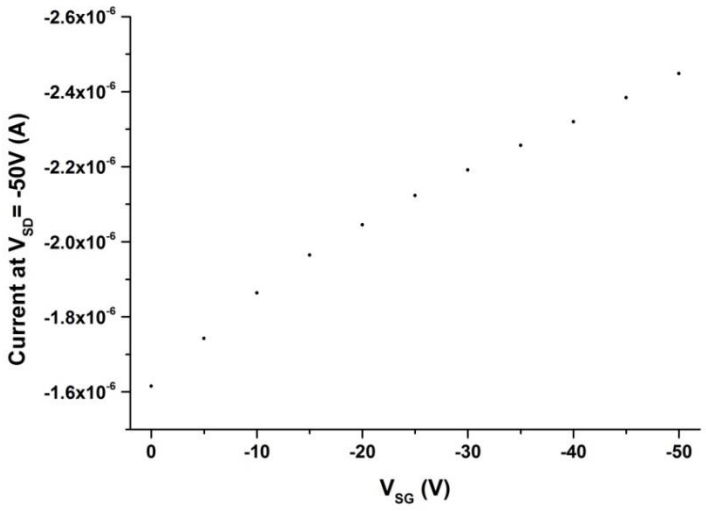

Figure 3.58: Current against applied negative gate potentials obtained at V_{SD} = -50 V

The current measured at V_{SD}= -50 V shows an almost linear relationship between the applied potential and the current. Initially, before V_{SG} = -20 V, the current increases in a logarithmical-like manner similar to the current measured in the positive region. The negative currents are a third of the positive currents, meaning that the sample shows better properties as an electron conductor than as a hole conductor. BuPTCDI is an n-type semiconductor, which agrees with measurements on similar PTCDI materials.[97, 113]

Both sets of I-V measurements were repeated after 24 hours to check the stability of the material. A plot of both sets of results is shown in Figure 3.59.

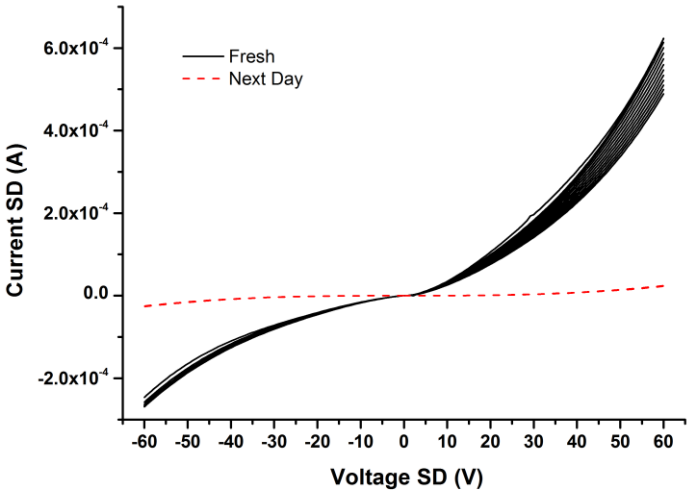

Figure 3.59: Fresh drain current I_d and current after 24 hours against source-drain potential V_d curves at various source-gate potentials for BuPTCDI field effect transistor.

The currents measured after 24 hours are an order of magnitude smaller than the initial current, the gate effect has become negligible and the maximum of the positive current is similar to the maximum of the negative value. This implies that there has been some degradation somewhere in the FET device. Since PTCDIs are very air stable it is possibly due to the material absorbing oxygen and/or water from the atmosphere which would act as a trap. Another possibility is a breakdown in the connection between the electrodes and the PTCDI. A similar breakdown happened with FETs made with octyl-PTCDI which suggests that the breakdown occurs when the sample is exposed to the atmosphere even for a short period of time.[113]

The exponential-like growth of the current and the logarithmic-like increase in current with increasing gate potential suggests that a bottleneck effect between the electrodes and the bulk material may be occurring.[114, 115] This is probably due to the thickness of the film which results in the accumulation of charge in the material. Since the BuPTCDI molecules are probably stacked perpendicular to the electrodes, quite a thick film has to be deposited before the film fibres are large enough to bridge the source-drain electrodes gap.[107] The thick film results in a large conduction

channel with a very high off current and makes the film hard to saturate. The device performance is consistent with the thickness and packing of the deposited film as the highest conduction direction is most likely perpendicular to the substrate.

Even though the material was not optimal, the developed electrodeposition method was successfully used to deposit undoped semiconducting material onto interdigitated electrodes, resulting in the fabrication of FETs.

3.3 3,4,9,10-perylene-tetracarboxylic bisbenzimidalzole

After the technique of electrochemical deposition was established using BuPTCDI, the same conditions were used to attempt to electrodeposit 3,4,9,10-perylene-tetracarboxylic bisbenzimidalzole (PTCBI). The molecular structure is more complex than BuPTCDI and other PTCDIs as the central core has been altered by attaching two benzimidazole groups, as is shown in Figure 3.60.

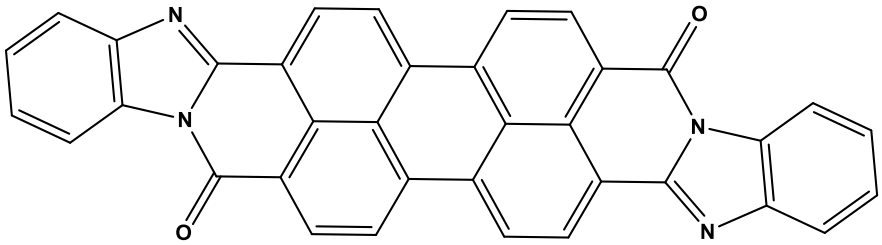

Figure 3.60: 3,4,9,10-perylene-tetracarboxylic bisbenzimidalzole (PTCBI)

The addition of the groups increases the π system of the molecule which causes a change in the HOMO and LUMO, resulting in a larger and red-shifted electronic absorption. This not only results in increased absorption in general, but also means that its absorption has been shifted into the highest intensity region of the solar spectrum.[116] This means that under the solar spectrum the photocurrent of PTCBI is larger than that of PTCDIs of the same thickness.[117]

However, the addition of the benzimidazole groups also affects the solubility of the molecule in two ways: firstly by increasing the size of the delocalised π structure, resulting in increased interaction between the molecules, and secondly by removing the imide sites so no solubilising groups can be attached. This causes the molecule to be very insoluble making it very difficult to solubilise. Therefore, deposition or purification by solution techniques are not possible and normally have to be done by vapour techniques.

This more complex perylene molecule has already been used in electronic applications, such as solar cells. It was one of the molecules used by Tang to create the first organic heterojunction solar cell in 1986.[10]

3.3.1 Molecular Properties

3.3.1.1 Absorption Spectroscopy

The absorption spectrum of PTCBI in THF was obtained and is shown in Figure 3.61.

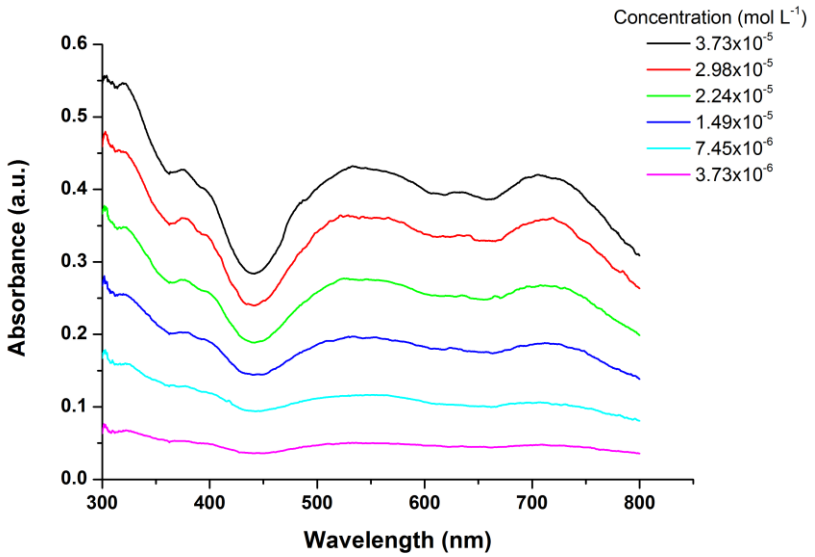

Figure 3.61: UV/Vis spectra of several concentrations of PTCBI in THF

Because of the strong intermolecular interactions, the PTCBI did not fully dissolve at any concentration measured. This results in the absorbance of PTCBI in THF being very different from BuPTCDI: the three signature peaks between 400 nm and 550nm are either not present or masked by a broad peak at 532 nm, which is probably due to aggregation-induced π-π stacking. There are also other peaks that were not present in the case of BuPTCDI such as peaks between 380 nm and 440 nm, two broad peaks around 532 nm and 705 nm with a smaller peak sandwiched between two peaks at 630 nm.

However, the overall absorption is much broader resulting in a large portion of the visible spectrum being absorbed, which is why PTCBI is an attractive molecule for use in solar applications.

3.3.2 Films

Films of PTCBI were prepared in the same way as films of BuPTCDI and the same set-up as shown in Figure 3.19 was used. The PTCBI was suspended in THF and left to react with a sodium mirror for approximately 14 hours.

3.3.2.1 Deposition

Depositions were then attempted at several voltages in THF. However, depositions performed at a lower voltage of 0.84 V were not as successful as those performed at 1.24 V as they did not cover all of the substrate exposed to the ion solution, suggesting that only a few nucleations had occurred. A plot of the charge per cm^2 against time of the deposition at 1.24 V is shown in Figure 3.62.

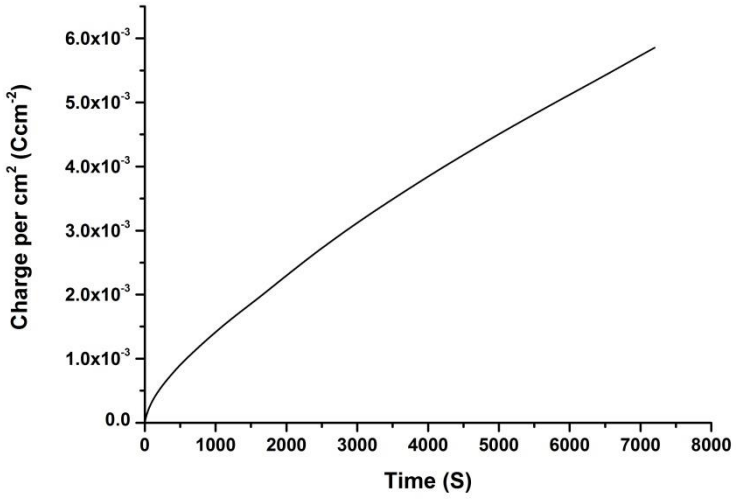

Figure 3.62: Total charge per cm^2 passed during a 120 minutes deposition while holding the potential at 1.24 V

The total charge per cm^2 is much less than the amount of charge passed in a third of the time for depositing BuPTCDI of equal concentration. This suggests that the deposition of the PTCBI anion is hindered compared to the BuPTCDI counterpart. To investigate this further a plot of charge per cm^2 against $t^{½}$ of a deposition is shown below in Figure 3.63.

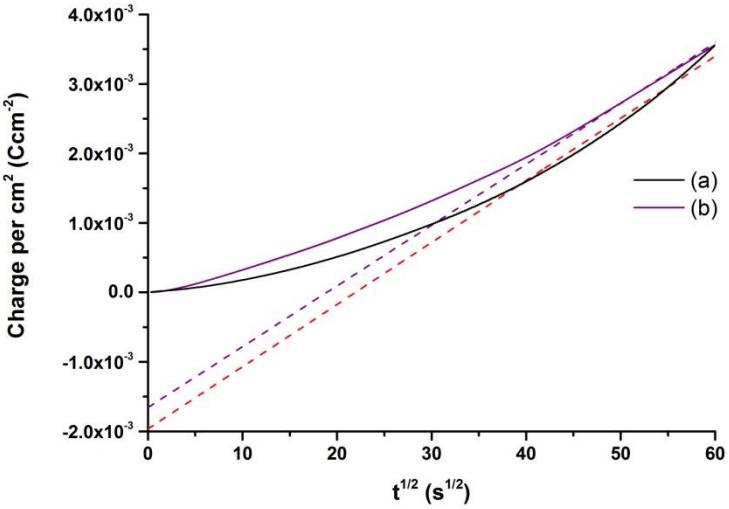

Figure 3.63: Total charge per cm^2 against t^{½} for a 30 minutes deposition while holding the potential at 1.24 V without [PTCBI]$^-$ (a) and with [PTCBI]$^-$ (b).

As before, a plot of charge per cm^2 against t^{½} has yielded a straight line and a negative intercept. Similar to the deposition of BuPTCDI, it suggests that the deposition is initially under mixed control before becoming diffusion controlled. There is no clear indication of stages as the slope is two orders of magnitude lower and the intercept is an order of magnitude lower than that of the electrodeposition of a BuPTCDI film. This agrees with the charge per cm^2 passed.

The values extrapolated from the PTCBI experiment are close to those of the blank experiment done in the same conditions which has a similar slope and intercept. This suggests that the current of both experiments is very similar, as shown in Figure 3.64.

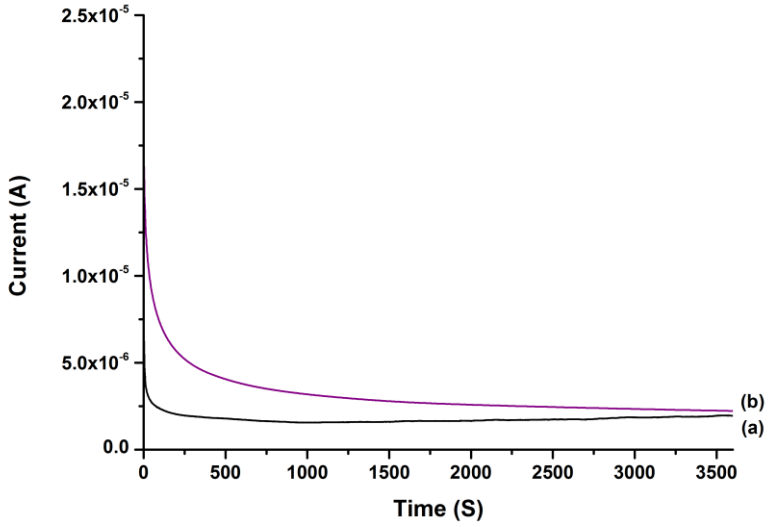

Figure 3.64: Current against time for the deposition of 30 minutes deposition while holding the potential at 1.24 V without $[PTCBI]^-$ (a) and with $[PTCBI]^-$ (b).

The current measured during the deposition of PTCBI is only slightly higher than the current passed during the blank "deposition" and after about 60 minutes the currents are almost identical. This means that the current due to the deposition of PTCBI is very small, suggesting that there is not much contribution from the PTCBI itself. Since the redox properties of the PTCBI core should be similar to those of other PTCDIs the deposition potential should be similar to that of BuPTCDI.[118, 119] The large overpotential required for nucleation and the low current both suggest that the concentration of $[PTCBI]^-$ present is very low. There are two possible reasons why this is the case. The first one is that despite there being the same initial concentration of PTCBI suspended in the THF with the sodium, less has reacted to produce the $[PTCDI]^-$ ion resulting in a very low concentration. Another possibility is that since PTCBI has a larger π core and no solubilising groups it is more likely to aggregate compared to BuPTCDI, again lowering the concentration in the deposition chamber.

This means that the low current and therefore charge per cm^2 is not due to the technique being unsuccessful but rather to the low concentration of PTCBI because of its limited solubility. If the initial reduction reaction was improved so that the concentration of $[PTCBI]^-$ was higher, the electrodeposition would probably yield better films.

3.3.2.2 Absorption Spectroscopy

Although only very thin films were deposited, their absorption was measured and is shown in Figure 3.65.

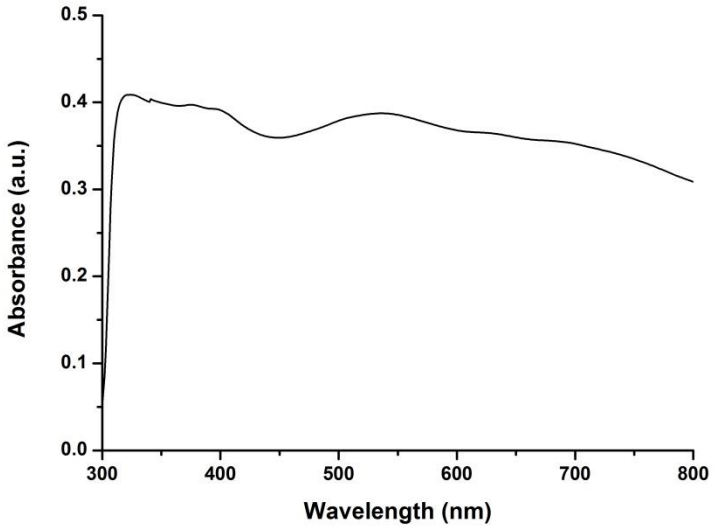

Figure 3.65: Absorbance of PTCBI deposited at 1.24 V for 120 minutes on FTO resulting in a total charge of 7.32×10^{-3} Ccm^{-2}

The film contains two peaks at 538 nm and 668 nm and then two shoulder peaks at 375 nm and 397 nm in the large peak at 310 nm. With the exception of the peak at 668 nm all the peaks are in an almost identical position to the absorption of the PTCBI in solution. The peak at 668 nm is probably the peak found at 630 nm in solution that has been red-shifted due to the stacking of the molecules.

3.4 Conclusion

The initial investigation of electrodeposition using BuPTCDI resulted in the deposition of continuous films of controllable thicknesses. Although the electrodeposition of metal ions to form films of metal had been developed and had already been used industrially, the same process had not been applied to non-metal molecules. The developed method of the electrochemical deposition of molecules of BuPTCDI is a novel method that can in principle be applied to any electroactive molecule.

The method of chemically reducing the BuPTCDI and then electrodepositing the ion resulted in controllable and repeatable film deposition. The films of BuPTCDI have similar optical properties as films deposited by other techniques such as solution deposition or vacuum deposition.

However, the morphology of the film was governed by the most energetically favourable stacking of the molecule. Therefore, rather than obtaining smooth terraces as seen in vapour deposition techniques, the film contained stacks of BuPTCDI, like PTCDI structures formed in self-assembled structures or single crystals.

3.5 Experimental

Synthesis of N,N dibutyl-3,4,9,10-perylene-bis(dicarboxime)

Perylene-3,4,9,10-tetracarboxylic-3,4,9,10-dianhydride (3.923g), n-Butylamine (0.741g) and dicyclohexylcarbodiimide (4.126g) were suspended in twice distilled quinoline (1 ml) and then heated to 230°C under nitrogen for 18 hours.

After cooling to room temperature, the mixture was diluted with methanol (15 ml), stirred for 30 minutes and then cooled to -10°C for 4 hours. The dark red residue was separated by filtration and washed with methanol and diethyl ether. The residue was treated with 5% sodium carbonate solution in water for 30 minutes at 90-100°C and this procedure was continued until all the excess anhydride had been removed. The product was then washed with DMSO, water and methanol. Yield: 0.868 g (17.9 %);

IR $\tilde{\nu}$/cm^{-1} = 3067 (w), 2880 (w), 1692 (m), 1654 (m), 1593 (m), 1436 (m), 1404 (m), 1338 (w), 1244 (m), 1180 (m), 1117 (m), 1075 (w), 979 (w), 849 (m), 809 (m),745 (m), 652 (m).

UV/Vis (THF): λ_{Max} 270 nm, 357 nm (w), 445 nm, 475 nm, 512 nm 560 nm(sh).

CHN: cal: C 76.48%, H 5.21%, N 5.57% found: C 76.75%, H 5.57%, N 5.70%

Synthesis of 3,4,9,10-perylene-tetracarboxylic bisbenzimidalzole

Perylene-3,4,9,10-tetracarboxylic-3,4,9,10-dianhydride (0.49g) and 1,2-phenylenediamine (0.41g) were suspended in quinoline (5 ml) and then heated to 230°C under an inert gas. The reaction was then left to react for 4 hours. After cooling to room temperature the mixture was diluted with methanol (10ml) and stirred. The resulting slurry was centrifuged and the liquid decanted. This was repeated eight times using methanol (10ml), 8x KOH in methanol (10gL^{-1})(12ml) and twice with methanol (10ml). The resulting solid was filtered, washed with DMSO, water and methanol and dried at 90°C. Yields: 0.630g (93.8%);

IR $\tilde{\nu}$=3056.94 (w), 1680.41 (s), 1588.92 (s), 1541.3 (s), 1502.96 (s), 1478.18 (m), 1446.61 (s), 1387.25 (m), 1349.38 (s), 1283.75 (s), 1234.26 (s), 1185.57 (s), 1138.63 (s), 1101.68 (s), 1049.44 (m), 983.71 (m), 956.12 (m), 930.24 (m), 898.52 (m),

886.16 (m), 842.19 (s), 821.46 (m), 804.85 (s), 788.05 (m), 764.37 (m), 747.34 (s), 699.73(s), 643.48(s).

UV/Vis (DMSO): λ_{Max} 287 nm, 317 nm (sh), 375 nm, 395 nm(s), 540 nm 630 nm, 710 nm.

CHN: cal: C 80.59%, H 3.01%, N 10.44% found: C 72.91%, H 3.15%, N 10.06%

Electrochemical deposition solution preparation

The desired amount of sodium (100 mg) was removed from the storage oil and placed in a test tube under N_2. The sodium was washed three times with degassed THF to remove any trace of the storage oil. The sodium was then evaporated to form a sodium mirror. The BuPTCDI or PTCBI (60 to 250 mg) in dry degassed THF (10 ml) was added to the sodium and stirred under N_2 for 3 to >12 hours. The solution (0.5 ml) was then filtered into a solution of dry degassed MeCN, $TBABF_4$ electrolyte (5 ml, 0. 1M) in deposition solution.

Glass preparation

Fluorine-doped tin oxide (FTO) coated glass (3.2 mm, 9 Ω sheet resistance, Pilkington) was washed with detergent, water, acetone, ethanol, propan-2-ol and finally ethanol again.

Field Effect Transistors (FETs)

FET interdigitated-electrode substrates were fabricated, consisting of a heavily-doped silicon wafer gate electrode with a 300 nm SiO_2 layer as insulating layer onto which platinum source and drain electrodes were deposited with an electrode width and gap of 8 µm. Current-potential measurements were recorded using a Keithley 2612 A source probe measuring the drain current (I_{SD}) as a function of the applied source drain potential (V_{SD}) at various applied gate potentials (V_{SG}).

4. Deposition of Copper Phthalocyanine

4.1 Introduction

Phthalocyanines, shown in Figure 4.1, are two-dimensional 18 π-electron aromatic porphyrin analogues.[120]

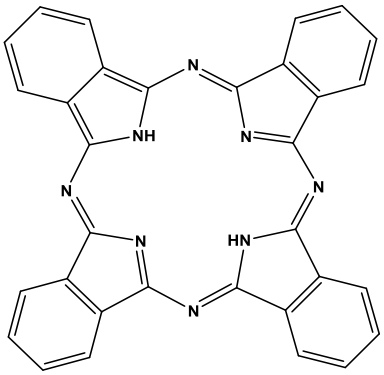

Figure 4.1: Phthalocyanine

First isolated in the 1930s, they have been used in several applications in molecular electronics that range from photovoltaics to electrochromic display devices and gas censors.[10, 121-124] They have also been studied as potential bridging molecules to combine silicon based nanotechnology and molecular electronics.[125]

Copper phthalocyanine, shown in Figure 4.2, was the first isolated phthalocyanine.

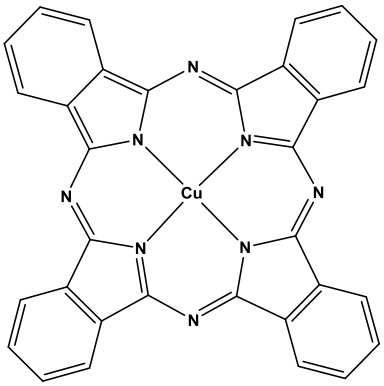

Figure 4.2: Structure of copper phthalocyanine

Originally used as a dye, copper phthalocyanine, CuPc, has more recently been used for organic electronics applications. It was used in the first organic heterojunction solar cell by Tang in 1986.[10] More recently it has been used in double heterojunction thin film solar cells with efficiencies as high as 5.5 %.[126]

Phthalocyanines and their homologues are among the most studied organic semiconductor materials. Their photophysical and electrochemical properties have resulted in them being used as electron-donors and electron-acceptors in multi-layered systems for energy and charge transfer processes.[38] However, the large π system that gives the molecules their charge carrying properties also results in them being very insoluble, meaning that solubilising groups have to be added to investigate the properties of the molecule in solution.[127] Both in solution and in thin films, CuPc exhibits electrochromism based on the charge of the molecule.[122]

Thin films of unsubstituted CuPc are traditionally vapour-deposited. At low temperatures the α-form is obtained, whereas if films are prepared at high temperatures or annealed after formation the β-form is obtained. The films are normally homogeneous with well-defined structures, which range in sizes between ~20 nm and ~80 nm.[128]

Electrodeposition of CuPc was performed to investigate whether films similar to those made by vapour deposition could be obtained using solution-based electrochemical deposition.

4.2 Results and Discussion

4.2.1 Deposition

Deposition of CuPc was achieved by the same method used to obtain films of BuPTCDI in section 3.2.2.1. The anionic form of CuPc, $CuPc^{-n}$, was prepared by suspending CuPc in THF and reacting it with sodium for approximately 12 hours. This was then diluted with THF electrolyte solution in the same electrochemical set-up as the deposition of the BuPTCDI mentioned in chapter 3. Several deposition attempts were performed on FTO, resulting in only partial deposition, suggesting that nucleation was not occurring or that the film was not being adhered to. It was not until a layer of PEDOT:PSS, a transparent, conductive polymer, was added to the FTO substrate that a uniform deposition was obtained. This is possibly due to the way CuPc deposits onto the substrates. A recent study on the orientation of CuPc molecules in vapour-deposited films found that the molecules deposited on FTO were oriented edge-on, meaning that the core was perpendicular to the substrate, whereas films deposited on FTO/PEDOT:PSS were oriented with the cores parallel to the substrate.[129] In the case of electrodeposition, molecules that deposited edge-on to the substrate would template the growth of crystallites that were oriented parallel to the FTO surface with poor conductivity in the perpendicular direction, so it is possible that a thin layer of insulating CuPc molecules was deposited on the FTO substrate which was too thin to detect using available techniques. However, CuPc molecules that were deposited parallel to the substrate would enable growth of crystals that conduct well in the perpendicular direction, allowing for continuous deposition.

During the initial investigation it was found that adding the $CuPc^{-n}$ anions to acetonitrile resulted in immediate aggregation so the deposition was performed in THF in which the aggregation of the CuPc occurred at a slower rate. A typical deposition plot at a 5.4×10^{-4} mol dm^{-3} CuPc solution potential of 1.20 V is shown in Figure 4.3.

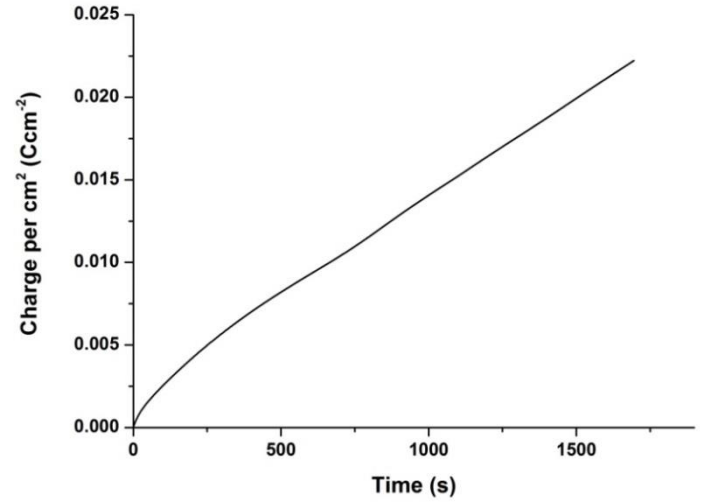

Figure 4.3: Charge per cm^2 against time for a 2.40x10^{-2} Ccm^{-2} deposition while holding the potential at 1.20 V

The plot shows that the deposited film is conductive as the charge per cm^2 increases steadily. The plot contains at least two sections: an initial section and a linear region, suggesting that the deposition occurs at a constant rate. More information about the stages of the deposition can be determined from the current shown in Figure 4.4.

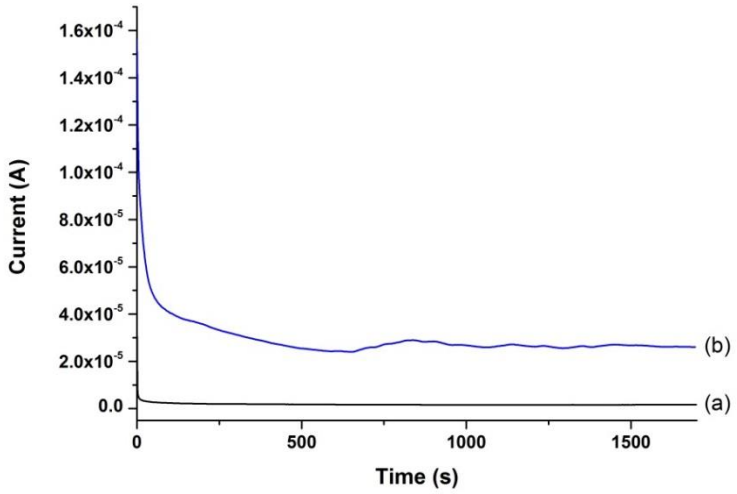

Figure 4.4: Current against time for a 30 minutes deposition while holding the potential at 1.20 V (a) without CuPc^{-n} and (b) with CuPc^{-n}

The plot shows that there are three different types of current present: the initial current which lasts for ~100 seconds is initially large then rapidly decreases. The

second type of current occurs between ~100 seconds and ~610 seconds, with the current slowly decreasing. After ~610 seconds the current increases and then fluctuates. This current is typical for all depositions with currents of the second stages ranging between $1x10^{-5}$ Acm^{-2} and $2x10^{-5}$ Acm^{-2}. The third stage is present in all depositions of more than 500 seconds.

The initial current suggests that the initial deposition is a combination of kinetic and mass transport factors. Changes in the initial kinetic conditions are expected during the first few seconds due to the formation of the double layer and the oxidation of any $CuPc^{-n}$ anions in contact with the film and in the immediate vicinity. However, the current decreases at this rate for ~100 seconds which suggests that the deposition rate is also due to the nucleation of the CuPc on the surface of the PEDOT:PSS layer. More activation energy is required due to nucleation, and subsequently less energy is required as the deposition of CuPc anions onto already deposited CuPc is more energetically favourable than CuPc onto the substrate. Once the nucleation barrier has been overcome the current is dependent on mass transport factors only and is expected to level off, decreasing because of the depletion of $CuPc^{-n}$ anions in the surrounding solution until the deposition is due to diffusion only.

The third type of current is not expected. However, since it does not start straight away, it is possible that it occurs due to the formation of continuous film on the surface of the substrate. At this point CuPc is only depositing on other CuPc molecules.

To understand more about the different stages in the deposition, a plot of the charge per cm^2 against the square route of time, $t^{½}$, for a 1.20 V deposition is shown in Figure 4.5.

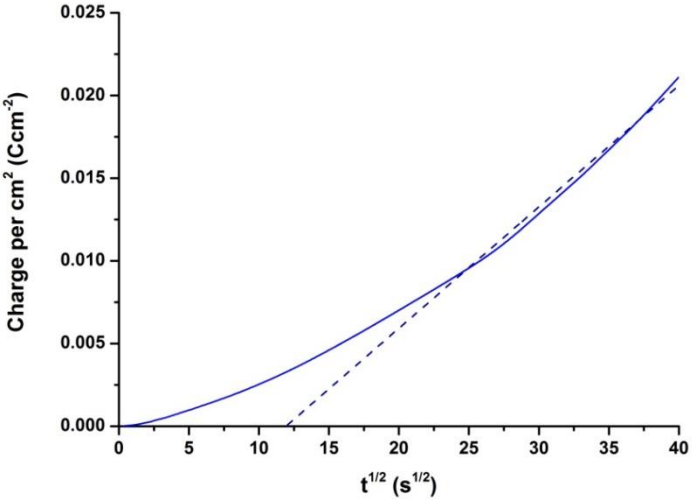

Figure 4.5: Total charge per cm^2 against $t^{½}$ for a $2.40x10^{-2}$ Ccm^{-2} CuPc deposition while holding the potential at 1.20 V

The plot shows that the deposition of CuPc happens in at least two stages. During the initial stage the deposition charge depends on several factors such as the immediate deposition of $CuPc^{-n}$ anions near the surface of the substrate, the rearrangement of the solvent due to the introduction of the electric field, the change in kinetics of the substrate surface and the diffusion of anions. Since the formation of the double layer should only take seconds, most of the kinetic part of the deposition is due to nucleation. Later the deposition becomes approximately linear because the charge per cm^2 is only due to the deposition of $CuPc^{-n}$ anions that have to diffuse towards the substrate. A line of best fit to this region of the graph gives a negative intercept, which confirms that the deposition rate in the initial stage is due to a combination of kinetic and mass control factors.

The effect of potential was investigated by varying the deposition potential when all the other conditions were kept the same. Using a CuPc electrolyte solution with a concentration of $2.40x10^{-4}$ mol dm^{-3} the time needed for the deposition of a charge per cm^2 of $5.00x10^{-3}$ Ccm^{-2} was measured. The results are show in Table 4.1.

Table 4.1: Potentials and time needed to reach a charge per cm^2 of $5.00x10^{-3}$ Ccm^{-2}

Potential (V)	Time to reach $5.00x10^{-3}$ Ccm^{-2} (s)
1.20	536.6
1.10	762.7
1.00	1096.5
0.90	1622.1
0.80	2392.2
0.70	4983.1
0.60	-

A plot of charge per cm^2 against $t^{½}$ for the depositions at different potentials is shown in Figure 4.6.

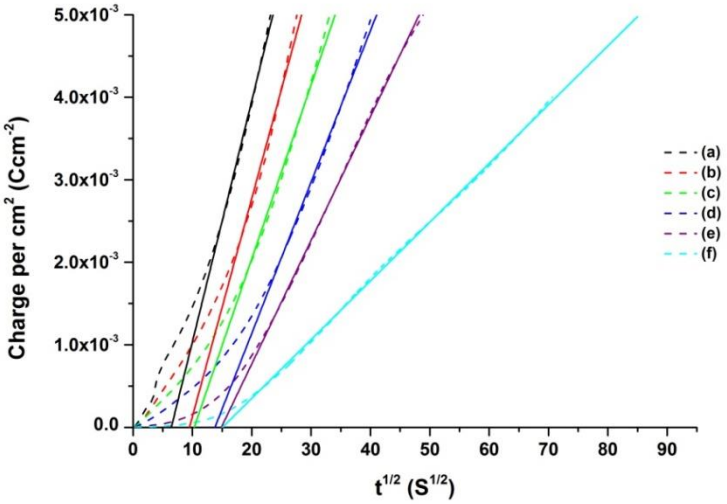

Figure 4.6: Charge per cm^2 against $t^{½}$ for the deposition of $5.00x10^{-3}$ Ccm^{-2} of CuPc while holding the potential at (a) 1.20 V, (b) 1.10 V, (c) 1.00 V, (d) 0.90 V, (e) 0.80 V and (f) 0.70 V

At potentials lower than 0.70 V films did not result in the deposition of a CuPc film. Using Equation 2.11 the rate constant of the cathodic process can be calculated:

$$Q = \frac{4nF\vec{k}}{\pi}[r^b]\left(t_L^{1/2}t^{1/2} - t_L\right)$$

Equation 2.11

The value of $t_L^{1/2}$ is the intercept of the line with the X-axis of the best fit of the section of the deposition which is diffusion controlled. Values of $t_L^{1/2}$ from Figure 4.6 are shown in Table 4.2.

Table 4.2: $t_L^{1/2}$ of CuPc depositions at different potentials

Potential (V)	$t_L^{1/2}$	t_L
1.20	6.5	42.3
1.10	9.5	90.1
1.00	10.3	105.7
0.90	13.8	190.4
0.80	14.8	219.0
0.70	15.1	226.8

The value of t_L and the value of the y-axis intercept were used to calculate the rate constant of the anodic process, $\vec{k}$, plotted in Table 4.3.

Table 4.3: $\vec{k}$ of CuPc depositions at different potentials

Potential (V)	t_L (s)	Y-axis intercept (Q)	$\vec{k}$ (s^{-1})
1.20	42.3	-1.88×10^{-3}	3.01×10^{-6}
1.10	90.1	-2.51×10^{-3}	1.89×10^{-6}
1.00	105.7	-2.17×10^{-3}	1.39×10^{-6}
0.90	190.4	-2.53×10^{-3}	9.01×10^{-7}
0.80	219.0	-2.23×10^{-3}	6.91×10^{-7}
0.70	226.8	-1.07×10^{-3}	3.2×10^{-7}

The rate constant of the anodic process increases with applied potential which confirms that an overpotential is required. This is most likely due to nucleation of the first layer of molecules. At higher potentials nucleation occurs faster as the kinetic barrier is more easily overcome.

Despite the lower limit potential being 0.70 V, the following depositions of CuPc were performed at 1.20 V. This was done for two reasons, both linked to the stability of the deposition solution. The first reason is that solutions of lower concentrations of CuPc could be used at this potential, which meant that there was a smaller chance

of aggregation. The second reason is that at the higher potential the deposition rate is faster allowing thicker films to be deposited in less time, again reducing the chance of aggregation.

Once an optimum potential had been selected the repeatability of the process was investigated. Several depositions of CuPc onto a 1 cm^2 masked slide were performed from a $2.40x10^{-4}$ mol dm^{-3} solution at 1.20 V. The deposition charges per cm^2 against time are shown in Figure 4.7.

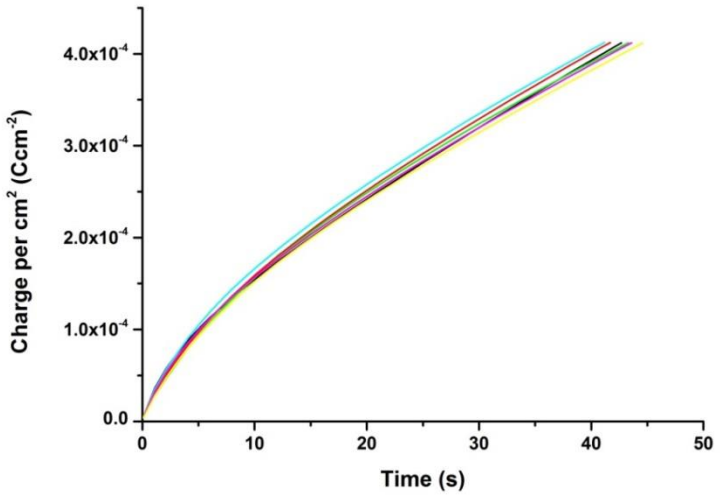

Figure 4.7: Several depositions of $4.10x10^{-4}$ Ccm^{-2} of CuPc

The charge per cm^2 of the depositions is almost identical suggesting that the method of deposition is very repeatable.

4.2.2 Absorption Spectroscopy

The absorbance spectra of several freshly deposited films of CuPc of a deposition charge per cm^2 of $9.19x10^{-3}$ Ccm^{-2} are shown in Figure 4.8.

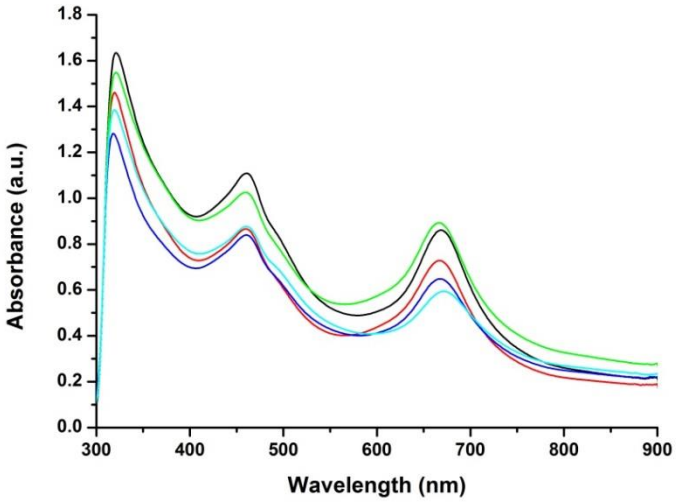

Figure 4.8: Absorbances of several depositions of $9.19x10^{-3}$ Ccm^{-2} of CuPc

Since all the films have the same charge per cm^2 and were deposited from solutions of the same concentration, they should be identical and the λ_{max} and peak widths of the spectra support this. The difference in absorbance is probably due to scattering by the film. This suggests that the absorbance values measured have an error of ±0.3 a.u.

The absorbance spectra of freshly deposited films of CuPc of different charges per cm^2 from a solution of $3.93x10^{-4}$ mol dm^{-3} were measured and the resulting spectra are shown in Figure 4.9.

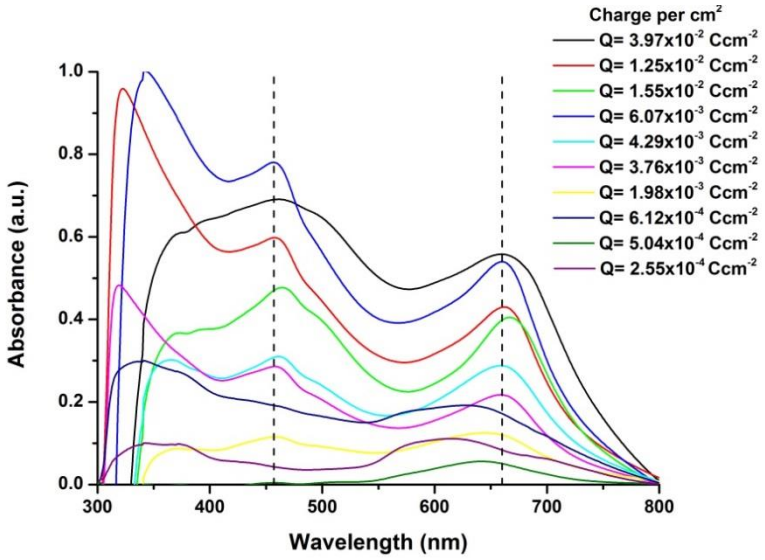

Figure 4.9: Electronic absorption of freshly deposited CuPc films at several different charges per cm^2

The electronic absorption of the films generally increases with increasing charge per cm^2; this is because the increasing charge per cm^2 results in thicker films which absorb more. The spectra of the films contain peaks at ~460 nm and ~664 nm with the transmittance of the films increasing until a charge per cm^2 of $6.20x10^{-3}$ Ccm^2 is reached. At this point the maxima of the spectra decrease which is probably due to the thicker films causing too much light scattering, making the measured spectra unreliable.

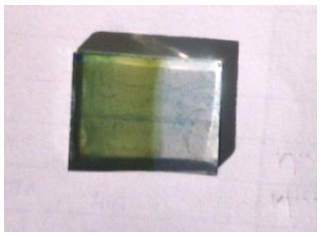

Figure 4.10: Picture of a freshly deposited $4.29x10^{-3}$ Ccm^{-2} CuPc film deposited at 1.20 V

The freshly deposited films were green, as shown in Figure 4.10, which was unexpected as the neutral CuPc and films in the literature are blue, suggesting that they are charged. The first three films with a small charge per cm^2 have different maxima compared to the rest of the depositions. The first has a maximum of 623 nm, the second has a maximum of 645 nm and all the depositions that take place

afterwards have maxima of 664 nm. This is probably due to the films still being in the nucleation stage of the deposition.

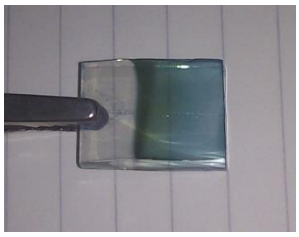

Figure 4.11: Picture of a film exposed to air deposited at 1.20 V

The films turned blue over time in air as shown in Figure 4.11. The rate at which the colour of the film changed depended on the thickness of the film. Thinner films changed colour in a couple of days and thicker films changed over a couple of weeks, with the colour change starting at the edge of the films and moving towards the centre. The normalised absorbance scans of a freshly deposited film, (a), and of the same film after having been exposed to air for 5 months, (b), are shown in Figure 4.12.

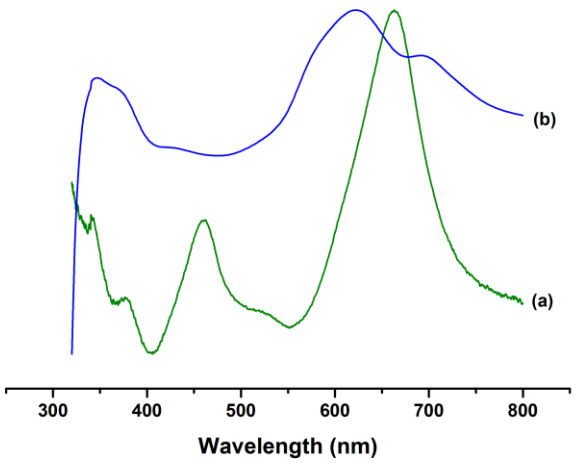

Figure 4.12: Normalised absorption by the same CuPc film scan (a) freshly deposited and (b) 5 months later

The fresh film spectrum, (a), contains three peaks at 341 nm, 458 nm and 664 nm. After 5 months the peaks in the spectrum are different: the peak at 458 nm is no longer present and there are peaks at 344 nm, 622 nm and 690 nm. It seems that the

peaks have red-shifted with the peak at 458 nm having shifted to a longer wavelength.

The same change could be more rapidly achieved by exposing the film to a methanol environment, as shown in Figure 4.13.

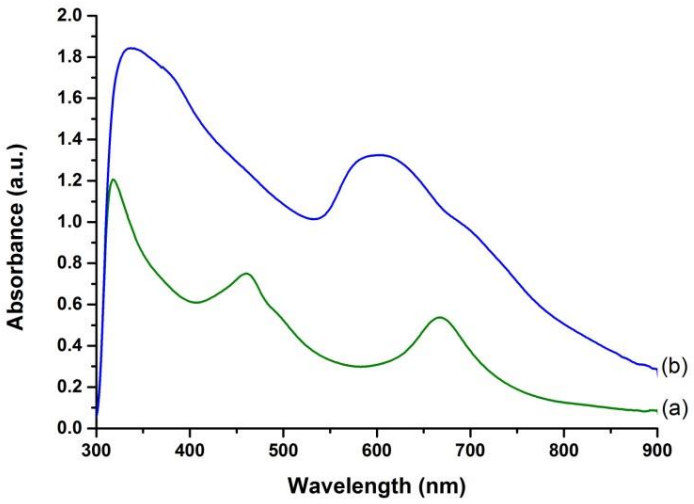

Figure 4.13: Electronic absorption by of a CuPc film scan (a) freshly deposited and (b) after 3 days exposure to methanol vapour

The fresh film has the same peaks as the fresh film in Figure 4.12. After 3 days of exposure to methanol, the peaks' maxima are in the same position as in the film that had been exposed to air. The electronic absorption indicates that the films are deposited in the charged form of the compound as in this state the films are a green colour. This suggests that the film is in a reduced state as $[CuPc]^-$ is known to be green whereas $[CuPc]^+$ is a red/purple colour.[127] When exposed to air the film gains electrons over time. This process is accelerated by the presence of the methanol vapour. The increase in intensity is also consistent with the changes in oxidation state.[128] This suggests that the thinner films are less charged than the thicker films due to absorbed dopants from the air and that therefore the difference in the spectra is due to the different ratio of charged and neutral molecules. A picture of a neutral film is shown in Figure 4.14.

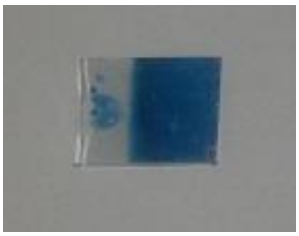

Figure 4.14: Picture of a methanol treated 3.97x10^{-2} Ccm^{-2} CuPc film deposited at 1.20 V

The spectrum of the neutralised electrodeposited film is identical to the spectra of vapour deposited films, which have peak maxima at 345 nm, 610 nm and 690 nm.[117] The bands between 600-700 nm are due to the π-π* transitions in the phthalocyanine ring. The second band at 345 nm is due to d-π* transitions.[130] The band at 458 nm in the charged film is probably due to a d-π* transition as a similar peak is observed in the *in situ* spectro-electrochemical study of the molecule.[127]

Since the films change colour over time they were exposed to methanol vapour for 7 days, so that this process would occur in an accelerated and controlled manner. The spectra of the films after the treatment are shown in Figure 4.15.

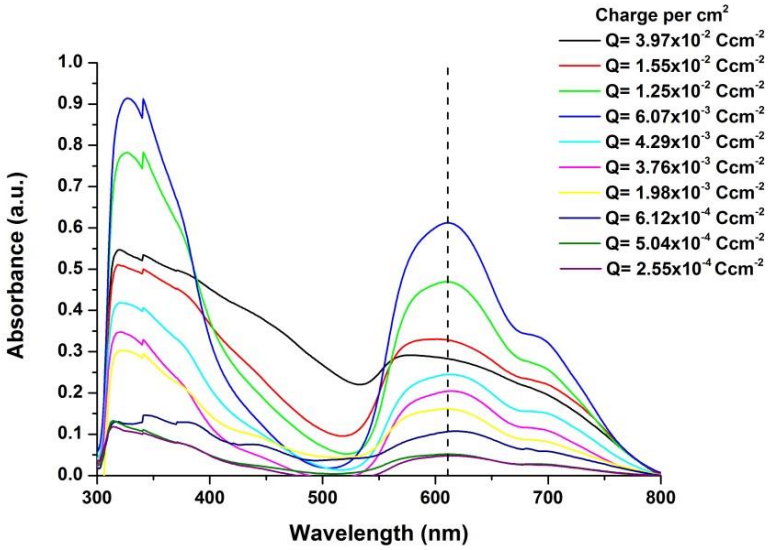

Figure 4.15: CuPc films at several different charges per cm^2 after 7 days' exposure to methanol vapour

After the methanol vapour treatment of the films the peaks around 340 nm have all shifted and now have very similar maxima. The films with a lower charge per cm^2 films have less intense maxima around 314 nm and the maxima then shift to 320 nm, while the rest have maxima at 327 nm.

Similar to the freshly-deposited films the methanol-treated films with a charge per cm^2 of $<1.00x10^{-2}$ Ccm^{-2} have a lower intensity, but after the treatment these spectra have visibly wider peaks.

To verify if there was a correlation between the charge per cm^2 and the absorbance of the film, a plot of the maxima at 611 nm against the charge per cm^2 of films with a charge per cm^2 $<2.00x10^{-2}$ Ccm^{-2} , with the error determined from Figure 4.9, is shown in Figure 4.16.

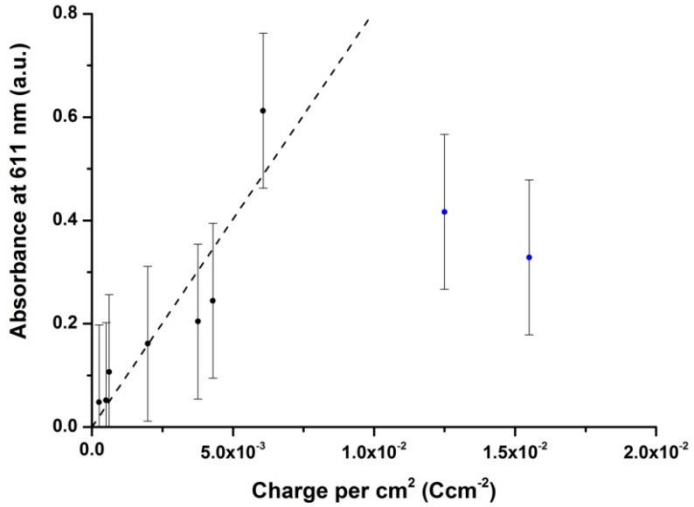

Figure 4.16: Charge per cm^2 against absorbance at 611 nm

The plot implies a linear correlation between the absorbance and the lower charge per cm^2 with a line of best fit giving the formula shown in Equation 4.1.

$$Absorbance(a.u.) = 80.5 \pm 9.0 Ccm^{-2}$$

Equation 4.1

The line of best fit breaks down at the higher charges per cm^2 because the thick films cause more scattering. This roughly linear correlation implies that the film thickness growth is linear with respect to charge per cm^2. This means that absorbance could be used to make an approximate estimation of the thickness of future films since a formula between charge per cm^2 and thickness has been established.

4.2.3 Emission Spectroscopy

Photoluminescence spectroscopy was performed on the films using an Ar^+ laser. The measured response is shown in Figure 4.17.

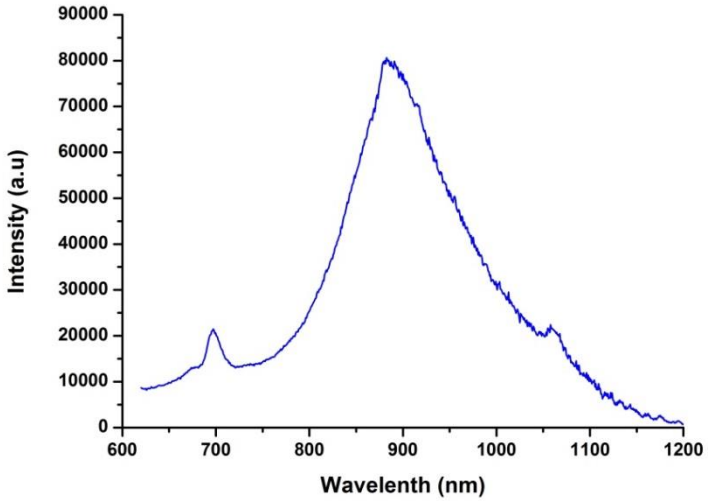

Figure 4.17: Emission of a CuPc film, Q=2.98x10^{-2} Ccm^{-2} (excited at 514 nm)

The emission spectrum of the CuPc film, Q=2.98x10^{-2} Ccm^{-2}, obtained contains two peaks at 696 nm and 883 nm. This suggests that there are two types of emissive sites present in the film. This is not expected as dimers and larger aggregations of phthalocyanines are usually non-emissive.[131] However, there are situations where the dimers and larger aggregations are emissive, normally when the CuPc centres are stacked cofacially.[132, 133] The emission at 696 nm is similar to the emission of monomeric CuPcTs, a sulfonated CuPc analogue, and is probably due to Raman scattering.[132, 134] However, this is dwarfed by the other emission at 883 nm, possibly due to the $S_1 \rightarrow S_0$ transition of the stacked π cores, which is similar to the emission observed in stacks of CuPc($C_{12}OCH_2)_8$, a CuPc with paraffinic side chains that also forms into cofacial stacks.[17]

4.2.4 Scanning Electron Microscopy

Scanning electron microscope images of the treated CuPc films at different thicknesses were taken. Figure 4.18 shows a thicker film of CuPc with a deposition of 6.00×10^{-3} Ccm^{-2}.

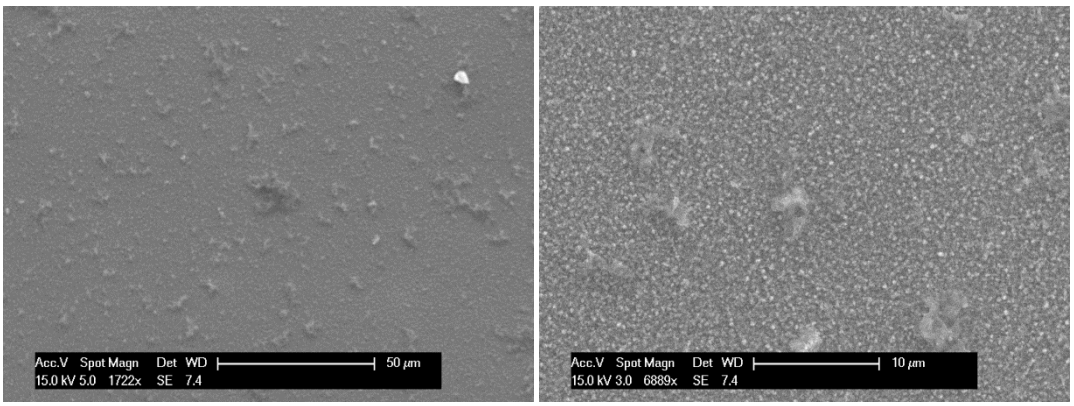

Figure 4.18: SEM images of different magnifications of a film with $Q=6.00 \times 10^{-3}$ Ccm^{-2}

The images show a compact layer made up of small granular crystallites with larger fibres visible on the surface. The size of the crystallites can be estimated from Figure 4.19.

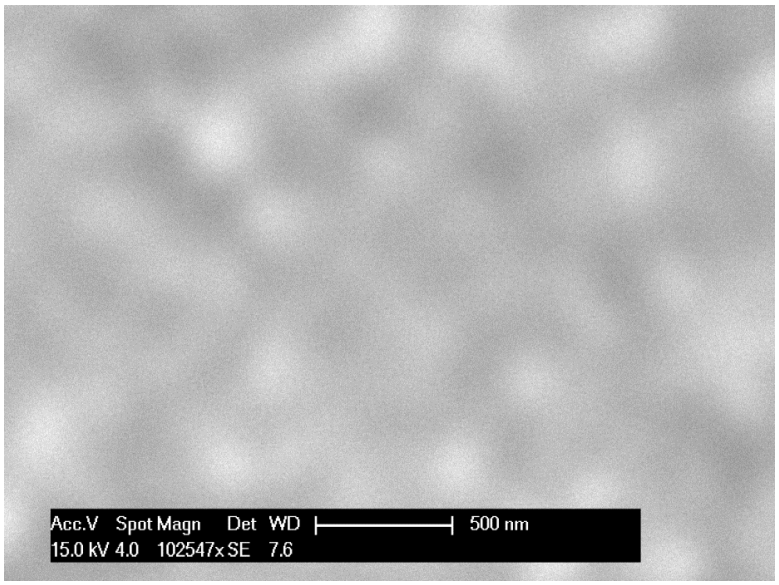

Figure 4.19: SEM image of the individual crystallites of a film with $Q=6.00 \times 10^{-3}$ Ccm^{-2}

The size of the crystallites is roughly between 200 nm and 300 nm, which is similar to the size of CuPc crystallites grown by ultrahigh vacuum organic molecular beam deposition.[135]

A scan of a thinner film is shown below in Figure 4.20 and Figure 4.21.

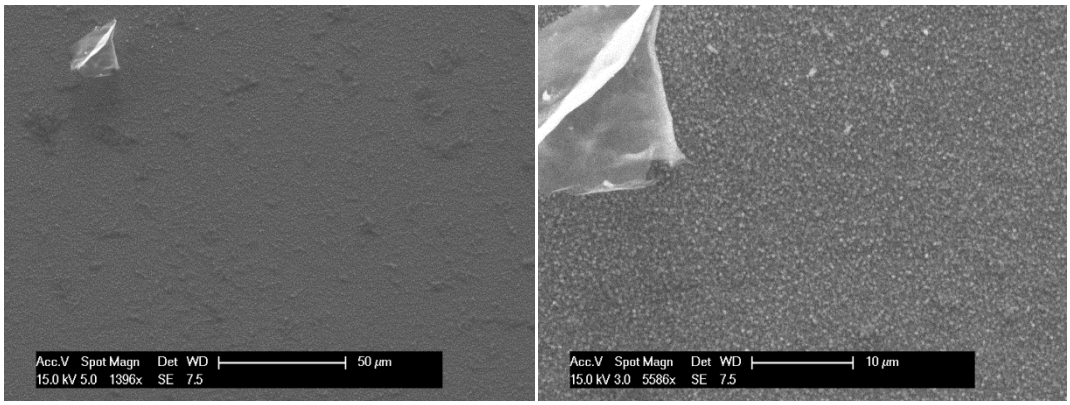

Figure 4.20: SEM images of different magnifications of a film with Q=3.76x10^{-3} Ccm^{-2}

At low magnification the film again seems flat and homogeneous. When the film is examined at a higher magnification it becomes apparent that it consists of similarly sized grains, which are shown in Figure 4.21, with some larger crystallites visible on the surface. The surface crystallites are smaller than those seen in the higher charge per cm^2 film in Figure 4.21.

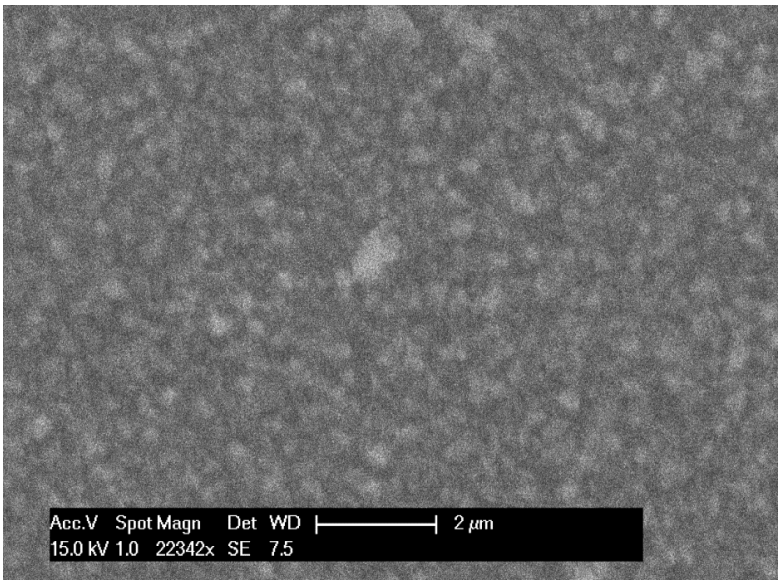

Figure 4.21: SEM image of a film with Q=3.76x10^{-3} Ccm^{-2}

The magnification in Figure 4.21 shows the small crystallites that make up the film. They are a few hundred nanometres in size, which agrees with Figure 4.19.

Images of even thinner films with a charge per cm^2 of $Q=2.55x10^{-4}$ Ccm^{-2} show the same packing with even fewer surface crystallites, as shown in Figure 4.22.

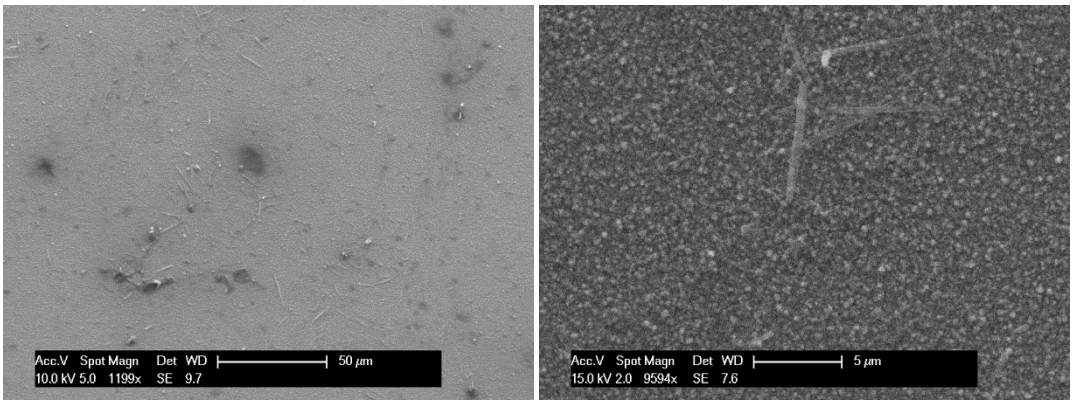

Figure 4.22: SEM images of different magnifications of a film of $Q=2.55x10^{-4}$ Ccm^{-2}

There is also the appearance of needle-shaped formations on the surface. There are two possible explanations as to why they have formed. The first is that they are the electrolyte that was not rinsed off after deposition and has crystallised during the exposure to methanol. Another possible explanation is that these crystallites are pockets of faster growing CuPc and therefore deposit more in that area. The presence of larger crystallites formed at higher charges per cm^2 suggests that the formation of these clusters is probably dependent on the length of the deposition.

To estimate the thickness of the films, images of the cross sections were recorded as shown in Figure 4.23 and Figure 4.24.

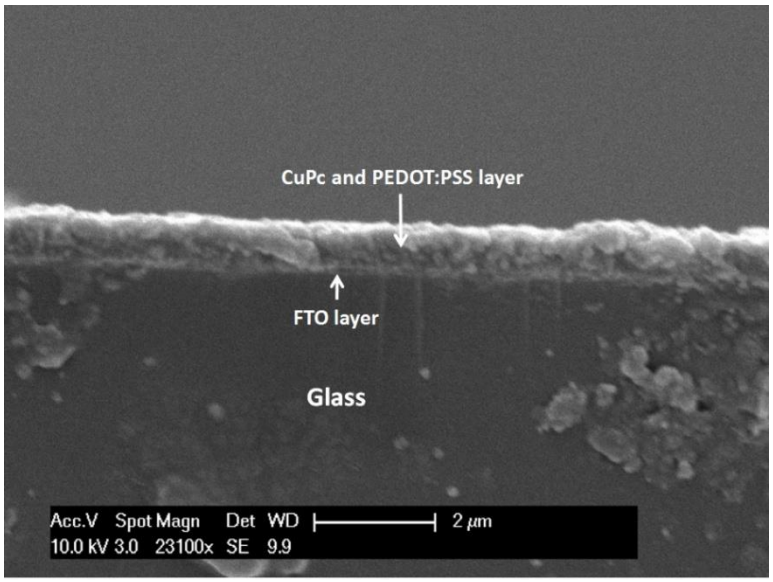

Figure 4.23: Cross section of a film with a Q=1.55x10^{-2} Ccm^{-2}

The cross section, shown in Figure 4.23, shows that the film is a homogeneous layer of CuPc. There are no visible pores suggesting that the CuPc anions do not form a mesh or larger crystallites like BuPTCDI, but are more closely packed.

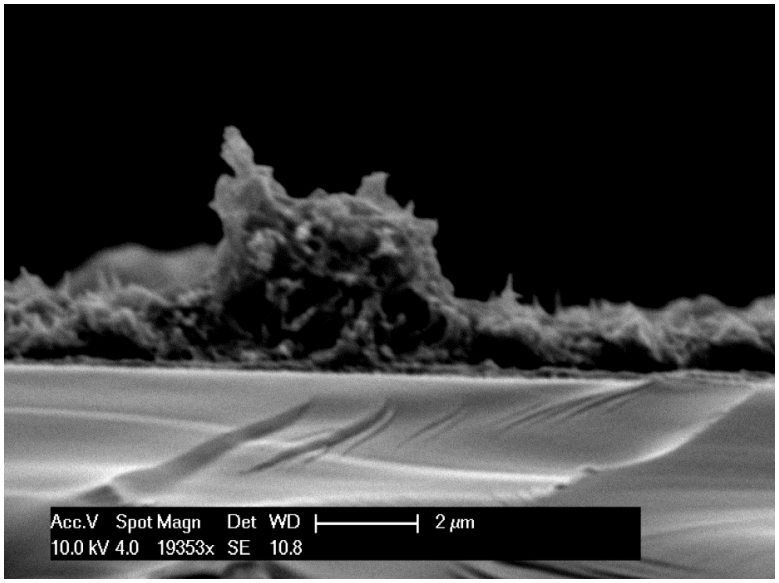

Figure 4.24: Cross section of a film with a Q=3.97x10^{-2} Ccm^{-2}

The cross section of the film with Q=3.97x10^{-2} Ccm^{-2} shows that the film contains a large feature incorporated into the film and which is therefore most likely the result of a pocket of faster stacking CuPc compared with the surrounding film.

To estimate the range of thicknesses, the height of the several points of the cross section were estimated and using them an average thickness of the film was calculated. The calculated values are in Table 4.4.

Table 4.4: CuPc thickness calculations

Charge per cm^2 (Ccm^{-2})	Average Thickness (µm)	Error (µm)
3.97x10^{-2}	1.56	0.168
1.55x10^{-2}	0.83	0.057
4.29x10^{-3}	0.29	0.01
3.76x10^{-3}	0.55	0.036
6.06x10^{-4}	0.97	0.027

A plot of charge per cm^2 against thickness is shown in Figure 4.25.

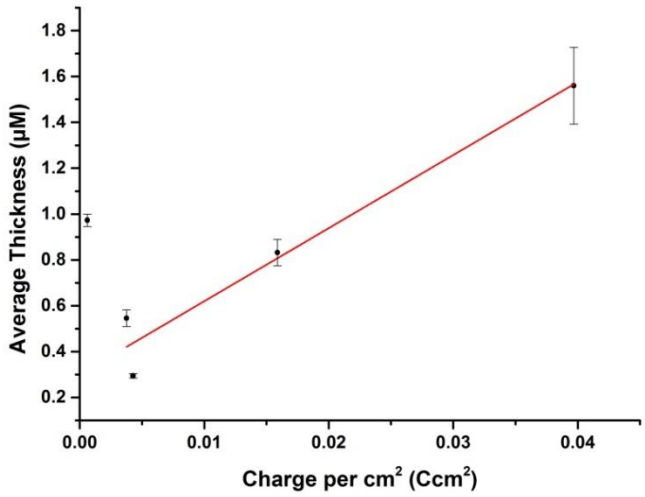

Figure 4.25: Charge per cm^2 against average thickness

A linear correlation between the charge passed and the average thickness can be observed in Figure 4.25 and the thickness can be calculated based on the charge per cm^2 passed using Equation 4.2.

$$Thickness(\mu m) = [35.0 \pm 10.0\ ]\mathrm{C}cm^{-2} + 0.30$$

Equation 4.2

The line in Figure 4.25 does not pass through the origin as the films contain the layer of spin coated PEDOT:PSS which adds to the observed thickness whilst being independent from the charge per cm^2 passed. The layer of 0.3 µm is an order of magnitude larger than the 30 to 60 nm expected for the spin coated layer.[136, 137] However, it is consistent with a cross section of the PEDOT:PSS layer observed in Figure 4.26 and is probably due to the rougher surface of FTO compared to ITO.

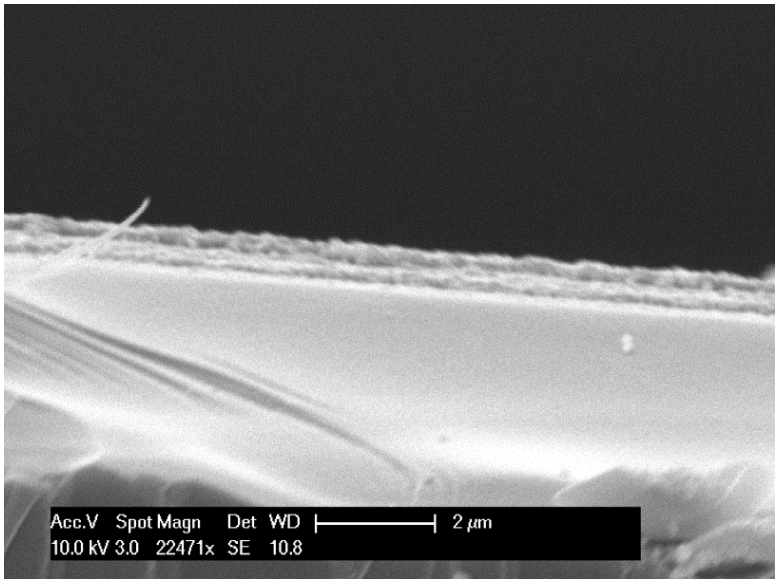

Figure 4.26: Cross section of a spin coated layer of PEDOT:PSS

It was also noted that the thicknesses at lower charges per cm^2 can be unreliable as the depositions were still in the nucleation stage.

The thickness based on the theoretical calculations using the single crystal density, the Nerst equation and charge per cm^2 passed, can be obtained using Equation 4.3

$$Thickness(\mu m) = 36.9\ Ccm^{-2}$$

Equation 4.3

This means that the films obtained are 94.9% of the thickness, based on the single crystal, suggesting that the films have a similar density to the crystal. It also suggests that the electrodeposition process is very efficient.

Similar to BuPTCDI, the electronic absorption of CuPc against charge per cm^2 and the thickness against charge per cm^2 are linearly correlated. By combining Equation 4.1 and Equation 4.3 an equation to work out the thickness based on the film absorbance at 611 nm can be obtained and is shown in Equation 4.4.

$$Thickness(\mu m) = 0.43 \pm 0.50\ Absorbance \text{ at } 611\text{nm}(a.u.) - 0.3$$

Equation 4.4

Using the Beer-Lambert Law (Equation 2.15) and Equation 4.4 the absorption coefficient for the films can be calculated.

$$Absorbance = \varepsilon cl$$

Equation 2.15

Rearranged Equation 4.4 gives:

$$Absorbance \text{ at } 611\text{nm}(a.u.) = \frac{thickness(\mu m)}{0.43 \pm 0.06}$$

Combining the rearranged Equation 2.15 and Equation 4.4:

$$\left(\frac{thickness(cm)}{0.43\ \pm 0.06}\right) \times 10000 = \varepsilon cl$$

Equation 4.5

Since in this case the thickness is equal to the length, they cancel each other:

$$\frac{10000}{0.43\ \pm 0.06} = \varepsilon c$$

Equation 4.6

The concentration of the solid can be calculated based on the density of the solid using Equation 4.7, Equation 4.8 and Equation 4.9:

$$c = \frac{moles}{v}$$

Equation 4.7

$$moles = \frac{mass}{molar\ mass}$$

Equation 4.8

$$\therefore c \times v = \frac{mass}{molar\ mass}$$

$$c \times molar\ mass = \frac{mass}{v}$$

Since density is equal to:

$$\rho = \frac{mass}{v}$$

Equation 4.9

$$\therefore c = \frac{\rho}{molar\ mass}$$

Which, assuming that the packing is the same as the crystal structure, is 1620 gdm^{-3} and the molar mass is 576.08 $gmol^{-1}$.

Then Equation 4.6 becomes:

$$\frac{10000}{0.43 \pm 0.06} = \frac{1620}{576.08}\varepsilon$$

Equation 4.10

resulting in an absorption coefficient, ε, of $8.27 \times 10^3 \pm 1.01 \times 10^3$ cm^{-1} at 611 nm. This is an order of magnitude lower than expected for CuPc. However, the absorption bands of the CuPc in a film are considerably broadened in comparison to the CuPc dissolved in solution.

4.2.5 X-ray diffraction

The X-ray diffraction pattern of CuPc deposited on PEDOT:PSS was measured and is shown in Figure 4.27.

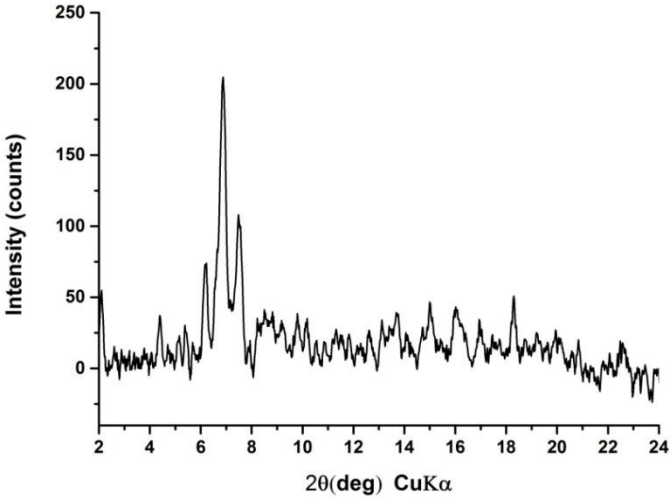

Figure 4.27: XRD pattern of a film with Q=4.87x10^{-3} Ccm^{-2}

The pattern shows little crystallinity with only two small peaks present with a very low intensity. This means that the electrodeposited film is largely amorphous and the CuPc molecules are not packed in long range unit cells. Since the low intensity peaks are sharp it suggests that they are due to some surface crystalline incorporated into the deposited film.

Despite the peaks being very weak, the d-spacing values of the peaks were calculated and are shown in Table 4.5.

Table 4.5: Calculations of d-spacings of the CuPc film

CuPc Film 2θ values	CuPc Film d values (Å)
6.87	12.85
7.48	11.80

The average size of the crystallites in the CuPc film were estimated using the Scherrer equation, Equation 3.20.

Table 4.6: Estimate of average crystal sizes of CuPc

CuPc Film 2θ values	β (º)	τ(Å)
6.87	0.15	537.0
7.48	0.16	489.6

From the three peaks in the XRD pattern the particle sizes in the film are calculated to be in the range of 49 nm to 53 nm. This is similar to one type of films deposited by vapour techniques.[128]

The peaks present in the pattern were also compared to the known crystal packings of CuPc and the closest matches are shown in Figure 4.28.

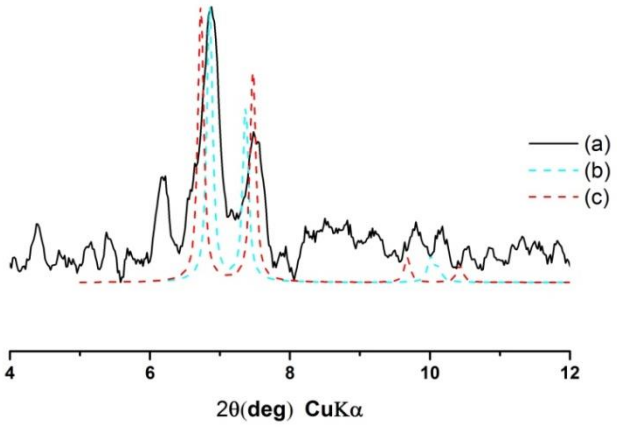

Figure 4.28: Different XRD patterns of CuPc: (a) Electrodeposited film Q=4.87x10^{-3} Ccm^{-2} and the calculated patterns from the single crystal data from (b) Hoshino and (c) Erk

The crystal structures with peaks with the closest match to the distinguishable peaks in the pattern of the CuPc film are the structures by Hoshino and Erk with peaks at 6.72º and 7.47º and 6.85º and 7.36º. Known as α-CuPc and γ-CuPc both structures are face-to-face stacked columns rather than face-to-edge herringbone formations, which agrees with the emission data in 4.2.3. The cell dimensions of both crystals are shown below in Table 4.7.

Table 4.7: Cell dimensions of the two crystal structures of CuPc (Å)

	Hoshino[20] (Å)	Erk[138] (Å)
a	12.89	26.33
b	3.77	3.81
c	12.06	23.71

The shortest dimensions in both films are the π-π stacked cores of the phthalocyanine which are ~3.8 Å. The simpler of the packings is the Hoshino crystal structure which contains one CuPc molecule per unit cell and is arranged in a rectangular cuboid of copper centres. This is known as the α-phase. A view of the crystal along the a-axis is shown in Figure 4.29.

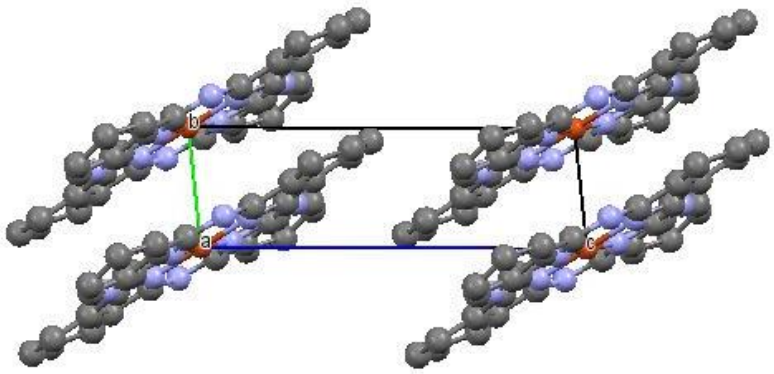

Figure 4.29: The b c plane (normal to the a axis) distances of the Hoshino packing

The longer dimensions of the crystal are determined by the distance between the copper centres of the CuPc molecules.

The π-π stacked cores of the γ-CuPc phase of are shown in Figure 4.30.

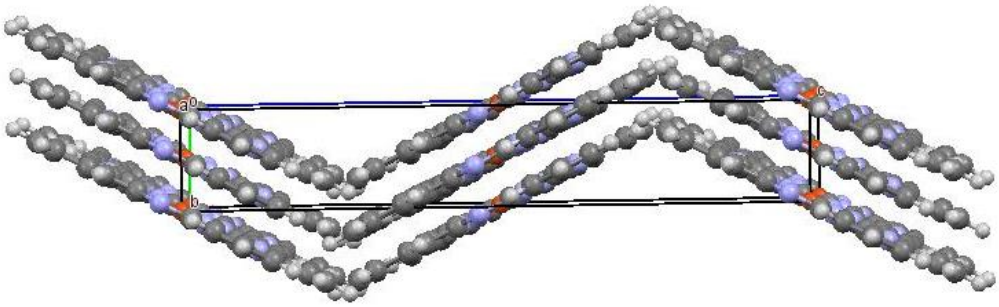

Figure 4.30: The b c plane (normal to the a axis) distances of the Erk packing

Figure 4.30 shows that the crystal contains a face-to-face herringbone packing. Again the longer distances in the crystal are determined by the copper centre to copper centre distance, which are longer due to the herringbone packing.

However, as no other distinguishable peaks are present, it is not possible to determine if the small amount of crystallinity detected is closer to the Hoshino or Erk structure. [138, 139] Also, if the electrodeposited film contained structures with a unit cell with a dimension larger than 22 Å, it would not have been detectable as the peak would have been at a lower 2θ angle than scanned. Therefore it is hard to tell whether the film contains a small number of crystallites with unit cells are 12.85 Å by 11.80 Å by ~3.8 Å or whether they are larger. However, the SEM image of the film shows that it is packed with small crystallites as found in the packing of the α-form.

The morphology of the film is not related to its thickness. The XRD patterns of two CuPc films are shown in Figure 4.31.

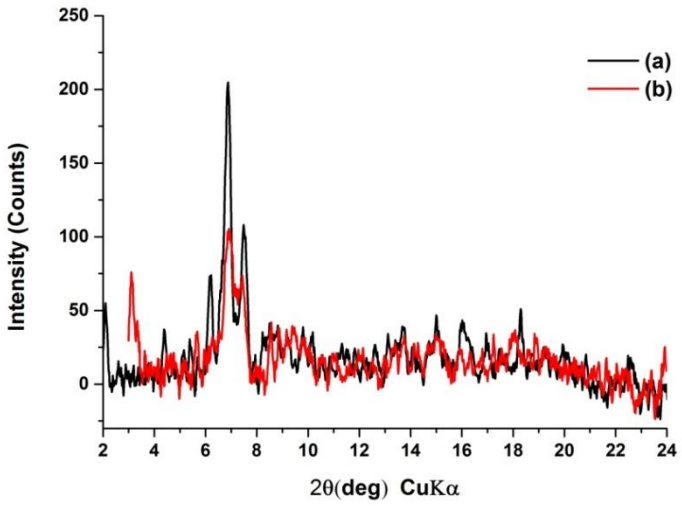

Figure 4.31: XRD patterns of a film with (a) Q=4.87x10^{-3} Ccm^{-2} and (b) Q=2.98x10^{-2} Ccm^{-2}

The patterns of both films overlap fairly well, suggesting that the films have the same crystal structure. However, the intensity of the peaks of the film with a higher charge per cm^2 is considerably less than the intensity of the other pattern with a lower charge per cm^2.

4.2.6 Photo-electrochemistry

The photo-electrochemical properties of a CuPc film were investigated. Investigations were initially performed in the presence of 0.1M hydroquinone, a sacrificial reducing agent, and then repeated without the hydroquinone to investigate any doping in the film. The current responses were measured against Ag/AgCl when the film was exposed to chopped light from a 1000 W halogen lamp at several fixed potentials. Typical current responses are shown in Figure 4.32.

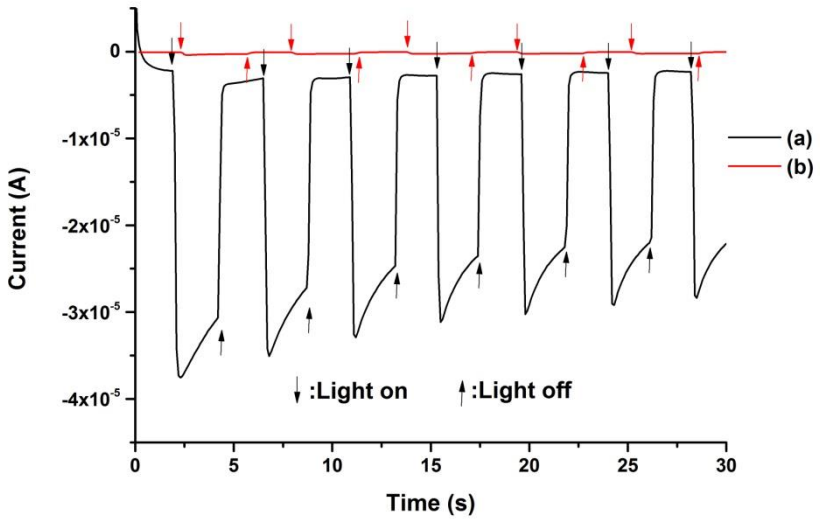

Figure 4.32: Current against time response of a 1.55x10^{-2} Ccm^{-2} CuPc film at potentials of 0.2 V (a) with 0.1M hydroquinone and (b) without hydroquinone

In the presence of hydroquinone, (a), the CuPc film shows a cathodic photocurrent response, meaning that the current becomes more negative when exposed to light, which is consistent with thin films of CuPc deposited by vapour techniques.[140, 141] At low fixed potentials the dark currents measured are reduction currents. As the potential is increased the dark current becomes less negative until 0.5 V when it becomes an oxidation current. The photocurrent response remains cathodic over all the fixed potentials applied. The photocurrent increases until the potential reaches 0.2 V and then deceases until it is an order of magnitude lower than the dark current at a potential of 0.5 V. At potentials above this, the photoresponse is not large enough to have an impact on the overall current of the system. The measured dark current and photocurrent at different potentials are presented in Table 4.8.

Table 4.8: Dark current and photocurrent at different potentials

Potential (V)	Dark Current (A)	Photocurrent (A)
-0.5	-6.32×10^{-5}	-7.44×10^{-6}
-0.2	-5.04×10^{-6}	-1.02×10^{-5}
0.0	-9.86×10^{-6}	-2.26×10^{-5}
0.1	-5.89×10^{-6}	-2.39×10^{-5}
0.2	-3.40×10^{-6}	-3.11×10^{-5}
0.3	-2.32×10^{-6}	-2.82×10^{-5}
0.4	-1.51×10^{-6}	-1.95×10^{-5}
0.5	1.74×10^{-6}	-7.54×10^{-6}

Since no sacrificial acceptor was used, the experiment was repeated without the presence of hydroquinone, as shown in Figure 4.32, (b), to discover where the sacrificial acceptor was originating. CuPc is known to absorb oxygen and water from the air.[124] In these cases the oxygen acts as an acceptor, increasing the charge transporting properties of the films as it accepts the photoexcited electron becoming $O_2^{-\cdot}$.[140, 142] Without any hydroquinone the anodic dark current is suppressed at -5.01×10^{-8} A, with a photocurrent of -1.98×10^{-8} A, both two orders of magnitude smaller than the currents with hydroquinone in Figure 4.32, (a). This confirms that the film has absorbed oxygen over time which results in a photocurrent, although it is less than one percent of that which occurs in the presence of hydroquinone. This suggests that although the hydroquinone was introduced as a sacrificial donor, it is apparently capable of some kind of electron accepting function as well, perhaps due to the presence of benzoquinone as an impurity or as a result of partial air oxidation.

4.3 Conclusion

The electrodeposition of CuPc films was investigated and successfully achieved on FTO/ PEDOT:PSS. The obtained films of CuPc were reproducible with a controllable thickness.

Several deposition potentials were investigated and higher potentials were deemed to be a better choice for the deposition of films as a shorter deposition time results in less aggregation of the $CuPc^{-n}$ anions in the solution which can be incorporated into the film.

The films were deposited in a charged form which initially affects the electronic absorption and results in films which were green before returning to blue when the molecules in the films returned to their neutral state.

The packing of the films is a dense layer of small crystallites similar to the films deposited by vapour deposition, suggesting that electrochemically deposited films of copper phthalocyanine are similar to films deposited by vapour deposition techniques.

4.4 Experimental

The Copper Phthalocyanine was purchased from Sigma Aldrich and purified by sublimation.

CuPc electrodeposition

The desired amount of sodium (100 mg) was removed from the storage oil and placed in a test tube under N_2. The sodium was washed three times with degassed THF to remove any trace of the storage oil. The sodium was then evaporated to form a sodium mirror. Copper (II) phthalocyanine (130 mg) in dry degassed THF (10 ml) was added to the sodium and stirred under N_2 for >12 hours. The solution (0.5 ml) was then filtered into a solution of dry degassed THF, $TBABF_4$ electrolyte (5 ml, 0.1M) in air resulting in a $[CuPc]^{-n}$ deposition solution ($2.40x10^{-4}$ M).

Device Fabrication

The following method was used in the preparation of the substrates for electrodeposition.

Poly(3,4-ethylenedioxythiophene) poly(styrenesulfonate) (PEDOT:PSS)(1.3 wt %) dispersed in water was spun onto the cleaned FTO at an initial rate of 1000 rpm for 15 seconds followed by a faster speed of 3000 rpm for 30 seconds.

5. Copper Phthalocyanine Heterojunction Devices

5.1 Introduction

The electrodeposition methods developed for BuPTCDI and CuPc were used to fabricate bilayer devices in an attempt to prepare organic solar cells. This was done to test whether this method would be a possible alternative to current film fabrication methods such as vapour deposition or solution processing techniques.

Electrochemical deposition of the dyes was attempted to make two different bilayers. Firstly, layers of CuPc were deposited onto PEDOT:PSS and layers of BuPTCDI were electrodeposited on top to see if a functioning heterojunction solar cell could be obtained as determined by Figure 5.1 (left).

For the second type of bilayer device TiO_2 was deposited by doctor blading, a simple printing technique where slurry is applied using constant pressure and then annealed to remove any solvent resulting in a film. CuPc was then electrodeposited on top to investigate the pore penetration of the dye and to see whether a functioning heterojunction solar cell could be obtained as determined by Figure 5.1 (right).

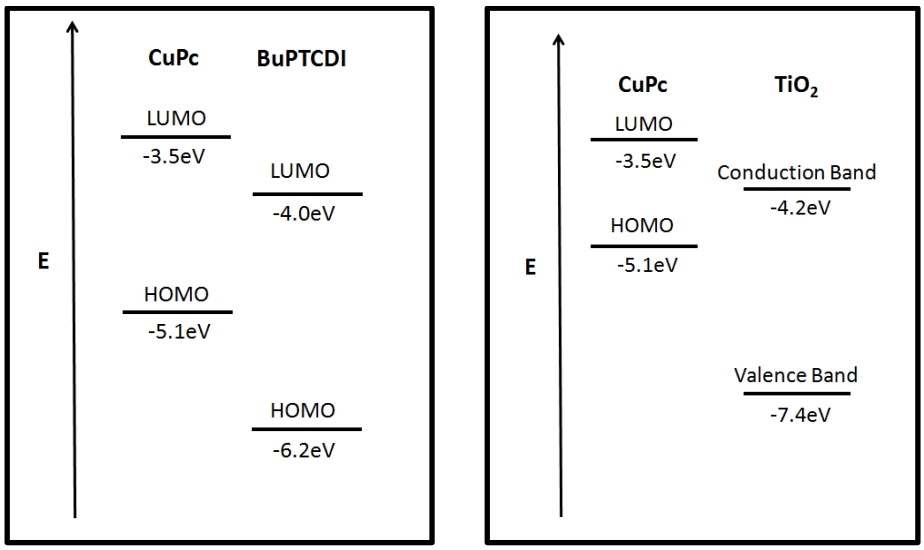

Figure 5.1: Energy levels of (left) CuPc and BuPTCDI and (right) of TiO_2 and CuPc

5.2 Heterojunction of Copper Phthalocyanine and N,N dibutyl-3,4,9,10-perylene-bis(dicarboxime)

The two dyes investigated in earlier chapters were deposited as donor and acceptor layers as a heterojunction solar cell.

5.2.1 Deposition

Since heterojunction solar cells normally contain thin layers of each molecule, the charges per cm^2 needed to deposit 30 nm of CuPc and 40 nm of BuPTCDI were calculated using Equation 4.2, Equation 3.15 and Equation 3.19. Since the BuPTCDI was being deposited onto CuPc both thickness equations, theoretical and experimental, were used as a precaution in case the CuPc acted as a template causing the BuPTCDI to deposit differently than onto FTO.

The effect on the morphology of BuPTCDI was investigated by also depositing thicker films of both CuPc and BuPTCDI in a bilayer structure.

Table 5.1: Bilayers deposition details and estimated thicknesses

Film No.	CuPc Deposition (Ccm^{-2})	CuPc estimated thickness (nm) Equation 4.2	BuPTCDI Deposition (Ccm^{-2})	BuPTCDI estimated thickness Equation 3.19 (nm)	BuPTCDI estimated thickness Equation 3.15 (nm)
1	$8.20x10^{-4}$	30	$2.60x10^{-4}$	160	40
2	$8.20x10^{-4}$	30	$1.04x10^{-3}$	40	10
3	$9.19x10^{-3}$	366	$1.27x10^{-2}$	1950	488

Plots of the typical charge per cm^2 against time for both the CuPc at 1.20 V in THF and BuPTCDI at 0.84 V in MeCN are shown in Figure 5.2.

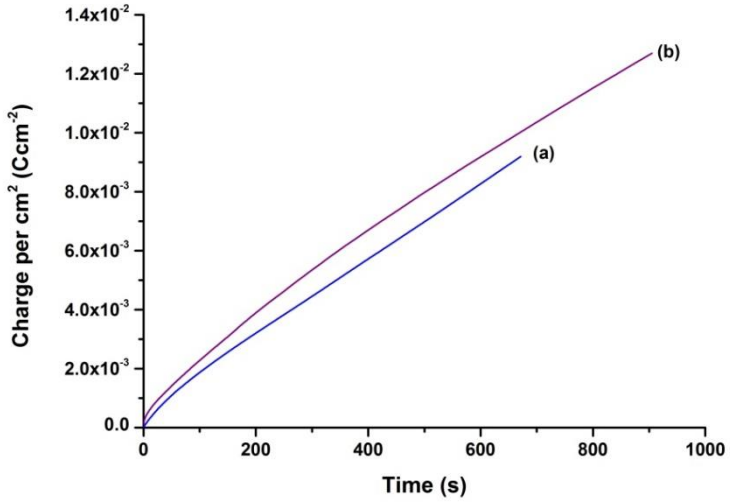

Figure 5.2: Deposition of (a) 9.19x10^{-3} Ccm^{-2} of CuPc and (b) 1.27x10^{-2} Ccm^{-2} of BuPTCDI

The deposition of the CuPc, (a), shows a typical deposition as seen in chapter 4. The deposition of the BuPTCDI, (b), is different from the deposition on FTO. There seem to be two parts to the deposition as there is a step change in the charge per cm^2 after the first second. The first five seconds of the deposition have been magnified and are shown in Figure 5.3. This step change is also visible in the current as shown in Figure 5.4.

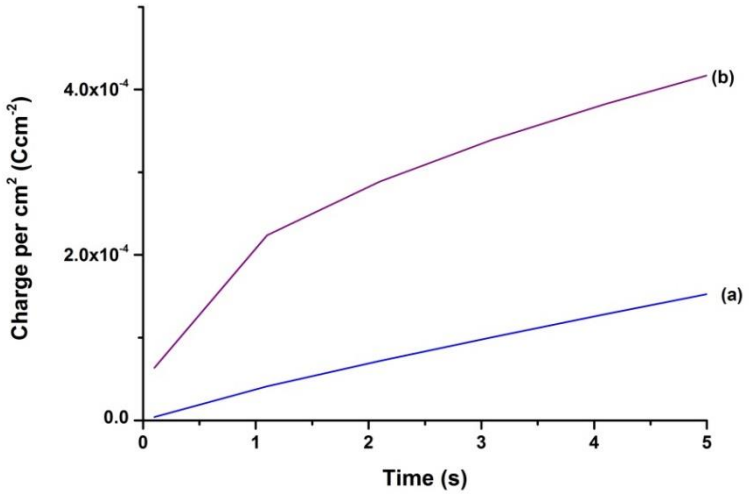

Figure 5.3: First five seconds of the deposition of (a) 9.19x10^{-3} Ccm^{-2} of CuPc and (b) 1.27x10^{-2} Ccm^{-2} of BuPTCDI

The step increase in the BuPTCDI is present in all the bilayers and is independent of the CuPc thickness. This suggests that some charging of the CuPc film is occurring and that any change in the film is happening just at the film surface. The currents of both depositions from Figure 5.2 are shown in Figure 5.4.

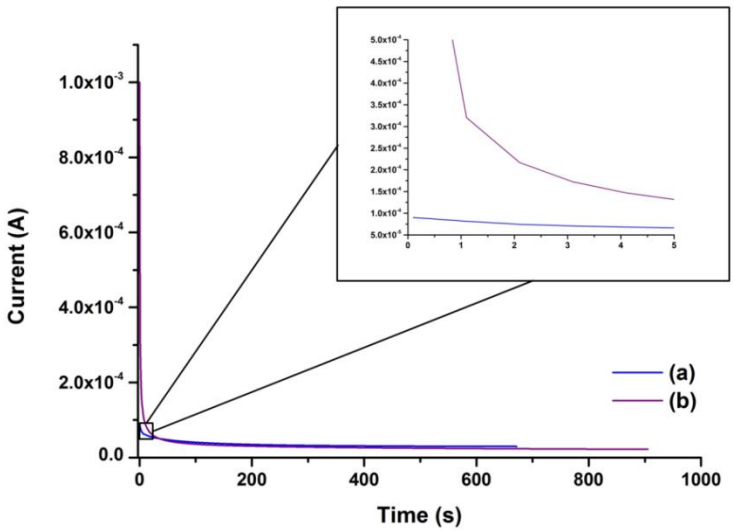

Figure 5.4: Deposition currents of (a) 9.19x10^{-3} Ccm^{-2} of CuPc and (b) 1.27x10^{-2} Ccm^{-2} of BuPTCDI

The deposition current of the BuPTCDI, (b), contains three steps instead of the two normally seen for such a short deposition time. The current of CuPc, (a), contains two sections which is expected for a deposition of this length. Therefore the initial current is due to the formation of the double layer and the nucleation of CuPc molecules already present at the substrate surface. The nucleation of the CuPc changes the kinetics of further deposition at the substrate. Once nucleation has occurred the current is due to the deposition of CuPc by diffusion.

However, the deposition of BuPTCDI is onto the already deposited CuPc film, which can become charged. This means that the initial step of the deposition the current, shown in the inset, is the result of the formation of the double layer, the charging of already deposited CuPc and the nucleation of BuPTCDI at the substrate surface changing the kinetics. Since the double layer takes only one second to form, the second step must again be due to the charging of the film and the deposition of

BuPTCDI changing the kinetics of the surface, as well as the deposition by diffusion. The third step is the result of the deposition of BuPTCDI by diffusion.

5.2.2 Electronic Absorption

Electronic absorptions of all the stages of the fabrication of the bilayers were taken to assess each film. Electronic absorptions of the deposition stages of bilayer No. 3 from Table 5.1 are shown in Figure 5.5.

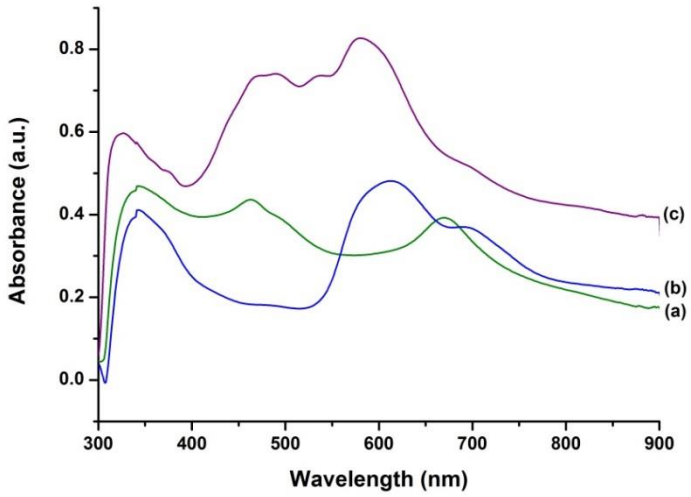

Figure 5.5: Electronic absorption of (a) $3.91x10^{-3}$ Ccm^{-2} of untreated CuPc, (b) $3.91x10^{-3}$ Ccm^{-2} of methanol treated CuPc and (c) bilayer (No. 3) of $3.91x10^{-3}$ Ccm^{-2} of methanol treated CuPc with $5.21x10^{-3}$ Ccm^{-2} of BuPTCDI

Since electronic absorption spectra of different compounds are cumulative, the spectrum of PEDOT:PSS with $3.91x10^{-3}$ Ccm^{-2} of methanol treated CuPc and $5.21x10^{-3}$ Ccm^{-2} of BuPTCDI will be a combination of the spectra of all three layers. Therefore to obtain the spectra of the individual layers of CuPc and BuPTCDI the spectra of the layers underneath must be subtracted. The spectrum of $3.91x10^{-3}$ Ccm^{-2} of CuPc is obtained by subtracting the spectrum of PEDOT:PPS on FTO and the spectrum of $5.21x10^{-3}$ Ccm^{-2} of BuPTCDI is obtained by subtracting the PEDOT:PSS with CuPc spectrum from the bilayer spectrum. The spectra of the individual components of the bilayer are shown in Figure 5.6.

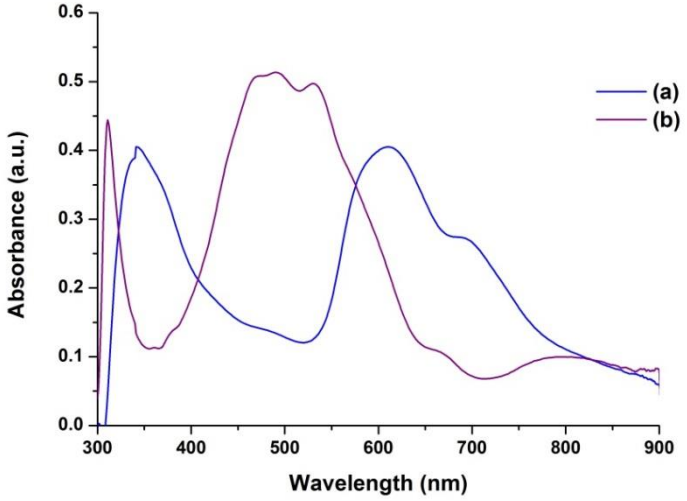

Figure 5.6: Electronic absorption of (a) $3.91x10^{-3}$ Ccm^{-2} of methanol treated CuPc and (b) $5.21x10^{-3}$ Ccm^{-2} of BuPTCDI

Using the absorbance of a CuPc film (a) at 611 nm and Equation 4.1 the thickness of the film can be calculated. With an absorbance of 0.40 a.u. at 611 nm the thickness of the CuPc film is estimated to be 0.48 µm ± 0.20 µm. The BuPTCDI film (b) has an absorbance of 0.49 a.u. at 507 nm. Although it is impossible to determine the thickness of the film based on the absorbance, there is a linear correlation between the increase in charge per cm^2 and the increase in absorption. This implies that the film morphology of the BuPTCDI films is the same in all the depositions and that the thickness is growing linearly with the charge per cm^2. The results for all three bilayers are in Table 5.2.

Table 5.2: Bilayer absorption details and estimated thicknesses

Film No.	CuPc absorbance at 611 nm (a.u.)	Estimated thickness (nm)	BuPTCDI absorbance at 507 nm (a.u.)
1	0.06	71.8 ± 30.2	0.10
2	0.06	71.8 ± 30.2	0.19
3	0.40	480 ± 200	0.49

5.2.3 Emission Spectroscopy

Photoluminescence spectroscopy was performed on the bilayer and is shown in Figure 5.7. The obtained results were then compared to the emission spectra of both the BuPTCDI and CuPc films.

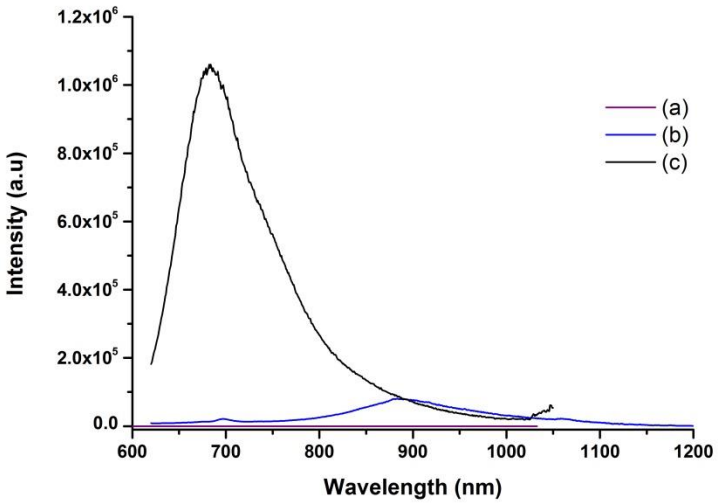

Figure 5.7: Emission of (a) BuPTCDI, (b) CuPc and (c) bilayer No. 2 all excited at 514 nm

The photoluminescent response of the bilayer is two orders of magnitude larger than the CuPc film and five orders of magnitude larger than the BuPTCDI film.

To compare the peak location the normalised spectra of the photoluminescence responses are shown in Figure 5.8.

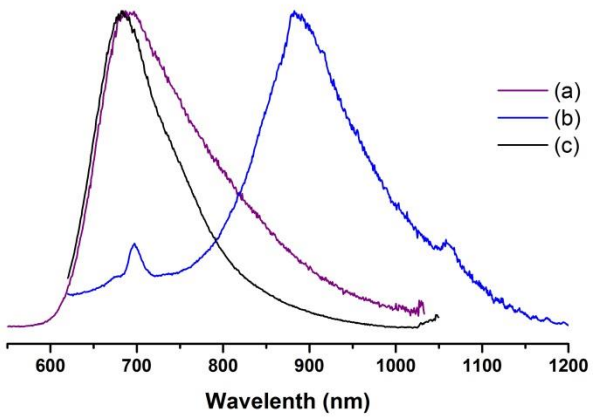

Figure 5.8: Normalised fluorescence of (a) BuPTCDI, (b) CuPc and (c) bilayer No. 2

The maximum of the photoluminescence peak of the bilayer is almost identical to that of the BuPTCDI, suggesting that most of the response is due to the top layer of BuPTCDI being irradiated. This is as would be expected as the bilayer was excited at 540 nm, which will be strongly absorbed by the BuPTCDI, rather than the CuPc which absorbs at around 700 nm. Higher excitation wavelengths were not available in the apparatus used.

5.2.4 Scanning Electron Microscopy

SEM imaging was performed on the bilayer to investigate whether electrodepositing the BuPTCDI on CuPc had affected its morphology. SEM images of bilayer No. 2 are shown in Figure 5.9.

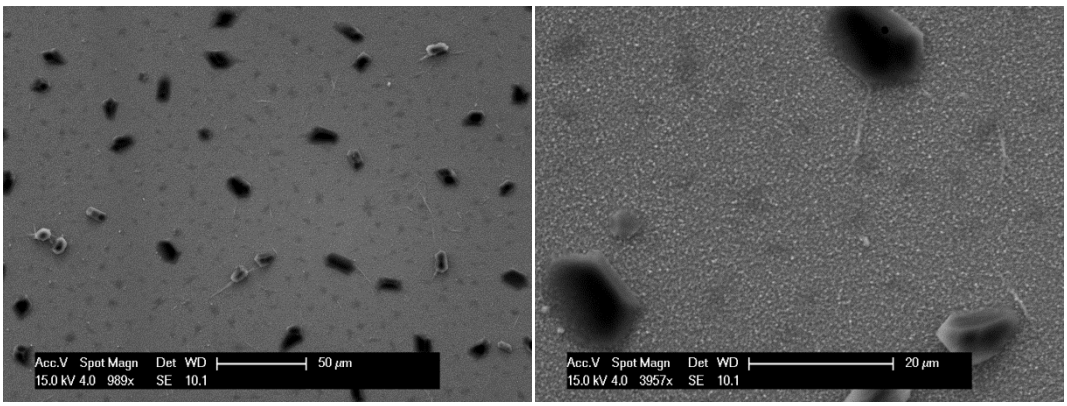

Figure 5.9: SEM images of bilayer No. 2

The images reveal that the BuPTCDI layer has deposited onto the CuPc layer as several large crystallites and not as a continuous film, meaning that thicker films are needed to cover the surface area of the CuPc film deposited.

A SEM image of bilayer No. 3 with thicker films is shown in Figure 5.10.

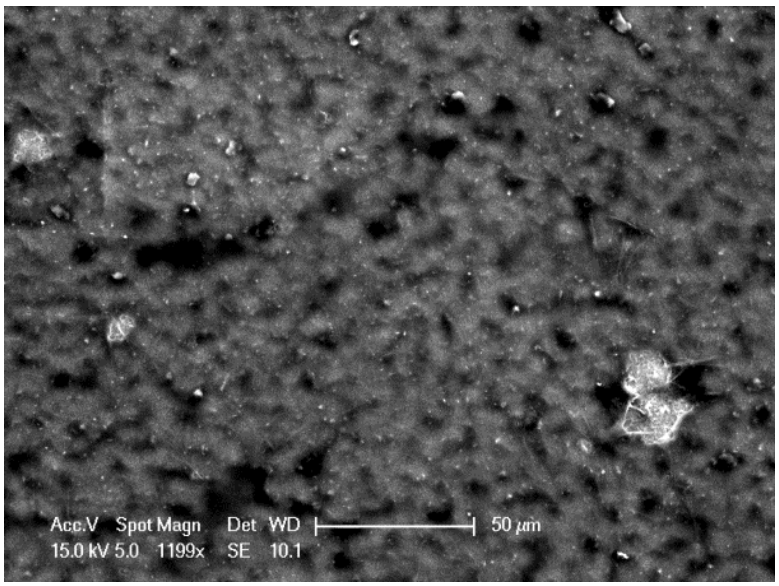

Figure 5.10: SEM image of bilayer No. 3

At lower magnification the thicker BuPTCDI film appears to be more continuous with only small portions of CuPc being visible as lighter areas, most likely due to not enough BuPTCDI being deposited to ensure a complete layer. However, the film is not homogeneous as the presence of lighter and darker areas suggests the presence of several different types of conductivities, implying different structures or thicknesses.

Higher magnifications of the film in Figure 5.10 are shown in Figure 5.11 and Figure 5.12.

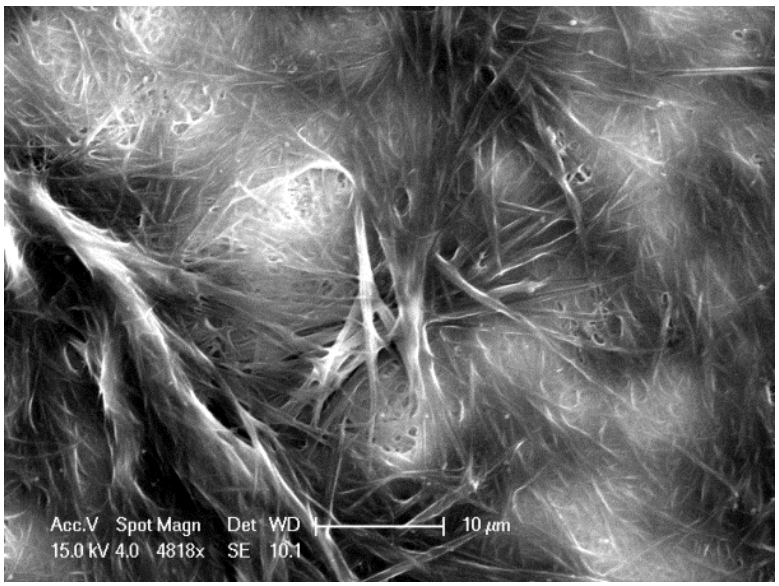

Figure 5.11: SEM image of bilayer No. 3

The images show that the top BuPTCDI layer is composed of an extended network of long crystallites, interwoven to form what appeared like a continuous film. There is also a gradient of brightness across the network of BuPTCDI crystallites, suggesting that areas are becoming charged. The darker areas are caused by very thick clusters of crystallites where the charge is able to migrate and the lighter areas are where the layers are becoming charged. Since the CuPc charges quickly at the current used, most of the lighter areas are where the CuPc layer is visible through the BuPTCDI fibres, which is less able to disperse charge compared to the BuPTCDI, as shown more clearly in Figure 5.12.

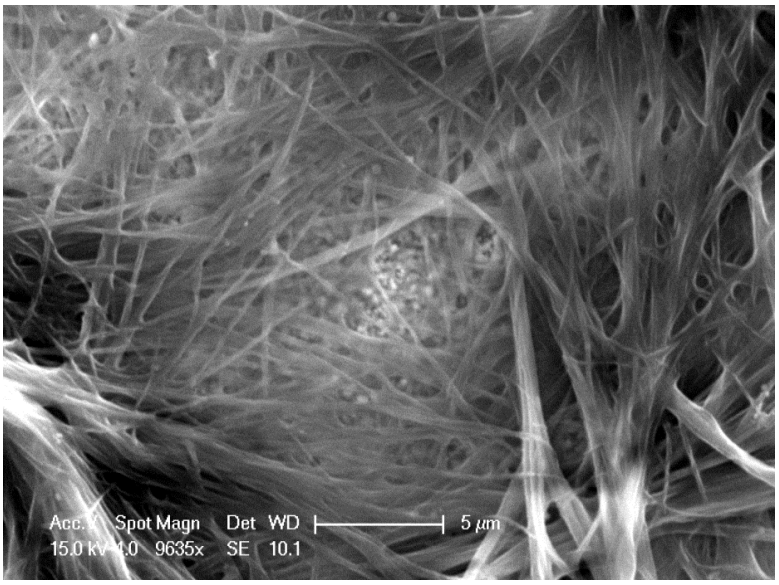

Figure 5.12: SEM image of bilayer No.3

The way in which the BuPTCDI deposits on top of the CuPc is not unexpected owing to the π-π stacking of the perylene cores, resulting in crystallites rather than a homogeneous film. However, there are some differences between the BuPTCDI crystallites on CuPc and the BuPTCDI crystallites on FTO. The crystallites' growth direction is parallel to the CuPc surface, suggesting that this may be the stacking direction, rather than perpendicular to the substrate as they were in chapter 3. Also, the BuPTCDI clusters deposited on FTO are normally much wider, being several microns across with a maximum length of approximately 20 μm depending on the total charge passed. Whereas the clusters deposited on CuPc have similar maximum lengths, they are thinner, being only hundreds of nanometres thick, an order of magnitude less than those on FTO. Clusters that appear thicker are in fact a group of several thin crystallites deposited with the same orientation, as shown in Figure 5.12.

This suggests that some form of templating is happening, which does not occur visibly in the thinner films. This could be due to the small charge per cm^2 passed, meaning that the templating effect was not measurable or templating sites are not present in a thinner film.

Both sets of bilayers deposited would not be suitable for photovoltaic cells owing to the porous nature of the BuPTCDI films. Any electrode applied to the BuPTCDI layer would also be in contact with the CuPc layer which would result in

short-circuiting. It means that the devices mentioned in section 5.2.6 are measuring the photoresponse of the CuPc film as the silver is probably penetrating through the porous PTCDI layer.

5.2.5 X-ray diffraction

The crystallinity of the films was measured using thin film XRD. The XRD pattern of a bilayer of 8.20×10^{-4} Ccm^{-2} of methanol treated CuPc and 1.04×10^{-3} Ccm^{-2} of BuPTCDI is shown in Figure 5.13.

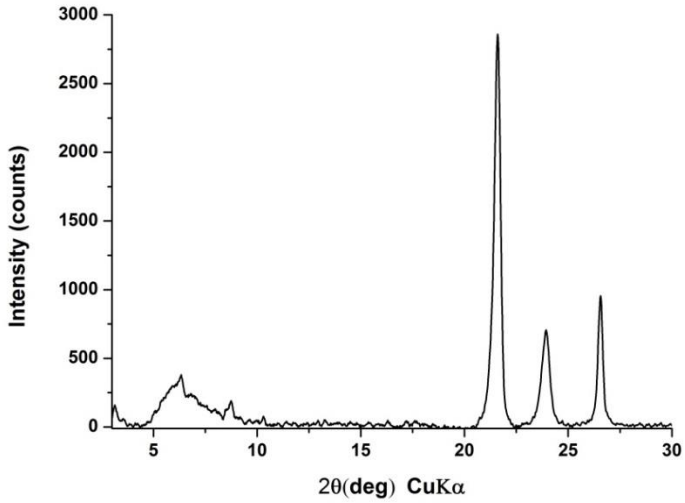

Figure 5.13: XRD pattern of electrodeposited bilayer No. 2

The pattern shows several peaks; there are several broad peaks between 3º and 10º and two sharp peaks at 21.29º and 23.96º. The peak at 26.53º is due to the FTO substrate. The d-spacings due to these peaks are calculated using Bragg's law and are shown in Table 5.3.

Table 5.3: Calculations of d-spacings of the CuPc and BuPTCDI bilayer

Bilayer films 2θ values	Bilayer films d values (Å)
3.18	27.76
6.34	13.93
6.87(sh)	12.86
8.70	10.16
10.29	8.59
21.29	4.17
23.96	3.71

The peaks of the bilayer suggest that some form of templating is occurring compared to the XRD patterns of the films of CuPc and BuPTCDI, as shown in Figure 5.14.

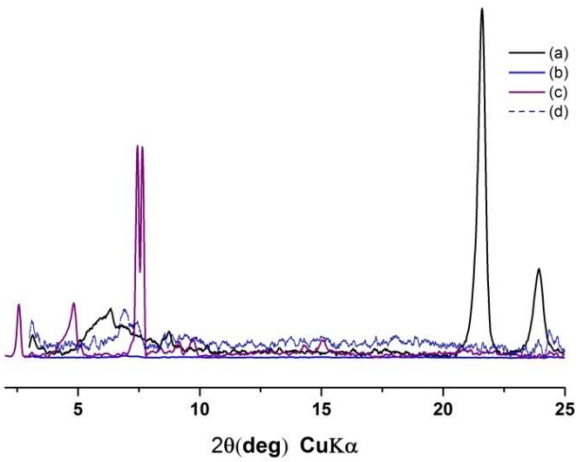

Figure 5.14: Normalised XRD patterns of electrodeposited (a) bilayer No. 2, (b) CuPc, (c) BuPTCDI and (d) CuPc XRD pattern x 20

Although it is not a prominent feature the shoulder peak at 6.87º in the bilayer is identical to that of the CuPc film on PEDOT:PSS suggesting that the CuPc layer is identical to the layer in previous chapters. The other peaks are probably due to the BuPTCDI film on top of the CuPc. These peaks are at different 2θ values compared with the BuPTCDI deposited directly onto FTO, which could be due either to changes in the preferred orientation caused by templating from the CuPc or to a different polymorph of BuPTCDI being favoured. The dominance of the peaks at

21.29º and 23.96º suggests that the BuPTCDI molecules are stacked parallel to the substrate rather than perpendicular as the distances of 3.7 Å and 4.1 Å both correspond to the π-π stacking distances.[8, 95] Therefore, when the film deposits on CuPc it does so with a 90º difference compared to the film on FTO.

The average size of the crystallites that cause the diffraction of peaks at 21.29º and 23.96º can be estimated using the Scherrer equation and the results are shown in Table 5.4.

Table 5.4: Estimate of average crystal sizes of bilayer

Bilayer Film 2θ values	B(º)	τ(Å)
21.29	0.35	233.59
23.96	0.44	185.50

The estimated size of the crystallites is ~20 nm which agrees with the clusters of stacked crystallites seen in the SEM image of the film in Figure 5.12.

5.2.6 Photodetector devices

Photodetector devices were prepared by evaporating a 100 nm layer of silver onto the electrodeposited bilayers on FTO.

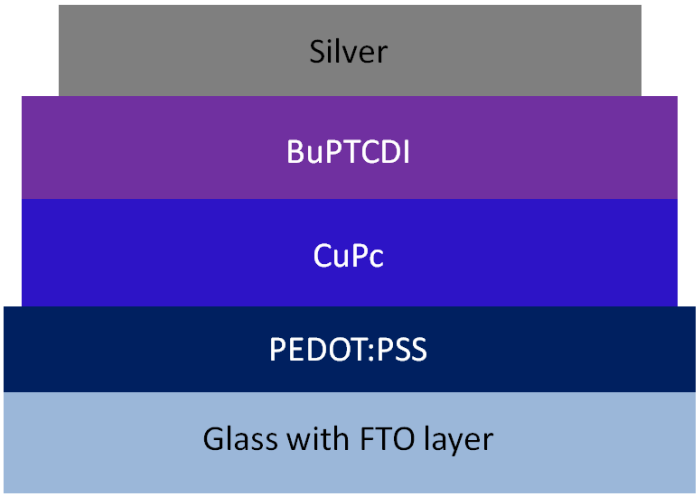

Figure 5.15: Schematic of the bilayer photodetector devices

Table 5.5: Estimated thickness of the bilayer photodetector devices

	No. 2	No. 3
Silver	~100 nm	~100 nm
BuPTCDI	~40 nm	~480 nm
CuPc	~71 nm	~480 nm
PEDOT:PSS	~3 μm	~3 μm

The photoresponse of the devices was assessed by measuring the current response of the devices to an applied potential in the dark and when exposed to AM 1.5.

The photoresponse of a device with a bilayer No. 2 is shown in Figure 5.16

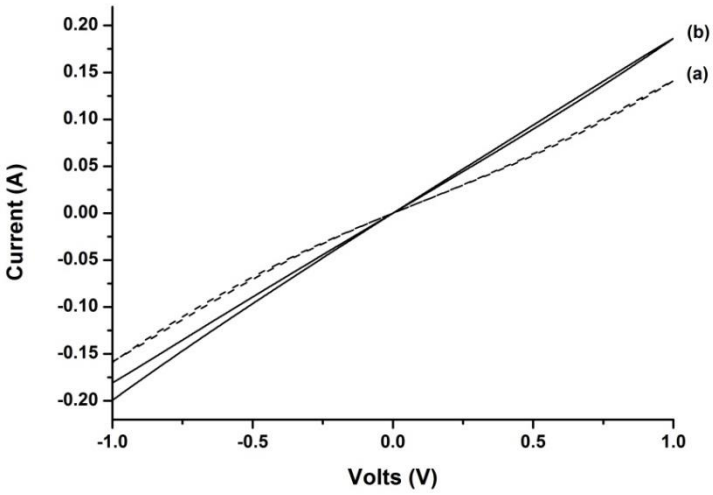

Figure 5.16: IV data of bilayer No. 2 (a) in the dark and (b) at AM 1.5

In the dark the device shows a weak diode response with a slight plateau region between -0.5 V and 0.5 V. The current response of the film increases when exposed to light, thus making the film a photoconductor. The plateau region is also no longer clearly visible. The photoresponse of the film depends on the applied potential. At low potentials the response is weak, but is a significant proportion of the current. For example, at a potential of 0.2 V the dark current is 2.40×10^{-2} A and the photocurrent is 1.28×10^{-2} A. The photoresponse at higher potentials is larger, but represents a smaller proportion in comparison to the dark current. At the potential of 1.0 V the dark current is 14.10×10^{-2} A and the photocurrent 4.50×10^{-2} A.

To verify if the response changed with the thickness of both films in the bilayer the photoresponse of a device with a bilayer No. 3 is shown in Figure 5.17.

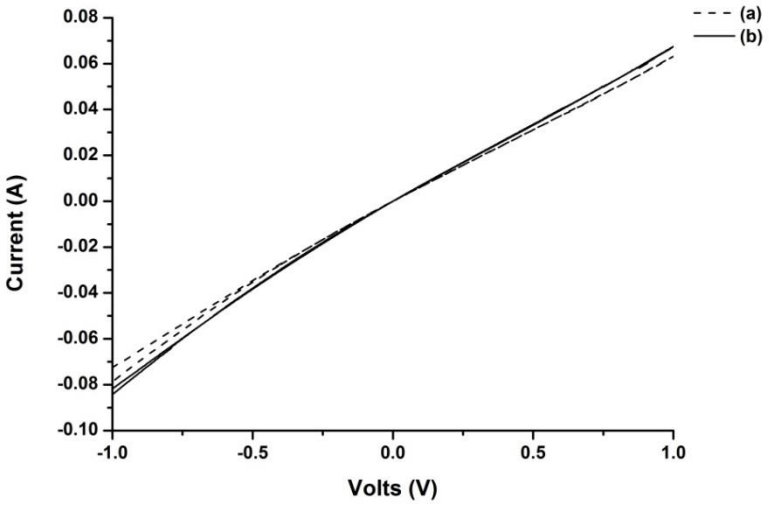

Figure 5.17: I-V data of bilayer No. 3 (a) in the dark and (b) at AM 1.5

The photoresponse of the thicker bilayer is weaker than its thinner counterpart with a dark current of 1.26×10^{-2} A and a photocurrent of 9.95×10^{-4} A at 0.2 V and a dark current of 6.32×10^{-2} A and a photocurrent of 4.45×10^{-3} A at 1.0 V. The most likely explanation for this change is the resistance of the film; the current has more film to flow through in the thicker device, resulting in the lower current.

Both devices are photoresistors, not photovoltaic cells as was the original objective. This suggests that one of the films is porous, resulting in one of the films in the bilayer being in contact with both electrodes. This will cause short-circuiting as the current will take the path of least resistance, flowing through the first film only and not the second. This agrees with the SEM images of the films in section 5.2.4.

5.3 Heterojunction of Titanium Dioxide and Copper Phthalocyanine

Devices containing heterojunctions of organic/inorganic photoactive materials are currently being investigated as solar cells. The inorganic materials have a high electron mobility, are thermally stable and robust.[143] This stability means that organic photoactive materials can be deposited onto them without damaging the inorganic layer. It also means that the two layers do not diffuse into each other over time due to thermal activation. Another advantage is that the inorganic layer can be used as a template to ensure that the interface between the two films is as large as possible. The electrodeposition of a dye onto nanoporous TiO_2 was performed to investigate whether this method could be used to deposit molecules into the pores of the film, which cannot be achieved by vapour deposition.

5.3.1 Deposition

Electrodeposition of CuPc onto a ~6µm thick, 1 cm^2 porous TiO_2 layer on FTO was performed. A plot of the charge per cm^2 against time is shown in Figure 5.18.

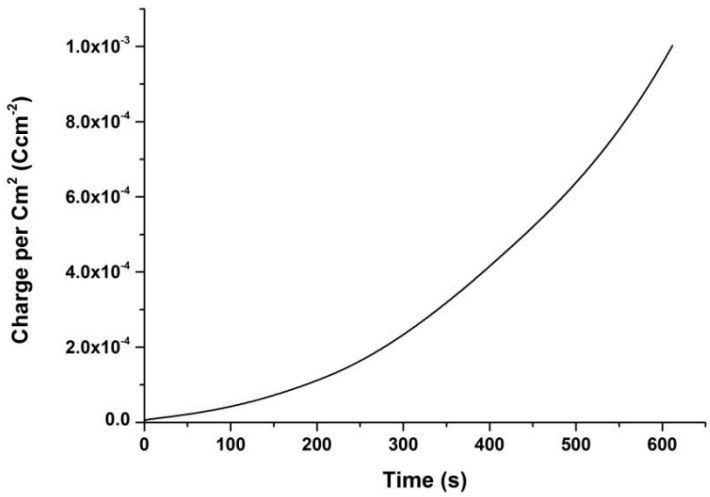

Figure 5.18: Deposition of $1.00x10^{-3}$ Ccm^{-2} of CuPc onto 1 cm^2 of porous TiO_2 at a potential of 1.20 V

The CuPc not only deposited onto the TiO_2, but it did so in preference to the FTO. It is possible that the CuPc deposited onto the FTO in a way that insulated it and onto the TiO_2 as a conductor, therefore resulting in bulk deposition onto the TiO_2 and only as a monolayer on the FTO. However, it is more likely that the CuPc did not nucleate on the FTO. A current of the deposition is shown below in Figure 5.19.

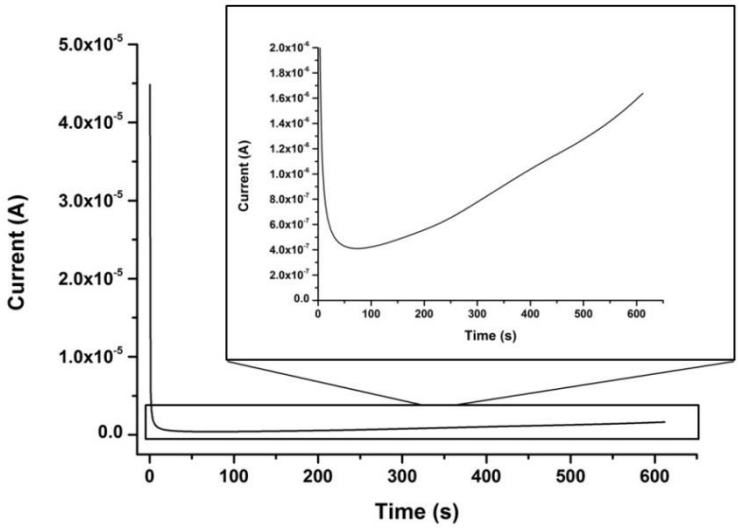

Figure 5.19: Current against time for the deposition of $1.00x10^{-3}$ Ccm^{-2} of CuPc onto 1 cm^2 of porous TiO_2 at a potential of 1.20 V

Initially the current is similar to that of the BuPTCDI being deposited onto the CuPc. At the start there is a very large current that decreases rapidly, and then a current that is the result of a combination of changing kinetics occurring on the substrate surface and diffusion of the dye in solution. In Figure 5.19 the initial current due to the formation of the double layer and the absorption of any CuPc anions already present at the surface of a nanoparticle seems almost instantaneous. The initial current is also much larger than for previous electrodepositions as the TiO_2 surface area is ~1000x larger than the flat substrates previously used. After this initial rearrangement the current is also influenced by other factors as it is slowly increasing rather than slowly decreasing as would be expected if the process was limited by the diffusion of dye only. The inset in Figure 5.19 shows the current in more detail. A possible explanation is that as the dye diffuses further into the pores, the amount of surface area that CuPc can deposit on increases, resulting in the kinetic set-up of the system constantly changing.

5.3.2 Electronic absorption

The electronic absorption of $1.00x10^{-3}$ Ccm^{-2} CuPc deposited on TiO_2, the blank TiO_2 and a deposition of $1.25x10^{-3}$ Ccm^{-2} CuPc on FTO/PEDOT: PSS are shown in Figure 5.20.

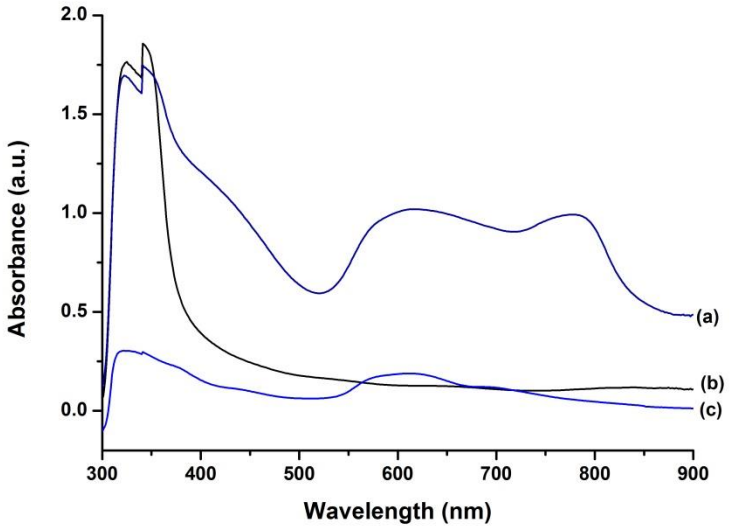

Figure 5.20: Electronic absorption of (a) $1.00x10^{-3}$ Ccm^{-2} of CuPc deposited on TiO_2, (b) Blank TiO_2 and (c) $1.98x10^{-3}$ Ccm^{-2} film of CuPc

Similar to the bilayer in section 5.2.2, the spectrum (a) of the TiO_2 with electrodeposited CuPc is a combination of both TiO_2 and electrodeposited CuPc. It contains a large absorption in the UV range peaking at 335 nm due to the TiO_2 and the CuPc, as well as two peaks at 618 nm and 777 nm due to the CuPc. The peaks of CuPc are red-shifted compared to the film on PEDOT:PSS, spectrum (c), which has two peaks at 609 nm and 690 nm.

It should also be noted that the CuPc deposited on TiO_2 does not become charged during the deposition process. The film comes out of the deposition solution a blue colour, whereas the charged film on PEDOT:PSS was a green colour.

Thicker layers of CuPc at a charge of $1.00x10^{-2}$ Ccm^{-2}, an order of magnitude larger, were deposited onto TiO_2. The deposited films are very thick and therefore no longer transparent and have a very dark colour as shown in Figure 5.21.

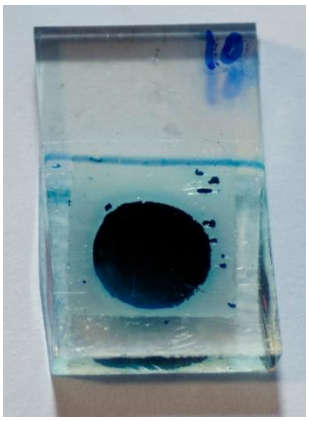

Figure 5.21: Thick electrodeposited layer of $1.00x10^{-2}$ Ccm^{-2} CuPc on TiO_2

A typical electronic absorption spectrum is shown in Figure 5.22.

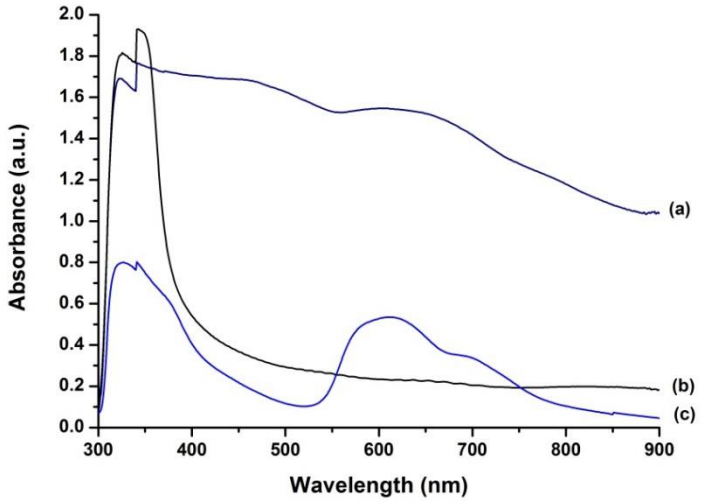

Figure 5.22: Electronic absorption of (a) $1.00x10^{-2}$ Ccm^{-2} of CuPc deposited on TiO_2, (b) Blank TiO_2 and (c) $1.25x10^{-2}$ Ccm^{-2} film of CuPc

Similar to the bilayer in Figure 5.6, the spectrum (a) is a combination of spectra of TiO_2 and CuPc. However, the very dark layer of CuPc is absorbing most of the light and scattering most of the rest. Despite this there is a distinguishable peak between 550 nm and 750 nm where CuPc absorbs normally. It is difficult to distinguish whether the light is being absorbed or scattered as the film of CuPc is probably several micrometres thick as it has possibly filled the TiO_2 pores.

5.3.3 Emission Spectroscopy

Photoluminescence spectroscopy was performed on the TiO_2 and CuPc layers. The resulting spectrum and that of the CuPc film studied in chapter 4 are shown in Figure 5.23.The obtained results were then compared to the emission spectra of the CuPc film studied in chapter 4 and to TiO_2 in literature.[144, 145]

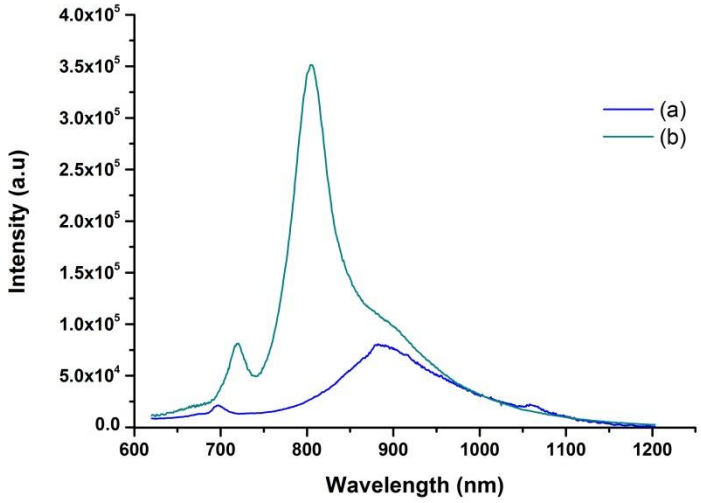

Figure 5.23: Photoluminescence of (a) $2.98x10^{-2}$ Ccm^{-2} of CuPc on PEDOT:PSS and (b) $1.00x10^{-2}$ Ccm^{-2} of CuPc deposited on TiO_2 (excited at 514 nm)

The excitation wavelength used will only excite the CuPc. Therefore all photoluminescence will be due to the CuPc and not the TiO_2. The main photoluminescence of the CuPc electrodeposited on the TiO_2 seems to be a combination of two peaks: a peak at 805 nm and a peak at 883 nm, which appears as a shoulder. There is also a small peak at 720 nm which is probably the result of Raman scattering.[134] This is similar to the CuPc on PEDOT:PSS as seen in chapter 4. The shoulder at 883 nm is identical to the CuPc on PEDOT:PSS film peak, (a), which indicates that not all the excited CuPc molecules deposited on the TiO_2 layer are packed in the same way. The main luminescence peak at 805 nm is blue-shifted compared to the CuPc on PEDOT:PSS, suggesting that the CuPc was templated into and onto the TiO_2 in a packing that allows for less π-π interaction. This is a promising result as the largest luminescence peak is from the CuPc templated on the TiO_2 suggesting that pore penetration has occurred. The strong luminescence of the CuPc on TiO_2 suggests however that any charge separation upon photoexcitation will

not be efficient, because, if it was, any excited electrons would be transferred to the TiO_2 conduction band, resulting in the luminescence being quenched.

5.3.4 Scanning Electron Microscopy

SEM imaging was performed on the CuPc deposited to investigate whether there was any sign of templating due to the TiO_2 nanoparticles or whether it deposited in a similar way as it did on just PEDOT:PSS. A SEM image of $5.00x10^{-2}$ Ccm^{-2} of CuPc electrodeposited on TiO_2 is shown in Figure 5.24.

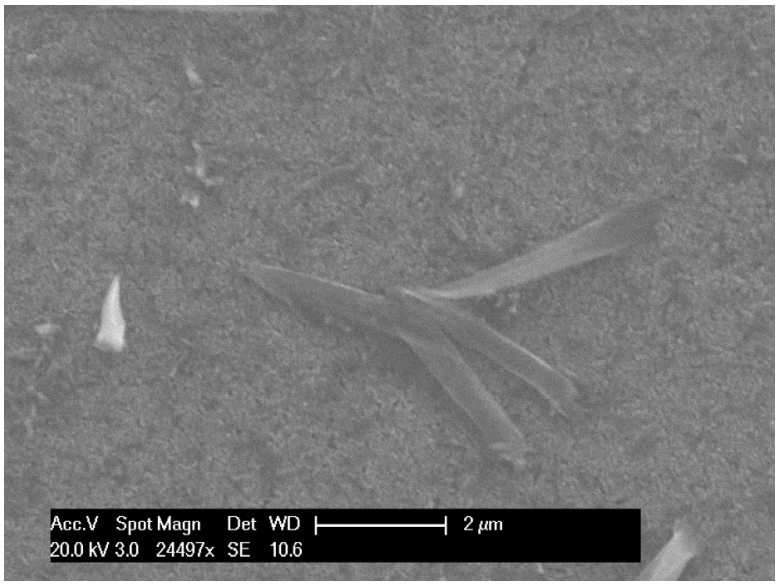

Figure 5.24: SEM image of $5.00x10^{-2}$ Ccm^{-2} of CuPc electrodeposited on TiO_2

The CuPc layer seems to be composed of two parts. Similar to the CuPc on PEDOT:PSS, the main layer of CuPc on the TiO_2 is made up of small crystallites. However, these crystallites are much smaller than the crystallites in films of CuPc electrodeposited on PEDOT:PSS, which are several hundred nanometres in diameter, whereas these are only between ~50 nm and ~100 nm, as shown in Figure 5.25.

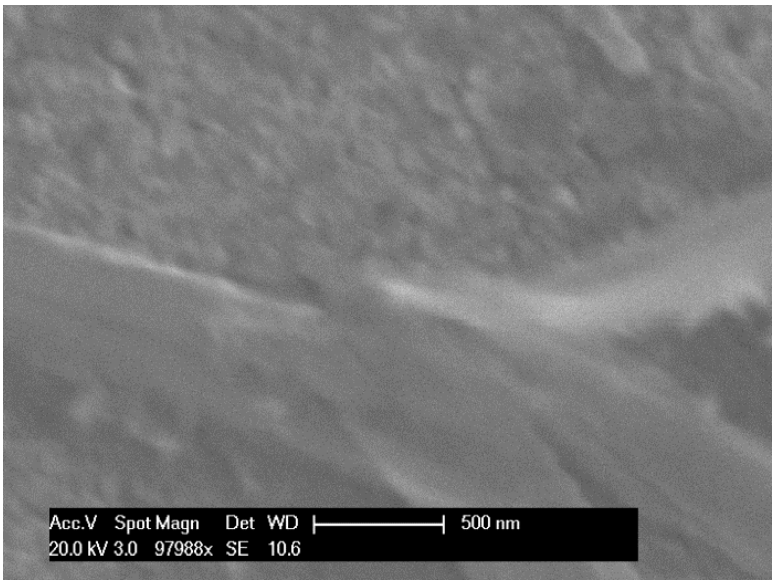

Figure 5.25: SEM of $5.00x10^{-2}$ Ccm^{-2} of CuPc electrodeposited on TiO_2

The crystallites of CuPc are still larger than the nanoparticles of the TiO_2 layer which are approximately 20 nm large.

The second part of the layer is the growth of needle-shaped crystals on the surface of the CuPc crystallite layer. A group of these are present in Figure 5.24. Needles were not present in the films of CuPc on PEDOT:PSS that were investigated, suggesting that they are the result of templating due to the TiO_2 layer resulting in pockets of fast growing CuPc. As these needles were infrequent, they were probably the result of imperfections in the surface of the TiO_2 layer which caused a rapid growth of the CuPc leading to the needle shapes.

An image of the cross section of the film in Figure 5.25 is shown in Figure 5.26.

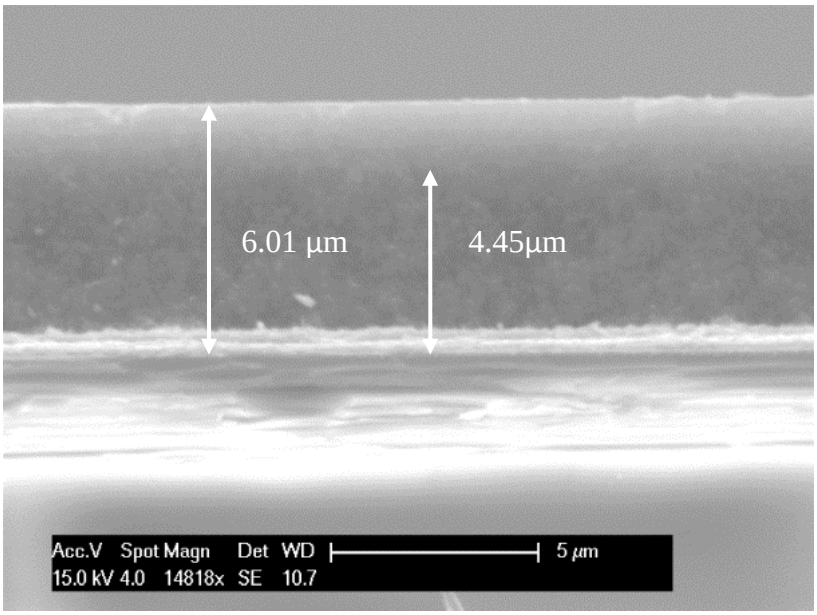

Figure 5.26: Cross section of a $5.00x10^{-2}$ Ccm^{-2} of CuPc electrodeposited onTiO_2

Due to the size similarities of the TiO_2 nanoparticles and the CuPc crystallites, it is not possible to distinguish between the two layers by their structures. However, it is possible to distinguish between the different levels of charging in the layers. From the high level of charging it appears that at least the top few microns of the film are CuPc. The top layer of the film is very light, indicating that it is charged. There is also a light to dark gradient down the first 2 µm of the top of the film, suggesting that there is a good penetration of the CuPc molecules during deposition, resulting in a large surface area between the CuPc and the TiO_2 layers. So, even if the top charging is just due to it being the surface of the film, the gradient is a strong indication that there is dye penetration into the pores rather than just deposition on top.

5.3.5 X-ray diffraction

The crystallinity of the films was measured using thin film XRD. The XRD pattern of a bilayer of TiO_2 with an electrodeposited CuPc layer at a charge of $1.00x10^{-2}$ Ccm^{-2} is shown in Figure 5.27.

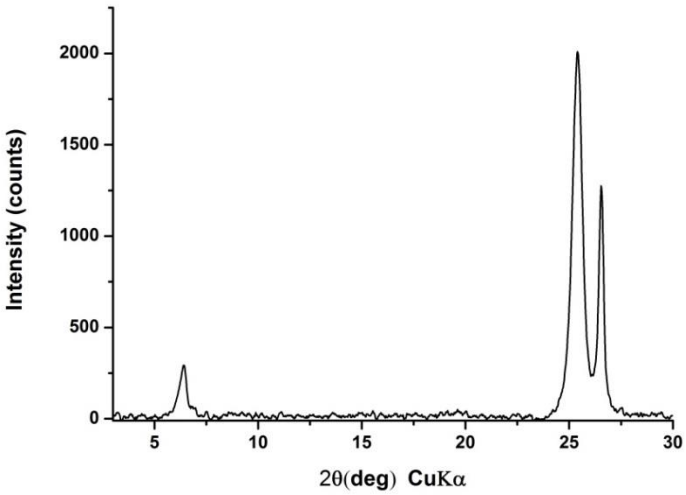

Figure 5.27: XRD pattern of 6 µm TiO_2 with a electrodeposited CuPc layer (Q= $1.00x10^{-2}$ Ccm^{-2})

The XRD pattern contains two very different types of peaks, one at 6.38º, resulting in d-spacings of 13.84 Å and a large peak at 25.39º resulting in a d-spacing of 3.51 Å. The peak at 26.53º is due to the FTO substrate. The large peak at 25.39º corresponds to anatase TiO_2.[146] The small peaks correspond to the CuPc layer. The CuPc peak at 6.38º is sharper than the peak of CuPc on PEDOT:PSS and using the Scherrer equation, Equation 3.20, the average crystal size is 189.4 Å. This is a third of the size of the CuPc on PEDOT:PSS which indicates that some templating has occurred and that some of the CuPc layer is more crystalline due to being deposited onto TiO_2.

5.3.6 Solar cell devices

Solar cell devices were fabricated by evaporating a 100 nm layer of silver onto the TiO_2 with two charges of electrodeposited CuPc of $Q=1.00x10^{-3}$ Ccm^{-2} and $Q=5.00x10^{-3}$ Ccm^{-2}. Since a template was not applied during the electrodeposition it would have resulted in CuPc covering the entire 3D structure of the TiO_2, as shown in Figure 5.28, making a channel down the side which would result in the devices short-circuiting.

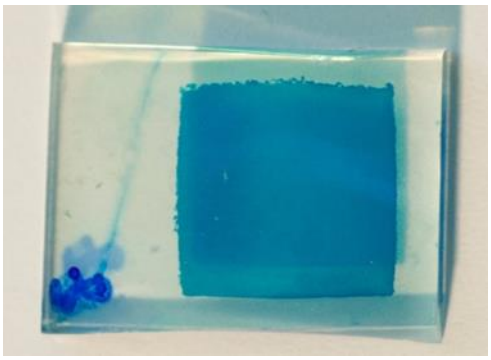

Figure 5.28: Thick electrodeposited layer of $1.00x10^{-3}$ Ccm^{-2} CuPc on 6 µm of TiO_2

To avoid short-circuiting the edge of the TiO_2 layer was scratched off to remove any CuPc deposited down the side.

One of the devices with a CuPc layer with a charge of $1.00x10^{-3}$ Ccm^{-2} showed a photovoltaic response when tested, as shown in Figure 5.29.

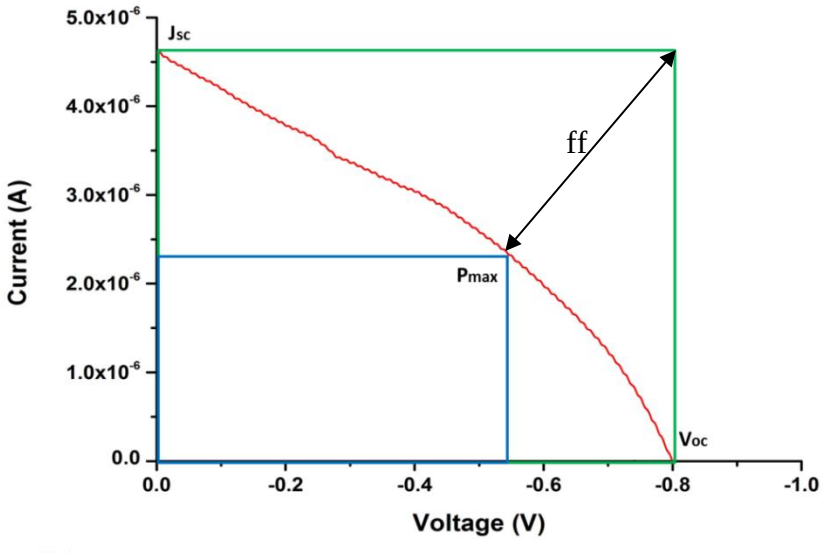

Figure 5.29: Illuminated I-V Sweep Curve

Using the values obtained from Figure 5.29 an efficiency of 0.024 % was calculated for the device based on the data in Table 5.6.

Table 5.6

V_{oc} (mV)	I_{sc} (mA)	ff	Efficiency
798.7	$4.00x10^{-3}$	0.37	0.024%

The cell has quite a high open circuit potential, but a low short-circuit current and a low fill factor which results in the low efficiency. The photovoltaic measurements of the other devices are shown in Figure 5.30.

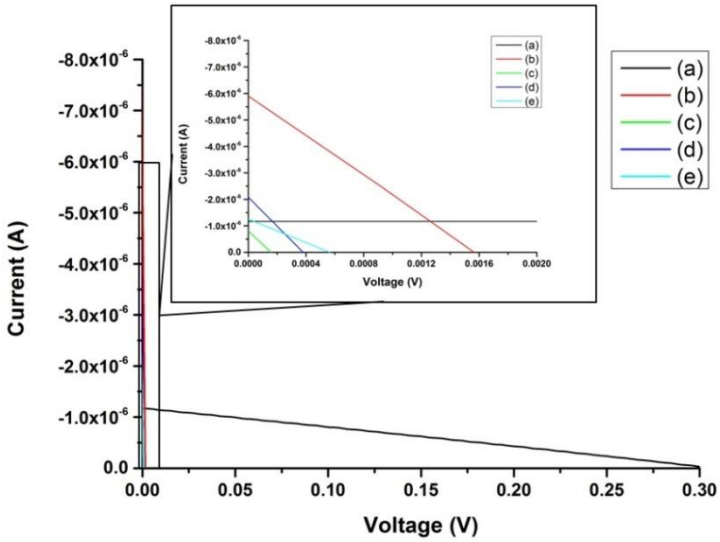

Figure 5.30: I-V characteristics of a TiO_2 with a layer of (a) Q=1.00x10^{-3} Ccm^{-2}, (b) Q= 5.00x10^{-3} Ccm^{-2}, (c) Q=5.00x10^{-3} Ccm^{-2}, (d) Q=5.00x10^{-3} Ccm^{-2} and (e) Q=5.00x10^{-3} Ccm^{-2} CuPc under AM 1.5

The devices all show a negligible photovoltaic response with the exception of (a) which shows a response of 0.01 % based on the data in Table 5.7.

Table 5.7

V_{oc} (mV)	I_{sc} (mA)	ff	Efficiency
309.9	1.17x10^{-3}	0.26	0.01 %

The results are consistent with the luminescence results seen in section 5.3.3 which showed poor charge separation. This suggests that the devices are not suitable for use in solar cells.

5.4 Conclusion

The technique shows some promise in the deposition of bilayers. The BuPTCDI successfully deposited onto the CuPc layer, suggesting that the technique can be used to deposit bilayers. However, the layer of BuPTCDI deposited in stacks, making the top layer porous. This made the bilayer unsuitable for photovoltaic devices.

The bilayer of the deposited CuPc on TiO_2 layers showed promising results as the deposition current, the emission spectroscopy results and the SEM images suggest that the CuPc layer penetrated into the pores of the TiO_2 layer rather than just being deposited on top of it. Although the interface between the two layers did not result in good charge transfer, the method could be used to electrochemically deposit materials into porous conductive semiconductors which would result in better charge transfer properties between the two materials.

5.5 Experimental

The following methods were used in the preparation for the substrates for electrodeposition.

Poly(3,4-ethylenedioxythiophene) poly(styrenesulfonate) glass substrates

Poly(3,4-ethylenedioxythiophene) poly(styrenesulfonate) (PEDOT:PSS) dispersed in water was spun onto the cleaned glass at an initial rate of 1000 rpm for 15 seconds followed by a faster speed of 3000 rpm for 30 seconds.

Titanium Dioxide nanoporous film

The cleaned glass was treated with a dilute $TiCl_4$ solution (40 nM, 80º C for 30 minutes), rinsed with water and then ethanol. The mesoporous TiO_2 layer (20 nm particles) was doctor bladed onto the FTO. This layer was levelled using ethanol and heated to 125º C on a hotplate (covered for 5 minutes and then uncovered for 2 minutes). The film was then heated up to 510º C stepwise on a controllable hotplate, left to cool down to room temperature and treated with the $TiCl_4$ solution again and sintered for 30 minutes at 500º C.

Silver layers

Layers of silver (~100 nm) were deposited using a Multi Pocket Electron Beam Evaporator EBE-4.

Solar Cell Efficiency

Solar cell efficiency data was collected using a solar simulator equipped with an AM 1.5G filter and a Keithley Source meter with a four wire set-up.

The overall efficiency is related to the amount of power produced compared to the amount of power put in, as shown in Equation 2.17:

$$\eta = \frac{P_{out}}{P_{in}}$$

Equation 2.17

A typical IV curve is shown in Figure 2.17.

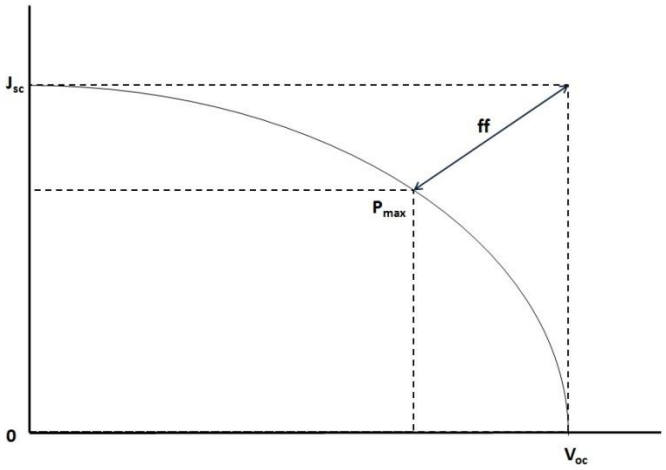

Figure 2.17: Schematic of the IV curve produced during a solar cell measurement

However, normally more factors are taken into account, as shown in Equation 2.18.

$$\eta = \frac{J_{sc} V_{oc} ff}{P_{in}}$$

Equation 2.18

where J_{sc} is the short circuit current density, V_{oc} is the open-circuit potential when no current is flowing and ff is the fill factor and is calculated by the ratio of power generated in the cell at the maximum power point (p_{max}) against the theoretical maximum power output. Using these values a better breakdown of the solar cell's performance can be estimated.

6. Electrodeposition of metal dithiolene complexes

6.1 Introduction

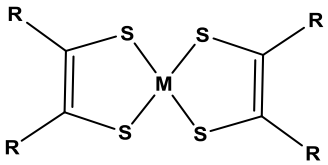

Figure 6.1: Metal dithiolene complex

Dithiolene complexes, Figure 6.1, have been investigated for their use as materials for electronic components since the early 1960s.[147] The molecule's large chain of sulfur-enriched carbon with alternating double and single bonds makes it ideal for charge transport if it is packed in a way that results in a strong intermolecular interaction. The molecule can be easily tailored for specific use by changing the central metal and side groups.

The stability of any redox processes due to the resonance forms of the metal dithiolene centre, as shown in Figure 6.2, and the large π system that results in charge transport also make the dithiolenes good candidates for electrodeposition. The redox-stable large π system of electrodeposited material should be less soluble in the electrolyte solution and therefore should not dissolve off the substrate.

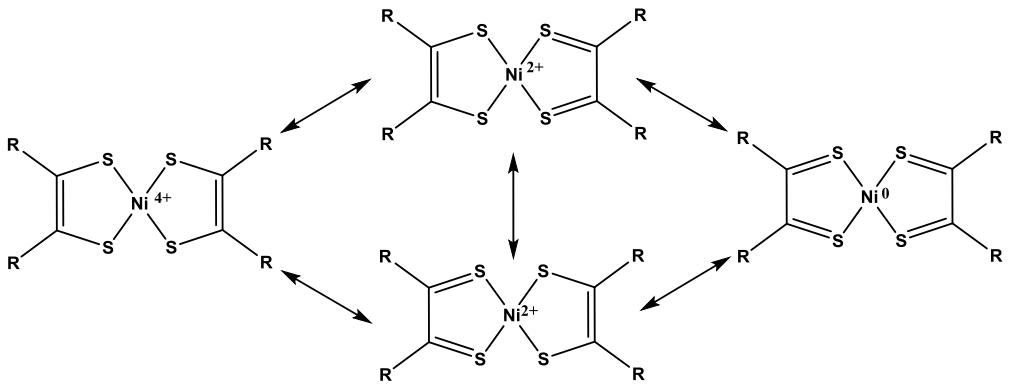

Figure 6.2: Resonance forms of a symmetrical neutral nickel dithiolene [148]

The electrochemical deposition of neutral dithiolene films has been investigated by Simon Dalgleish, a previous member of the research group, and led to two discoveries.

The first is that the electrodeposited neutral Ni(b-3ted)$_2$, Figure 6.3 was more crystalline than solution-processed films and therefore the conductivity was higher.[80]

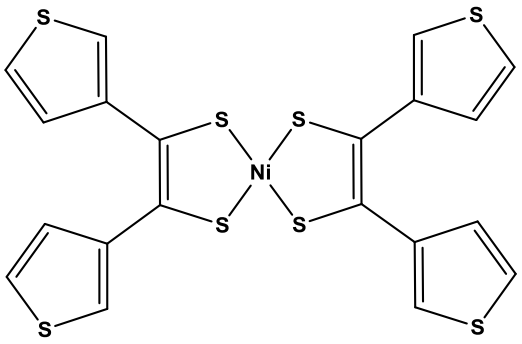

Figure 6.3: Nickel (bis(3-thienyl)-1,2-ethylenedithiolene)$_2$, Ni(b-3ted)$_2$ [80]

The second is that a thin film of neutral Cu(mi-5hdt)$_2$, Figure 6.4, was deposited during the study of the electrochemical properties of the anionic copper dithiolene salt.[81]

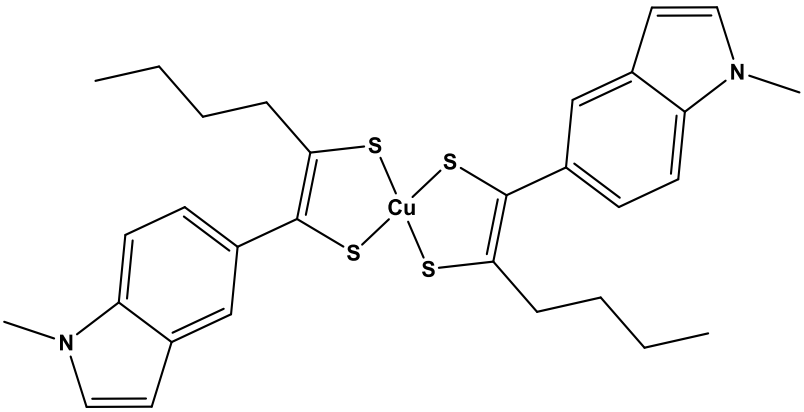

Figure 6.4: Copper (4-Butyl-5-(1-methyl-5-indol-5-yl)-[1,3]dithiol-2-one)$_2$, Cu(mi-5hdt)$_2$ [81]

Anionic copper dithiolenes are quite common and have been studied as part of several series of dithiolenes.[149, 150] Unfortunately neutral copper dithiolene salts can be difficult to synthesise as they are unstable in solution and therefore impossible to isolate by chemical methods.[82] However, the films formed during electrodeposition were stable and offer the chance to investigate the properties of the neutral complex which was found to absorb in the infrared area of the spectrum, as shown in Figure 6.5.

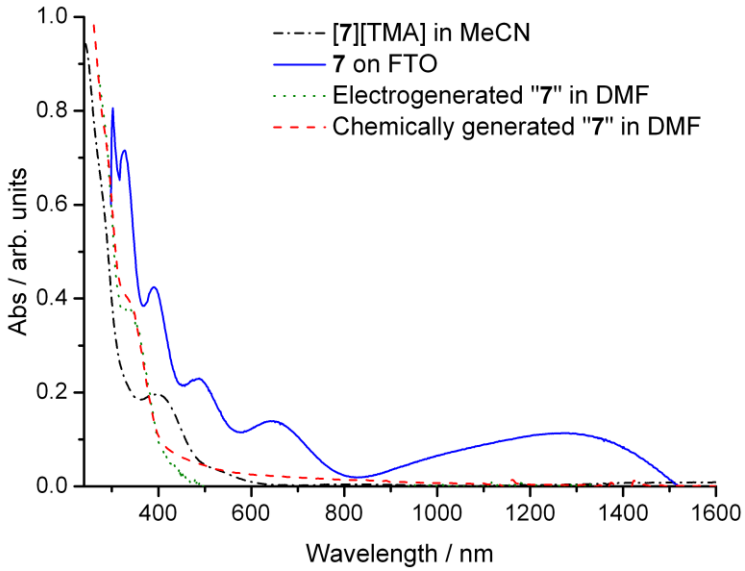

Figure 6.5: Experimental and calculated UV/Vis/NIR spectroscopy of an electrodeposited film of Cu(mi-5hdt)2 (labelled as 7) on FTO [81]

During this project a nickel dithiolene salt was used to investigate the suitability and conditions needed to electrodeposit the neutral analogue of the complex onto FTO and interdigitated electrode substrates so as to investigate the optical, charge transport and magnetoresistive properties of the neutral nickel dithiolenes. Having established a method for nickel, the copper dithiolene analogue was synthesised and films of the neutral copper complex were deposited using this method. The optical, charge transport and magnetoresistive properties of the neutral copper complex were then also investigated and compared with the nickel complex. These complexes were designed to show a more planar structure, giving stronger intermolecular interactions, compared with those studied by Dalgleish. To achieve this, the molecular design included one substituent on each ligand with one H-atom at the other position. This should minimise the torsional twist of the end groups and enhance planarity.

6.2 Electrodeposition

Two transition metal dithiolene salt complexes were synthesised to investigate the isolation of the neutral molecule by electrodeposition.

TMA copper (2-(5-butylthiophene-2-yl)-1,2-dithiolene)$_2$, TMA[Cu(Ti-C2)$_2$], shown in Figure 6.6, was synthesised to investigate whether the neutral copper dithiolene could be isolated by electrodeposition.

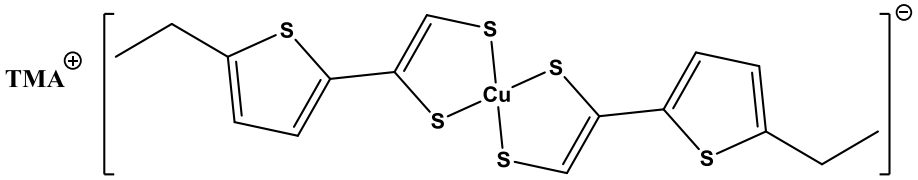

Figure 6.6: TMA copper (2-(5-butylthiophene-2-yl)-1,2-dithiolene)$_2$

The nickel analogue, TBA nickel (2-(5-butylthiophene-2-yl)-1,2-dithiolene)$_2$, TBA[Ni(Ti-C2)$_2$], Figure 6.7, was investigated as a comparison.

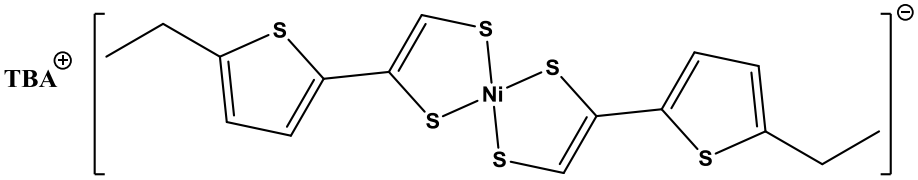

Figure 6.7: TBA nickel (2-(5-butylthiophene-2-yl)-1,2-dithiolene)$_2$

The chemically synthesised Ni(Ti-C2)$_2$ complex was investigated for potential solution processing, but the limited solubility of the resulting neutral complex meant that it was difficult to process in solution, as expected, and therefore the properties of the solution-processed films were not investigated further. This underlines the importance of the electrodeposition approach to the processing of such materials.

Both metal dithiolene salt complexes when reduced would give the neutral complex, resulting in the simplified molecular orbital energies shown in Figure 6.8.

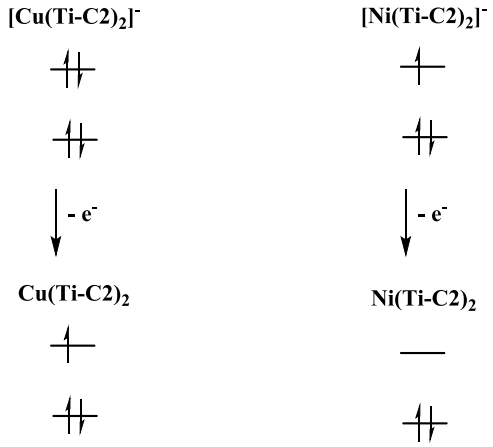

Figure 6.8: Molecular orbital energies of the (left) charged and neutral copper dithiolene complex and (right) charged and neutral nickel dithiolene complex

6.2.1 Electrochemistry

The redox properties of TMA[Cu(Ti-C2)$_2$] and TBA[Ni(Ti-C2)$_2$] were investigated by cyclic voltammetry to find the potential needed for electrodeposition by chronocoulometry. Cyclic voltammograms of TMA[Cu(Ti-C2)$_2$] and TBA[Ni(Ti-C2)$_2$] are shown in Figure 6.9.

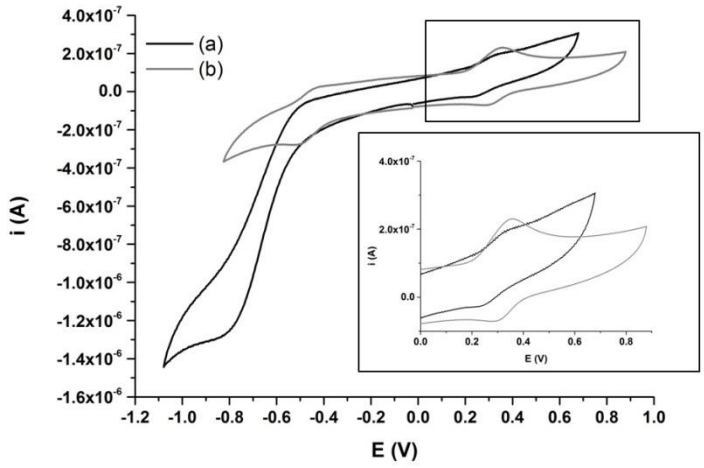

Figure 6.9: Cyclic voltammograms of (a) TMA[Cu(Ti-C2)$_2$] and (b) TBA[Ni(Ti-C2)$_2$] in 0.3 M TBABF$_4$ in CHCl$_2$

The cyclic voltammogram of TMA[Cu(Ti-C2)$_2$], (a), contains two redox processes at E_{peak}=-0.74 V (irreversible) and $E_{½}$=0.31 V (reversible), which are $[Cu(Ti\text{-}C2)_2]^{-2/-1}$ and $[Cu(Ti\text{-}C2)_2]^{-1/0}$ redox couples respectively. Similar to the copper complex the

cyclic voltammogram of TBA[Ni(Ti-C2)$_2$], (b), contains two redox processes at $E_{½}$=-0.47 V and $E_{½}$=0.34 V (both reversible), which correspond to [Ni(Ti-C2)$_2$]$^{-2/-1}$ and [Ni(Ti-C2)$_2$]$^{-1/0}$ redox couples.

6.2.2 Electrochemical deposition

6.2.2.1 Electrodeposition onto FTO substrates

The electrodeposition of the dithiolene complexes was investigated in acetonitrile, as the dithiolene salts were soluble and the neutral dithiolene complexes were less likely to be soluble since acetonitrile is more polar than DCM. It was also the solvent used in the electrodeposition of Ni(b-3ted)$_2$ in the initial investigation.[80]

Several potentials above E_{ox}=0.31 V for the Cu(Ti-C2)$_2$ and E_{ox}=0.34 V for the Ni(Ti-C2)$_2$ were investigated for the electrodeposition of both complexes. Depositions were attempted at 1.06 V, 0.96 V, 0.86 V and 0.76 V for both films to investigate the potential needed to electrodeposit from a solution with a dithiolene salt concentration of approximately 5x10^{-4} mol dm^{-3} in MeCN. Deposition at 1.06 V resulted in black fibres rather than a uniform film for Ni(Ti-C2)$_2$. Uniform films occurred at 0.96 V for the Cu(Ti-C2)$_2$ and at 0.86 V for the Ni(Ti-C2)$_2$. Typical depositions of Cu(Ti-C2)$_2$ at 0.96 V, (a), and Ni(Ti-C2)$_2$ at 0.86 V, (b), in 0.1M TBABF$_4$ MeCN electrolyte are shown in Figure 6.10.

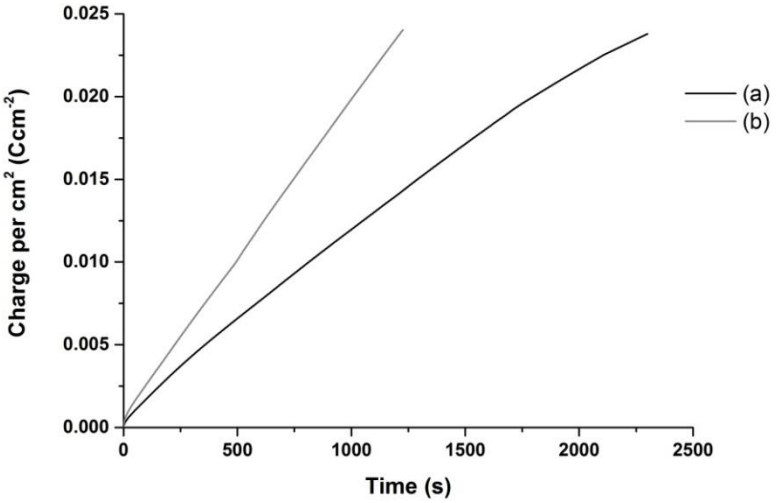

Figure 6.10: Deposition of 2.40x10^{-2} Ccm^{-2} of (a) Cu(Ti-C2)$_2$ at 0.96 V and (b) Ni(Ti-C2)$_2$ at 0.86 V

The charge per cm^2 of the deposition of the films of $Cu(Ti\text{-}C2)_2$ and $Ni(Ti\text{-}C2)_2$ onto FTO continues to rise steadily with time suggesting that both dithiolene films are conductive and transport the current to the surface of the formed film. More details can be extrapolated from the plot of the charge per cm^2 against the square root of time, as shown in Figure 6.11.

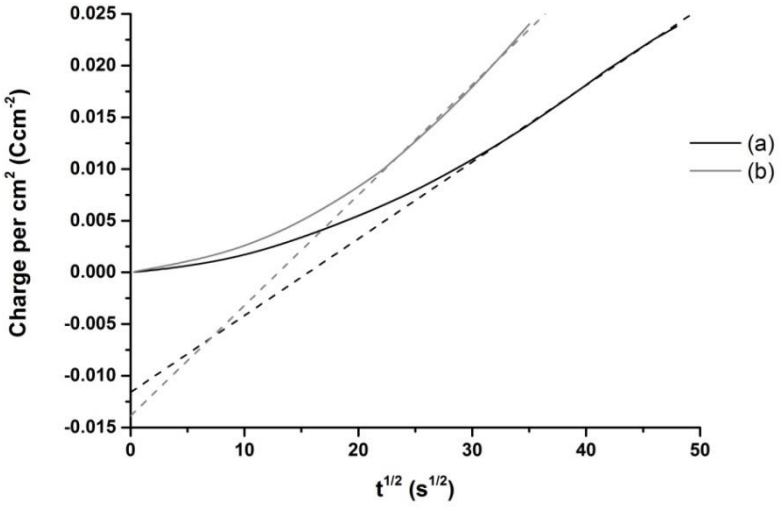

Figure 6.11: Typical charge per cm^2 against $t^{½}$ of (a) $Cu(Ti\text{-}C2)_2$ and (b) $Ni(Ti\text{-}C2)_2$

The plot of charge per cm^2 against $t^{½}$ of both films contains a linear region with a line of best fit that intercepts the y-axis at a negative value. These values indicate that both depositions happen in two stages. The linear region indicates that at that point the deposition is diffusion-controlled.

The negative intercept of the line is an indication that initially the kinetics of the electron transfer are also influencing the rate of deposition. This suggests that the initial rate of deposition is mixed controlled, influenced by both the diffusion of the anions and the changes in electron transfer conditions due to the formation of the double layer during the first few seconds and the change in kinetic conditions during the formation of a film of deposited molecules. This suggests that the nucleation of the dithiolenes is less energetically favourable than deposition onto already deposited molecules. After the kinetics of the film stabilise the deposition becomes diffusion-controlled. This is confirmed by the currents observed for both depositions in Figure 6.12.

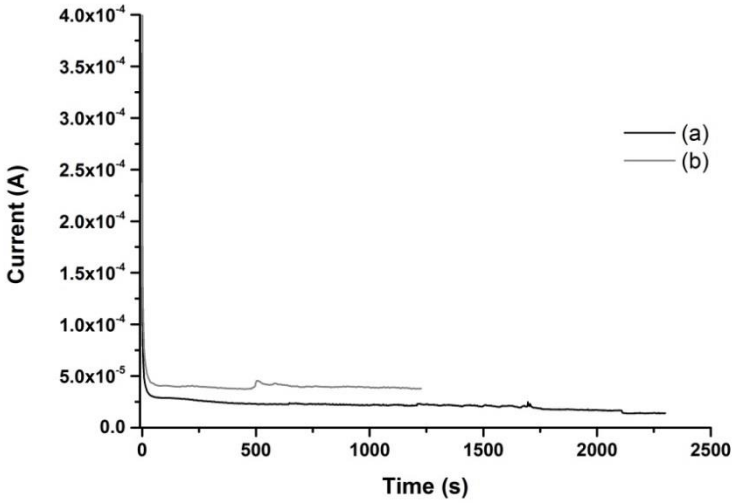

Figure 6.12: Deposition current of $2.40x10^{-2}$ Ccm^{-2} of (a) $Cu(Ti\text{-}C2)_2$ and (b) $Ni(Ti\text{-}C2)_2$

The initial current is very large due to the formation of the double layer and the initial absorption of any dithiolene monoanions present at the surface of the FTO substrate. It then decreases rapidly until it levels off and becomes approximately linear, decreasing very slowly which indicates that the formation of the film is diffusion dependent. This is probably due to the formation of a continuous layer of neutral complex on the substrate surface, since as mentioned, the deposition of molecules onto already deposited molecules is more energetically favourable than the nucleation of molecules on the substrate surface. The rate of deposition stays constant until the depletion of anions close to the film, at which point it becomes diffusion-dependent.

6.2.2.2 Field Effect Transistor (FET) Electrodeposition

The electron transport properties of the films were investigated by electrodepositing the dithiolene monoanions onto interdigitated electrodes to allow measurements of conductivity and to obtain field effect transistors. Typical deposition plots of $Cu(Ti\text{-}C2)_2$ and $Ni(Ti\text{-}C2)_2$ onto 8μm x 8μm interdigitated electrodes are shown in Figure 6.13. Higher potentials were required as films were not obtained at 0.96 V and 0.86 V.

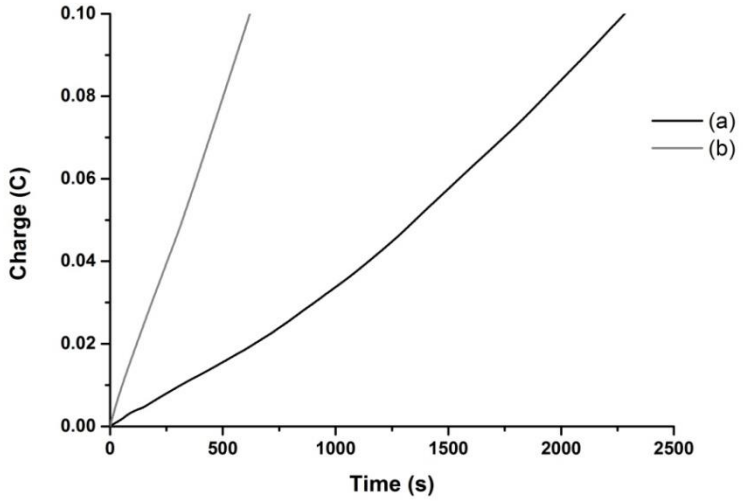

Figure 6.13: Deposition of a charge of 0.1 C on 8 μm x 8 μm interdigitated electrodes of (a) $Cu(Ti\text{-}C2)_2$ held at 1.16 V and (b) $Ni(Ti\text{-}C2)_2$ held at 1.26 V

The plots of charge against time increase almost linearly over time. The initial rate of deposition of the $Cu(Ti\text{-}C2)_2$, (a), is slow but after about 1000 seconds it increases, probably because of the increased surface area due to the film bridging the interdigitated electrodes. The rate of deposition of the $Ni(Ti\text{-}C2)_2$, (b), is faster, making any changes difficult to distinguish. More information can be inferred from the deposition currents against time shown in Figure 6.14.

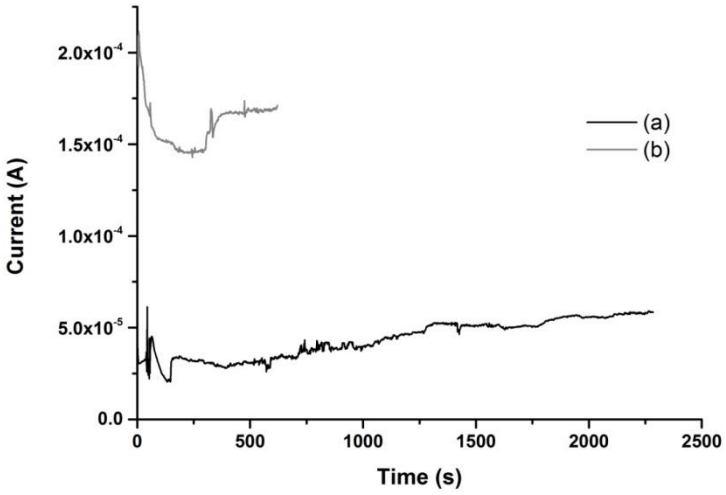

Figure 6.14: Current of deposition of a charge of 0.1 C on 8 µm x 8 µm interdigitated electrodes of (a) $Cu(Ti\text{-}C2)_2$ held at 1.1 V and (b) $Ni(Ti\text{-}C2)_2$ held at 1.2 V

The initial currents are typical for an electrodeposition. They begin large due to the formation of the double layer and the absorption of any dithiolene molecules at the surface of the substrate. They then decrease rapidly and level off as the depositions become diffusion controlled. However, there is an increase in current after 400 seconds for $Cu(Ti\text{-}C2)_2$ and 300 seconds for $Ni(Ti\text{-}C2)_2$ which is probably due to the growth in area of deposition as the dithiolene molecules start to bridge over the non-conductive part of the substrate, enlarging the surface area. Another possibility is that the type of film depositing has changed as discussed below. An image of the $Ni(Ti\text{-}C2)_2$ FET is shown in Figure 6.15.

Figure 6.15: Film of $Ni(Ti\text{-}C2)_2$ on 8 µm x 8 µm interdigitated electrodes

From this it is possible to see two types of deposited layers: a uniform layer covering the conducting part of the substrate, which appears brown in the photo, and several small black crystals. These different types of deposition could account for the two different currents observed.

6.2.3 Electronic Absorption

6.2.3.1 Electronic Absorption of Copper dithiolene salt

The absorbance of several concentrations of TMA[Cu(Ti-C2)$_2$] salt in MeCN was measured by UV/Vis spectroscopy at 298 K and is shown in Figure 6.16.

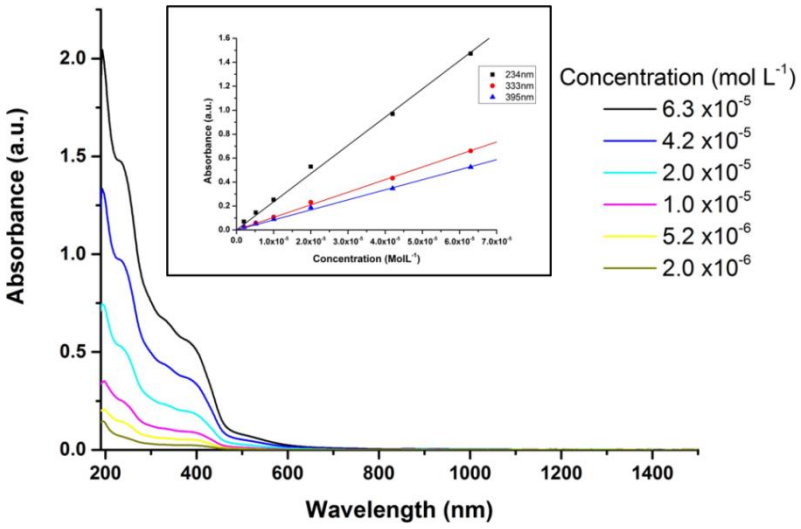

Figure 6.16: Electronic absorption spectra of several concentrations of TMA[Cu(Ti-C2)$_2$] salt in MeCN. Inset: Beer-Lambert plot of the absorbance maxima against concentration

The maximum of the absorption occurs between 200 nm and 400 nm, with weaker absorptions also in blue and green and no absorption past 600 nm, meaning that the sample does not absorb past the orange part of the spectrum. The main absorption of the complex appears to be in the UV region of the electromagnetic spectrum with shoulder peaks at 234 nm, 333 nm and 395 nm. The molar extinction coefficients of these shoulders were calculated from the Beer-Lambert plot of absorption maxima against concentration (Figure 6.16 insert) and are shown in Table 3.1.

Table 6.1: Molar extinction coefficients of TMA[Cu(Ti-C2)$_2$]

λ_{max} (nm)	$\tilde{\nu}$ (cm^{-1})	ε (M^{-1}cm^{-1})
234	43000	23500
330	30000	10500
395	25300	8400

6.2.3.2 Electronic Absorption of Cu(Ti-C2)$_2$ films

The electronic absorptions of the electrodeposited films at several charge densities were measured and are shown in Figure 6.17.

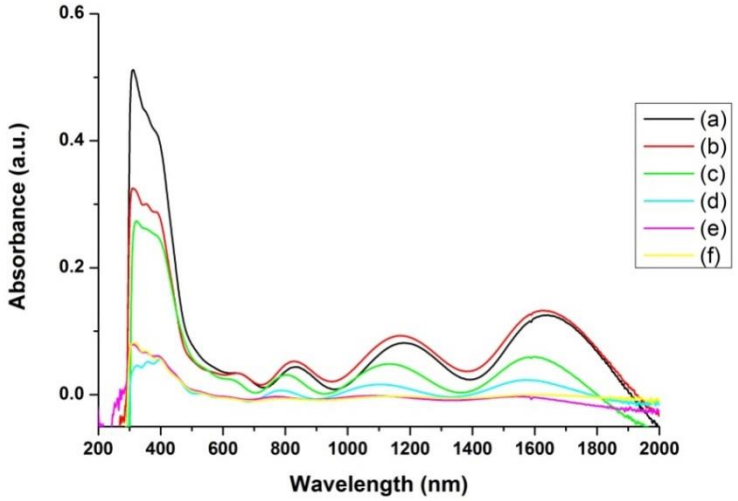

Figure 6.17: Electronic absorption of Cu(Ti-C2)$_2$ films: (a) 5.68x10^{-2} Ccm^{-2}, (b) 4.35x10^{-2} Ccm^{-2}, (c) 2.38x10^{-2} Ccm^{-2}, (d) 5.80x10^{-3} Ccm^{-2}, (e) 2.94x10^{-3} Ccm^{-2} and (f) 2.30x10^{-3} Ccm^{-2}

The films show similar absorptions to the TMA[Cu(Ti-C2)$_2$] in solution, between 300 nm and 600 nm, although red-shifted in a similar way to the other electrodeposited complexes. However, there are also three absorptions in the IR region of the electromagnetic spectrum at 830 nm, 1170 nm and 1628 nm for higher charges per cm^2, with faint absorptions in the thinner films. The presence of these two NIR peaks and one MIR peak confirms that the neutral Cu(Ti-C2)$_2$ has been formed as this complex is now isoelectronic with the near-IR absorbing monoanionic [Ni(Ti-C2)$_2$]$^-$ complex.

The peaks are also very broad covering the range of 800 nm to 2000 nm compared to the previously electrodeposited neutral Cu(mi-5hdt)$_2$ in Figure 6.5, which had a peak from 800 nm to 1500 nm.[81] This is probably due to these compounds only having one heterocycle on each ligand, compared to the previous compound which contained an alkyl chain, as shown in Figure 6.4, which interfered with π-π stacking due to the torsional twist of the end groups.

6.2.3.3 Electronic Absorption of Ni(Ti-C2)$_2$ films

The electronic absorptions of a few of the electrodeposited Ni(Ti-C2)$_2$ films are shown in Figure 6.18.

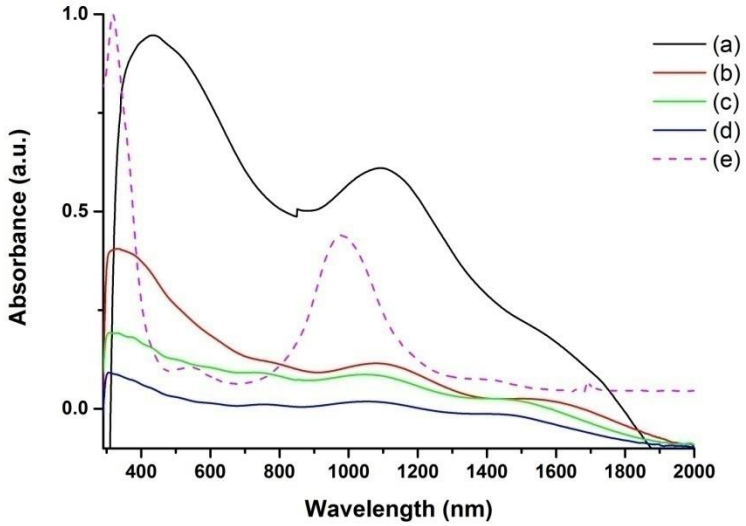

Figure 6.18: Electronic Absorption of Ni(Ti-C2)$_2$ films: (a) 1.54x10^{-1} Ccm^{-2}, (b) 6.38x10^{-2} Ccm^{-2}, (c) 3.85x10^{-2} Ccm^{-2}, (d) 2.40x10^{-2} Ccm^{-2} and (e) TBA[Ni(Ti-C2)$_2$] in DCM

Table 6.2: Peak positions of the films in Figure 6.18

Film (Ccm^{-2})	Peak Positions (nm)			
2.40x10^{-2} (a)	305	758	1051	1455
3.85x10^{-2} (b)	305	757	1050	1464
6.38x10^{-2} (c)	319	786	1091	1556
1.54x10^{-1} (d)	434		1095	1668
Solvent (e)	316	551	980	

The electronic absorption of the thinner neutral films on FTO has peaks at 305 nm, 758 nm, 1051 nm and 1455 nm for the thinnest film, (a). The electronic absorption of

the neutral films has a new band at low energy implying a new strong intermolecular interaction. Apart from the broad peak at around 300 nm, all the other peaks have red-shifted and become broader, attributed to π-π stacking. Similar to the $Cu(Ti\text{-}C2)_2$ the absorption peaks are very wide due to the extensive π-π stacking network formed.

Films with a low charge per cm^2, less than $5.00x10^{-2}$ Ccm^{-2}, have similar peak positions, with the exception of the last peak at around 1400 nm, whereas for the thicker films the peaks start to red-shift with increasing thickness, probably due to the increase in the extensive π-π stacking.

The peak at around 500 nm is not present in the sample in solution suggesting that it is due to π-π stacking of the molecules in the solid state.

6.2.3.4 Comparison of Electronic Absorptions of the neutral complexes with the monoanionic complexes

The stability of the neutral molecules of both films dissolved from the FTO into DCM was compared with the monoanionic salt, as shown in Figure 6.19 and Figure 6.20.

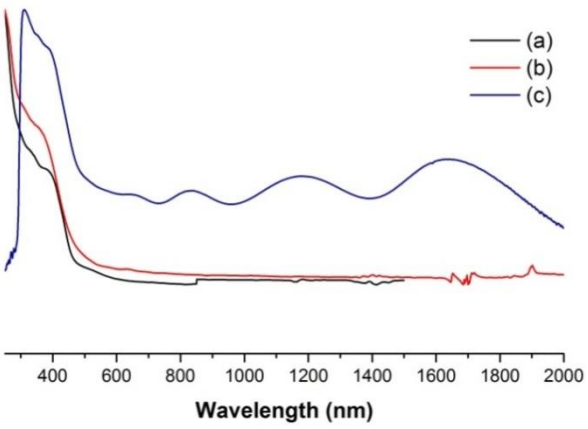

Figure 6.19: Normalised electronic absorption of (a) $TMA[Cu(Ti\text{-}C2)_2]$ in DCM, (b) $Cu(Ti\text{-}C2)_2$ in DCM and (c) $Cu(Ti\text{-}C2)_2$ on FTO

From the electronic absorption of the anionic form of the $TMA[Cu(Ti\text{-}C2)_2]$ in solution, (a), and the neutral $Cu(Ti\text{-}C2)_2$ on FTO, (c), it appears that the solution that

contained the neutral $Cu(Ti\text{-}C2)_2$ contains the monoanionic $[Cu(Ti\text{-}C2)_2]^-$ or only a decomposition product, which agrees with previous data that the neutral molecule is not stable in solution. This confirms that electrodeposition is a unique way to obtain the neutral, NIR-absorbing $Cu(Ti\text{-}C2)_2$ which is on the FTO.

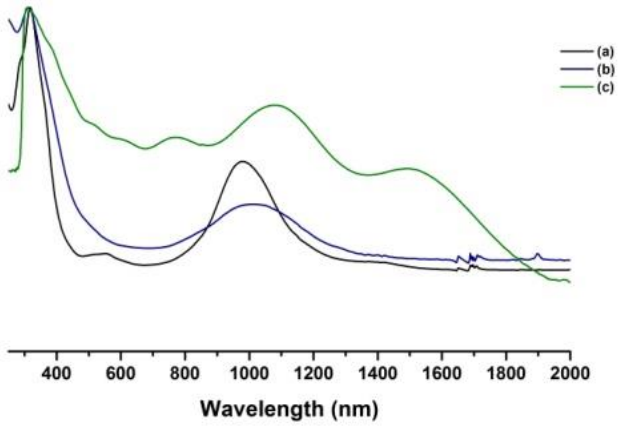

Figure 6.20: Normalised electronic absorption of (a) TBA[$Ni(Ti\text{-}C2)_2$] in DCM, (b) $Ni(Ti\text{-}C2)_2$ in DCM and (c) $Ni(Ti\text{-}C2)_2$ on FTO

The absorption of the neutral $Ni(Ti\text{-}C2)_2$ in solution contains two peaks at 316 nm and 1007 nm, one less than the TBA[$Ni(Ti\text{-}C2)_2$], which contains peaks at 316 nm, 551 nm and 980 nm. The red-shifting and broadening of the peak in the near IR region is probably due to aggregation of the poorly-soluble $Ni(Ti\text{-}C2)_2$ in solution causing the higher baseline and scattering. The extra low energy absorption peak and the broadening of the peaks in the film compared to both species in the solution is due to intermolecular interaction. This is because of the design of the $Ni(Ti\text{-}C2)_2$ which packs better than the $Ni(b\text{-}3ted)_2$ resulting in much stronger intermolecular interaction.

6.2.4 X-ray diffraction

The crystallinity of the film was measured using thin film XRD. Typical XRD patterns of $Cu(Ti\text{-}C2)_2$ and $Ni(Ti\text{-}C2)_2$ films on FTO are shown in Figure 6.21.

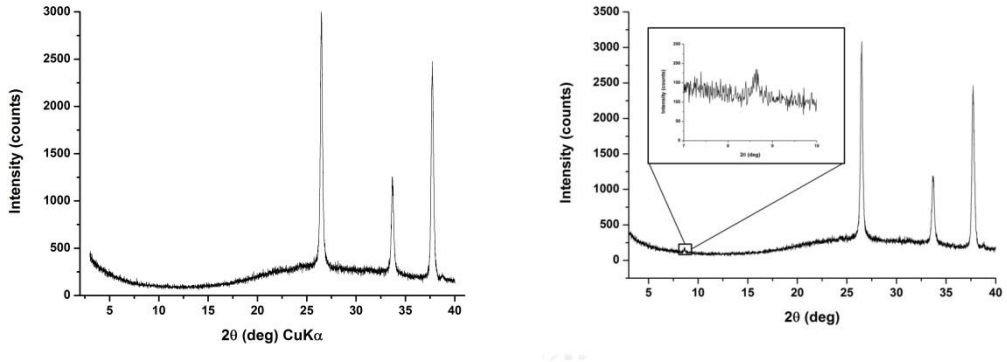

Figure 6.21: XRD patterns of electrodeposited (left) $Cu(Ti\text{-}C2)_2$ film and (right) $Ni(Ti\text{-}C2)_2$ film

The patterns show that $Cu(Ti\text{-}C2)_2$ films and $Ni(Ti\text{-}C2)_2$ films are not very crystalline with the three peaks between 25º and 40º caused by the FTO surface. The $Ni(Ti\text{-}C2)_2$ contains a small peak at 8.6º due to the film, which would correspond to a spacing of 10.6 Å. However, this peak is not very pronounced and was not consistently observed in repeat measurements on several films, which suggests that both types of film are amorphous and that any features present are not large enough to give a strong signal. The amorphous character is clearly different from the very crystalline films observed by Dalgleish for $Ni(b\text{-}3ted)_2$.

6.2.5 Scanning Electron Microscopy

6.2.5.1 Films on FTO conducting glass

SEM imaging of several films of $Cu(Ti\text{-}C2)_2$ and $Ni(Ti\text{-}C2)_2$ was performed and typical images of the surface of the films are shown in Figure 6.22 and Figure 6.23.

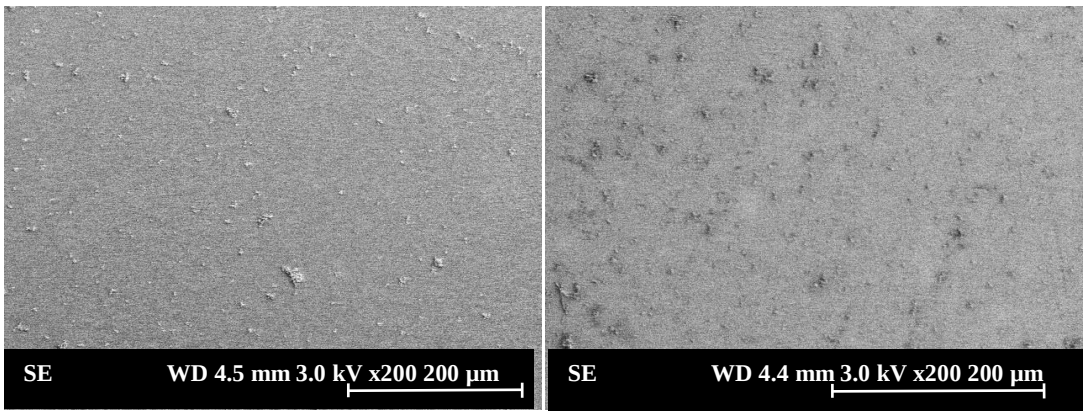

Figure 6.22: SEM images of electrodeposited (left) $Cu(Ti\text{-}C2)_2$ and (right) $Ni(Ti\text{-}C2)_2$

At low magnification the films of $Cu(Ti\text{-}C2)_2$ and $Ni(Ti\text{-}C2)_2$ appear to be composed of two parts: a continuous lower layer with several features on the surface. The lower layers appears continuous and does not seem to contain any large holes or pores. This is very similar to the way in which CuPc electrodeposited onto the surface of PEDOT: PSS, suggesting that the features are probably due to areas of fast depositing material. A higher magnification of the lower layer layers of films are shown in Figure 6.23.

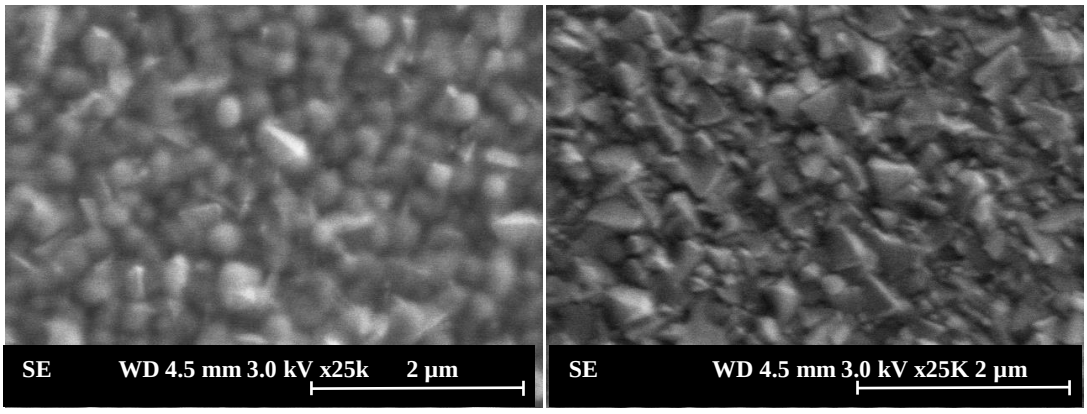

Figure 6.23: SEM images of the features of (left) $Cu(Ti\text{-}C2)_2$ and (right) $Ni(Ti\text{-}C2)_2$

The continuous films of both $Ni(Ti\text{-}C2)_2$ and $Cu(Ti\text{-}C2)_2$ contain features of between 50 nm and 500 nm in size.

6.2.5.2 Interdigitated electrode substrates

SEM imaging of the interdigitated electrodes was performed and the results are shown in Figure 6.24 and Figure 6.25.

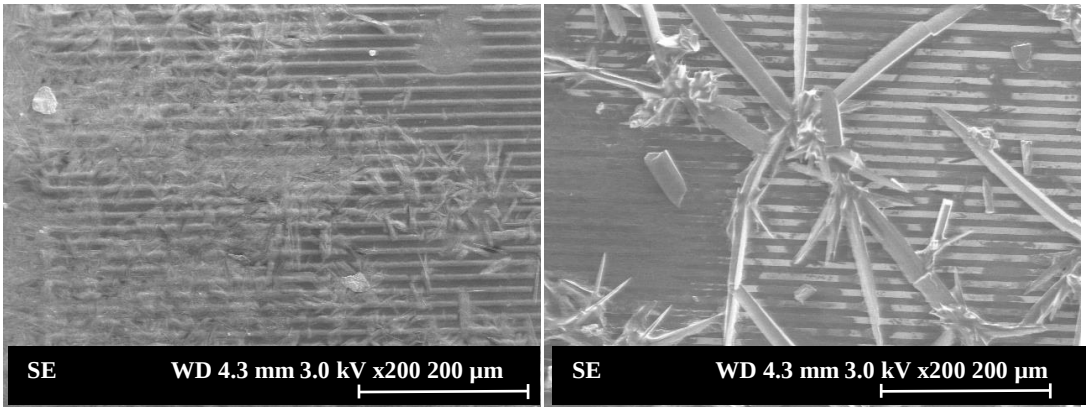

Figure 6.24: SEM images of (left) $Cu(Ti\text{-}C2)_2$ and (right) $Ni(Ti\text{-}C2)_2$ electrodeposited on 8 µm x 8 µm interdigitated electrodes

The SEM images of the interdigitated areas show that both dithiolenes deposit as a combination of a thin film and fibres. The $Cu(Ti\text{-}C2)_2$, (left), has deposited as an even layer with small needle-shaped fibres crossing the electrodes. The $Ni(Ti\text{-}C2)_2$, (right), has also deposited as a thin film and needle-shaped fibres but in this case both types of deposition also seem to be in competition as there is no thin film for about 20 µm where the fibres have formed. A magnification of the fibres of $Ni(Ti\text{-}C2)_2$ is shown in Figure 6.25.

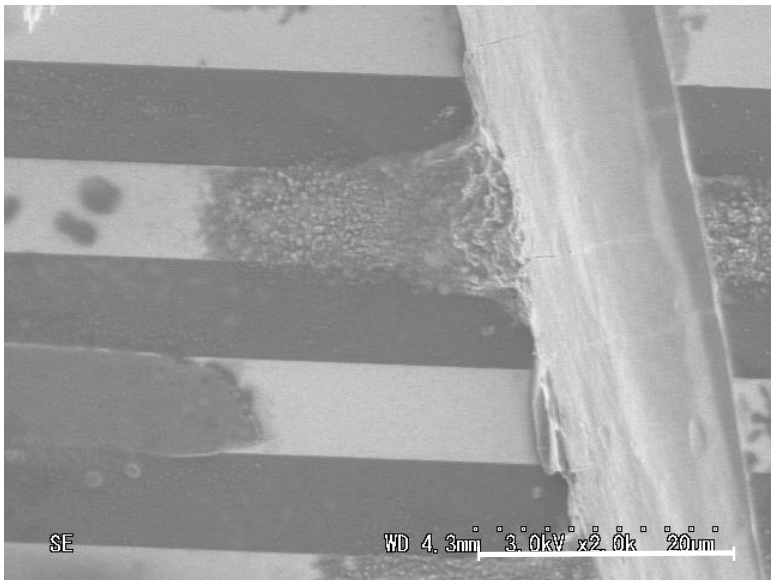

Figure 6.25: SEM image of Ni(Ti-C2)$_2$ electrodeposited on 8 µm x 8 µm interdigitated electrodes

The SEM image also shows that the fibres are attached to the electrodes. If this occurs in more than one place bridging the two electrodes, it is possible that the fibres conduct some of the current.

Therefore the conductivity of both the Cu(Ti-C2)$_2$ and the Ni(Ti-C2)$_2$ will be due to the thin film of electrodeposited material and any fibres on the surface.

6.2.6 Electronic Transporting Properties

The electronic transporting properties of $Cu(Ti\text{-}C2)_2$ and $Ni(Ti\text{-}C2)_2$ films on 8 µm x 8µm interdigitated electrodes were investigated by measuring the I-V characteristics while applying a gate potential.

Plots of the I-V characteristics while applying a gate potential of $Cu(Ti\text{-}C2)_2$ under negative and positive conditions are shown in Figure 6.26.

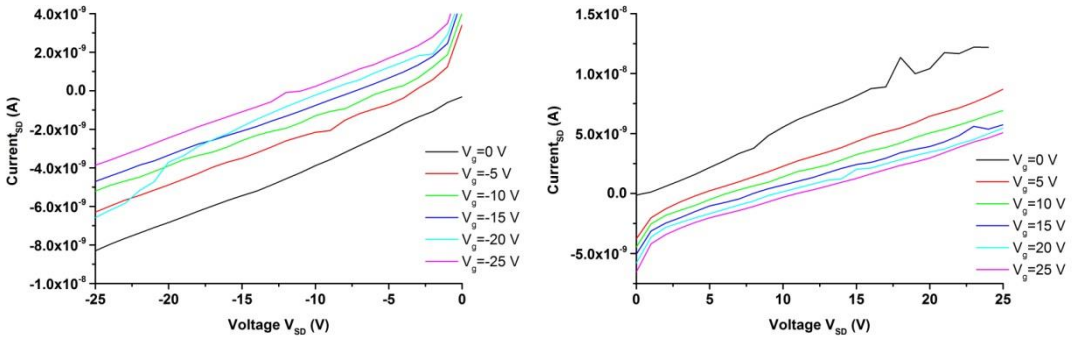

Figure 6.26: Drain current Id against (left) negative source-drain potential and (right) positive source-drain potential V_{SD} curves at various source-gate potentials for $Cu(Ti\text{-}C2)_2$ field effect transistors.

At positive source-drain potential, as shown in Figure 6.26 (right), when no gate potential is applied, the current increases linearly with applied source-drain potential. When a positive gate potential is applied the current starts off negative and increases linearly with increasing source-drain potential. This suggests that applying a gate potential causes impurities present in the film to move due to the gate field. Since the current is initially negative it suggests that the impurities and source-drain potential related current are flowing in opposite directions which results in them competing. Since the FETs were not always under inert conditions it is possible that the dopant is oxygen or water from the air, the effects of which are being counteracted by the gate potential. Holding the potential at 0.06 V for 10 minutes to drain away any excess charge did not change the results. The negative source-drain potential currents measured, as shown in Figure 6.26 (left), are similar to the currents measured for the electrodeposited film of BuPTCDI in an earlier chapter.

The electronic transporting properties of the $Ni(Ti\text{-}C2)_2$ show similar properties to the $Cu(Ti\text{-}C2)_2$. Plots of the I-V characteristics while applying a gate potential of $Ni(Ti\text{-}C2)_2$ under negative and positive conditions are shown in Figure 6.27.

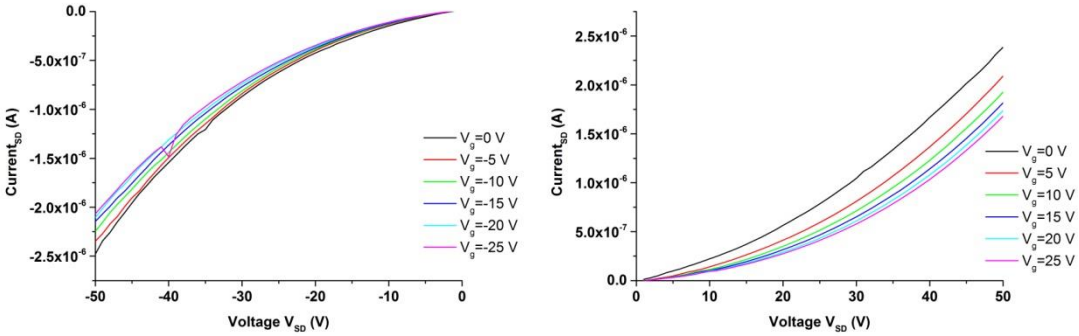

Figure 6.27: Drain current Id against (left) negative source-drain potential and (right) positive source-drain potential V_{SD} curves at various source-gate potentials for $Ni(Ti\text{-}C2)_2$ field effect transistors.

The currents measured show an exponential-like increase with the application of higher potentials. There is also a gate effect, though this is the opposite to what was expected, as the current decreases with the application of higher gate potentials, turning the device off, rather than increasing the performance. This still occurred even after the device was held at a potential of 0.06 V for 10 minutes to drain away any stored charge or after the device was a few days old. The gate effect also becomes less pronounced with increasing gate potentials.

The currents of both films show similar results to the FETs of BuPTCDI. This suggests that bulk transport is occurring, implying that the film is too thick for a saturation region to occur.

6.2.7 Magnetoresistance measurements

The effect of a magnetic field on the current response of electrodeposited films of $Cu(Ti\text{-}C2)_2$ and $Ni(Ti\text{-}C2)_2$ was measured at several temperatures.

Both films were monitored while they were being cooled. Using the current measured and the applied potential the resistance of the film can be calculated. A plot of resistance against temperature of the film cooling process is shown in Figure 6.28.

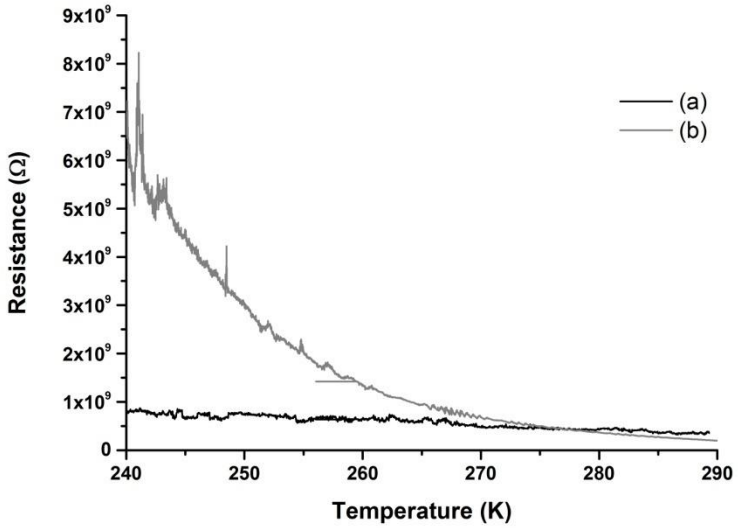

Figure 6.28: Plot of resistance against temperature for the cooling of 8 µm x 8 µm interdigitated electrodes of (a) $Cu(Ti\text{-}C2)_2$ and (b) $Ni(Ti\text{-}C2)_2$

The activation energy of the complexes can be calculated from the resistance during the cooling of the sample using Equation 6.1.

$$\sigma = \sigma_0 e^{\frac{-E_a}{RT}}$$

Equation 6.1

where σ is the conductivity, σ_0 is the pre-exponential factor, E_a is the activation energy, R is the gas constant and T is the temperature in K. By rearranging Equation 6.1, the following equation is obtained:

$$Ln(\sigma) = Ln(\sigma_0) - \frac{E_a}{R}\frac{1}{T}$$

Equation 6.2

From Equation 6.2 a plot of the Ln(σ) against 1/T should result in a plot where the intercept is $Ln(\sigma_0)$ and the gradient of the plot is $-E_a/R$. The plots of Ln(σ) against 1/T for both complexes are shown in Figure 6.29.

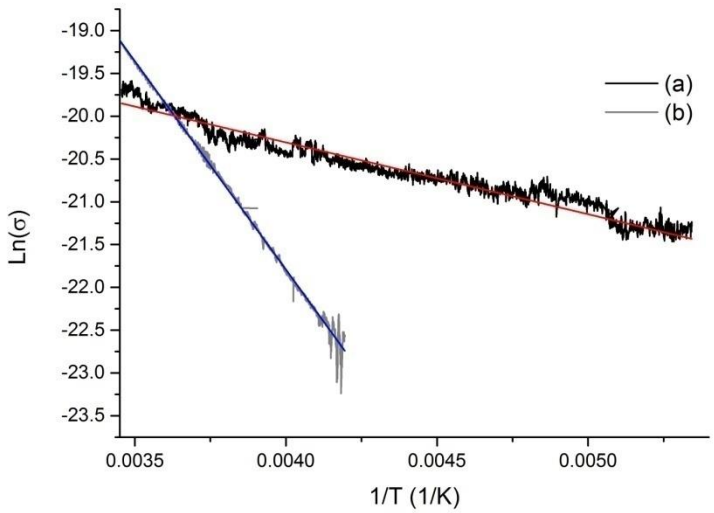

Figure 6.29: Plot of Log(σ) against 1/T of cooling of (a) $Cu(Ti\text{-}C2)_2$ and (b) $Ni(Ti\text{-}C2)_2$

Using the gradient of the lines the activation energy of $Cu(Ti\text{-}C2)_2$ was calculated to be $7.2x10^{-2}$ eV and the activation energy of $Ni(Ti\text{-}C2)_2$ to be 0.42 eV. The activation energy of the $Ni(Ti\text{-}C2)_2$ film broadly agrees with the electronic absorption measurements from Figure 6.18 where the absorption peak at 1455 nm corresponds to a separation of 0.85 eV and, assuming similar behaviour to a band semiconductor, the activation energy equals the bandgap divided by two. Both measurements suggest that the films contain effectively π-stacked molecules which result in significant intermolecular interaction, showing a narrow gap between the occupied and unoccupied levels. The $Cu(Ti\text{-}C2)_2$ activation energy is about a fifth of that of $Ni(Ti\text{-}C2)_2$. This does not correspond to a similar transition in the electronic absorption measurements for $Ni(Ti\text{-}C2)_2$ from Figure 6.18 where the absorption peak at 1628 nm corresponds to a separation of 0.76 eV. This suggests that the extra

electron in the $Cu(Ti\text{-}C2)_2$ is playing a role, giving an exceptionally low activation energy.

The magnetoresistance of the films was investigated by measuring the current response when a magnetic field was applied at several different temperatures at a fixed potential. The obtained current and applied potential were used to calculate the resistance and the percentage difference between the resistances, when a magnetic field was applied and when no field was applied, was obtained at each temperature.[151]

A plot of the percentage difference in resistance was obtained during the application of a magnetic field measured at several temperatures on a film electrodeposited on 2 µm x 2 µm interdigitated electrodes. This small gap was used to minimise the effect of temperature on the electrodes. The percentage differences of resistance when the magnetic field is applied at various temperatures at 7 V for $Cu(Ti\text{-}C2)_2$ and at 130 V for $Ni(Ti\text{-}C2)_2$ are shown in Figure 6.30.

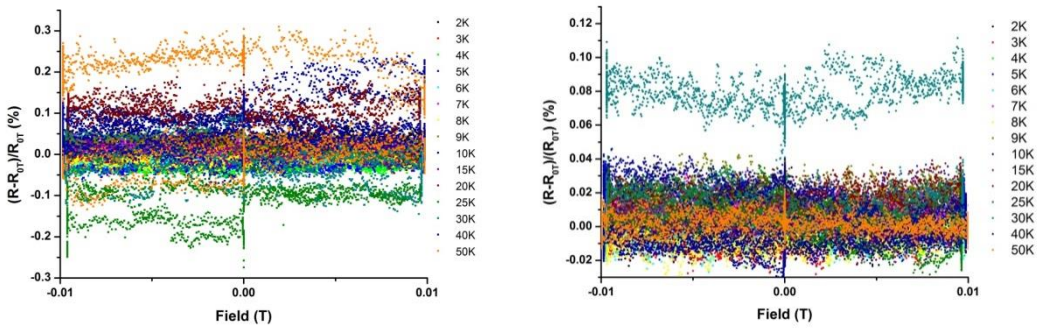

Figure 6.30: Magnetic field dependence of the magnetoresistance of electrodeposited films on 2 µm x 2 µm interdigitated electrodes at various temperatures (left) $Cu(Ti\text{-}C2)_2$ at 7 V and (right) $Ni(Ti\text{-}C2)_2$ at 130 V

The negligible difference in resistance between the current when a magnetic field is applied and when no magnetic field is applied suggests that there is no magnetoresistance for either the electrodeposited $Cu(Ti\text{-}C2)_2$ or $Ni(Ti\text{-}C2)_2$. It is possible that since the films of both materials have a low activation energy, they are slightly doped giving a large off current, which may mask any possible magnetoresistive effects.

6.3 Conclusion

Neutral films of both $Cu(Ti\text{-}C2)_2$ and $Ni(Ti\text{-}C2)_2$ were obtained using electrochemical deposition. The films produced had similar characteristics of closely compacted features of 50 nm – 500 nm in size.

The isolation of the neutral $Cu(Ti\text{-}C2)_2$ films confirms that electrochemical deposition is a promising method for the isolation of neutral copper dithiolenes. That the deposited film absorbed in the NIR region of the electromagnetic spectrum confirms the isolation of the neutral complex. Once removed from the substrate the neutral complex is unstable and decomposes in solution.

The isolated films of the neutral $Cu(Ti\text{-}C2)_2$ and $Ni(Ti\text{-}C2)_2$ show a higher degree of molecular interaction compared to previously deposited films of $Cu(mi\text{-}5hdt)_2$ and $Ni(b\text{-}3ted)_2$, resulting in broader electronic absorptions.

When $Cu(Ti\text{-}C2)_2$ and $Ni(Ti\text{-}C2)_2$ were used to fabricate FETs, the electronic properties of the material showed some unexpected results, suggesting that both films may have been doped. The activation energy of the $Ni(Ti\text{-}C2)_2$ agreed with the data obtained from the electronic absorption whereas the activation energy of the $Cu(Ti\text{-}C2)_2$ was exceptionally small, attributed to the additional unpaired electron for this complex.

6.4 Experimental

Nickel (2-(5-butylthiophene-2-yl)-1,2-dithiolene)$_2$ TBA

The Nickel (2-(5-butylthiophene-2-yl)-1,2-dithiolene)$_2$ TBA was obtained from Georg Silber.

Copper (2-(5-butylthiophene-2-yl)-1,2-dithiolene)$_2$ TMA

4-(ethyl-thiophene)-1,3-dithiol-2-one (547mg, 2.40 mmol) in THF (15 ml) was added to [TMA][OH]·5H2O (956 mg, 5.28 mmol) in MeOH (4 ml). After 5 minutes, CuCl2·2H2O (204 mg, 1.20 mmol) in MeOH (4 ml) was added and the reaction mixture stirred at room temperature overnight. The precipitate was filtered off and washed with EtOH(10 ml).

NMR: δH (500 MHz; CDCl3) 1.27 (t, 6H, Me, J =7.5, 1.3 Hz e), 1.60 (s, 12H, TMA), 2.20 (q, 4H,-CH^2-, J =7.3, 1.8 Hz d), 6.71 (s, 2H, C(S)H, a) 6.71 (d, 2H, -CH=, J =7.2, 1.2Hz b) 6.89 (d, 2H, =CH-, J =11.4, 1.2Hz c)

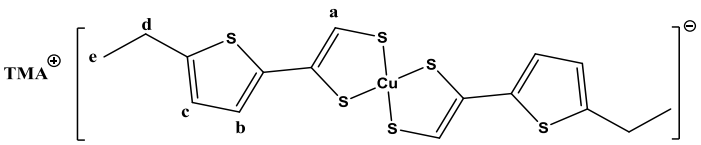

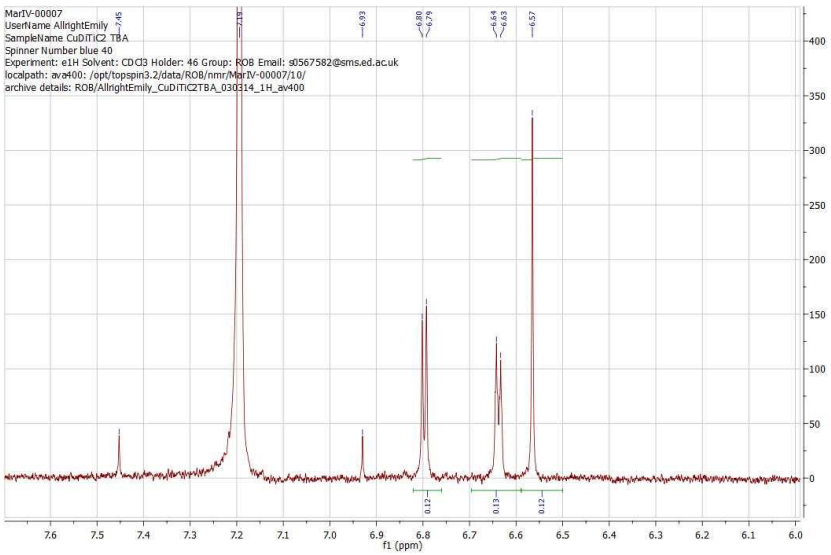

Figure 6.31: NMR of the aromatic region of Cu(Ti-C2)$_2$

CHN: cal: C 44.62%, H 5.24%, N 2.60% found: C 38.99%, H 5.07%, N 2.46%

The copper analogue was shown to be analytically pure by NMR, as shown in Figure 6.31. Any attempts to purify the complex further led to degradation.

7. Conclusion

Films of several different molecular electronic materials were electrochemically deposited and the properties of the resulting films were investigated.

The technique of chemically reducing small molecules with a large delocalized π system and then depositing a film by electrochemically oxidising it with a fixed potential was pioneered using BuPTCDI. Continuous films of controllable thicknesses were successfully deposited onto conducting glass substrates as well as interdigitated electrodes. The films had similar optical properties to films deposited by other techniques. The morphology of the BuPTCDI films was controlled by the most energetically favourable stacking of the molecules and resulted in the films containing stacks of BuPTCDI molecules rather than the flatter terraces seen in vapour deposited films.

The developed technique was then used to investigate the electrodeposition of CuPc. Similar to BuPTCDI, continuous films with controllable thicknesses of CuPc were deposited onto FTO/ PEDOT: PSS. These were initially deposited as charged green coloured films of $[CuPc]^-$ which affected the electronic absorption before losing the charge after which the films became neutral and blue in colour. The morphology of the films can be described as a dense layer of small crystallites similar to films deposited by vapour deposition techniques.

Electrodeposition of a molecular electronic material onto an already deposited electronic material layer was investigated. BuPTCDI layers were successfully deposited onto electrodeposited films of CuPc. The film of CuPc changed the orientation of the stacks of the BuPTCDI resulting in porous films. Although the resulting morphology was unsuitable for solar cells, the developed method could be used to deposit entire devices.

CuPc was also electrodeposited onto porous TiO_2. Analysis of the films strongly suggested that the CuPc layer had penetrated into the pores of the TiO_2 layer rather than just depositing onto the surface. Although charge transfer did not occur

efficiently at the interface of the two layers, electrodeposition showed promise as a method to deposit redox active molecules into porous materials.

Continuous films of neutral metal dithiolene complexes, $Cu(Ti\text{-}C2)_2$ and $Ni(Ti\text{-}C2)_2$, with large degrees of molecular interaction were obtained by electrodeposition. Both films absorbed in the near infrared. Electrodeposition of the neutral films from the salt of the complexes offered a unique way of obtaining films since neutral $Cu(Ti\text{-}C2)_2$ is unstable and decomposes in solution and neutral $Ni(Ti\text{-}C2)_2$ has a very low solubility making solution processing impossible in both cases.

The electrodeposition method developed could be used to deposit any electroactive molecule and has been used in several unique ways including depositing continuous films of several materials, most of which are difficult or impossible to deposit using normal solution based process techniques. It has also been used to insert molecules into porous materials.

8. Future work

The process developed in this thesis has only scratched the surface of the potential of this technique in the deposition of organic electronic materials and there are several areas that could be investigated further including:

- Expanding the technique to include more electroactive molecules already used in applications, including those that would require chemical oxidation followed by electrochemical reduction.
- The sodium mirror used to chemically reduce the electrodeposited molecules was in excess, which could have resulted in the molecules being reduced several times. This could be investigated further, including the effect of the charge of the anion on the deposition method and resulting film.
- Another area to investigate is to see if the electrodeposition method can be modified to affect the film produced. For example, the applied charge could be pulsed to see if the packing of the deposited molecules can be changed.
- Some effects of templating were seen when BuPTCDI was deposited on CuPc and when CuPc was deposited on TiO_2. Further investigation of the effect templating has on the deposited film could help tailor the films for use in devices. This could be done by depositing on different types of substrates or by pre-treating the substrate. Pre-treatment could include hole blocking layers or a mono-layer of molecules similar to the ones being electrodeposited, which would result in the desired packing.
- Another area to investigate is post-treatment of the electrodeposited films such as heating and annealing.

9. References

1. H. N. McCoy and W. C. Moore, *Journal of the American Chemical Society*, 1911, **33**, 273-292.
2. C. D. Dimitrakopoulos and P. R. L. Malenfant, *Advanced Materials*, 2002, **14**, 99-117.
3. B. Mann and H. Kuhn, *Journal of Applied Physics*, 1971, **42**, 4398-4405.
4. M. Ratner, *Nat Nano*, 2013, **8**, 378-381.
5. M. Bendikov, F. Wudl and D. F. Perepichka, *Chemical Reviews*, 2004, **104**, 4891-4946.
6. A. Pron, P. Gawrys, M. Zagorska, D. Djurado and R. Demadrille, *Chemical Society Reviews*, 2010, **39**, 2577-2632.
7. H. Dong, H. Zhu, Q. Meng, X. Gong and W. Hu, *Chemical Society Reviews*, 2012, **41**, 1754-1808.
8. F. Wurthner, *Chemical Communications*, 2004, 1564-1579.
9. K. Kudo, M. Yamashina and T. Moriizumi, *Japanese Journal of Applied Physics*, 1984, **23**, 130.
10. C. W. Tang, *Applied Physics Letters*, 1986, **48**, 183-185.
11. R. Kato, *Chemical Reviews*, 2004, **104**, 5319-5346.
12. N. Robertson and L. Cronin, *Coordination Chemistry Reviews*, 2002, **227**, 93-127.
13. N. Karl, *Synthetic Metals*, 2003, **133–134**, 649-657.
14. J. L. Brédas, J. P. Calbert, D. A. da Silva Filho and J. Cornil, *Proceedings of the National Academy of Sciences*, 2002, **99**, 5804-5809.
15. T. Holstein, *Annals of Physics*, 1959, **8**, 325-342.
16. G. Horowitz, *Advanced Materials*, 1998, **10**, 365-377.
17. P. A. Cox, *The electronic structure and chemistry of solids*, Oxford University Press, Oxford, 1989.
18. H. Dong, C. Wang and W. Hu, *Chemical Communications*, 2010, **46**, 5211-5222.
19. S. Allard, M. Forster, B. Souharce, H. Thiem and U. Scherf, *Angewandte Chemie International Edition*, 2008, **47**, 4070-4098.
20. A. Hoshino, Y. Takenaka and H. Miyaji, *Acta Crystallographica Section B*, 2003, **59**, 393-403.
21. E. Hadicke and F. Graser, *Acta Crystallographica Section C*, 1986, **42**, 189-195.
22. F. Xinliang, W. Pisula and K. Müllen, *Pure & Applied Chemistry*, 2009, **81**, 2203-2224.
23. J. E. Anthony, *Chemical Reviews*, 2006, **106**, 5028-5048.
24. K. Balakrishnan, A. Datar, T. Naddo, J. Huang, R. Oitker, M. Yen, J. Zhao and L. Zang, *Journal of the American Chemical Society*, 2006, **128**, 7390-7398.
25. G. Klebe, F. Graser, E. Hadicke and J. Berndt, *Acta Crystallographica Section B*, 1989, **45**, 69-77.
26. N. Kaiser, *Applied Optics*, 2002, **41**, 3053-3060.
27. in *Building Integrated Photovoltaic Thermal Systems: For Sustainable Developments*, The Royal Society of Chemistry, pp. 50-102.

28. A. Kar and A. Kar, in *Automation, Control, Energy and Systems (ACES), 2014 First International Conference on*, 2014, pp. 1-6.
29. U. Mehmood, S.-u. Rahman, K. Harrabi, I. A. Hussein and B. V. S. Reddy, *Advances in Materials Science and Engineering*, 2014, **2014**, 12.
30. J.-M. Nunzi, *Comptes Rendus Physique*, 2002, **3**, 523-542.
31. W. Y. Liang, *Physics Education*, 1970, **5**, 226.
32. Y. S. Eo, H. W. Rhee, B. D. Chin and J.-W. Yu, *Synthetic Metals*, 2009, **159**, 1910-1913.
33. E. Kozma, D. Kotowski, F. Bertini, S. Luzzati and M. Catellani, *Polymer*, 2010, **51**, 2264-2270.
34. J. Ouyang, C. W. Chu, F. C. Chen, Q. Xu and Y. Yang, *Advanced Functional Materials*, 2005, **15**, 203-208.
35. J. H. Park, J.-I. Park, D. H. Kim, J.-H. Kim, J. S. Kim, J. H. Lee, M. Sim, S. Y. Lee and K. Cho, *Journal of Materials Chemistry*, 2010, **20**, 5860-5865.
36. J. Roncali, *Chemical Society Reviews*, 2005, **34**, 483-495.
37. M. Tao, in *Terawatt Solar Photovoltaics*, Springer London, 2014, pp. 9-20.
38. N. Kaur, M. Singh, D. Pathak, T. Wagner and J. M. Nunzi, *Synthetic Metals*, 2014, **190**, 20-26.
39. J. Burschka, N. Pellet, S.-J. Moon, R. Humphry-Baker, P. Gao, M. K. Nazeeruddin and M. Gratzel, *Nature*, 2013, **499**, 316-319.
40. N. C. f. Photovoltaics, http://www.nrel.gov/ncpv/images/efficiency_chart.jpg. Visited 25th June 2014
41. H. Sirringhaus, *Advanced Materials*, 2014, **26**, 1319-1335.
42. M. Paunovic, M. Schlesinger and D. D. Snyder, in *Modern Electroplating*, John Wiley & Sons, Inc., 2010, pp. 1-32.
43. F. C. Krebs, *Solar Energy Materials and Solar Cells*, 2009, **93**, 394-412.
44. J. L. Plawsky, M. Ojha, A. Chatterjee and P. C. Wayner, *Chemical Engineering Communications*, 2008, **196**, 658-696.
45. C. J. Lawrence, *Physics of Fluids*, 1988, **31**, 2786-2795.
46. K. Norrman, A. Ghanbari-Siahkali and N. B. Larsen, *Annual Reports Section "C" (Physical Chemistry)*, 2005, **101**, 174-201.
47. S. E. Shaheen, R. Radspinner, N. Peyghambarian and G. E. Jabbour, *Applied Physics Letters*, 2001, **79**, 2996-2998.
48. M. M. Ling and Z. Bao, *Chemistry of Materials*, 2004, **16**, 4824-4840.
49. M. Robinson, *Journal of The Electrochemical Society*, 1968, **115**, 131C-137C.
50. J. P. Celis, J. R. Roos, C. Buelens and J. Fransaer, *Transactions of the Institute of Metal Finishing*, 1991, **69**, 133-139.
51. M. Musiani, *Electrochimica Acta*, 2000, **45**, 3397-3402.
52. J. R. Roos, J. P. Celis, J. Fransaer and C. Buelens, *JOM*, 1990, **42**, 60-63.
53. A. Hovestad and L. J. J. Janssen, *Journal of Applied Electrochemistry*, 1995, **25**, 519-527.
54. J. W. Dini and D. D. Snyder, in *Modern Electroplating*, John Wiley & Sons, Inc., 2010, pp. 33-78.
55. W. D. l. Rue, *London Edinburgh Philos. Mag.*, 1836, **9**, 484.
56. G. Fulop and R. Taylor, *Annual Review of Materials Science*, 1985, **15**, 197-210.

57. E. Fortunato, P. Barquinha and R. Martins, *Advanced Materials*, 2012, **24**, 2945-2986.
58. D. Lincot, *Thin Solid Films*, 2005, **487**, 40-48.
59. J.-J. Wu, W.-P. Liao and M. Yoshimura, *Nano Energy*, 2013, **2**, 1354-1372.
60. I. M. Dharmadasaz and J. Haigh, *Journal of The Electrochemical Society*, 2006, **153**, G47-G52.
61. K. Keiji Kanazawa, A. F. Diaz, W. D. Gill, P. M. Grant, G. B. Street, G. Piero Gardini and J. F. Kwak, *Synthetic Metals*, 1980, **1**, 329-336.
62. R. J. Waltman and J. Bargon, *Canadian Journal of Chemistry*, 1986, **64**, 76-95.
63. A. Tsumura, H. Koezuka and T. Ando, *Applied Physics Letters*, 1986, **49**, 1210-1212.
64. W. Yu, B. Xu, Q. Dong, Y. Zhou, J. Zhang, W. Tian and B. Yang, *Journal of Solid State Electrochemistry*, 2010, **14**, 1051-1056.
65. W. Chen, J. Akhigbe, C. BruÌˆckner, C. M. Li and Y. Lei, *The Journal of Physical Chemistry C*, 2010, **114**, 8633-8638.
66. P. Batail, K. Boubekeur, M. Fourmigué and J.-C. P. Gabriel, *Chemistry of Materials*, 1998, **10**, 3005-3015.
67. E. Budevski, G. Staikov and W. J. Lorenz, *Electrochimica Acta*, 2000, **45**, 2559-2574.
68. J. R. Bates, R. W. Miles and P. Kathirgamanathan, *Synthetic Metals*, 1996, **76**, 313-315.
69. G. Cui, W. Xu, C. Guo, X. Xiao, H. Xu, D. Zhang, L. Jiang and D. Zhu, *The Journal of Physical Chemistry B*, 2004, **108**, 13638-13642.
70. D. de Caro, M. Basso-Bert, H. Casellas, M. Elgaddari, J.-P. Savy, J.-F. Lamère, A. Bachelier, C. Faulmann, I. Malfant, M. Étienne and L. Valade, *Comptes Rendus Chimie*, 2005, **8**, 1156-1173.
71. W. E. Buschmann, S. C. Paulson, C. M. Wynn, M. A. Girtu, A. J. Epstein, H. S. White and J. S. Miller, *Chemistry of Materials*, 1998, **10**, 1386-1395.
72. M. Z. Jacobson, *Energy & Environmental Science*, 2009, **2**, 148-173.
73. I. M. Dharmadasa, R. P. Burton and M. Simmonds, *Solar Energy Materials and Solar Cells*, 2006, **90**, 2191-2200.
74. M. Uhlemann, A. Gebert, M. Herrich, A. Krause, A. Cziraki and L. Schultz, *Electrochimica Acta*, 2003, **48**, 3005-3011.
75. A. Zaban and Y. Diamant, *The Journal of Physical Chemistry B*, 2000, **104**, 10043-10046.
76. Y. Diamant and A. Zaban, *Journal of The Electrochemical Society*, 2001, **148**, C709-C714.
77. S. K. Lee, Y. Zu, A. Herrmann, Y. Geerts, K. Müllen and A. J. Bard, *Journal of the American Chemical Society*, 1999, **121**, 3513-3520.
78. B. A. Gregg and R. A. Cormier, *The Journal of Physical Chemistry B*, 1998, **102**, 9952-9957.
79. T. Anjos, S. J. Roberts-Bleming, A. Charlton, N. Robertson, A. R. Mount, S. J. Coles, M. B. Hursthouse, M. Kalaji and P. J. Murphy, *Journal of Materials Chemistry*, 2008, **18**, 475-483.
80. S. Dalgleish, H. Yoshikawa, M. M. Matsushita, K. Awaga and N. Robertson, *Chemical Science*, 2010, **2**, 316-320.

81. S. Dalgleish, K. Awaga and N. Robertson, *Chemical Communications*, 2011, **47**, 7089-7091.
82. R. Burns and C. McAuliffe, *Adv. Inorg. Chem. Radiochem*, 1979, **22**, 303-348.
83. P. A. Christensen and A. Hamnett, *Techniques and mechanisms in electrochemistry*, Blackie Academic & Professional, London, 1994.
84. R. Greef and Southampton Electrochemistry Group., *Instrumental methods in electrochemistry*, Ellis Horwood, New York ; London, 1990.
85. P. W. Atkins and J. De Paula, *Atkins' Physical chemistry*, Oxford University Press, Oxford, ; New York, 2006.
86. D. F. Shriver and P. W. Atkins, *Inorganic chemistry*, Oxford University Press, Oxford, 2006.
87. L. Reimer, *Scanning electron microscopy : physics of image formation and microanalysis*, Springer, Berlin ; London, 1998.
88. D. Chescoe, P. J. Goodhew and Royal Microscopical Society (Great Britain), *The operation of transmission and scanning electron microscopes*, Oxford University Press; Royal Microscopical Society, Oxford, 1990.
89. H. Smith, ed., *High Performance Pigments*, Wiley-VCH Verlag, Weinheim, 2002.
90. E. Kozma and M. Catellani, *Dyes and Pigments*, 2013, **98**, 160-179.
91. P. Dhagat, H. M. Haverinen, R. J. Kline, Y. Jung, D. A. Fischer, D. M. DeLongchamp and G. E. Jabbour, *Advanced Functional Materials*, 2009, **19**, 2365-2372.
92. L. Gisslén, Walter Schottky Institut, Technische Universität München, 2009.
93. H. Langhals, S. Demmig and H. Huber, *Spectrochimica Acta Part A: Molecular Spectroscopy*, 1988, **44**, 1189-1193.
94. G. Türkmen, S. Erten-Ela and S. Icli, *Dyes and Pigments*, 2009, **83**, 297-303.
95. J. Mizuguchi, *Dyes and Pigments*, 2006, **70**, 226-231.
96. W. Herbst, K. Hunger, G. Wilker, H. Ohleier and R. Winter, in *Industrial Organic Pigments*, Wiley-VCH Verlag GmbH & Co. KGaA, 2005, pp. 421-566.
97. D. Lehmann and D. R. T. Zahn, *Applied Physics A: Materials Science & Processing*, 2009, **95**, 203-207.
98. K. Balakrishnan, A. Datar, R. Oitker, H. Chen, J. Zuo and L. Zang, *Journal of the American Chemical Society*, 2005, **127**, 10496-10497.
99. Y. Zhang, L.-Z. Cai, C.-Y. Wang, G.-Q. Lai and Y.-J. Shen, *New Journal of Chemistry*, 2008, **32**, 1968-1973.
100. T. Kircher and H. G. Lohmannsroben, *Physical Chemistry Chemical Physics*, 1999, **1**, 3987-3992.
101. Y. Geerts, H. Quante, H. Platz, R. Mahrt, M. Hopmeier, A. Bohm and K. Mullen, *Journal of Materials Chemistry*, 1998, **8**, 2357-2369.
102. V. Parra, T. Del Cano, M. L. Rodriguez-Mendez, J. A. de Saja and R. F. Aroca, *Chemistry of Materials*, 2003, **16**, 358-364.
103. D. Schlettwein, A. Back, B. Schilling, T. Fritz and N. R. Armstrong, *Chemistry of Materials*, 1998, **10**, 601-612.
104. W. Yip and D. H. Levy, *The Journal of Physical Chemistry*, 1996, **100**, 11539-11545.

105. S. Rodrıguez-Llorentez, R. Aroca and J. Duff, *Spectrochimica Acta Part A: Molecular and Biomolecular Spectroscopy*, 1999, **55**, 969-978.
106. J. Perlstein, *Chemistry of Materials*, 1994, **6**, 319-326.
107. R. J. Chesterfield, J. C. McKeen, C. R. Newman, C. D. Frisbie, P. C. Ewbank, K. R. Mann and L. L. Miller, *Journal of Applied Physics*, 2004, **95**, 6396-6405.
108. O. Guillermet, M. Mossoyan-Déneux, M. Giorgi, A. Glachant and J. C. Mossoyan, *Thin Solid Films*, 2006, **514**, 25-32.
109. J. Mizuguchi, Z. Kristallogr. NCS, 2003, pp. 131-133.
110. P. Scherrer, 1918, 98-100.
111. C. W. Struijk, A. B. Sieval, J. E. J. Dakhorst, M. van Dijk, P. Kimkes, R. B. M. Koehorst, H. Donker, T. J. Schaafsma, S. J. Picken, A. M. van de Craats, J. M. Warman, H. Zuilhof and E. J. R. Sudhölter, *Journal of the American Chemical Society*, 2000, **122**, 11057-11066.
112. P. Vivo, A. S. Alekseev, K. Kaunisto, O. Pekkola, A. Tolkki, V. Chukharev, A. Efimov, P. Ihalainen, J. Peltonen and H. Lemmetyinen, *Physical Chemistry Chemical Physics*, 2010, **12**, 12525-12532.
113. P. R. L. Malenfant, C. D. Dimitrakopoulos, J. D. Gelorme, L. L. Kosbar, T. O. Graham, A. Curioni and W. Andreoni, *Applied Physics Letters*, 2002, **80**, 2517-2519.
114. D. Natali and M. Caironi, *Advanced Materials*, 2012, **24**, 1357-1387.
115. B. K. Sarker, J. Liu, L. Zhai and S. I. Khondaker, *ACS Applied Materials & Interfaces*, 2011, **3**, 1180-1185.
116. M. Hiramoto, H. Fukusumi and M. Yokoyama, *Applied Physics Letters*, 1992, **61**, 2580-2582.
117. K. Triyana, T. Yasuda, K. Fujita and T. Tsutsui, *Japanese Journal of Applied Physics*, 2005, **44**, 1974.
118. T. D. Heidel, D. Hochbaum, J. M. Sussman, V. Singh, M. E. Bahlke, I. Hiromi, J. Lee and M. A. Baldo, *Journal of Applied Physics*, 2011, **109**, -.
119. S. N. Inamdar, P. P. Ingole and S. K. Haram, *ChemPhysChem*, 2008, **9**, 2574-2579.
120. T. Torres, *Angewandte Chemie International Edition*, 2006, **45**, 2834-2837.
121. R. P. Linstead, *Journal of the Chemical Society (Resumed)*, 1934, 1016-1017.
122. M. Bakkush, M. M. Salleh, M. Yahaya and I. A. Talib, *Solid State Ionics*, 1996, **86–88, Part 2**, 983-985.
123. M. J. Cook, *Pure and Applied Chemistry*, 1999, **71**, 2145-2152.
124. G. Guillaud, J. Simon and J. P. Germain, *Coordination Chemistry Reviews*, 1998, **178–180, Part 2**, 1433-1484.
125. M. Hersam, N. Guisinger and J. Lyding, *Nanotechnology*, 2000, **11**, 70.
126. J. Xue, S. Uchida, B. P. Rand and S. R. Forrest, *Applied Physics Letters*, 2004, **85**, 5757-5759.
127. A. Koca, Ş. Bayar, H. A. Dinçer and E. Gonca, *Electrochimica Acta*, 2009, **54**, 2684-2692.
128. L. Gaffo, A. W. Rinaldi, M. J. L. Santos and E. M. Girotto, *Journal of Porphyrins and Phthalocyanines*, 2007, **11**, 618-622.
129. J. M. Mativetsky, H. Wang, S. S. Lee, L. Whittaker-Brooks and Y.-L. Loo, *Chemical Communications*, 2014.

130. M. M. Al-Amar, K. J. Hamam, G. Mezei, R. Guda, N. M. Hamdan and C. A. Burns, *Solar Energy Materials and Solar Cells*, 2013, **109**, 270-274.
131. J. D. Spikes, *Photochemistry and Photobiology*, 1986, **43**, 691-699.
132. N. M. Speirs, W. J. Ebenezer and A. C. Jones, *Photochemistry and Photobiology*, 2002, **76**, 247-251.
133. B. Blanzat, C. Barthou, N. Tercier, J. J. Andre and J. Simon, *Journal of the American Chemical Society*, 1987, **109**, 6193-6194.
134. D. R. Tackley, G. Dent and W. Ewen Smith, *Physical Chemistry Chemical Physics*, 2001, **3**, 1419-1426.
135. S. Heutz, S. M. Bayliss, R. L. Middleton, G. Rumbles and T. S. Jones, *The Journal of Physical Chemistry B*, 2000, **104**, 7124-7129.
136. J. Hwang, F. Amy and A. Kahn, *Organic Electronics*, 2006, **7**, 387-396.
137. D. Alemu, H.-Y. Wei, K.-C. Ho and C.-W. Chu, *Energy & Environmental Science*, 2012, **5**, 9662-9671.
138. P. Erk, H. Hengelsberg, M. F. Haddow and R. van Gelder, *CrystEngComm*, 2004, **6**, 475-483.
139. C. J. Brown, *Journal of the Chemical Society A: Inorganic, Physical, Theoretical*, 1968, 2488-2493.
140. T. Oekermann, D. Schlettwein and N. I. Jaeger, *Journal of Electroanalytical Chemistry*, 1999, **462**, 222-234.
141. N. Minami, T. Watanabe, A. Fujishima and K.-I. Honda, *Berichte der Bunsengesellschaft für physikalische Chemie*, 1979, **83**, 476-481.
142. A. K. Hassan and R. D. Gould, *Journal of Physics: Condensed Matter*, 1989, **1**, 6679.
143. S. Dowland, T. Lutz, A. Ward, S. P. King, A. Sudlow, M. S. Hill, K. C. Molloy and S. A. Haque, *Advanced Materials*, 2011, **23**, 2739-2744.
144. N. D. Abazović, M. I. Čomor, M. D. Dramićanin, D. J. Jovanović, S. P. Ahrenkiel and J. M. Nedeljković, *The Journal of Physical Chemistry B*, 2006, **110**, 25366-25370.
145. Y. Liu and R. O. Claus, *Journal of the American Chemical Society*, 1997, **119**, 5273-5274.
146. K. Thamaphat, P. Limsuwan and B. Ngotawornchai, *Kasetsart J.(Nat. Sci.)*, 2008, **42**, 357-361.
147. G. N. Schrauzer and V. Mayweg, *Journal of the American Chemical Society*, 1962, **84**, 3221-3221.
148. S. Dalgleish and N. Robertson, *Coordination Chemistry Reviews*, 2010, **254**, 1549-1558.
149. C. T. Vance, J. H. Welch and R. D. Bereman, *Inorganica Chimica Acta*, 1989, **164**, 191-200.
150. S. Rabaça, A. C. Cerdeira, A. I. S. Neves, S. I. G. Dias, C. Mézière, I. C. Santos, L. C. J. Pereira, M. Fourmigué, R. T. Henriques and M. Almeida, *Polyhedron*, 2009, **28**, 1069-1078.
151. L. Pilia, M. Serri, M. M. Matsushita, K. Awaga, S. Heutz and N. Robertson, *Advanced Functional Materials*, 2014, **24**, 2383 - 2388.

Publication

Journal of Materials Chemistry C

PAPER

View Article Online
View Journal

Cite this: DOI: 10.1039/c4tc01134a

Electrochemical deposition as a unique solution processing method for insoluble organic optoelectronic materials†

Emily Allwright,[a] Dominik M. Berg,[b] Rabie Djemour,[b] Marc Steichen,[b] Phillip J. Dale[b] and Neil Robertson*[a]

Received 30th May 2014
Accepted 11th July 2014

DOI: 10.1039/c4tc01134a

www.rsc.org/MaterialsC

Electrochemical deposition is shown to be a novel technique to deposit films of *N*,*N*′-dibutylperylene-3,4:9,10-bis(dicarboximide) (BuPTCDI) dye that avoids the need for high vacuum or solubilising side chains on the molecule. The technique exploits the higher solubility of the reduced ionic form of the dye over the neutral form. BuPTCDI was chemically reduced to solubilise and then electrochemically oxidised to form a film on various substrates. The properties of the films were investigated by UV/Vis spectroscopy, Photoluminescence, Raman spectroscopy, X-ray diffraction, SEM and photoconductivity showing the successful deposition of the BuPTCDI molecules. The technique was also used to deposit films on interdigitated-electrode substrates enabling measurement of field-effect mobility.

Introduction

Research into the deposition of organic thin films for optoelectronic applications has resulted in the development of several methods of fabrication,[1] mainly divided into two types: solution deposition and vapour deposition. Solution deposition techniques such as spin coating[2,3] and dip coating[4] have been used to deposit repeatable, uniform thin films on a small scale. Larger scale production methods undergoing research include screen printing,[5] spray deposition[6] and ink jet printing.[7,8] These techniques however, rely on the deposited material being soluble. To achieve effective charge transport, organic semiconductor materials are designed to have a large degree of intermolecular interaction which most of the time is obtained by large π-stacked systems. This often results in the parent molecule being insoluble, requiring addition of solubilising substituents such as alkyl chains. It may be difficult to deposit good quality films of these materials by solution techniques and the films produced inevitably contain insulating alkyl domains that affect the desired semiconducting properties. Vapour techniques are also used to produce thin films; the advantage of this method is to allow fabrication of high quality thin films of well controlled thickness and the fabrication of complex multi-layered architectures.[9] This technique however, also has disadvantages as a commercially viable option for large area depositions as it requires vacuum and is generally time consuming.[10] Another problem relates to the temperature required, as large π-stacked systems normally have high sublimation points and many will decompose before subliming. Compounding this, very high substrate temperatures may be needed to achieve good crystallinity.[11]

Electrochemical deposition has the potential to be used as an alternative method for depositing insoluble molecules onto conductive substrates. This method works by chemically changing the redox state of a molecule to solubilise it, then electrochemically changing it back to its insoluble form at a conducting substrate. For extended-lattice materials, the electrochemical deposition of inorganic semiconductor thin films has emerged as an alternative to vapour deposition techniques over the past decade.[12–15] In contrast however, electrodeposition of small molecules for use in molecular electronics has received almost no attention. An early study used an electrode formed from the neutral compound. This was partly dissolved on reduction and then oxidised onto a titanium dioxide slide.[16] The technique showed promise in the deposition of thin films but has not received subsequent attention.[17] More recently, we have shown, in the case of metal-bis-1,2-dithiolene complexes, that the deposition of the neutral molecules onto field-effect transistor (FET) substrates and fluorine doped tin oxide (FTO) conducting glass was successfully achieved from the dissolved molecular anions using potentiostatic electrodeposition.[18,19] The films deposited using this method were found to be polycrystalline, with higher conductivity than films deposited by solvent casting. Dithiolene complexes provided a convenient test case to explore the electrodeposition method due to both the neutral and anionic states being readily isolated and stable

[a]School of Chemistry and EaStCHEM Research School, University of Edinburgh, King's Buildings, West Mains Road, Edinburgh, EH9 3JJ, UK. E-mail: neil.robertson@ed.ac.uk
[b]Université du Luxembourg, Laboratory for Energy Materials, 41 rue du Brill, L-4422 Belvaux, Luxembourg

† Electronic supplementary information (ESI) available: Fig S1: Raman spectra, optical picture of film, UV/Vis of re-dissolved film; Fig. S2 XRD single crystals and film comparison; Fig. S3 additional FET data. See DOI: 10.1039/c4tc01134a

in air. This feature however, is not commonly shared by molecules used in organic electronics. This has prompted us to further develop the technique and we report here a general approach to the electrodeposition method that should be broadly applicable to all small molecules suitable for organic optoelectronic materials. This may prove particularly relevant for molecules unsuitable for solution processing or vapour processing due to their poor solubility or poor thermal stability respectively.

To establish our new methodology, we have studied perylene-3,4,9,10-bis(dicarboximide) (PTCDI) dyes, which have attracted interest due to their organic, electronic and optical properties.[20] In this paper we have studied the electrodeposition of *N*,*N*′-dibutylperylene-3,4,9,10-bis(dicarboximide) (*BuPTCDI*) and the properties of the resulting films. Most significantly, we present a general experimental approach to film processing that may be applied to any molecule under study for organic electronic materials, and suggest this as a novel processing route, complementary to typical solution or vapour deposition.

Experimental

All solvents used were dried and purified by passage through activated alumina columns using a solvent purification system. Chemicals used were purchased from Aldrich. The perylene diimide derivative, BuPTCDI, was prepared by the condensation of perylenetetracarboxylic dianhydride with *n*-butylamine as previously described by Schnurpfeil.[21] UV-Vis (THF): $\lambda_{max} = 270$, 357, 445, 475, 512 560 nm. CHN: cal: C 76.5%, H 5.2%, N 5.6% found: C 76.7%, H 5.6%, N 5.7%.

Electrodeposition

Sodium (*ca.* 200 mg, 8.7 mmol) was removed from the storage oil and placed in a test tube under N_2. The sodium was washed three times with degassed THF to remove any trace of the storage oil. The sodium was then evaporated to form a sodium mirror. BuPTCDI (44 mg, 0.087 mmol) suspended in dry degassed THF (3 ml) was added to the sodium and stirred under N_2 for *ca.* 240 min. The solution was then filtered into an electrochemical cell containing a solution of dry degassed acetonitrile (10 ml) containing 0.1 M $TBABF_4$ electrolyte. Film deposition was performed using a modified three electrode setup. FTO coated glass was used as the working electrode, a Pt pseudo reference electrode calibrated against ferrocene/ferrocenium was used with a standard Pt counter electrode. The latter was separated from the other electrodes by a porous glass frit. Electrochemistry experiments were performed using an Autolab type III potentiostat using GPES software. Electrochemical data are quoted against ferrocene/ferrocenium.

X-ray diffraction of the film was performed on a Bruker Discover D8 with a Cu $K_{\alpha 1}$ source and a scintillation detector. Raman spectra were recorded using a Horiba Labram HR high resolution spectrometer equipped with a mulitchannel detection system in the backscattering configuration. Solution emission spectra were recordeded at 77 K using a Fluoromax2 fluorometer controlled by ISAmain Software. The film excitation was performed using an Ar ion laser (514 nm). Photoelectrochemical measurements were performed by chopping a standard halogen cold mirror lamp with nominal light intensity of 100 mW cm^{-2}. Photocurrents were recorded using a three-electrode setup with a platinum wire counter electrode and a Ag/AgCl reference electrode in 0.1 M KCl aqueous solution with hydroquinone (0.1 M), a sacrificial electron donor. The film was treated with a napthol polymer to fill any holes present. To ensure that the film was not rendered completely passive the amount of current required to cover a third of the film's area was calculated. The film was then treated several times to make sure that the pores present were completely filled. Once the photocurrent response stopped increasing and started decreasing it suggested that the pores were full and that napthol was depositing on the film's surface. Field-effect transistor measurements were performed by electrochemically depositing BuPTCDI onto interdigitated-electrode substrates, consisting of a silicon wafer gate electrode with a SiO_2 layer as the insulating layer. Platinum source and drain electrodes were deposited onto the insulating layer with an electrode gap of 8 μm. Current–voltage measurements were recorded using a Keithley 2612A source probe measuring the drain current (I_{SD}) as a function of the applied source drain voltage (V_{SD}) at various applied gate voltages (V_{SG}).

SEM images were obtained using Philips XL30CP with PGT Spirit X-ray analysis and HKL Channel5 Electron Backscatter Diffraction (EBSD) systems. The specification of the instrument is a tungsten filament source electron gun and the resolution of the microscope is 3.5 nm at 30 kV using the secondary electron (SE) detector.

Results and discussion

Film deposition

Cyclic voltammetry performed on the neutral BuPTCDI molecule in THF, in which it shows slight solubility, revealed two reversible reductions at $E_{1/2} = -1.04$ V and $E_{1/2} = -1.36$ V (Fig. 1 inset). This is consistent with literature values of other PTCDI cores as the carbonyl groups allow for the formation of a stable

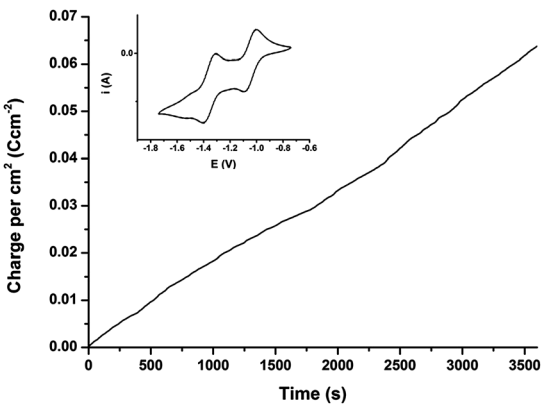

Fig. 1 Total charge per cm^2 passed during a 60 minute (3600 s) deposition holding the voltage at 0.30 V. Inset: cyclic voltammogram of BuPTCDI between −1.0 and 0 V in 0.1 M $TBABF_4$ in THF.

anion and dianion at reduction voltages depending on the specific groups present in the imide positions.[22] After preparing the solution of Na_x[BuPTCDI] as described in the Experimental section, the films were deposited by holding the working electrode at a constant voltage of 0.3 V for a set amount of time. The potential was chosen to give a reasonable rate of deposition without being sufficiently positive to damage the film, which was observed for example at +1.0 V. The steady current indicates that the film is sufficiently conducting to continue to enable further film growth on the deposited material. The exact stoichiometry of the reduction process is not known with the possibility of mono or dianionic BuPTCDI. The resulting films on FTO, prepared using different deposition times, were rinsed with acetonitrile and left in air to dry.

Raman spectroscopy of the deposited films was carried out and the resulting spectra (Fig S1, Table S1†) were compared with spectra of perylene-diimide thin films studied by Rodríguez-Llorente *et al.* to identify the main peaks of the BuPTCDI.[23] The peaks observed confirm that the thin film is composed of BuPTCDI showing similar proprieties to the film deposited by thermal evaporation. Furthermore, re-dissolution of the deposited film in excess THF showed the UV/Vis spectrum to be the same as that of the starting BuPTCDI (Fig. S1†). No evidence of any decomposition of the molecules was therefore observed during the electrodeposition process.

SEM imaging and thickness determination

Images of the films' surface and cross sections were obtained by scanning electron microscopy (SEM) which showed that the films contained various sizes of crystallites rather than a homogeneous flat surface (Fig. 2), and that the majority of the larger elongated crystallites appeared to grow perpendicular to the surface. This suggests that the material growth occurs preferentially upon BuPTCDI seed points rather than the bare FTO surface, such that micron scale film thickness is required before continuous film coverage is achieved. An SEM image of the cross section (Fig. 3) further shows that there are little or no crystallite structures parallel to the FTO surface, with most at angles greater than 45°.

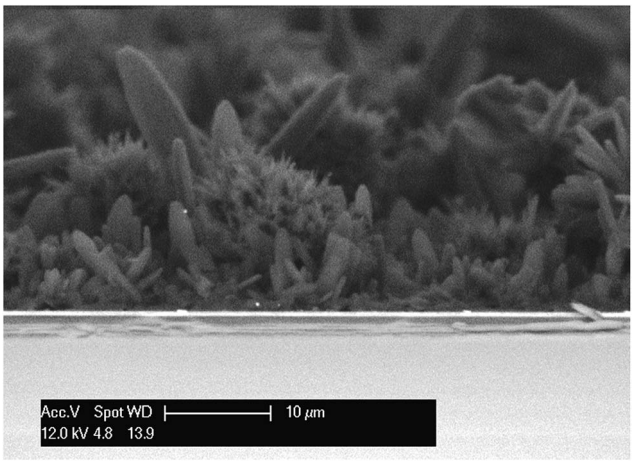

Fig. 3 SEM image of an electrodeposited BuPTCDI film cross-section (3600 s).

Elongated crystal growth perpendicular to the substrate is consistent with the electrochemical mechanism, with preferred growth, consistent with higher conductivity, along the needle axis. This can be attributed to cofacially stacked perylene cores with π-stacking in the perpendicular direction,[24] resulting in columnar stacks.[25]

The thicknesses of the films were determined by snapping the FTO substrate and analysing the cross-section of the film *via* SEM. Since the films were rough due to crystallite formation, an average thickness was estimated along with a minimum and maximum height. A plot of the average thickness, with minimum and maximum film thickness shown as vertical bars, against the charge per cm^2 passed during the electrochemical deposition is shown in Fig. 4.

As would be expected, the average thickness, as well as the range for the maximum and minimum thickness, increased with the amount of charge passed during deposition. By comparing the observed thickness with the charge passed per

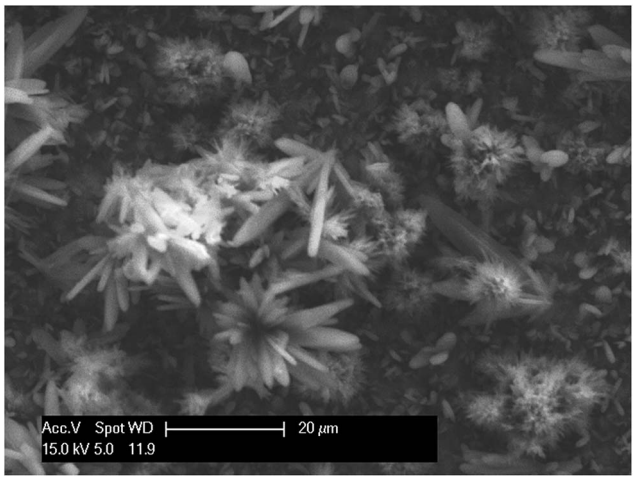

Fig. 2 SEM image of a BuPTCDI film surface on FTO after deposition (3600 s).

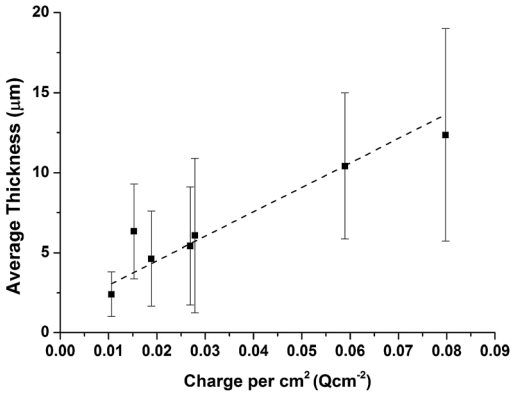

Fig. 4 Average film thickness *versus* charge per cm^2 passed. The bars represent maximum and minimum thicknesses observed across the film.

cm^2 it is possible to estimate the charge per cm^2 needed to produce a film of a determined thickness. A line of best fit applied to Fig. 4 gave the formula:

$$\text{Thickness(observed)}/\mu\text{m} = (153 \pm 18) \times \text{Charge}/(\text{C cm}^{-2})$$

Based on the crystal structure and assuming a one-electron redox process, the charge required to give a particular thickness of a dense film is described by the following formula:

$$\text{Thickness(theory)}/\mu\text{m} = (36.6) \times \text{Charge}/(\text{C cm}^{-2})$$

This indicates that the electrodeposited films are ~4 times thicker than would be expected from theory (or 8 time thicker for a two-electron redox process) for a dense single-crystal film with zero porosity. This is consistent with Fig. 2 and 3 which show that the electrodeposited film is not a uniform compact crystal and possess considerable unfilled volume. Although not possible to directly calculate, this also suggests that the electrodeposition is reasonably efficient with the reductive current leading to deposited film without excessive material being lost.

X-ray diffraction

The X-ray diffraction pattern of an electrodeposited BuPTCDI film on FTO was recorded and is shown in Fig. 5 below. Using Bragg's Law the *d*-spacings corresponding to the observed peaks were calculated (Table 1). The peaks present were compared to the simulated powder patterns of the two known single-crystal polymorphs obtained by Graser[26] and Mizuguchi[27] respectively, as well as XRD patterns of PTCDIs films deposited by other techniques found in literature. The cell dimensions of the two known single crystal structure are displayed in Table 2.

The XRD pattern of the film suggests a combination of two types of crystalline material. Two strong sharp peaks dwarf several broader peaks, suggesting that the films are made up of very crystalline structures as well as less crystalline material. This agrees with the cross-section SEM image in Fig. 3 where there is a combination of needle-like crystallites and smaller clusters of material. Additionally however, the dominance of the two peaks with *d*-spacings of 11.9 Å and 11.6 Å may suggest some preferred orientation within the more crystalline material.

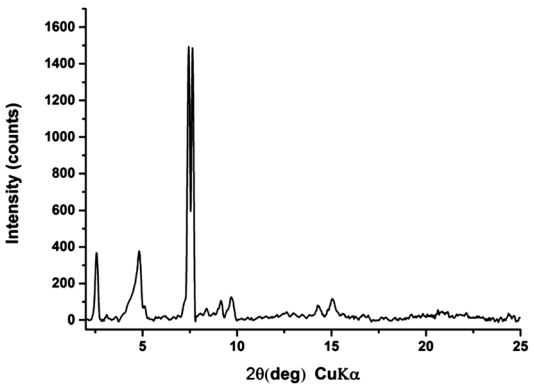

Fig. 5 XRD pattern of an electrodeposited BuPTCDI film.

Table 1 Calculation of *d*-spacings

BuPTCDI Film 2θ values	BuPTCDI Film *d* values (Å)
2.56	34.48
4.8	18.39
7.43	11.89
7.61	11.61
9.14	9.67
9.7	9.11
14.31	6.18
15.05	5.88

The electrodeposited film pattern shows that the packing of the molecules in the film is different to both known single crystal structures (Fig. S2†). It also does not show close similarities with thin-film structures of related RPCDTI molecules prepared by vapour deposition.[24,25] In both known crystal structures of BuPTCDI the perylene forms a herringbone-type packing with the smallest dimension for both structures being the π–π stacking of the cores at about 4.6 Å. Our film data however, do not enable resolution of a corresponding Bragg peak that would be expected at high angle.

For the electrodeposited film, the largest *d*-spacings, 34.2 Å and 18.2 Å are probably cell lengths, broadly comparable with one of the literature structures (Table 2) although with the longest axis somewhat longer, perhaps suggesting a smaller tilt angle of the BuPTCDI stacks compared with the herringbone packing seen by Graser and Mizuguchi.

Absorption spectroscopy

The solution UV/Vis absorbance of BuPTCDI in different solvents was measured and compared with the spectrum of the electrodeposited film (Fig. 6).

Perylene complexes in solution have a characteristic absorption between 445 nm and 520 nm and this is clearly observed in the two solution spectra. In addition, there is also the development of a shoulder in the DMSO spectrum, attributed to the π–π interactions of the molecules due to aggregation. The films of BuPTCDI clearly display absorbance across a similar spectral region consistent with the deposition of BuPTCDI molecules. The considerable band broadening is attributed to molecular packing leading to significant intermolecular interactions as would be expected in the solid state. This is accompanied by a red shift of the low energy absorption

Table 2 Cell dimensions of the two known crystal structures of BuPTCDI (Å)

	Graser[26] (Å)	Mizuguchi[27] (Å)
a	4.73	18.41
b	28.23	4.63
c	9.40	27.61

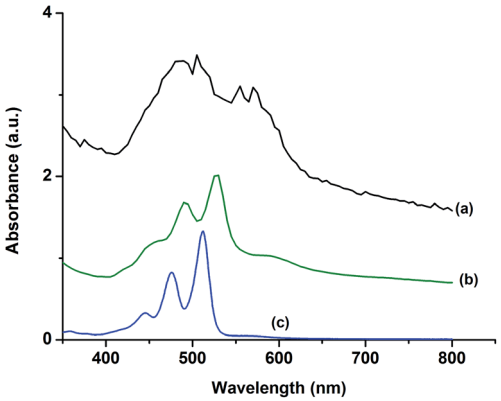

Fig. 6 UV/Vis spectra of BuPTCDI (a) electrodeposited on FTO, (b) dissolved in DMSO and (c) dissolved in THF.

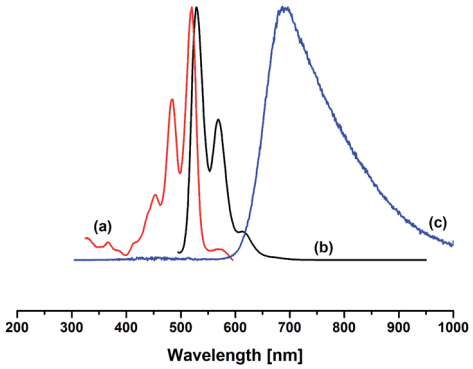

Fig. 8 Photoluminescence of BuPTCDI: (a) excitation spectrum in THF (monitored at 614 nm) (b) emission spectrum in THF (excited at 475 nm) (c) emission of an electrodeposited BuPTCDI film (excited at 514 nm).

onset compared to the spectra of the BuPTCDI in solution consistent with greater electron delocalisation from the intermolecular π-stacking.[28] Such absorption characteristics due to π–π interactions are important for organic electronics and agree with data of films deposited by vapour deposition.[29]

Comparing different depositions, we observe a general trend relating the absorbance and the quantity of material deposited (Fig. 7), with higher absorbance resulting from increased charge passed per cm^2. Numerical correlation between absorbance and charge passed was not possible however due to the significant scattering observed in many of the films that made accurate absorbance values not possible to determine. Some example films where scattering was less dominant are shown in Fig. 7.

Photoluminescence

The photoluminescent response of BuPTCDI was measured in solution and in an electrochemically deposited film (Fig. 8). BuPTCDI in solution shows fluorescence with emission maxima at 454, 485 and 520 nm. The proximity of the two peaks and the near mirror symmetry of the absorption and emission spectra suggest that there is little distortion in the configuration of the molecule when it is excited from the ground state to the excited state.[30] The emission spectrum of the film shows a very different response to the isolated molecule in solution. The spectrum of the film is a broad featureless band with a maximum around 679 nm, due to the excimers in the perylene film[28,31] and typical also of other thin solid films.[32] Again these results are consistent with deposition of intact perylene molecules showing considerable intermolecular interaction in the film.

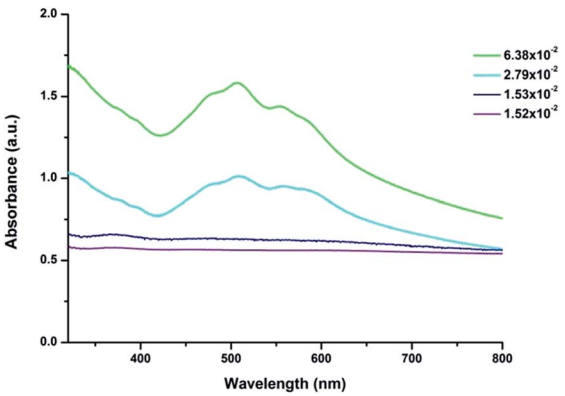

Fig. 7 Absorbance of several different films deposited with differing total charge passed (Ccm^{-2}, indicated by the inset) showing increased absorbance for the thicker films.

Charge mobility and photoconductivity

The electrodeposition technique was also used to grow films of BuPTCDI on interdigitated-electrode substrates suitable for study of field-effect transistor (FET) properties. The charge transport characteristics of several different PTCDI compounds have previously been studied[24,33–36] and have shown that most PTCDIs show electron transporting properties. In previous work on vapour-deposited BuPTCDI, the measured current has shown a typical field-effect response with a range of μFET from 4×10^{-6} cm^2 V^{-1} s^{-1} to 0.6 cm^2 V^{-1} s^{-1}.[35,36]

Films were deposited directly onto platinum-electrode substrates and were then held at a constant voltage of 0 V until they showed no more signs of decharging. In order to observe a field-effect of the conductivity, it is essential to minimise any doping that may remain from the deposition process which would result in a high off-current and holding the films at a low voltage ensured that the films were not charged. Field-effect measurements were carried out on a freshly deposited BuPTCDI film on interdigitated platinum-electrode substrates (Fig. 9).

Fig. 9 shows the current measured between the source and drain electrodes as a function of the applied source–drain voltage for increasing source–gate voltages. The currents measured show a stepwise increase in current with the increased source–gate voltage, indicating that the applied source–gate voltage is affecting the flow of electrons in the deposited film. The current measured is also typical of bulk transport of electrons with a large off-current, which is likely due to the relative thickness of the film. These observations agree with the SEM images which suggest that the crystals grow perpendicular to the substrate, hence complete coverage of the

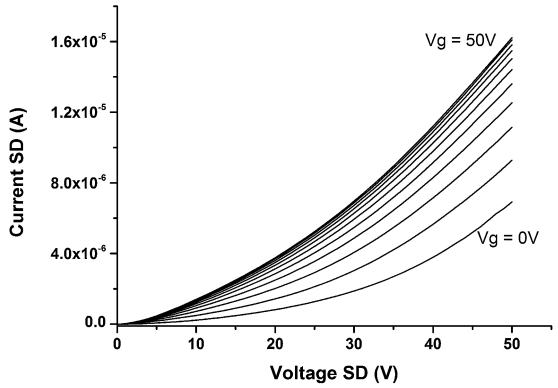

Fig. 9 Drain current *vs.* source–drain voltage curves at various source–gate voltages for BuPTCDI field effect transistors.

gaps in the interdigitated electrode requires a thick film. The observed mobility is also expected to be low due to the undesirable orientation of the long crystallite axes perpendicular to the source–drain direction.

Extraction of an accurate mobility from the data is somewhat compromised by the large off-current, however an estimate can be made. Applying a linear fit to the current, the calculated electron mobility of the material is $\mu FET = 2.3 \times 10^{-8}$ cm^2 V^{-1} s^{-1}. This is lower than previously-reported field-effect mobilities measured for perylenediimide molecules, although this is as expected for the reasons described above. The current measured decreases over time, which suggests that there is some degradation in the device (Fig. S3†). This is consistent with previous studies of related molecules, in which the field-effect disappeared due to degradation between the FET substrate and the deposited film.[34]

To further probe the electronic properties of the films, photoelectrochemical studies were performed by monitoring the electrochemical response of the film on FTO under chopped illumination by a halogen light at 100 mW cm^{-2}. To minimise any effect at the bare electrode, the film was treated with naphthol to fill any holes between the BuPCDTI crystallites. The response is plotted in Fig. 10 and shows an increase in current when the film is exposed to light and a subsequent decrease when the light is off. The photocurrent response of the untreated film shows a significant off-current, contrasting with the naphthol-treated film where the off-current is suppressed (Fig. 10). This indicates that the untreated films are porous enough for the electrolyte to directly interact with the FTO substrate irrespective of illumination. These observations are consistent with the crystalline, rather than continuous nature of the films shown by SEM (Fig. 2 and 3). The photoelectrochemical response again illustrates in general the formation of a light-absorbing BuPTCDI film able to transport charge.

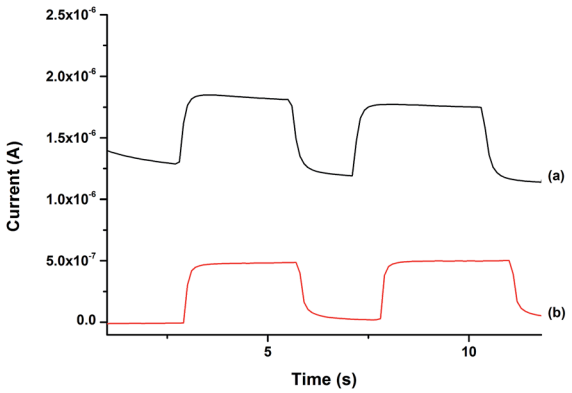

Fig. 10 Current against time response at 0.1 V to a chopped halogen lamp showing higher current with light on: (a) untreated film and (b) naphthol-treated film.

Conclusions

Electrochemical deposition has been developed as a novel technique for the formation of *N*,*N*′-dibutylperylene-3,4,9,10-bis(dicarboximide) films. The chemical reduction of the PTCDIs to enable dissolution, followed by the electrochemical oxidation onto FTO substrates offers a unique method of deposition as an alternative to other solution and vapour processing techniques.

Several methods were applied to the deposited films to analyse their optical and electronic properties and to compare them to the powder form of the molecule and to films deposited by other techniques. Raman and UV/Vis absorption spectroscopy confirmed that the electrodeposited films include the intact molecules, with similar properties to thin films deposited by other techniques. SEM imaging and X-ray diffraction showed the morphology of the film was polycrystalline and included elongated crystallites perpendicular to the FTO substrate. This perpendicular growth is likely the result of the stacked perylene π-cores giving higher conductivity, hence a preferential growth direction perpendicular to the substrate. A plot of average thickness against charge per cm^2 enables prediction of film thickness, controlled by the amount of current passed. The electronic properties of the films measured on electrodeposited field effect transistors showed bulk electron transport and evidence of controlled doping *via* application of a potential at the gate electrode. On FTO, the films showed visible-light photoconductivity.

Although the material properties of the BuPTCDI film are not optimised for device function, in particular due to the crystalline rather than continuous nature, the key demonstration of this work is a novel approach to film deposition in organic (opto)electronic materials. The electrodeposition method may in principle be applied to any electroactive molecule, offering a solution-processing route for insoluble or involatile materials, without the need for extensive alkyl substitutents to achieve high solubility and without the need for thermal stability to enable vapour processing. In particular, we see opportunities for this method as a complementary approach where the established deposition techniques are not suitable. For example, electrodeposition may be used to deposit organic materials on non-planar surfaces such as mesoporous solids, and further work is ongoing to explore other molecules, substrates and devices.

Acknowledgements

We thank Fonds National de Luxembourg for a studentship for EA.

Notes and references

1 (*a*) F. C. Krebs, *Sol. Energy Mater. Sol. Cells*, 2009, **93**, 394–412; (*b*) Y. Wen, Y. Liu, Y. Guo, G. Yu and W. Hu, *Chem. Rev.*, 2011, **111**, 3358; (*c*) A. C. Arias, J. D. MacKenzie, I. McCulloch, J. Rivnay and A. Salleo, *Chem. Rev.*, 2010, **110**, 3.

2 Y. Lin, P. Cheng, Y. Liu, X. Zhao, D. Li, J. Tan, W. Hu, Y. Li and X. Zhan, *Sol. Energy Mater. Sol. Cells*, 2012, **99**, 301–307.

3 H. Shang, H. Fan, Q. Shi, S. Li, Y. Li and X. Zhan, *Sol. Energy Mater. Sol. Cells*, 2010, **94**, 457–464.

4 Z. Hu, J. Zhang, S. Xiong and Y. Zhao, *Sol. Energy Mater. Sol. Cells*, 2012, **99**, 221–225.

5 S. E. Shaheen, R. Radspinner, N. Peyghambarian and G. E. Jabbour, *Appl. Phys. Lett.*, 2001, **79**, 2996–2998.

6 N. A. Azarova, J. W. Owen, C. A. McLellan, M. A. Grimminger, E. K. Chapman, J. E. Anthony and O. D. Jurchescu, *Org. Electron.*, 2010, **11**, 1960–1965.

7 C. N. Hoth, S. A. Choulis, P. Schilinsky and C. J. Brabec, *Adv. Mater.*, 2007, **19**, 3973–3978.

8 F. C. Krebs, M. Jørgensen, K. Norrman, O. Hagemann, J. Alstrup, T. D. Nielsen, J. Fyenbo, K. Larsen and J. Kristensen, *Sol. Energy Mater. Sol. Cells*, 2009, **93**, 422–441.

9 B. Kippelen and J.-L. Bredas, *Energy Environ. Sci.*, 2009, **2**, 251–261.

10 J. K. Kim, W. Kim, D. H. Wang, H. Lee, S. M. Cho, D.-G. Choi and J. H. Park, *Langmuir*, 2013, **29**, 5377–5382.

11 D. B. Mitzi, *Adv. Mater.*, 2009, **21**, 3141–3158.

12 W. E. Buschmann, S. C. Paulson, C. M. Wynn, M. A. Girtu, A. J. Epstein, H. S. White and J. S. Miller, *Chem. Mater.*, 1998, **10**, 1386–1395.

13 D. Lincot, *Thin Solid Films*, 2005, **487**, 40–48.

14 C. J. Hibberd, E. Chassaing, W. Liu, D. B. Mitzi, D. Lincot and A. N. Tiwari, *Prog. Photovoltaics*, 2010, **18**, 434–452.

15 A. P. Samantilleke, M. Sahal, L. Ortiz, M. F. Cerqueira and B. Marí, *Thin Solid Films*, 2011, **519**, 7272–7275.

16 A. Zaban and Y. Diamant, *J. Phys. Chem. B*, 2000, **104**, 10043–10046.

17 Y. Diamant and A. Zaban, *J. Electrochem. Soc.*, 2001, **148**, C709–C714.

18 S. Dalgleish, H. Yoshikawa, M. M. Matsushita, K. Awaga and N. Robertson, *Chem. Sci.*, 2010, **2**, 316–320.

19 S. Dalgleish, K. Awaga and N. Robertson, *Chem. Commun.*, 2011, **47**, 7089–7091.

20 F. Gao, Y. Zhao and W. Liang, in *The Journal of PhysicalChemistry B*, American Chemical Society, 2011, pp. 2699–2708.

21 G. Schnurpfeil, J. Stark and D. Wöhrle, *Dyes Pigm.*, 1995, **27**, 339–350.

22 G. Türkmen, S. Erten-Ela and S. Icli, *Dyes Pigm.*, 2009, **83**, 297–303.

23 S. Rodríguez-Llorente, R. Aroca and J. Duff, *Spectrochim. Acta, Part A*, 1999, **55**, 969–978.

24 R. J. Chesterfield, J. C. McKeen, C. R. Newman, C. D. Frisbie, P. C. Ewbank, K. R. Mann and L. L. Miller, *J. Appl. Phys.*, 2004, **95**, 6396–6405.

25 C. W. Struijk, A. B. Sieval, J. E. J. Dakhorst, M. van Dijk, P. Kimkes, R. B. M. Koehorst, H. Donker, T. J. Schaafsma, S. J. Picken, A. M. van de Craats, J. M. Warman, H. Zuilhof and E. J. R. Sudhölter, *J. Am. Chem. Soc.*, 2000, **122**, 11057–11066.

26 E. Hadicke and F. Graser, *Acta Crystallogr., Sect. C: Cryst. Struct. Commun.*, 1986, **42**, 189–195.

27 J. Mizuguchi, *Z. Kristallogr. New Cryst. Struct.*, 2003, 131–133.

28 V. Parra, T. Del Cano, M. L. Rodriguez-Mendez, J. A. de Saja and R. F. Aroca, *Chem. Mater.*, 2003, **16**, 358–364.

29 J. Mizuguchi, *Dyes Pigm.*, 2006, **70**, 226–231.

30 T. Kircher and H. G. Lohmannsroben, *Phys. Chem. Chem. Phys.*, 1999, **1**, 3987–3992.

31 D. Schlettwein, A. Back, B. Schilling, T. Fritz and N. R. Armstrong, *Chem. Mater.*, 1998, **10**, 601–612.

32 W. Yip and D. H. Levy, *J. Phys. Chem.*, 1996, **100**, 11539–11545.

33 R. J. Chesterfield, J. C. McKeen, C. R. Newman, P. C. Ewbank, D. t. A. da Silva Filho, J.-L. BrÃ©das, L. L. Miller, K. R. Mann and C. D. Frisbie, *J. Phys. Chem. B*, 2004, **108**, 19281–19292.

34 G. Horowitz, F. Kouki, P. Spearman, D. Fichou, C. Nogues, X. Pan and F. Garnier, *Adv. Mater.*, 1996, **8**, 242–245.

35 D. Lehmann and D. R. T. Zahn, *Appl. Phys. A: Mater. Sci. Process.*, 2009, **95**, 203–207.

36 P. R. L. Malenfant, C. D. Dimitrakopoulos, J. D. Gelorme, L. L. Kosbar, T. O. Graham, A. Curioni and W. Andreoni, *Appl. Phys. Lett.*, 2002, **80**, 2517–2519.